RAPID SCANNING LONGWAVE INFRARED ABSORPTION SPECTROSCOPY OF CHEMICAL NERVE AGENT SIMULANT DESTRUCTION IN FIREBALLS

BY

AUSTIN JOSIAH BUTLER

DISSERTATION

Submitted in partial fulfillment of the requirements
for the degree of Doctor of Philosophy in Mechanical Engineering
in the Graduate College of the
University of Illinois Urbana-Champaign, 2022

Urbana, Illinois

Doctoral Committee:

Professor Nick G. Glumac, Chair and Director of Research
Professor Emeritus Herman Krier
Professor Tonghun Lee
Professor Gregory S. Elliott

Abstract

Chemical warfare using highly toxic organophosphorus nerve agents poses an extreme threat to national security, in part because chemical weapons of mass destruction are more readily attainable than nuclear weaponry. Study of the destruction of such compounds is necessary to developing effective countermeasures, and destruction by exposure to combusting fireballs is a chief area of interest. Absorption spectroscopy targeted at the longwave infrared "fingerprint" region is a common technique used in the measurement of nerve agent and simulant materials due to the wealth of information that can be obtained from measurements taken over a wide spectral range. Difficulties arise in the area of fireball destruction as these events tend to destroy the substances on the order of 10^{-3} to 10^{-2} seconds, too quickly for traditional longwave Fourier Transform Infrared spectroscopy systems, limited to a few hundred hertz, to monitor.

In this research, a new diagnostic system was designed, constructed, and validated which allowed for kilohertz speed measurement of the longwave infrared region. The system, a dispersive scanning spectrometer using a rapidly rotating grating, was inspired by the work of Pimentel and other researchers from the 1960s. In addition to a 1.2 kHz average repetition rate, the scanning spectrometer is capable of scanning the infrared region of 850cm^{-1} to 1350cm^{-1} with a spectral resolution better than 10cm^{-1}. This developed system was used to collect a robust set of benchmark data for the validation of computational models of the destruction of the nerve agent simulant Diisopropyl Methylphosphonate (DIMP) inside fireballs. An experimental apparatus and test procedures were developed to facilitate the measurement of DIMP destruction in constant volume fuel and oxidizer "closed bombs." Data were obtained for four distinct closed bomb conditions, and supplemental data were obtained from a series of six tests using small scale explosive charge detonations. Collected data has been analyzed to ensure its quality as a robust set of benchmark data. Experimental repeatability and measurement variability across multiple repeat tests is discussed, and time resolved absorption spectra are investigated for indicators of potential decomposition products.

for Nova

Acknowledgments

I would first like to thank and acknowledge my advisor and co-advisor, Professor Nick Glumac and Professor Herman Krier. Prof. Glumac taught me a great deal of things during my time at the UIUC. He introduced me a field of science I never considered prior but that I cannot imagine not doing now. It has truly been a remarkable experience working for someone who is so clearly an expert in his field. I thank him for putting me in a position were I'm not only *not* discouraged from lighting things on fire or exploding them but am instead actively encouraged to do so. I thank him for his guidance and for continuing to believe in me through my times of trouble.

I thank Prof. Krier for his guidance throughout my graduate student career and his sage wisdom on how to be a better scientist and how to have a long and happy marriage.

Next I must thank my family. My mom, dad, my sister Jacqueline, and my brothers Michael, Robert, and Logan. I would not be who I am or where I am today were it not for all of you. More specifically I would like to thank my dad for the constant support of my academic career, emotional and financial. It's hard to recall life before graduate school, but I think it was you who put the idea of a graduate degree in my head to begin with.

I must also thank the two teachers who have had the most positive impact on my academic career. The first is Jeremy Raper, my High School introduction to engineering teacher and robotics team manager. I was fairly certain of pursuing an engineering degree from a young age, but your classes solidified the choice for me. The other is Dr. Thomas Burch, who taught me during my bachelors at Auburn University. I very much enjoyed your style of teaching and appreciate your guidance in the process of deciding on pursuing a graduate degree.

To all of my fellow graduate students who I have had the pleasure of working alongside of during these past years, I thank you for the comradery, commiseration, celebrations, and cooperation. For that very special group who were there when I started in 2018, I consider the times I spent with you to be "the good ol' days." LtCdr. (US Navy Ret.) Dr. David Amondson, Ph.D., the man who, on top of his title, was pizza and ice cream chef, child at heart, and an invaluable source of experience and grounding. Lt. Dan Meaney, the man who taught me that when the curves look good, that's all you really need. Joel Schwallier, the curator of the timeless collection of Joel S.tool Samples. Rylie Lodes, the man who showed us all just how much smoke you could cram into a

single chicken wing. Nick Poirier, the guy that refused to stand with Blitzchung. Emily Weerakkody, crossword master, proofreader, and the woman that would eat a whole shrimp head and fish brain and look at me like *I* was weird because I didn't. Terry Yu, the guy that absolutely had the power. Lastly, Damon Chen, the guy I have shared my entire graduate college career with and who managed to blow apart two different trash cans.

I cannot forget those who have come and gone while I have been here. Michael Ho, the guy that would take an hour and a half to eat his meal only to eat an entire mochi in one bite. William Morningstar, the party animal who spent 16 continuous hours at my Bloody Mary party, introduced me to the joys of snowboarding concussions, and was a great friend to me and my dog, Nova. I have been blessed to have known so many great people. I have truly enjoyed working with and alongside you all. I will always remember all the cookouts, hangouts, and crossword puzzles.

For those youngsters that still have a ways to go. Lake Spradling, the world's fastest man who has the $1000s in speeding tickets to prove it. Sam Brunkow, the world's biggest sigher. Colton Willhardt, the world's most dedicated sometimes pescatarian. Finally, Skyler Hausback, the world's biggest liberal. You guys have brought some enjoyable life to the workplace these past few months, and I wish you all the best of luck.

Finally, and dare I say *most importantly*, I thank my wife, Cary. Cary, as you are well aware, graduate school has not been a smooth ride and instead full of unexpected roadblocks and hardships. I am doubtful that I would have made it through these past few years without your steadfast love and support, and I thank you dearly for that. I thank you for those late nights you spent with me during the hardest times of this whole process, and I thank you for bearing the brunt of the day-to-day responsibilities allowing me to focus on finishing during this intense final stretch. I hope to repay you in kind soon. There is no one else I would rather have experienced this journey with, and I am excited to see what life holds in store for us next.

I love you, Cary, forever and for always.

Table of Contents

List of Figures

CHAPTER 1: INTRODUCTION AND MOTIVATION

"Whether or not gas will be employed in future wars is a matter of conjecture. But the effect is so deadly to the unprepared that we can never afford to neglect the question." - General John J. Pershing

1.1. Motivation

Organophosphorus chemical nerve agents such as Sarin are highly toxic chemicals with the potential to be made into indiscriminate weapons of mass destruction (WMD). Despite widespread banning of such weapons, the threat of chemical attacks from antagonistic organizations remains present. As such, chemical WMD pose an extreme risk to national security, motivating the study of such compounds to inform the development of effective countermeasures. Primary interest in the Counter WMD (CWMD) research community exists in the study of how such compounds can be neutralized so as to render them harmless, but developing a full understanding of such processes as they relate to any real-world neutralization scenarios requires wide reaching study. Such processes are diverse in the method of neutralization and relevant time scales over which neutralization can occur span many orders of magnitude. Therefore, there is great interest in the development of new diagnostic tools which are able to capture experimental data at previously unattainable small timescales and in the data collected from those tools.

1.2. Historical Background

Chemical warfare, the act of using hazardous chemical compounds to kill or otherwise incapacitate enemy combatants, has existed for thousands of years [1]. However, it was not until the First World War that chemical warfare was waged on a large scale. Even before the first chemical attack of the war, attributed to the German chlorine gas attack near Ypres in 1915 [2], fear over the potential use of chemicals in war led to the Hague Declaration of 1889 [3]. In spirit, this declaration banned the use of chemical warfare, but the text said, "… to abstain from the use of projectiles the sole object of which is the diffusion of asphyxiating or deleterious gases." As such, nations found ways to implement chemical weaponry while adhering to the letter of the law. Throughout the conflict, chemical weapons making use of chlorine, mustard, and phosgene gas were used by both sides, resulting in an estimated 1.3 million casualties, about 91,000 of these being deaths [4]. The war

marked the beginning of a chemical arms race as both sides strove to find more effective chemicals, new methods of deployment, and new defenses for chemical warfare.

Following WWI, the Geneva Protocol more explicitly banned the use of chemical weapons, with the exception that they were permitted in retaliation to a chemical attack [5]. With nothing hampering the development and stockpiling of weapons, the arms race continued. Between 1936 and 1949, German scientists discovered and developed a new breed of chemical agent, the "G-series" organophosphorus nerve agents. These compounds, including Tabun (GA), Sarin (GB), Soman (GD), and cyclosarin (GF), were tens to hundreds of times more lethal than anything used prior, and the compounds alone are considered weapons of mass destruction by the United Nations [6]. Sarin is perhaps the most widely recognized of these agents, and its selection as a weapon stemmed from the chemical's combination of high toxicity and high volatility. All of these agents exist as liquids under normal conditions, so high volatility means that Sarin can easily to turn into a gas and cause much more damage.

Despite being banned, these nerve agents have been used aggressively several times since their development. A variety of chemical weapons were used in the Iran-Iraq War between 1980 and 1988, with the Halabja chemical attack of 1988 resulting in an estimated 5000 casualties [7], [8]. Later, a Japanese terrorist cult released an impure version of Sarin, killing 13 people [9]. Even though the production and stockpiling of chemical agents was banned in 1997 [10], there have been several instances of suspected chemical attack in Syria since 2013, with the use of Sarin being confirmed by the UN [11].

1.3. Agent Defeat

What history shows is that signed treaties do not ensure safety from chemical attack, and the development of countermeasures against such attacks is an unfortunate necessity. Today, the largest threat of chemical attack results from the use of organophosphorus nerve agents due to their high toxicity and demonstrated use in recent years. In the world of CWMD, the term "agent defeat" is often used to describe the neutralization of chemical agents within these countermeasures.

1.3.1. *Agent Defeat Scenarios*

Despite the wide-scale shunning of chemical weapons, many stockpiles exist worldwide which pose a threat to U.S. national security, requiring that countermeasures be devised for a variety of

situations. Three main groupings of agent defeat scenarios can easily be imagined: peaceful stockpile destruction, chemical attack defense, and aggressive stockpile destruction. Peaceful destruction of stockpiles pertains to those agencies which willingly destroy their chemical stockpiles in accordance with the Chemical Weapons Convention of 1997 [10]. Primarily, work relating to this scenario focuses on ensuring that the agent defeat process fully destroys the compounds and that no dangerous chemicals are produced as a result of the process. To date, nearly all of the chemical weapon stockpiles of agreeing nations have been eradicated, so more focus is placed on the other two scenarios.

In the realm of chemical attack defense, the focus would be towards destruction of an agent that has already been dispersed or is actively being dispersed. In such an event, rapid response is necessary as the problem becomes increasingly difficult to neutralize the more time the agent is allowed to disperse. The final strategy follows "the best defense is a good offense" line of thinking and involves the preemptive destruction of an enemy organization's chemical stockpile. In taking such an action, the goal would be to completely destroy a large stockpile of chemical agent with the requirement that the agent is not inadvertently released in the process. Such stockpiles may be located near or within civilian population centers, making a failed destruction attempt functionally the same as a chemical attack on that population using that stockpile.

1.3.2. *Agent Defeat Strategies*

Given the wide range of potential defeat scenarios, and the large cost of life associated with ineffective agent defeat, it becomes necessary to develop many agent defeat strategies. In the field of chemical agent defeat there are three defeat mechanisms which garner the most attention: chemical, catalytic, and thermal.

Chemical agent defeat primarily involves reducing toxicity of the agent through exposure to a chemical solution. Often times these processes occur for chemical agents in the liquid phase, and the destruction reactions are slower than the other two defeat mechanisms [12], [13]. As such, chemical defeat applies more to decontamination of environments or bulk liquid agent stockpile destruction rather than rapid agent defeat situations.

Catalytic agent defeat is a form of rapid agent defeat that utilizes catalysts to adsorb agent molecules and promote their destruction [14], [15]. These processes can occur either in solution or

for agents in the gaseous phase, and the process can be effective even at ambient temperature. Metal oxides are often used as destruction catalysts. These include aluminum, magnesium, iron, and titanium oxides [16], [17], and the catalytic defeat of metal oxides can couple well with practical thermal defeat methods, which will be discussed next, through the burning of metal particles.

Finally, thermal destruction of organophosphorus compounds makes use these compounds' general instability at elevated temperatures and/or reactivity in flames. Consequently, decomposing nerve agents via an explosively generated fireball is a practical agent defeat mechanism that is readily applicable to real world scenarios. Explosive charges necessary to create fireballs can be delivered to remote target locations through ballistic means, and metal additives or the explosive's metal casing can form the catalytic oxides to further increase defeat effectiveness. However, caution must be observed due to the possibility of the pressure wave generated by the explosion dispersing the agent away from the fireball. This dispersion might lead to a failed defeat attempted, or worse, an inadvertent release [18]. While catalytic and thermal defeat can be coupled in practice, here the focus is on thermal defeat only. The goal is to deepen the understanding of thermal defeat of organophosphorus agents through experimental measurement to ultimately improve the effectiveness of explosive decomposition.

1.3.2.1. Nerve Agent Simulants

Experimental testing of highly toxic chemical nerve agents is not viable due to restrictions on acquiring the agents and the high risks associated with handling them. Some research efforts have been undertaken on destruction of the true agents [19]–[21], but most work is done on relatively non-toxic simulant materials. There are many simulant options to choose from, and choice of

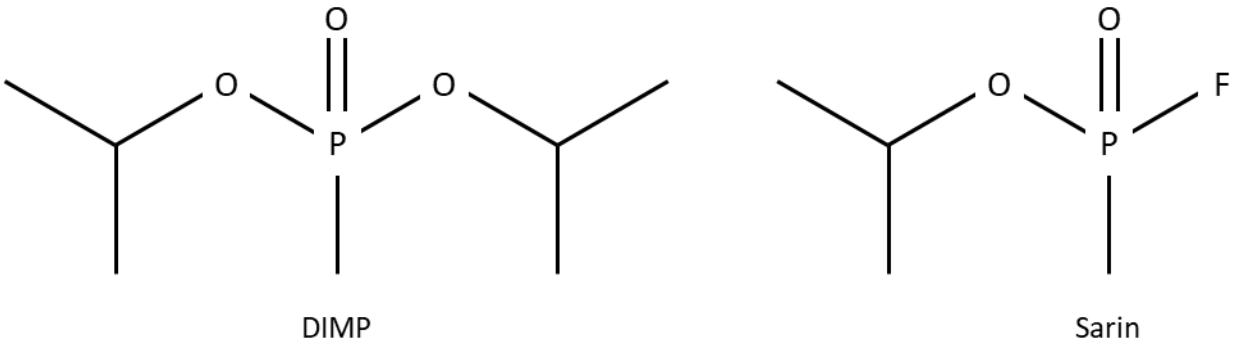

Figure 1.1 - DIMP and Sarin skeletal chemical structure [22]

simulant is often dictated by the nerve agent being simulated. A common choice among work related to Sarin, as in this work, is the compound Diisopropyl Methylphosphonate (DIMP); however, since no one simulant can fully mimic the behavior of the true agent, use of several simulants is ultimately necessary. When limiting a study to a single simulant, DIMP is a good choice for Sarin given the similarity in chemical structure as shown in Figure 1.1 [22]. DIMP differs from Sarin only in that the Fluorine atom, the main source of Sarin's toxicity, is replaced by a second isopropyl group. This is attractive given that a primary step in thermal decomposition for both chemicals involves the separation of an isopropyl group from the molecule.

1.3.2.2. Pyrolysis vs. Combustion Decomposition

In thermal defeat of chemical agents an important distinction to note is the difference between "thermal decomposition" and "combustion destruction." Thermal decomposition of organophosphorus compounds, as studied by Zegers and Fisher [23] and Yuan and Eilers [24], involves the compounds undergoing the process of pyrolysis. Pyrolysis involves heating the compounds and allowing them to break apart due to their instability at elevated temperatures. Such unimolecular decomposition has been studied for DIMP resulting in a proposed decomposition mechanism by Zegers and Fisher, and a modified mechanism by Yuan and Eilers. The modified mechanism is given in Figure 1.2, where Zegers and Fisher's original mechanism is marked. These mechanisms suggest that primary decomposition products of interest include the phosphorus compounds isopropyl methylphosphonate (IMP) and methylphosphonic acid (MPA), and the hydrocarbons isopropyl alcohol (IPA) and Propene.

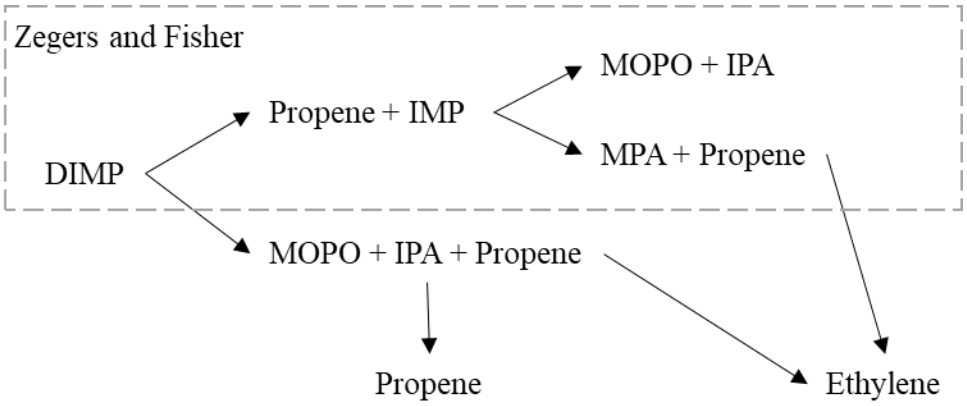

Figure 1.2 - DIMP pyrolysis decomposition pathways, taken from [24].

Alternatively, during the complex chemical reactions that occur during combustion reactions, a class of short-lived, highly reactive chemical species called combustion radicals are formed. Radicals play a critical role in the combustion process by breaking the chemical bonds in fuels and oxidizers, which is necessary to continue the reaction. However, these radicals will also break down the bonds in the organophosphorus compound in ways significantly different than pyrolysis. Previous works have concluded that, although high temperatures exist in flame environments, decomposition through thermal pathways is insignificant in flames with sufficiently high concentrations of the radical species H, O, and OH [25]. Instead, in such environments, decomposition is dominated by radical destruction. An alternate pathway comprised of radical destruction reactions is proposed by Korobeinichev [25] with the following key reactions:

$$DIMP + OH \rightarrow \boldsymbol{IMP} + \boldsymbol{C_3H_7O} \quad (1)$$

$$DIMP + H \rightarrow IMP + \boldsymbol{C_3H_7} \quad (2)$$

$$DIMP + OH \rightarrow PO(CH_3)(C_3H_7O)C_3H_6O^{\cdot} + H_2O \quad (3)$$

$$PO(CH_3)(C_3H_7O)C_3H_6O^{\cdot} + OH \rightarrow IMP + C_3H_6O \quad (4)$$

$$C_3H_7O + OH \rightarrow \boldsymbol{C_3H_6O} + H_2O \quad (5)$$

$$C_3H_7O + H + M \rightarrow \boldsymbol{C_3H_8O} + M \quad (6)$$

$$IMP + OH \rightarrow \boldsymbol{MPA} + C_3H_7O \quad (7)$$

$$IMP + H \rightarrow MPA + C_3H_7 \quad (8)$$

Bolded in the proposed reactions are key intermediates product species, including IMP and MPA, as seen in thermal decomposition, and a series of hydrocarbon species. Mass spectrometry was used to determine the presence of these chemical species in the flames studied, so some uncertainty exists in the identification of hydrocarbons. Still, the following assignments have been made: C_3H_8O is isopropyl alcohol, C_3H_7 is isopropyl radical, and C_3H_6O is acetone.

An important factor to determine is which mechanism, thermal or radical decomposition, prevails inside fireballs. A comparison of the two proposed mechanisms reveals that the presence or absence of a few key species could provide insight as to which mechanism is dominant. Propene is notably absent from the radical destruction mechanism, so its detection would be a good

indicator of thermal decomposition. Conversely, C_3H_6O, C_3H_7, and C_3H_7O are potential indicators of radical destruction

1.3.3. *Gap in Knowledge*

Demonstration of a sufficient level of knowledge of thermal agent defeat is best achieved through the development of predictive computational models. Development of advanced thermal agent defeat strategies in CWMD scenarios is also greatly improved by these models due in part to the cost of performing large scale explosive testing and the hazards of experimenting on nerve agents (or even their simulants). Such computational models are under development by CRAFT Tech Inc. in conjunction with this research, but these must be validated against experimentally obtained data to be trustworthy. The focus of many research efforts, both concluded and ongoing) has been collecting experimental data on the decomposition of organophosphorus compounds for this very purpose.

DIMP has already been studied widely across different agent defeat mechanisms, but the data available in the realm of thermal defeat is incomplete. The existing work in this realm was summarized by Senyurt et al. and is presented in Figure 1.3 . Experiments that have already been performed include laser heating [22], shock tube heating [26], pyroprobe heating [24], and relatively low temperature flow reactor heating [27]. Clearly, these works span a wide range of temperature and time regimes; however, there is a notable gap in the data for exposure times on the order of ones to tens of milliseconds and for conditions which one might expect inside an explosive fireball.

The lack of data in this region is primarily due to the difficulty of taking appropriate measurements on the millisecond time scales. Based on the existing data, a fireball might be expected to decompose DIMP on the order of 10ms, and, while data have been collected at shorter time scales, the scope of information obtained from very short time scale measurements is very limited. Laser heating methods which produce very short-lived high temperatures are restricted in their measurements to probing post heating products with no time-resolved information. Shock tube measurements which occur on longer time scales are able to produce time-resolved measurements, but these measurements are often limited to probing a single chemical species, not a wide variety of potential species.

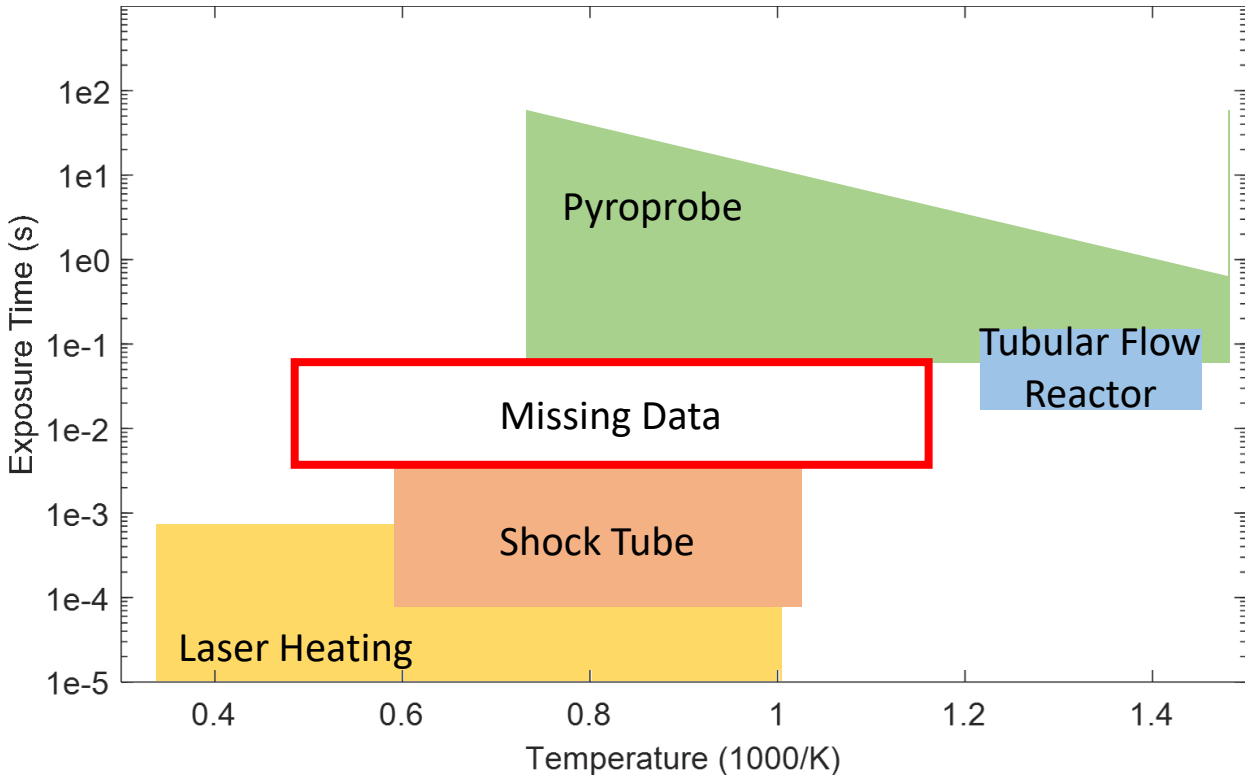

Figure 1.3 – Approximate temperature and exposure time regimes for DIMP thermal decomposition studies, taken from Senyurt et al. [27]

Considering the different destruction pathways described, confirming that a computational model predicts the correct pathway would be beneficial to its validation. As such, in these environments it is necessary to collect data that can potentially measure the presence of a variety of potential product species. The goal of this work is to collect data on DIMP decomposition when exposed to explosive fireball conditions without the limitations of existing short time-scale measurements.

1.4. Technical Background

Absorption spectroscopy is often used in the study of these chemicals and is a primary feature of this work as well. A brief overview of spectroscopy is provided [28].

1.4.1. *Fundamentals of Absorption Spectroscopy*

Spectroscopy is a powerful diagnostic technique that can be used to probe parameters such as temperature and species concentrations in a non-invasive manner. By definition, spectroscopy is the study of the interaction of light with matter. Light interacts with matter through two fundamental processes: absorption and emission, as represented in Figure 1.4. In absorption, light energy carried in a photon may be transferred into an atom or molecule, consuming the photon and

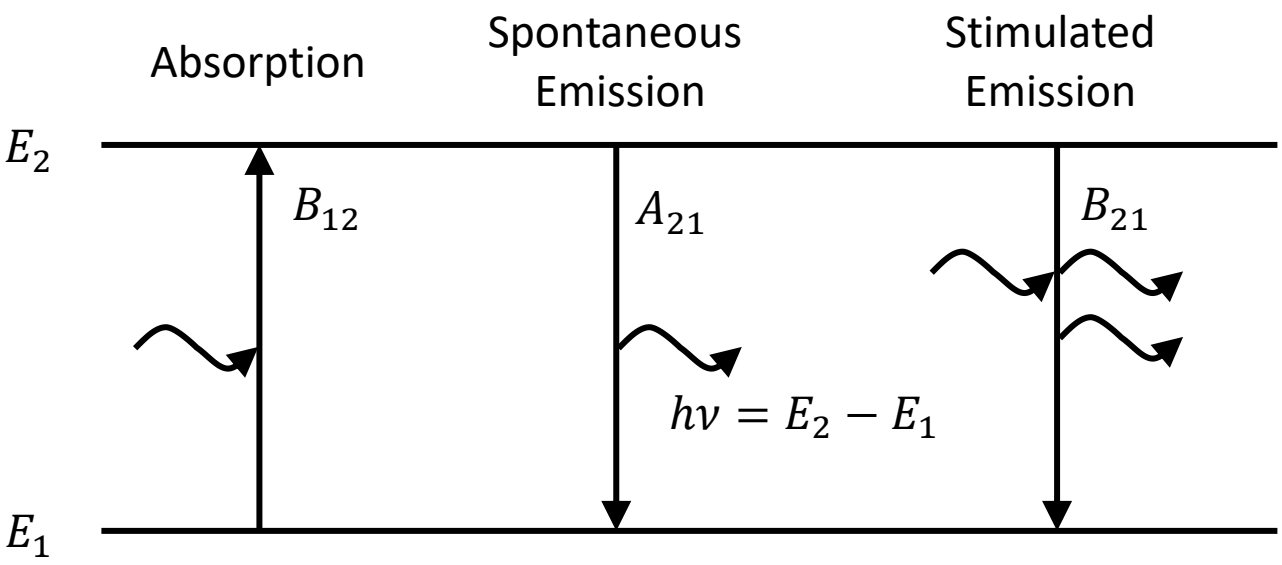

Figure 1.4 - Fundamental processes in spectroscopy

causing the atom or molecule to enter an excited energy state. Emission is the opposite process in which an atom or molecule initially in an excited energy state relaxes to a lower energy state, producing a photon of light that then emits from the atom or molecule. Emission can be spontaneous (with no external stimuli) or stimulated by the presence of another photon as occurs in lasers.

Quantum mechanical rules inform us that atoms and molecules cannot hold arbitrary amounts of energy and are in fact limited to discrete energy states. Consequently, the energy changes between allowable energy states are discrete, and since energy must be conserved in light-matter interactions, only photons with specific energies will react with a given chemical species. What results is a characteristic set of light frequencies for all species which will interact with the given species. These characteristic spectra of light produce identifiable spectral fingerprints that can be used to identify the presence of species. Furthermore, absorption spectroscopy can be used to determine the amount of a given species that is present, information that is particularly valuable for model validation.

Absorption measurements are performed by shining light through a medium that is to be measured. As the light passes through the substance, the intensity of the light can be increased due to emission or decreased due to absorption. If one assumes that only absorption is occurring in the medium (no emission or other processes), light intensity I_ν through a differential distance dx is differentially decreased according to the equation:

$$dI_\nu = k_\nu I_\nu dx \tag{1}$$

where k_ν is the spectral absorption coefficient at the light frequency ν. For a single absorption transition, k_ν is given by the equation

$$k_\nu = \frac{h\nu}{c} n_1 B_{12} e^{\left(1-\frac{h\nu}{kT}\right)} \phi(\nu) \tag{2}$$

In Eq. 2 h, c, and k are Planck's constant, speed of light, and Boltzmann constant, B_{12} is the Einstein coefficient of absorption from state 1 to state 2, and $\phi(\nu)$ is the spectral line shape. More importantly to this discussion, n_1 is the number density of the absorbing species in energy state 1 and T is temperature of the species.

When local thermodynamic equilibrium is assumed, the total population of the measured species n can be related to the population in a given energy state n_i through the Boltzmann distribution

$$\frac{n_i}{n} = \frac{g_i e^{-\frac{E_i}{k_B T}}}{Z} \tag{3}$$

provided that the energy level of the state, E_i, state degeneracy, g_i, and species partition function Z are known.

In the idealized case where a sample is uniform over a given distance l, k_ν is constant over l and Eq. 1 can be integrated to give:

$$I_\nu(l) = I_\nu(0) e^{-k_\nu l} \tag{4}$$

Eq. 4 relates incident light intensity $I_\nu(0)$ to absorbed light intensity $I_\nu(l)$, the two parameters that are measured in absorption experiments. Often these values are reported as a spectral transmittance T_ν or a spectral absorbance ABS where

$$T_\nu = \frac{I(l)}{I(0)}, \qquad ABS = -\log(T_\nu) = k_\nu l \tag{5}$$

Such representation is useful in that absorbance becomes directly proportional to k_ν which is directly proportional to species number density. However, in non-uniform samples, k_ν will vary along l, and what results from a measurement made through the non-uniform sample is an absorbance due to an average k_ν over l. While deconvolving spatial variations from a single

absorption measurement is not possible without additional information, the path average measurement retains the dependence on those spatial variations. As such, these measurements can provide critical information on the presence and amount of a nerve agent or decomposition product present in the probed gas, which is vital information for model validation. Furthermore, absorption measurements made on species with temperature sensitive spectra can be useful in obtaining temperature information of the probed gas.

1.4.2. *Organophosphorus Signatures in the Longwave Infrared*

In applying the principal of absorption spectroscopy to a given application, one must make the critical decision of where in the electromagnetic spectrum to probe. Key factors to consider are the presence of spectral features for the species of interest, the uniqueness of those features with respect to other species that may be present, and if temperature information is desired, the sensitivity of the probed features with respect to temperature. The first two factors are important for organophosphorus decomposition measurements. It is an easy decision to make as the

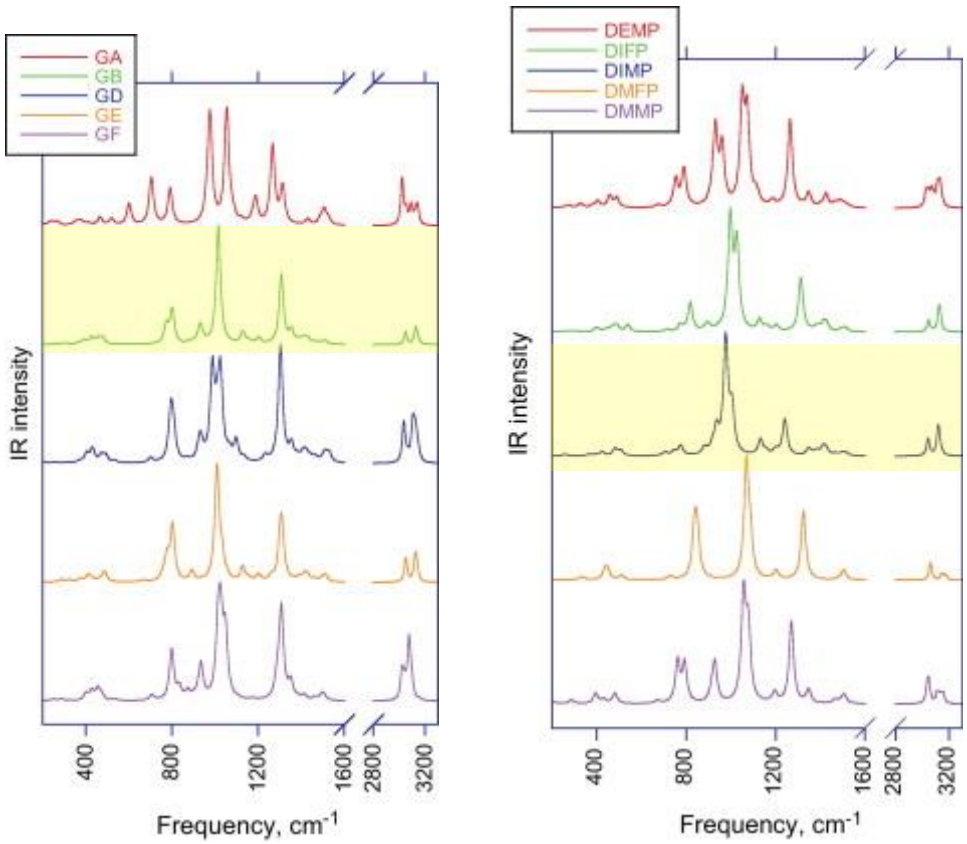

Figure 1.5 - Calculated absorption spectra for G-series nerve agents and some simulants, taken from Mott & Perez [14]

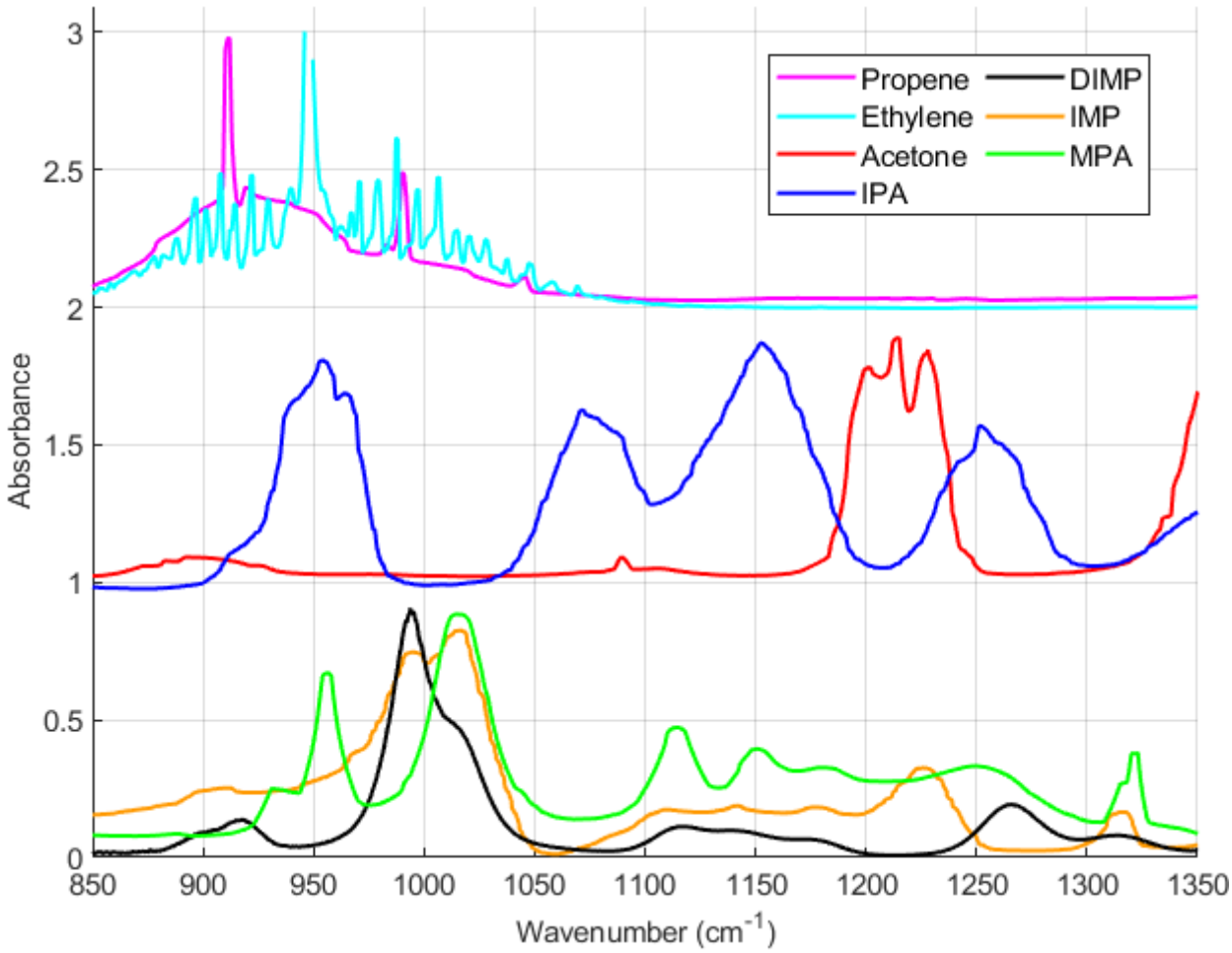

Figure 1.6 – Measured longwave infrared absorbance spectrum of DIMP, IMP spectrum digitized from [24], and remaining decomposition products, taken from NIST [30]

longwave infrared (LWIR) region between 8μm and 12μm is the only spectral region to contain unique spectral features of many organophosphorus compounds and some of their known decomposition products. Figure 1.5 provides absorption spectra, calculated by Mott and Perez [29], of the G-series nerve agents, as well as for several common surrogate materials. Here, Sarin (GB) and DIMP have been highlighted.

Of the potential product species highlighted in Section 1.3.2, NIST Chemistry WebBook SRD 69 contains spectra for propene, ethylene, IPA, acetone, and MPA [30]. These spectra, along with a measured DIMP spectrum and an IMP spectrum digitized from [24], are given in Figure 1.6. Two important characteristics of these spectra are worth addressing. First, spectral features of these species are typically very broad, and secondly, many spectral features overlap inside the region of interest. These result in two important design characteristics for instruments seeking to measure these compounds. First, an instrument can afford relatively low spectral resolution (around 10cm-

[1]) without much loss of information, and secondly, an instrument should scan at least several hundred wavenumbers to allow for deconvolution of potentially multiple overlapped spectra. These two system parameter considerations combined with the aforementioned speed requirement form the full set of system requirements for DIMP decomposition measurements in fireballs:

Measurement Speed: >1 kHz

Spectral Scan Range: 8-12µm (~850-1250cm^{-1})

Spectral resolution: ~10cm^{-1}

1.4.3. *Complications of Longwave Infrared Spectroscopy*

Longwave infrared absorption spectroscopy carries with it a few noteworthy complications not prevalent to visible or ultraviolet spectroscopy, which will be discussed briefly. Primarily, complications arise from hardware limitations in light sources and detectors, and in the issue of thermal background interference. No issue is too great to overcome, but these must be kept in mind when designing an infrared spectroscopy experiment. Another important consideration is the choice of optical material.

Thermal light sources are at an inherent disadvantage in the longwave infrared due to the shape of the Plank emission curve, which tails off in intensity at longer wavelengths. Still, thermal sources are commonly used, the most readily available being a resistively heated silicon carbide element referred to as a "globar." Element temperatures vary but can be as high as 1500-1700K [31]. Notably, these temperatures are far lower than quartz tungsten halogen (QTH) lamps in which tungsten filaments exceed temperatures of 2950 K. However, poor emissivity of tungsten and respectable emissivity of silicon carbide in the LWIR makes the globar a better emitter in this region despite its lower temperature [32]. Additionally, globar elements are simple to operate, requiring only a 12V DC power supply, and are inexpensive. Generated light requires no special safety precautions, and the element can be left on for extended periods without the source position changing.

It is important to note that higher output alternatives to the globar are available in the form of arc sources such as carbon arcs. Carbon arc sources make use of an electrical arcing between carbon electrodes causing the heating of an electrode to approximately 4,000K [33], [34]. When

considering carbon emissivity, this would result in an approximately two-fold increase in signal in the longwave infrared. The carbon arc source does also carry with it additional complications, one of which being that the carbon electrodes erode with use. As the electrode erodes, the position of the emission changes. Additionally, the arcs produce a dangerous intensity of visible light, requiring the use of eye protection such as welding goggles. Finally, carbon arc sources require continuous high voltage sources which are hazardous. It is often the case that the 2x increase in light intensity provided by a carbon arc is deemed insufficient to make up for the added experimental complexity.

Detectors of longwave infrared light also have hardware limitations. Unlike for the UV and visible spectrum, for which fast CCD and CMOS array detectors are prevalent, LWIR detectors are most commonly photoconductive elements. While all cameras benefit from cooling, such LWIR detectors require cooling to function at all. For some, multistage thermoelectric cooling sufficiently reduces element temperature for desired sensitivity, but, for others, liquid nitrogen or even liquid helium cooling is necessary. By and large, longwave infrared detectors are limited to a single pixel, especially when response time and light sensitivity are priorities. LWIR array detectors do exist but are often prohibitively expensive and limited in the number of elements [35], [36].

The last major complication is thermal background radiation, the light generated from warm materials. Bodies at room temperature produce significant amounts of LWIR light that poses an ever-present complication to LWIR infrared measurements. While dark signals, taken without the incident light source on, are meant to capture this thermal background, changes in the temperature of bodies within view of the detector will change the dark signal. Even changes in room temperature can have an effect. A larger issue, as will be discussed in detail later, is the light generated from the hot combusting gases inside the fireball. This radiation can be of comparable intensity to the incident light source and will throw off absorption measurements if not accounted for.

Finally, suitable optical materials are another important consideration in the longwave infrared. Fireball measurements in a laboratory setting require containing the event inside a chamber. Viewing ports must be installed with infrared transparent windows to allow for measurements within the chamber. These windows must be resilient enough to withstand the fireball event which

will subject the window to rapid changes in pressure and temperature in most cases. As a general rule, windows requiring an antireflective coating to have high transmission are undesirable as the coatings are delicate and would be rapidly deteriorated by exposure to the fireball.

In terms of windows that do not require coatings, options include potassium bromide (KBr), barium fluoride (BaF_2), and sodium chloride (NaCl). All of these materials have wide spectral ranges of about 90% transmission, but they are also all water soluble. If exposed to humid air for extended periods of time, the window surfaces will be degraded by the moisture in the air. With exposure to environments of higher water concentration, such as post-combustion environments, degradation can occur very rapidly. These materials are also all sensitive to thermal and mechanical shock, requiring that they be handled with care and limiting the environments they can be exposed to.

Focusing optics such as lenses and mirrors are also required, and these optics do not need the same resilience as windows since they are not in contact with the fireball. A very standard choice lenses is zinc selenide (ZnSe). ZnSe optics can be coated with a variety of anti-reflective coatings depending on the IR wavelength range of interest, including the longwave, to provide very high (>96%) transmission. However, without a coating, transmission is only approximately 70%, making uncoated ZnSe unviable in systems that require low losses. This material makes great lenses since it is not water reactive but it is very brittle and toxic, so great care is required when handling it. Germanium optics are also highly efficient in the longwave, but they are opaque to visible light, which complicates alignment. Mirrors with silver or gold reflective surfaces are also suitable as exterior focusing optics, but the delicacy of their coatings prevents them from use inside chambers unless they are disposable.

1.4.4. *Present Day Longwave Infrared Diagnostics*

As mentioned, infrared detectors are often limited to a single element, which has led to the development of various infrared diagnostic techniques that require only a single detector element. Among the techniques commonly used today for LWIR measurements are Fourier Transform Infrared spectroscopy (FTIR), fixed wavelength laser, and External Cavity Quantum Cascade Laser (ECQCL) systems. A brief overview of these systems will be provided along with their limitations to show how they are all unable to meet the required measurement parameters for the proposed work.

1.4.4.1. Fourier Transform Infrared Spectroscopy

Perhaps the most pervasive infrared spectroscopic diagnostic technique in use today is FTIR. An in-depth description of FTIR is not necessary for this discussion, but the following references are provided should the reader desire more information [37], [38]. In brief, FTIR is a form of interferometry, the study of constructive and destructive interference of light resulting from the wave nature of light. An interference pattern is collected resulting from the adjustment in length of one arm of an interferometer, and a Fourier transform is applied to that pattern resulting in a wavelength spectrum.

Commercially available FTIR systems are capable of very wide spectral measurements, in the 1000s of wavenumber and with high spectral resolutions <1 cm^{-1} [39]. However, the primary drawback with these systems is their speed. Thousands of wavenumber scans can only be achieved in 1Hz scale repetition rates. Speed can be increased at the cost of resolution and range, but even the fastest systems are only capable of a few hundred Hertz and even then with resolutions of 15-20 cm^{-1} [40]. Some systems take this to the extreme allowing for kilohertz speeds but with very poor resolutions on the order of 100 cm^{-1} [41].

1.4.4.2. Parked Quantum Cascade Laser

Single wavelength laser systems offer the extreme in terms of high speed but narrow measurement range. Such systems for the longwave infrared tune a QCL to a set wavelength, presumably corresponding to a single absorption peak of a single chemical species of interest and monitor the absorbance at that wavelength over time. As these systems have no temporal scanning component, their speeds are limited only by the response time of the detector being used. However, with no spectra being collected, the information available from this method is limited and applicable only to narrow features with no overlap with any other features. Often, as organophosphorus features are broad and have many overlaps, this method is restricted to probing lines of CO, a known product of organophosphorus decomposition [42]. In fact, it is CO measurements made in this manner that comprise the majority of data obtained in the ultrafast region of DIMP decomposition described earlier.

1.4.4.3. External Cavity Quantum Cascade Laser

ECQCL systems are the most promising for the future of infrared diagnostics. An ECQCL is a special type of laser sweeping method that relies on the rapid tuning of a quantum cascade laser. However, unlike tunable diode lasers, which can be tuned electronically, the ECQCL is tuned mechanically. In such systems, the QCL will emit a broad spectrum of light which is collected and directed to a diffraction grating. The angle of the grating is tuned to direct a certain wavelength of that spectrum back into the QCL medium, simulating the emission of that wavelength and producing lasing. Rapid oscillation of the grating will change the lasing wavelength.

While still a relatively young technology, ECQCL systems boast an impressive combination of repetition rate, spectral widths, and spectral resolutions. In 2017 Phillips [43] demonstrated one such system in the LWIR with 100Hz repetition rate, 135 cm^{-1} range, and 0.2 cm^{-1} resolution. Later that same year, system speeds of 200Hz were demonstrated with the same range [44], and then in 2020 the system was shown with a wider 2.1μm range at 400Hz [45]. Finally, as part of this research effort, the same ECQCL was shown to run at 500Hz with a spectral range of 950-1170 cm^{-1} while retaining 0.4 cm^{-1} resolution. 1kHz speed was also briefly obtained during these experiments, but with inadequate range and resolution. These ECQCL systems show great promise and rapid development, but still lack the capability to scan the full range of interest at kilohertz speeds.

1.4.5. *Performance of previous scanning spectrometers*

In summary, the common diagnostic techniques of today are all insufficient to meet the measurement parameters required for the desired measurement of DIMP decomposition in fireballs. FTIR is lacking in speed, laser methods lack the scan range, and ECQCL system, while approaching the desired specifications, still fall just shy of both. Instead, to find a suitable technique, we look toward instruments of the past. In the 1960s, Pimentel and others worked on rapid scanning spectrometers, instruments which swept dispersed spectra across detectors in time to generate spectral scans [46]. Figure 1.7, taken from Pimentel, helps to describe the operation of these systems. As depicted, while not scanning, these systems would operate as monochromators. Light passed through an inlet slit would be collimated and directed to a dispersing optical element, a prism in the case shown. The dispersed beam would then be collected and refocused, optionally through a turning mirror M1, onto an exit slit, S. The narrow slit S would pass a small portion of

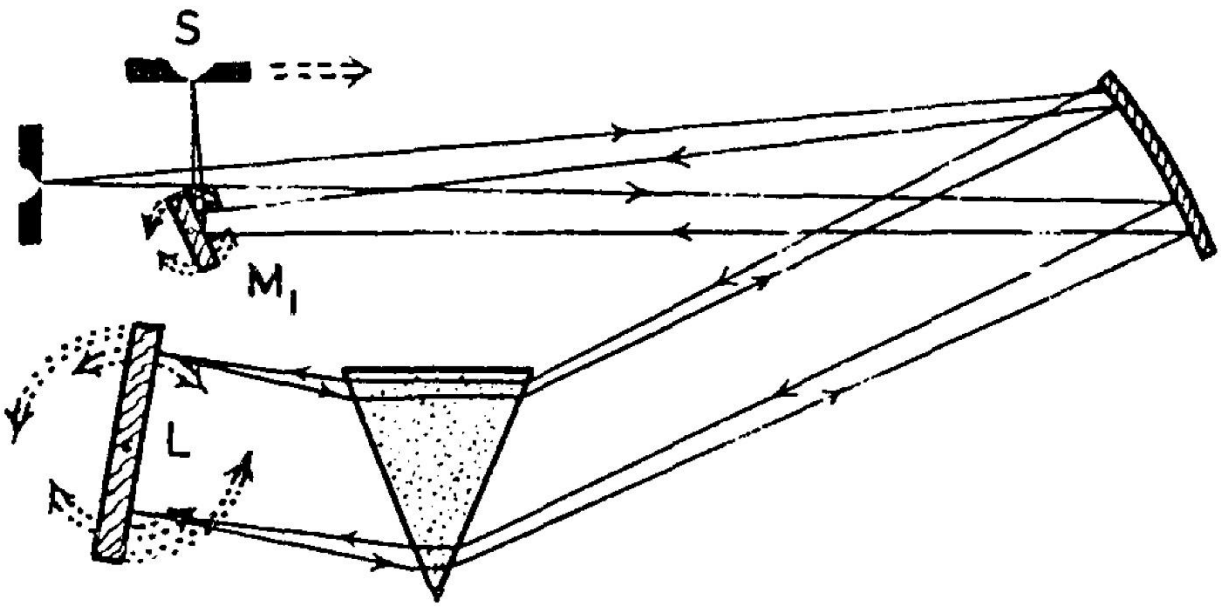

Figure 1.7 – Scanning spectrometer diagram, taken from Pimentel

the dispersed image, ideally a single wavelength, to then be measured by a detector on the other side. To scan spectra, the wavelength passed to the detector would be changed in time, and there were three possible ways to do this. First, the position of the exit slit could be moved in time across the dispersed image, although this method was not common. Second, the turning mirror M1 could be rotated in time, causing the position of the focused spectrum relative to slit to change in time. Finally, the center wavelength of light directed back along the optical path could be changed in time through the same mechanism used to tune a monochromator to a new wavelength. In the diagram shown in which a prism was used, this could be achieved through rotation of the Littrow mirror L. Were the prism/mirror replaced with a reflective diffraction grating, this could be done by rotating the grating. A visualization of how these three methods pass a spectrum is provided in Figure 1.8 which depicts the focused spectrum on the plane of the exit slit.

The second method, rotation of M1, has the advantage that the light hitting the mirror is already partially focused, meaning that M1 can be a small mirror that is rotated very rapidly. Faster rotation equates to faster scan speeds and higher repetition rates. The downside is that the image being swept is only optimally focused on the exit slit for one mirror position. Sub-optimal mirror positions result in poor focus on the slit due to optical aberrations, and therefore have increasingly poor resolution as the mirror moves away from its optimal position.

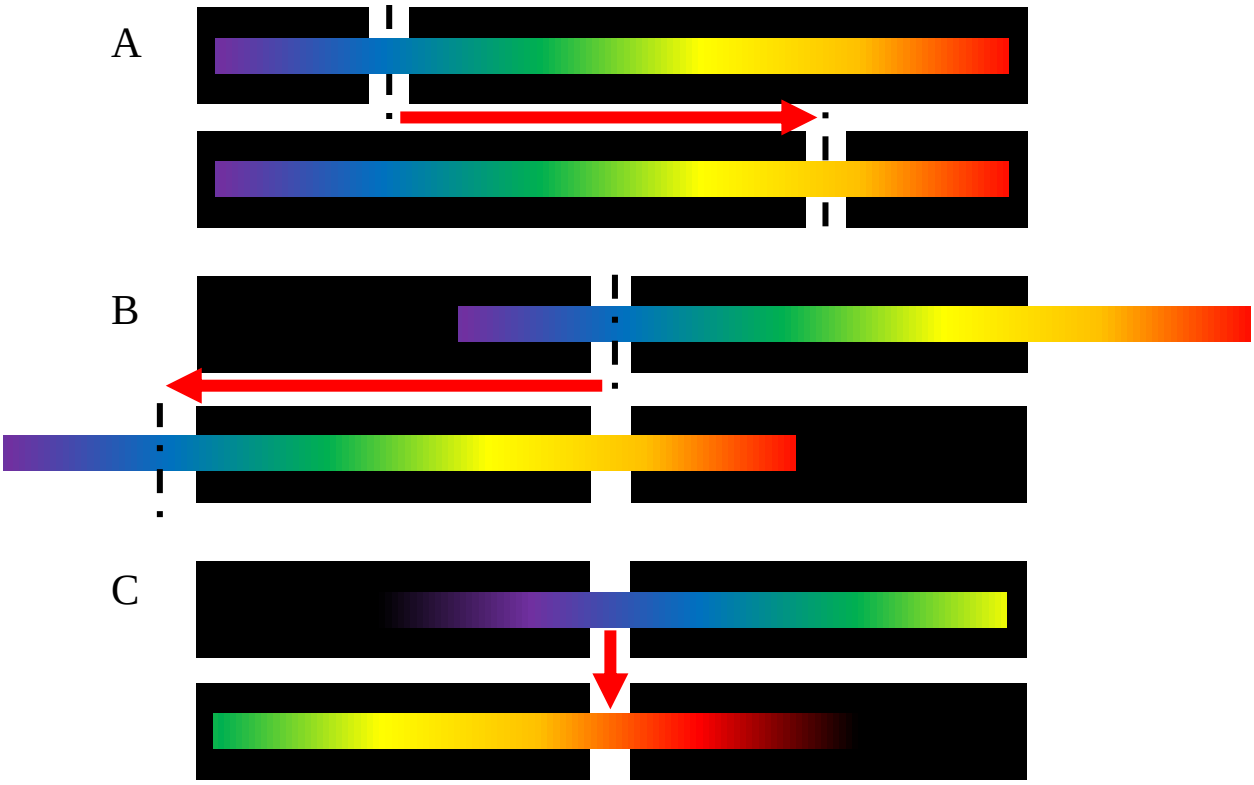

Figure 1.8 – Spectral scanning visualization by A.) Slit repositioning, B.) Dispersed image sweeping, and C.) Center wavelength tuning

The final method of rapid wavelength tuning results in the dispersed image remaining optimally focused on the exit slit throughout the scan. However, as the diffraction element requires collimated light, the Littrow mirror or reflective gratings would need to be larger. As such, repetition rate could become limited by the allowable rotation speed of the dispersive elements, since larger bodies are subject to greater stresses under rotation. Speed limitations could be overcome through clever design of optical trains making use of multiple rotating elements or telescope systems [46].

Many such systems were geared toward ultrafast scan times with less emphasis on repetition interval. Prism systems could make use of multi-faced polygonal Littrow mirrors to increase scan time and frequency. One such system scanned 650-5000 cm^{-1} in 200μs at 200Hz using a Globar light source and liquid helium cooled detector [47]. Herr and Pimentel devised a system using a rotating grating that would scan 200 cm^{-1} in 200μs also at 200Hz and with 1.5 cm^{-1} resolution [46], [48], [49]. This system was further improved upon and used for further study of radical species [50], [51].

While many systems existed during the time, the best performing scanning spectrometer was the instrument devised by Hexter and Hand [52], [53]. This system placed emphasis on repetitive scanning, and scan speeds of 20 kHz were obtainable with scan widths spanning many hundreds of wavenumbers and spectral resolution between 5 and 15 cm^{-1}. These parameters were met through the use of a prism, a six-sided mirror rotating at 3350 rps, and a liquid helium cooled detector.

Given that the demonstrated performance of these scanning spectrometer systems would meet the measurement requirements of this work, they seemed to be the best option to pursue. Unfortunately, since the advent of FTIR technology, these scanning spectrometers have become less popular. Few, if any, such systems are in use today, and certainly no systems are readily available. However, given the existing literature on the systems and the relative simplicity of their operating principles, it was sought to create a scanning spectrometer system.

1.5. Statement of Purpose

The purpose of this research is to produce a set of benchmark data to be used as validation for computational models of DIMP decomposition in fireball environments. Target models for which this data is intended are both chemical reaction solving and absorption spectra simulating, meaning that collection of reference spectra is sufficient for validation. As such, an in-depth analysis of collected spectra for quantitative measures of observed species is beyond the scope of the presented work. Greater emphasis is placed on the methods used to obtain the spectra.

Since the scanning spectrometers capable of collecting the desired spectra are no longer commercially available today, a significant portion of this research effort focused on the development of such a system. Another significant portion was the design of the experiment in which the desired data could be collected. As the purpose of this work is to validate models, it is the goal of this work to provide data with maximal utility toward that outcome. Explosive fireballs themselves are complex and difficult environments to solve computationally so it is beneficial to first validate models in simplified environments that mimic those of explosive fireballs but are easier to model. To this end, the set of benchmark data will be obtained on constant volume, premixed fuel-oxidizer combustion “closed bombs.” The rapid burning of premixed hydrocarbon-oxygen flames would produce temperature conditions similar to those experienced in an explosive fireball, providing a good surrogate environment.

A detailed description of the scanning spectrometer development process will be provided in Chapter 2. This description will include the development process of the physical instrument and the development of data processing techniques. Chapter 3 is devoted to the design of the experiment for creating DIMP decomposition in closed bombs. That discussion includes the design of a custom test chamber for containing the closed bombs, determination of a set of test conditions, and the operating procedure for performing the experiments. Chapter 4 contains the discussion of collected data, and finally, conclusions and recommendations for future work are presented in Chapter 5.

CHAPTER 2: INSTRUMENTATION DEVELOPMENT

Previous work by Pimentel and others [46] proved that the desired spectral scan speeds, scan range, and resolution could be achieved with broad scanning spectrometers. However, a decline in popularity of such devices since the 1960s meant that few existed today and none were readily available for purchase, so construction of a new instrument from base components was necessary. This section will detail the process of developing a scanning spectrometer inspired by Pimentel and others' designs, provide sample output obtained from the device, and detail the development of data processing procedures.

2.1. Preliminary Design

2.1.1. *High Throughput Spectrometer Design*

Pimentel and others' designs provided the foundation upon which the developed spectrometer was based, and IR challenges and target performance goals guided the core design of the system. In its most fundamental form, system design began according to the schematic in Figure 2.1. Light is focused through an inlet slit onto an off-axis parabolic mirror, directing it as a collimated beam

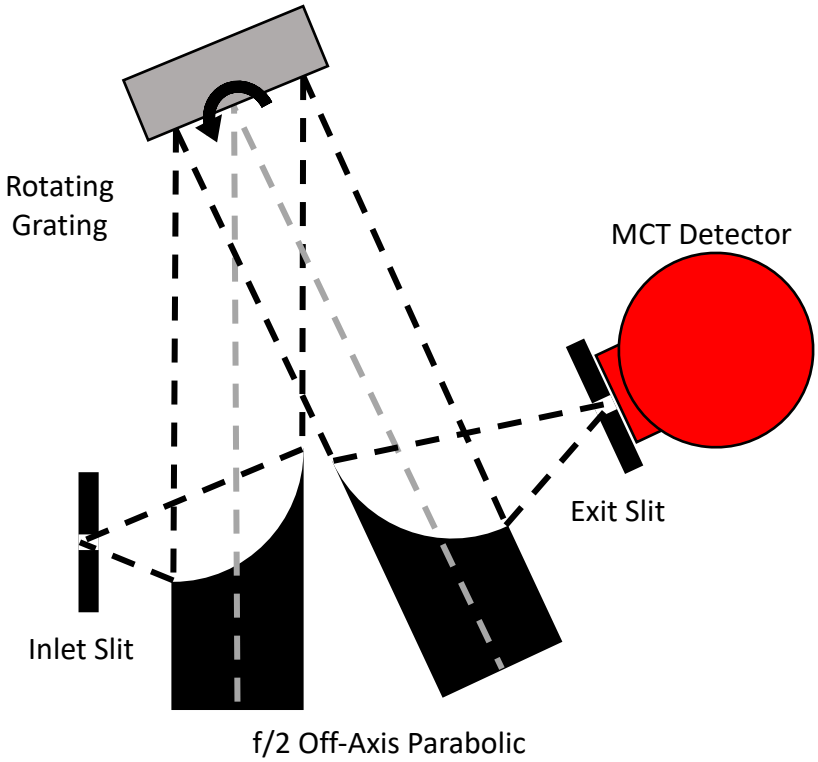

Figure 2.1 – Fundamental spectrometer design

onto a reflective grating. The dispersed light is collected by a second parabolic mirror and imaged through an exit slit to a detector. Notably, this design features minimal optical components, with scanning of spectra achieved through direct rotation of a reflective grating. Operating in such a way greatly simplifies the system over some of the complex optical trains seen in previous works, requiring only a single moving part, minimizing surface losses, and simplifying alignment.

2.1.1.1. The Grating Equation

When a beam of broadband light impacts a reflective diffraction grating, a diffraction pattern of light is created as depicted in Figure 2.2. Light from the incident beam is diffracted into multiple fans of dispersed light called diffraction orders. The 0^{th} order contains all wavelengths at a single angle while the non-zero orders contain wavelengths which are angularly separated. First order fans have the least angular dispersion but are typically the highest intensity aside from the 0^{th} order. Second order fans have twice the angular separation as first order, but lower intensity. Importantly, while not depicted, diffraction orders can overlap with one another, and the number of diffraction orders is not limited to two.

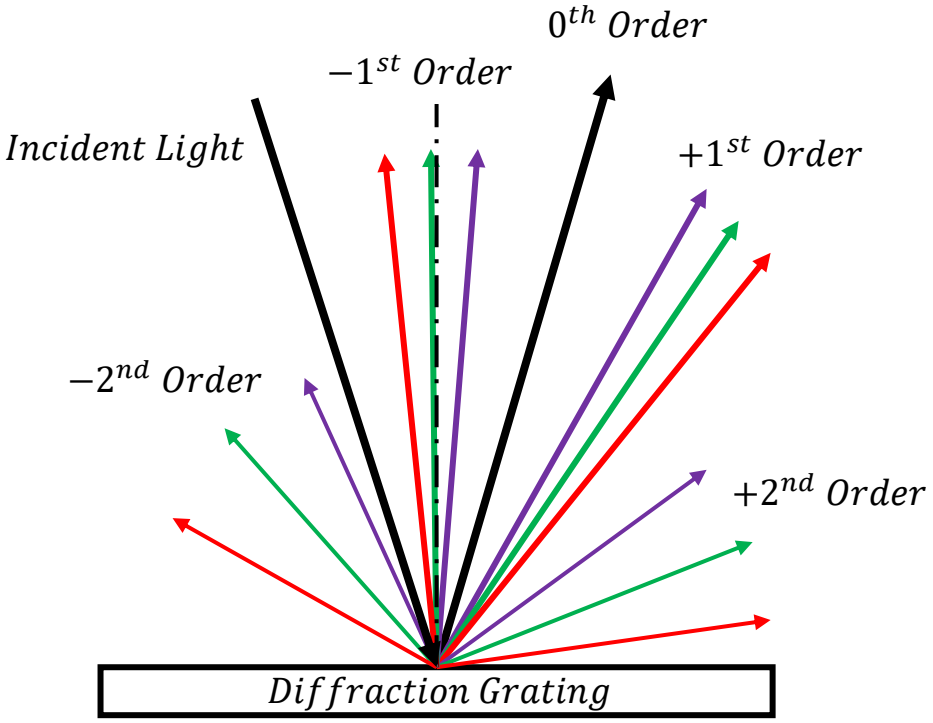

Figure 2.2 - Grating Diffraction Diagram

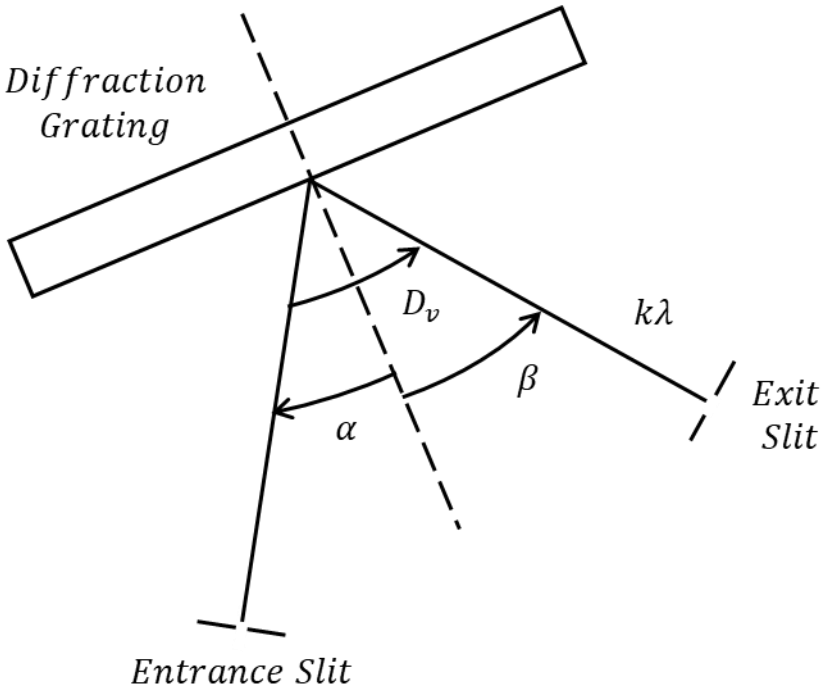

Figure 2.3 - Monochromator diagram, taken from Lerner [54]

When the diffraction grating is rotated, the position of the diffraction pattern is changed according to the grating equation. To help define this equation, a schematic of monochromator operation is provided in Figure 2.3 [54]. The diagram depicts a simplified monochromator with an input beam of broadband light impacting a diffraction grating with n grooves per millimeter. The monochromator isolates a single color of the diffracted spectrum by placing an exit slit at a fixed location such that only the light diffracted at a particular angle, D_v, from the input beam is passed through the exit slit. The wavelength of passed light λ depends on the grating groove density and grating angle, which is defined by α, the angle between the input light ray and grating normal, and β, the angle between the exit ray and grating normal. This dependence is given by the grating equation:

$$10^{-6} kn\lambda = 2 \sin\left(\frac{\beta + \alpha}{2}\right) \cos\left(\frac{\beta - \alpha}{2}\right) \tag{6}$$

where λ is in nm and k is the diffraction order. Here it becomes clear that harmonics of a given wavelength overlap in the diffraction pattern. If the grating were angled to pass λ_1 in first order, the monochromator would also pass $\lambda_1/2$ in second order, $\lambda_1/3$ in third order, $\lambda_1/4$ in forth order, and so on. This can lead to issues where measurement of those shorter wavelengths is not desired.

Through one full rotation of the grating, the entire diffraction pattern of the grating will be swept across the exit slit. This includes all positive and negative orders as well as zero order. The range of wavelengths swept is determined by grating groove density and the physical limitation that light must be able to reach the reflective surface and the exit slit. In other terms, $\alpha > -90$ and $\beta < 90$.

For the designed system, a reflective grating of 100 gr/mm was chosen as was a deviation angle of approximately 20 degrees. With these parameters, a full rotation of the grating would sweep 19.4μm to 0μm in negative first order and 0μm to 19.4μm in positive first order. From this sweep the desired region of 8-12μm could be measured twice per rotation.

2.1.1.2. System f-number

The need for fast measurement speeds and the relative low intensity of infrared sources dictated that the devised system has very high throughput, meaning the system collects and processes large amounts of light. A fundamental parameter of any optical system is the f-number at which it operates, where the f-number is a metric of how much light the system accepts. The f-number, N, is defined by the equation

$$N = \frac{1}{2nsin(\theta)} \approx \frac{f}{D} \tag{7}$$

where f is an optic's focal length and D is the optic's diameter. It relates the parameters of an optic to the half angle of the cone of radiation θ accepted by the optic. Larger half angles equate to more light such that collected intensity I is proportional to f-number, represented as f/N, by:

$$I \propto \frac{1}{(f/N)^2} \tag{8}$$

Clearly, low f/N allows for greater intensity, allowing a given system to operate at higher speeds. Maximizing system throughput by minimizing f/N was crucial to developing a system that would operate at kHz speeds. Past experience had shown that reflective dispersive systems have a practical lower limit of $f/2$, so the system was designed to operate at $f/2$.

2.1.1.3. Optical Aberrations

While low f-number is beneficial for signal strength, and in fact necessary for the new diagnostic, it does amplify the issue of optical aberrations. Optical aberrations exist in all optical systems and

result in imperfectly focused images, equating to degraded spectral resolution in spectroscopic applications. Five basic monochromatic aberrations were described by von Seidel in 1857: spherical, coma, astigmatism, field curvature, and distortion. The magnitude of distortion caused by these aberrations, AA_{max}, in terms of the coefficients for each aberration a, the degree to which the object is away from the optical axis θ, and the f-number is given by the equation [55]:

$$AA_{max} = \frac{a_s}{(f/N)^3} + a_c \frac{\theta}{(f/N)^2} + a_a \frac{\theta^2}{f/N} + a_f \frac{\theta^2}{f/N} + a_d \theta^3 \quad (9)$$

According to these equations, aberration magnitude increases at low f/N and large off-axis distance with varying powers of dependence for the five aberrations. Spherical aberration, given by the first term with a $(f/N)^{-3}$ dependence, is most greatly affected by low f/N and arises from spherical optics being imperfect shapes to focus light. Beneficially, this aberration can be dealt with by using mathematically ideal optics such as parabolic mirrors or aspheric lenses, and hence the decision was made to use off-axis parabolic mirrors in the spectrometer design.

All other aberrations exhibit a dependence on the off-axis distance to the effect that these aberrations do not exist on-axis. Avoiding these aberrations can then be accomplished through only operating on the optical axis. To ensure this, all light sources and focused images must be positioned on the optical axis, and collimated light must travel parallel to the optical axis. This again motivates the use of off-axis parabolic mirrors as the performance of such optics degrades rapidly off optical axis.

Retaining on-axis operation was another key motivating factor in the decision to rotate the reflective grating as a means of scanning spectra, as rotation of the grating around its reflective face does not affect the position of the optical axis. Instead, in this design as the grating angle changes, the wavelength of dispersed light that falls in line with the refocusing off-axis parabolic mirror's optical axis changes. Consequently, the wavelength of light focused into the exit slit and into the detector changes in time.

2.1.1.4. Optic Diameter

Optics used in the spectrometer, and elsewhere in the experimental setup, were all 25.4cm (1 inch) in diameter. This is a readily available optic size that can be purchased commercially, but keeping collimated beam diameters at one inch had another benefit over larger diameters beyond cost

considerations. To maintain signal level, the grating width would need to be wider than the optic diameter to ensure the full beam was reflected when the grating was angled relative to the beam. Consequently, smaller beam diameters would allow smaller gratings, lower rotational weights, and therefore faster allowable rotational speeds.

2.1.1.5. Detector and Amplifier

Finally, the detector used to record the dispersed light was a photoconductive mercury cadmium telluride (MCT) detector coupled to a preamplifier supplied by the same manufacturer, Infrared Associates [56]. The detector is shown in Figure 2.4. According to the manufacturer's specifications, the specific detector model has an element size of 1mm x 1mm, an upper measurement bandwidth of ~400kHz, a wavelength range of 2μm to 12μm, and a specific detectivity $\geq 4.0E10\ cmHz^{1/2}\ W^{-1}$. Specific detectivity is a normalized metric for detector sensitivity, and this detector's value is among the highest available for comparably fast LWIR detectors. As mentioned, these detectors are reliant on cooling, and this detector is able to achieve these sensitivities through liquid nitrogen cooling.

Figure 2.4 - Liquid nitrogen cooled MCT detector

2.1.2. *Grating Rotation Mechanical Design*

The grating mount was originally rotated using a water-cooled electric motor capable of reaching speeds up to 24,000 rpm. High-speed rotation brings with it the potential for ejecting material at high speeds and significant forces, so safe operation of the motor required special mounting considerations to ensure that the grating would remain stable. To this end, a motor and grating mount assembly were constructed as shown in Figure 2.5. The mount frame is fabricated from aluminum, consisting of a base plate, vertical plate, and a motor clamp. Inside the base plate is a recess designed to accept a high-speed ball bearing into which the bottom of the grating mount is inserted for added stability. The motor clamp is attached to the vertical plate through several bolts, with slop in the bolt holes allowing for slight adjustments in motor position.

Maintaining low rotational weight was critical in the grating mount design, as any imbalance would be magnified at high speed. It was also desirable to keep the reflective surface of the dispersive grating in line with the axis of rotation such that during rotation, only the angle of the

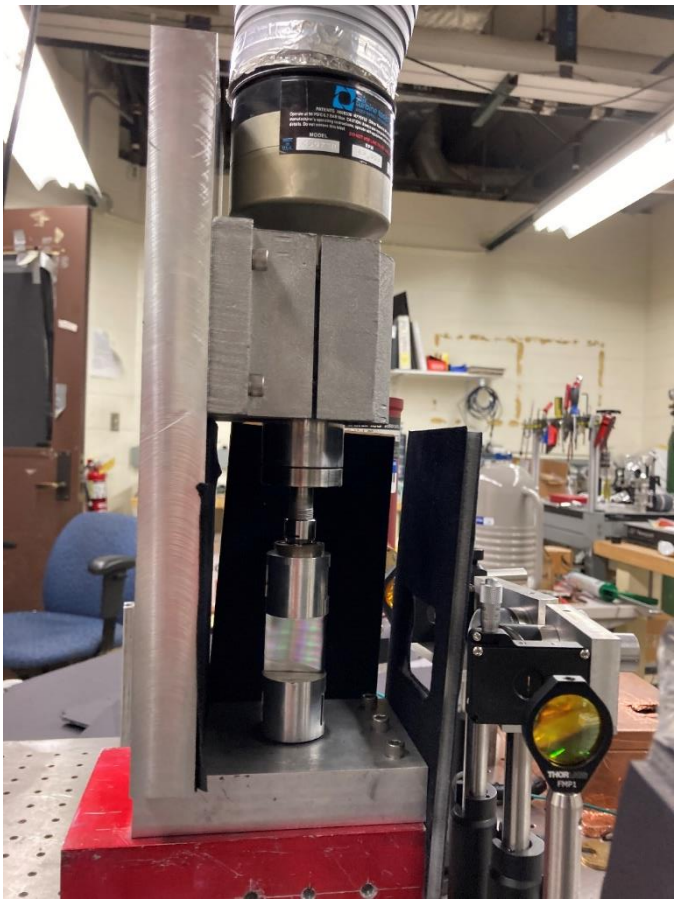

Figure 2.5 - Rotating Grating Motor Mount

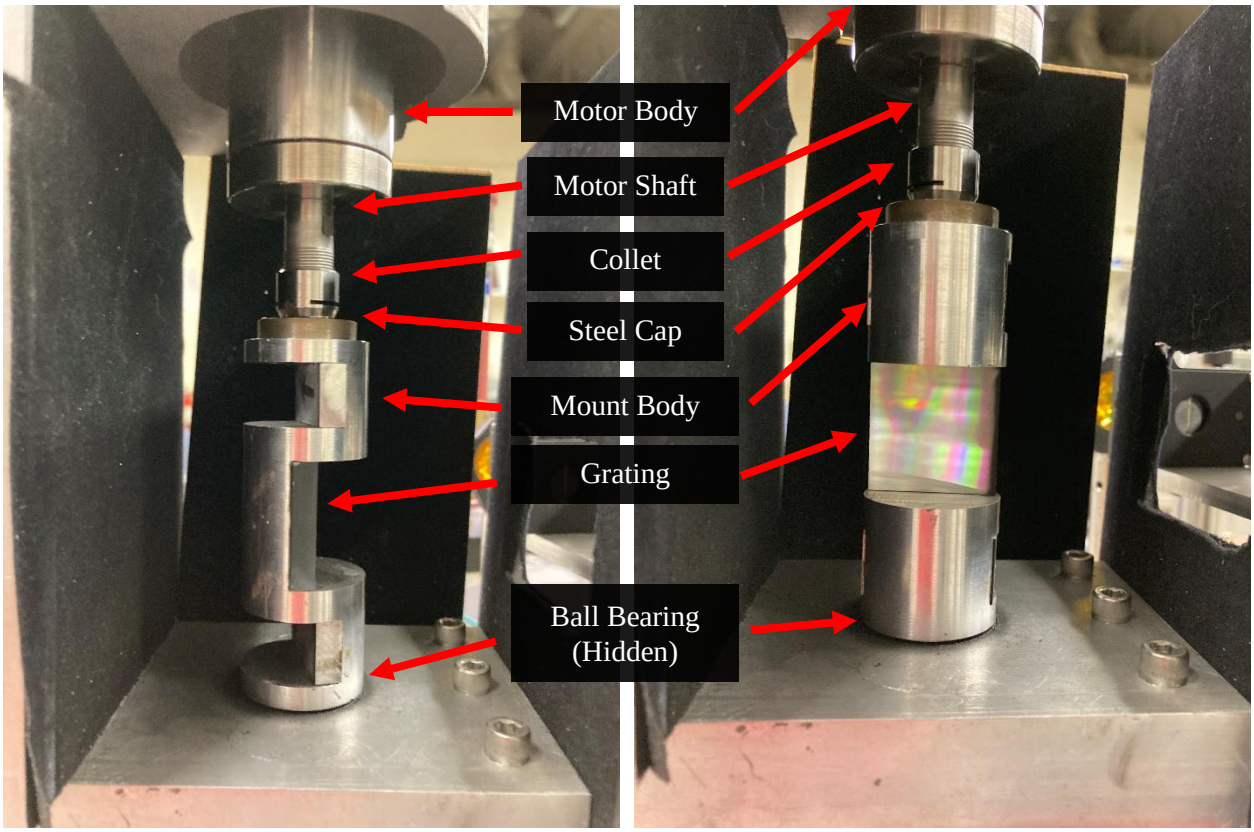

Figure 2.6 – Grating mount design

reflective surface would change and not its position. These two considerations led to the grating mount design shown in Figure 2.6. Aluminum was used as the material for the mount due to its low weight. Three slots were made in the aluminum: the center slot was made to recess the reflective grating as desired, and the other two were made to balance the mount accounting for both the removed aluminum and the weight of grating. Epoxy was used to adhere the grating to the aluminum mount as screws would be subject to loosening during rotation.

Close inspection of the top of the grating mount shows that a cap was added which attaches to the motor collet. This steel cap was added because rotational forces were too high for the original 7mm diameter aluminum nipple that attached to the collet. At some point in operation, the aluminum nipple sheared off from the rest of the grating mount. The steel cap has worked well as a replacement, and future improved designs should make use of stronger material than aluminum.

2.1.3. *Integration into Experiment*

This spectrometer was then integrated into an experimental setup to take absorption measurements. A globar light source, collimating lens, focusing lens, and longpass filter were added to the system

as shown in Figure 2.7. Here, the globar light source is collected by a 1" diameter 100.2 mm focal length ZnSe plano-convex spherical lens coated with an E3 antireflective coating designed for the 7-12µm wavelength range. The collected light is collimated, passed through the measurement area, and then focused into the spectrometer as an f/2 cone by a 1" diameter 50.1 mm focal length plano-convex spherical ZnSe lens.

Finally, a 7.3µm cut-on longpass filter was added to the exit. As described in Section 2.1.1.1, higher order reflections of lower wavelength light could interfere with measurements. It was found that, given the detector's lower sensitivity of 2µm, significant interference from higher order diffractions was occurring. In placing a 7.3µm cut on filter, higher order diffractions would interfere with first order diffraction only for 14.6µm and above. Since the detector was not sensitive to higher than 12µm, higher order interference would no longer occur.

The choice of an f/4 lens to collect the globar light is worth addressing, as doing so appears at first glance to not make full use of the spectrometer's f/2 design. First, it was deemed necessary to collect light at f/4 to prevent damage to the lens. A 1" diameter f/2 lens in this position would only be 2" from the globar element which would radiate light and heat at ~1700K. Conversely, an f/4 lens would be 4" from the element, equating to a 4x reduction in heating power to extend the life

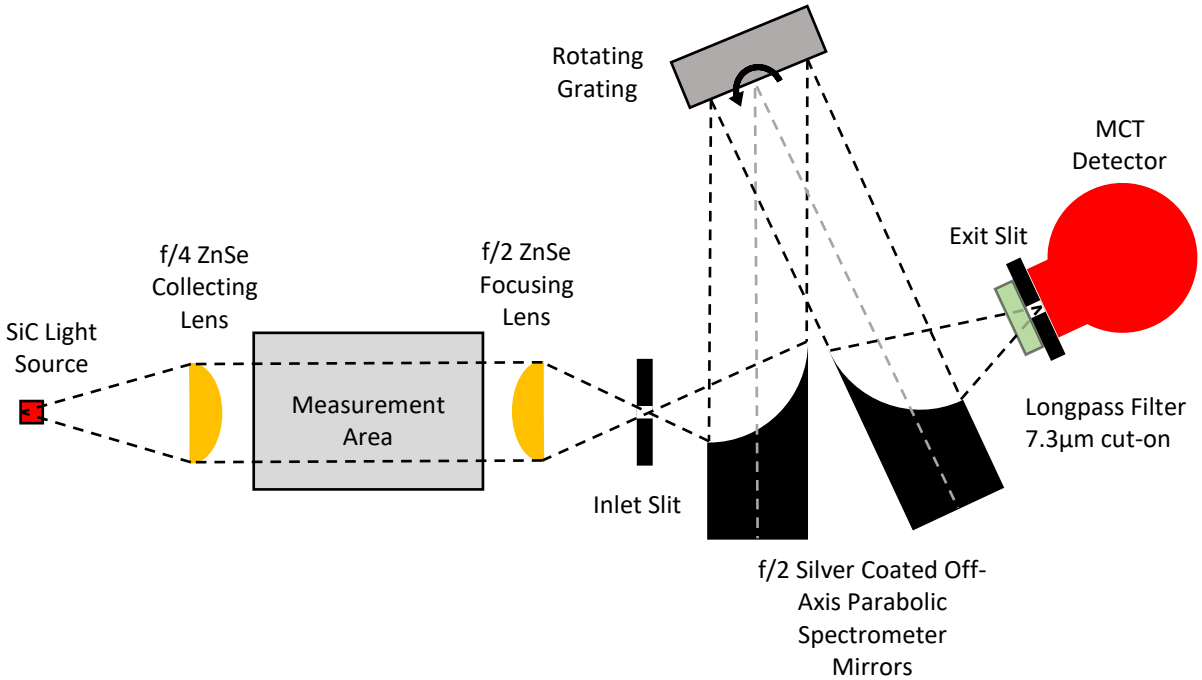

Figure 2.7 – Initial integrated spectrometer design

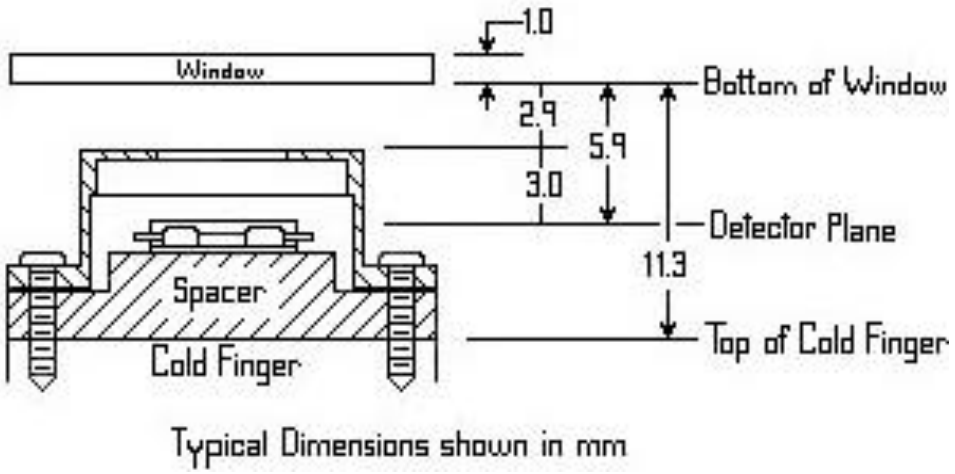

Figure 2.8 – Typical geometry of LN2 cooled MCT detectors supplied by Infrared Associates Inc. [56]

of the lens. Second, the emitting element has a physical size and is not a point source. Importantly, this means that focusing the collected light produces an image of some physical size which depends on the magnification of the optical system, $M = f_i/f_o$, where f_i is the focal length of the image and f_o is the focal length of the object. In this system, magnification is 0.5, reducing the area of the focused image by ¼ , and increasing the intensity of the image by a factor of 4. So long as slit widths remain smaller than the image, as is always the case in these experiments, demagnification cancels the effect of collecting light at f/4.

A fundamental flaw existed with the design in Figure 2.7 regarding the placement of the MCT detector. As described, the detector used has a 1mm x 1mm sensing element. It was originally thought that the detector could be placed against the exit slit as depicted, but doing so yielded no detectable signal. Further investigation of the detector geometry, as shown in Figure 2.8, revealed that the sensing element was actually recessed nearly 7mm behind the front face of the detector. The slit image expanding in an f/2 cone through this distance would become 3.5mm wide, greatly reducing intensity on the sensing element. To account for this increased 7mm recess, a third lens was added that would collect and refocus the exit slit image onto the detector. This final design is shown in Figure 2.9. Here, the longpass filter has been moved to the detector's front face to remove any interference it may have been causing when it was placed in front of the exit slit.

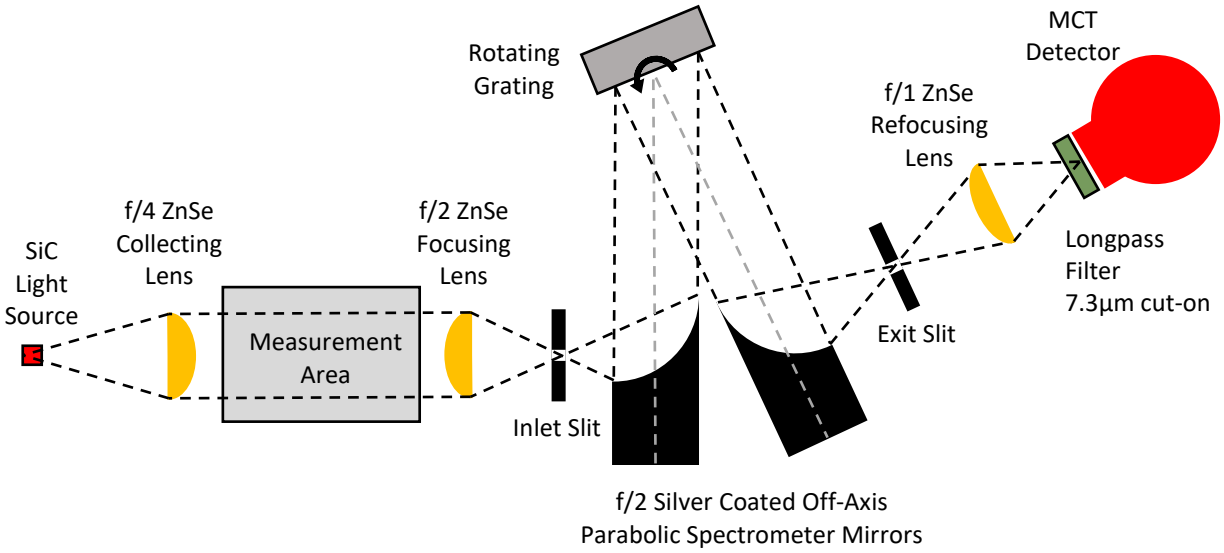

Figure 2.9 – Final spectrometer optical layout

2.2. Design Improvements

With the system assembled as described to this point, dispersion spectra could be measured. However, signal levels were low, noise levels were high, rotational speed of the motor was insufficient, and system resolution was lower than desired. The following section will describe the steps taken to address each of these issues.

2.2.1. *Exit Slit Repositioning*

In order to improve signal, the exit slit needed to be repositioned. The final design for the mounts which housed the off-axis parabolic mirrors and inlet and exit slits is shown in Figure 2.10. Originally, both mounts were constructed like the left mount such that the slit center was positioned precisely 2” from the off-axis mirror’s center, and both the slit and mirror center were 1” from the aluminum block in which the mirrors were mounted.

Issues arose with the original configuration regarding the exit slit. During the alignment process, a low-power visible wavelength laser would be used to set the correct position and orientation of optical components. With the laser beam defining the optical axis, the inlet slit mount would be positioned such that the beam passed through the inlet slit, ran parallel with the mount’s vertical block, hit the center of the parabolic mirror, and was then reflected to the center of the rotating grating. To align the exit slit mount, the grating would be positioned to reflect the highest intensity

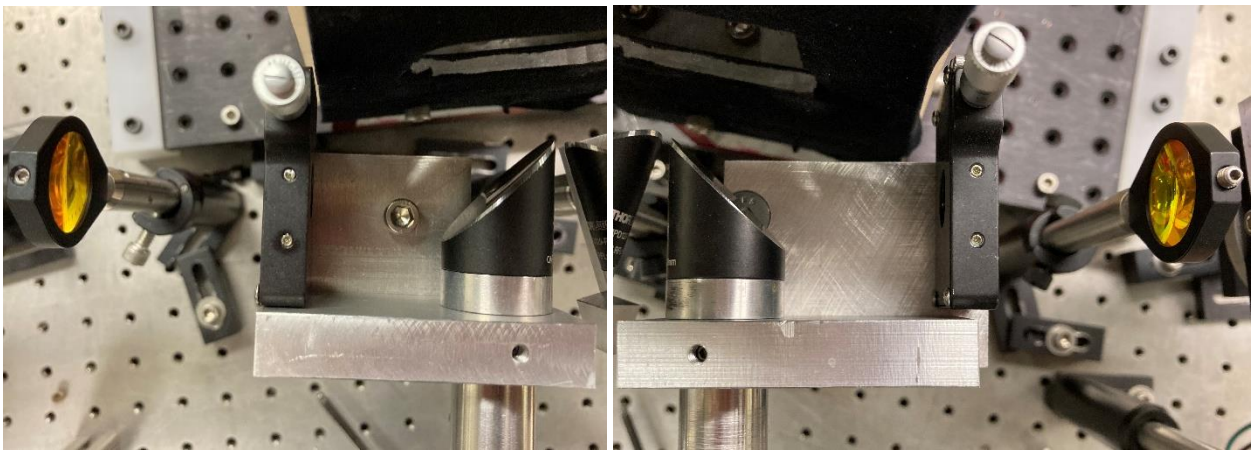

Figure 2.10 – Mirror and slit mounts

diffraction of the laser beam out at a deviation angle of approximately 20 degrees. The exit mount would then be positioned such that the diffracted beam hit the center of the mirror, reflected 90 degrees, and passed through the exit slit.

With the positions of both mounts set, the laser beam would then be expanded at its source, and the expanded beam would then be focused into the inlet slit with an f/2 lens. By expanding and focusing the beam, the ability of the system to focus light at low f/n (where aberrations are highest) could be evaluated. Upon performing this final step, it was found that the light focused on the exit

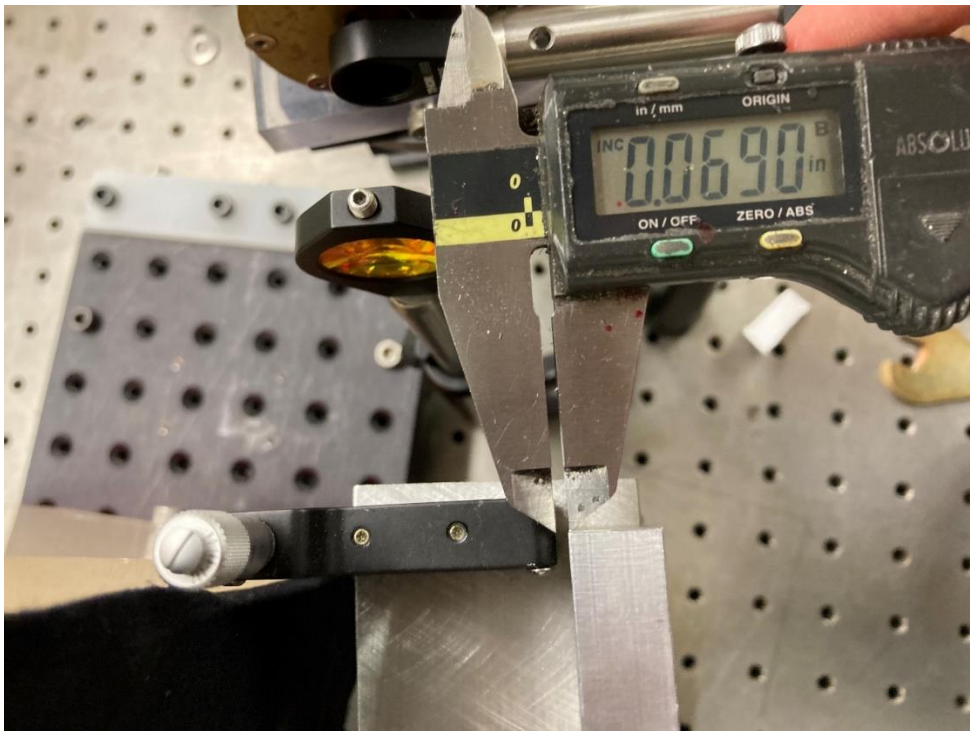

Figure 2.11 – Exit slit position adjustment

slit plane was not well focused at the position of the slit. Instead, the light was best focused a short distance to the left of the slit. This was believed to at least partially explain an observed signal level that was lower than expected. While the cause of the shifted focus was not known, the slit position was adjusted by 0.069" (<1.75mm), as shown in Figure 2.11, to position it at the spot of best focus. A significant increase in signal level was observed upon repositioning the slit in this manner.

2.2.2. *Electrical Interference*

The next issue to fix was that of high signal noise levels. Even after increasing signal through exit slit repositioning, detector noise remained too high to achieve viable SNR. Furthermore, large increases in detector electrical noise were observed upon powering the original electric motor. This made it apparent that the MCT detector was incredibly sensitive to external sources of electrical noise. Insight gained from Prof. Grubelle at the UIUC revealed several precautions that needed to be taken when operating that detector and its preamplifier for them to work properly. Most importantly, the detector's power supply (+-15V DC) needed to be completely removed from wall power as power lines pick up and transmit a great deal of noise. Some of this noise permeates through all line powered circuits, including AC to DC power converters like the supply originally used, and detector sensitivity is so great that this noise becomes an issue. To address this, the detector's power supply was changed to a pair of rechargeable lithium polymer batteries.

Other useful tips were to electrically float the detector and its pre-amplifier, ensuring that the only path to ground for both was through a dedicated grounding tab on the detector housing, and to cool the pre-amp if needed. Switching to battery power and floating the pre-amp proved to be adequate to achieve desired system performance, so pre-amp cooling has not been necessary. Separating the pre-amp as far from any line powered devices as possible was found to be necessary to minimize noise as well. For example, turning off a power strip located underneath the optical table on which the detector sat resulted in a noticeable drop in detector noise, and this held true when there were no devices plugged into the power strip.

As mentioned, the electric motor was a large source of noise that required attention. Replacing the motor was already necessary as the 24,000 rpm limit was insufficient to reach the desired 1kHz scan rate, but the decision was made to replace it with an air turbine motor to eliminate the electrical noise source. A compressed air powered, 40,000 rpm rated motor was purchased as the

replacement. The 40,000 rpm was near the upper speed limit of commercially available motors, and increasing speed by a factor of two would have required a custom motor. Compressed air used to supply the motor could be obtained from the building's supply, but this supply was slightly insufficient for the motor. Consequently, the motor only achieved ~37,000 rpm with small fluctuations in speed during operation. Despite not realizing the full speed of the motor, the 37,000 rpm was sufficient for achieving the desired, i.e. >1kHz, scan rate.

Finally, to achieve the desired resolution performance at maximum speed, the detector pre-amplifier needed to be upgraded. The standard pre-amp had a listed upper bandwidth limit of 150kHz. This proved to be a limiting factor in system performance when operating the system at maximum motor speed. At these speeds, the system scans across first order dispersions at a rate of approximately 7.6 $cm^{-1}/\mu s$, so a resolution limit of about $50cm^{-1}$ might be expected from 150kHz bandwidth. In reality, the amplifier's upper bandwidth is not a hard limit and gradually decreases in performance at higher speeds resulting in measured resolutions of 15-20 cm^{-1}. To increase resolution, a 1MHz pre-amp was purchased, causing the detector itself to become the limiting factor due to its ~400kHz upper bandwidth. Still, with the gradual drop in performance above those speeds, 10 cm^{-1} measured resolution became attainable.

2.2.3. *Vibrational Interference*

Vibrations caused by operating the new air turbine motor at maximum speed were intense enough to displace optical elements during operation, so vibrational isolation needed to be added. To isolate its vibration, the motor mount assembly was placed on a separate optical breadboard. This breadboard was fitted with four vibration-dampening rubber feet to lift it off the main optical table. Low density polyethylene supports were installed to lock the motor in place while preventing metal-on-metal contact between the motor mount and optical table. These measures sufficiently reduced vibration transmission into the main table.

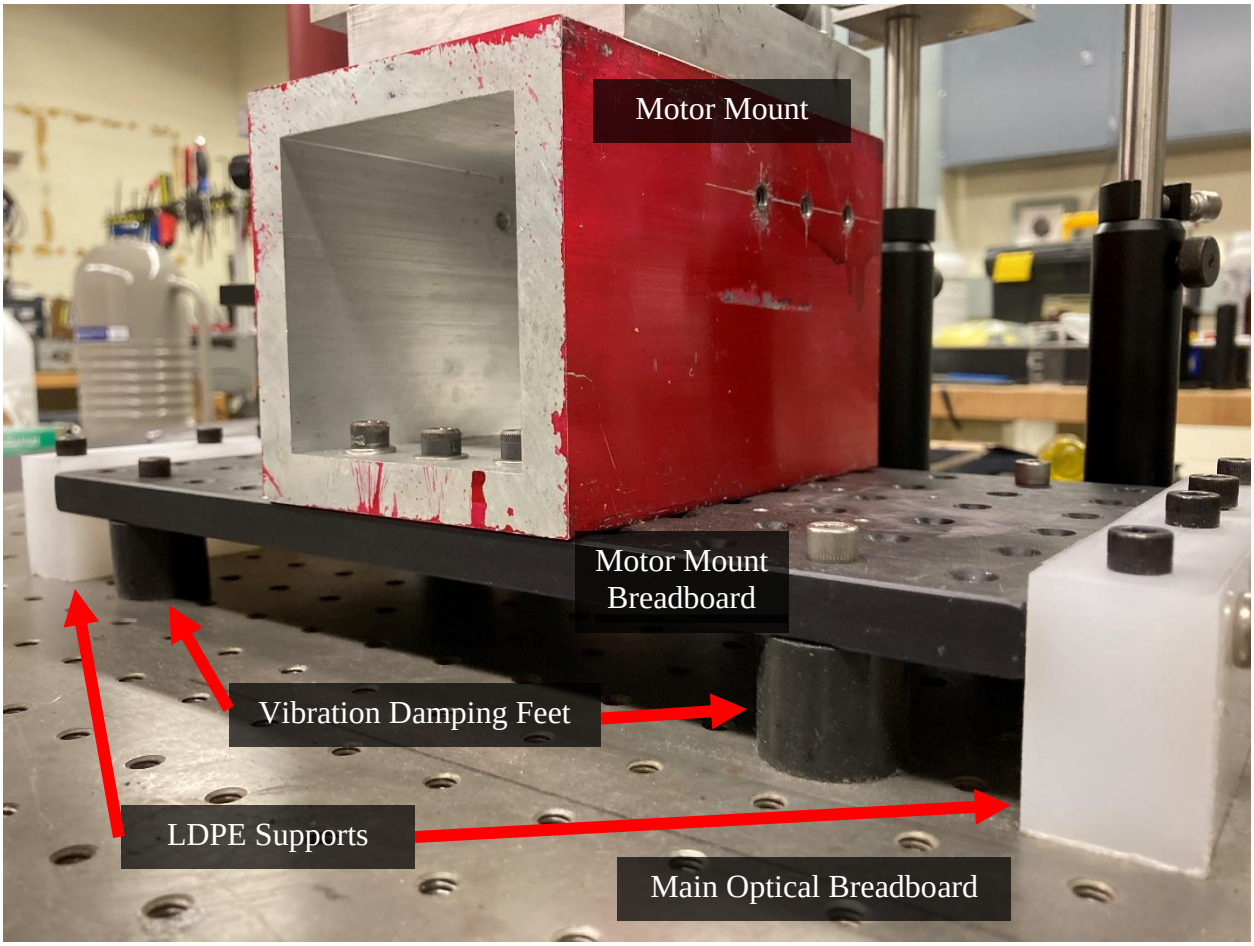

Figure 2.12 - Motor mount vibration dampening

2.3. Sample Data

Operation of the spectrometer as designed produces voltage vs. time data as shown in Figure 2.13. Included are two small sections of the data obtained for two capture cases, 1.) without the globar on, referred to as the Dark signal, and 2.) with the globar on and chamber empty, the reference I_0 signal. For both cases, three full grating rotations are given.

Observation of the I_0 signal shows the presence of the dispersion orders present in the detector each rotation, where negative voltage indicates increased light intensity. An out-of-range negative spike indicates 0^{th} order. On either side are positive and negative 1^{st} order, beginning at about

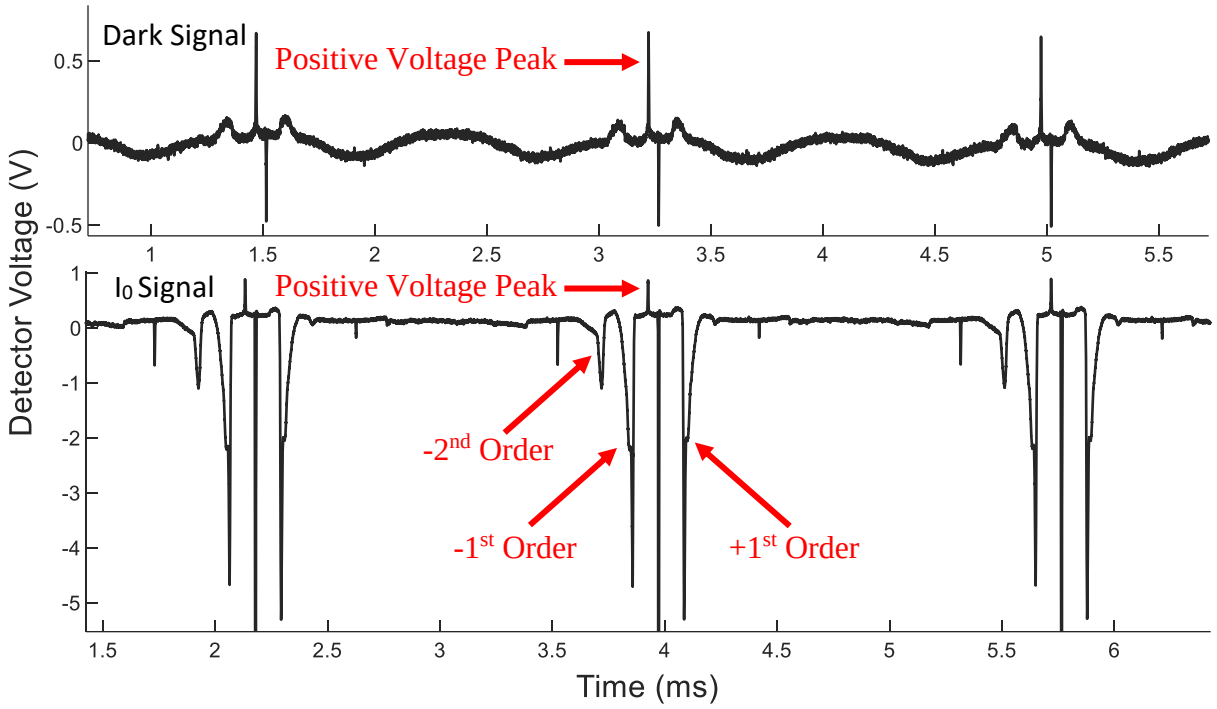

Figure 2.13 - Sample raw data for Dark (top) and I_0 (bottom) signals

7.3µm close to the 0th order peak and tailing off to ~12µm further out. Beyond first order lies the second order scans. Negative 2nd order, to the left, is much stronger than positive 2nd order, which is nothing more than a small blip on the trace. Between scans exist a barren region during which the grating faces away from the spectrometer mirrors in its rotation.

The Dark signal shows the complex baseline on which the I_0 signal rides. Even without a dedicated light source, a small 0th order dispersion signal can be seen. This signal is caused by emission from warm bodies within the spectrometer's optical path. Furthermore, positive voltage features can be seen in this trace: a spike occurring just before the 0th order scan and a pair of smooth humps flanking it. The smoother humps are undesirable as they overlap with the position of first order scans, but the central positive spike is present in both Dark and I_0 measurements and is beneficial for data processing in a way that will be described in the following section.

2.4. Processing Procedure

2.4.1. *Wavelength Conversion*

2.4.1.1. Time to Angle Conversion

As the first step in the processing of raw voltage vs. time measurements, the data is broken into individual grating rotations for easier handling. As part of this step, the time referenced measurements would be converted into grating angle-based measurements. Converting time to rotation angle was achieved by using the small positive voltage peak that occurs each rotation. Due to unknowns in the experimental apparatus, the angular separation between recurring features within a scan was not certain. Consequently, an arbitrary angular position could be applied to only one feature per rotation with any confidence. The small positive peak was chosen for this feature as it occurred in all measurements, meaning the arbitrary angle assignment would be consistent across all measurements. The following process describes how this peak would be used to distinguish individual rotations.

Before the grating angle conversion could be determined, the raw data required some processing to allow the positive peaks to be isolated systematically. First, the Electromagnetic Pulse (EMP) generated from the discharging spark would sometimes create spikes on the detector reading that would interfere with the peak detection function used to find the positive peak. These spikes were removed by applying a moving average filter to the data in a narrow time window around the EMP location. Next, low frequency variations in the detected signal would be removed. This correction was performed by fitting a heavily smoothed version of the data set with a coarsely fitting spline function, and then subtracting the spline from the raw data. A high-pass filter was also attempted to remove the low frequency variation, but it was not as reliable as the spline method.

With the signal riding a flat baseline and any EMP spikes removed, approximate locations of all the peaks could be performed using a peak finding function. More accurate positions of each peak were determined by taking the average time for which the peak remained above a threshold voltage as a user-defined tuning parameter during processing. Each consecutive peak time position was then prescribed an angular position as a corresponding multiple of 360 degrees. This approach provided a mostly linear relationship between time and total angle swept, but inconsistency in the grating rotation speed meant the relationship was not perfectly linear. To correct for this

nonlinearity, a linear fit was applied to the data and the error of that fit calculated for each peak. The error values vs. time were then fit with a smoothing spline function, and both fits were applied to the entire capture time vector and added together. The resulting total angular position vector benefited from variations in angular velocity during a given rotation being smoothed out. An alternative method of assuming a constant speed for each rotation resulted in noticeable errors, and therefore illustrated the need for this more complex method.

Finally, with a conversion to total swept angle complete, the full-time sequence could be broken up into individual rotations by taking 360-degree portions. As the positive feature used to identify rotations was positioned between positive and negative first order scans, individual rotations were centered on this feature with the peak designated as zero degrees. Additionally, the times at which each first order scan occurred were recorded for later use.

2.4.1.2. Wavelength Calibration Function

A wavelength calibration requires the use of a physically relevant function to convert the measurement domain, grating angle, to wavelength. The grating equation (Eq. 6) provides this relevant function but must be rearranged to provide a direct relationship between measured wavelength and grating angle. First, by virtue of the spectrometer having fixed entrance and exit slit positions, deviation angle in this system is a constant given by

$$D_v = \beta - \alpha \tag{10}$$

Making this substitution, the grating equation (Eq. 6) can be rearranged into the form

$$k\lambda = \frac{2\cos\left(\frac{D_v}{2}\right)}{10^{-6}n}\sin\left(\beta - \frac{D_v}{2}\right) \tag{11}$$

Here one can define an arbitrary grating angle,

$$\theta_{arb} = \beta - \frac{D_v}{2}, \tag{12}$$

making it clear that the wavelength passed by the exit slit varies as a sine function with the grating angle. Therefore, wavelength calibrations must be fit with sine functions to be physically relevant. An additional benefit of this fitting function is that it applies to the entire rotation, requiring only a single function to calibrate positive and negative first order scans.

Finally, the grating equation as shown applies to wavelength, measured in nm or μm, but a more common domain variable for the infrared is wavenumber (cm^{-1}). The conversion is straightforward and given by:

$$Wavenumber\ (cm^{-1}) = \frac{10{,}000}{Wavelength\ (\mu m)} \tag{13}$$

However, the sinusoidal function which allows for simultaneous calibration of both orders applies only to wavelength. To calibrate to wavenumber, a wavelength calibration would first be done and then the wavelength to wavenumber conversion applied.

2.4.1.3. Wavelength Calibration References

Performing spectral wavelength calibrations requires measuring the signal from a known calibration source that contains many spectral features of known position within the region of measurement. Two different sources were used in this work to provide spectral calibration, ammonia gas and a polystyrene calibration film.

Ammonia gas has many narrow absorption features within the longwave region, making it an excellent source for calibration reference locations. Furthermore, these ammonia transitions have well defined constants, allowing for modeling of the transitions. An example of a simulated absorption spectrum is provided in Figure 2.14. Required transition information was taken from NIST Atomic Spectra Database SRD 78 [57].

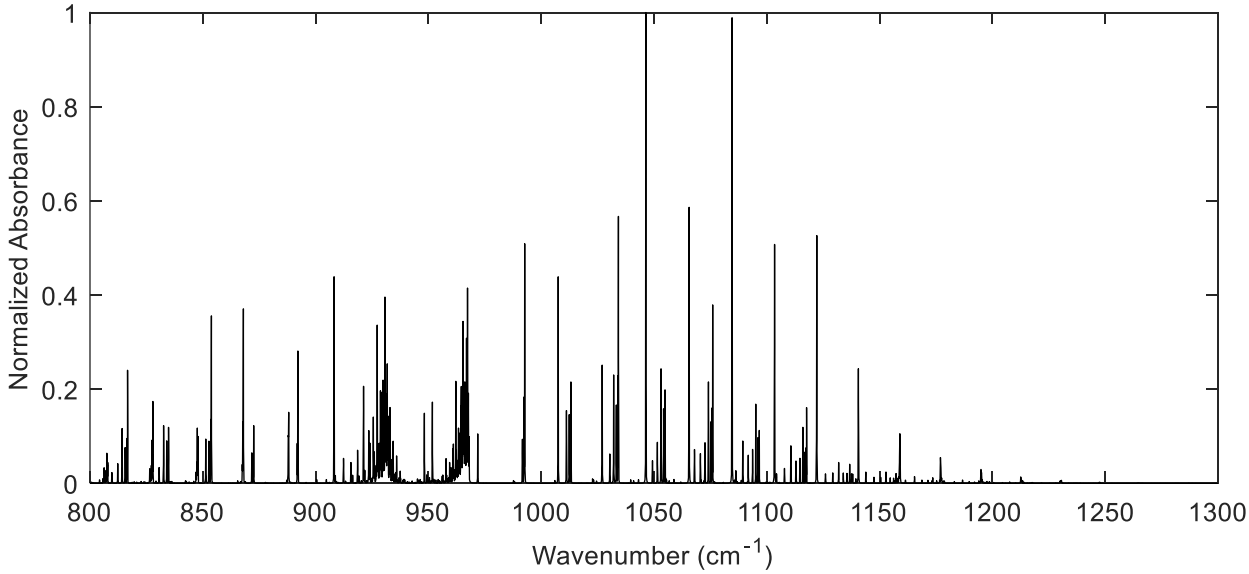

Figure 2.14 - Ammonia absorption simulation, transition information taken from NIST [57]

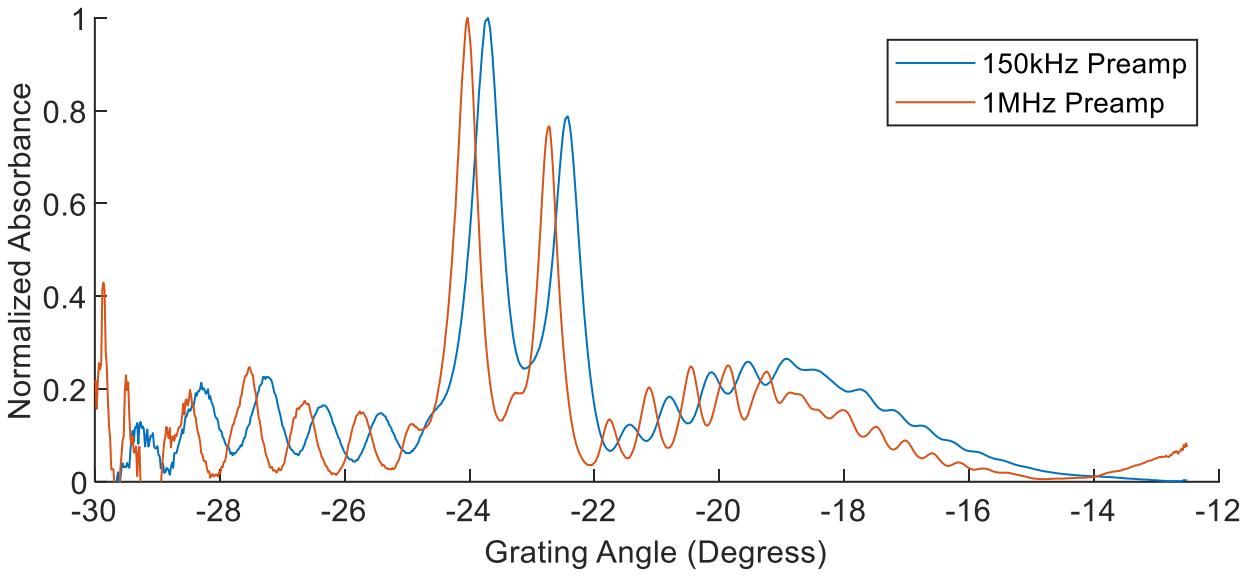

Figure 2.15 - Measured ammonia spectra using 150kHz and 1MHz preamps

Measured ammonia spectra are provided in Figure 2.15. To obtain these spectra, a closed cell chamber was evacuated, filled with ~0.1bar of anhydrous ammonia gas, and placed inside the spectrometer measurement path. The spectrometer grating was brought up to full speed and an absorption measurement taken. Presented spectra are averaged over many grating rotations to remove noise. Here two spectra are provided, one obtained using the original 150 kHz preamplifier and the other obtained using the 1 MHz preamplifier. Interestingly, despite grating angle being determined in the same way for both cases, the spectra do not overlap in terms of feature location. 1MHz preamp measurements appear at lower grating angle corresponding to an earlier time. This suggests that the 150kHz preamp measurement lags behind the actual timing of light on the detector due to its slower time response, and the same could be true for 1MHz preamp measurements but to a lesser extent. Consequently, calibration measurements needed to be performed with full grating rotation speed to account for this time response effect.

Both spectra are considerably less resolved than the simulated spectra shown in Figure 2.14, showing that system resolution is primarily a function of instrumental broadening. But it is readily apparent that the 1MHz amplifier gives better resolution than the 150kHz amplifier. Because of the broadening, no individual ammonia transitions are resolved and tabulated transition locations cannot be used to calibrate wavelength. Instead, an instrumental broadening function must be applied to simulated spectra in order to obtain accurate reference features. Doing so has the added benefit of allowing for the determination of system resolution, as the degree of instrumental

broadening required on the simulated spectra describes the resolution of the system. Instrumental broadening is often described with a Gaussian function, in which every point on the ideal spectrum is smeared out in the shape of a Gaussian profile. The severity of instrumental broadening, and therefore the system resolution, is defined by the full width at half max (FWHM) of the Gaussian function. In practice, instrumental broadening can be applied to simulated spectra by convolving the simulation with a Gaussian curve of a set FWHM.

Calibration using ammonia is an iterative process requiring the simultaneous determination of the wavelength calibration function and the necessary instrumental broadening function. This approach was necessary because varying the degree of instrumental broadening also affects the locations of peaks as they get more or less smeared into or out of other features. Further complications arise from the resolution being variable across the scan. Still, to perform the calibration a first guess at instrumental broadening was applied to the simulation and broadened simulated peak locations assigned to the corresponding peaks in the measured spectrum. From those pairs, the sinusoidal calibration function was determined and applied to the measured spectrum. Measured and simulated spectra were then overlaid and visually compared. If the simulated features were wider than their measured counterparts, the process was repeated with a lower FHWM instrumental broadening function. The inverse was done if simulated features were too narrow. The process was repeated until sufficient agreement was obtained.

Figure 2.16 is the result of this iterative process. Here along with the measure spectra are final simulated absorption spectra with instrumental broadening applied. For the 150 kHz preamp, a FHWM of 13cm^{-1} produces good agreement, while a 9cm^{-1} FHWM is best for the 1MHz preamp. In both cases the inconsistent resolution can be seen, with lower resolution at high wavenumber and higher resolution at lower wavenumber. When using a single FHWM for fitting the entire scan, resolution with the best agreement in the center of the range near 1000 cm^{-1} was desirable.

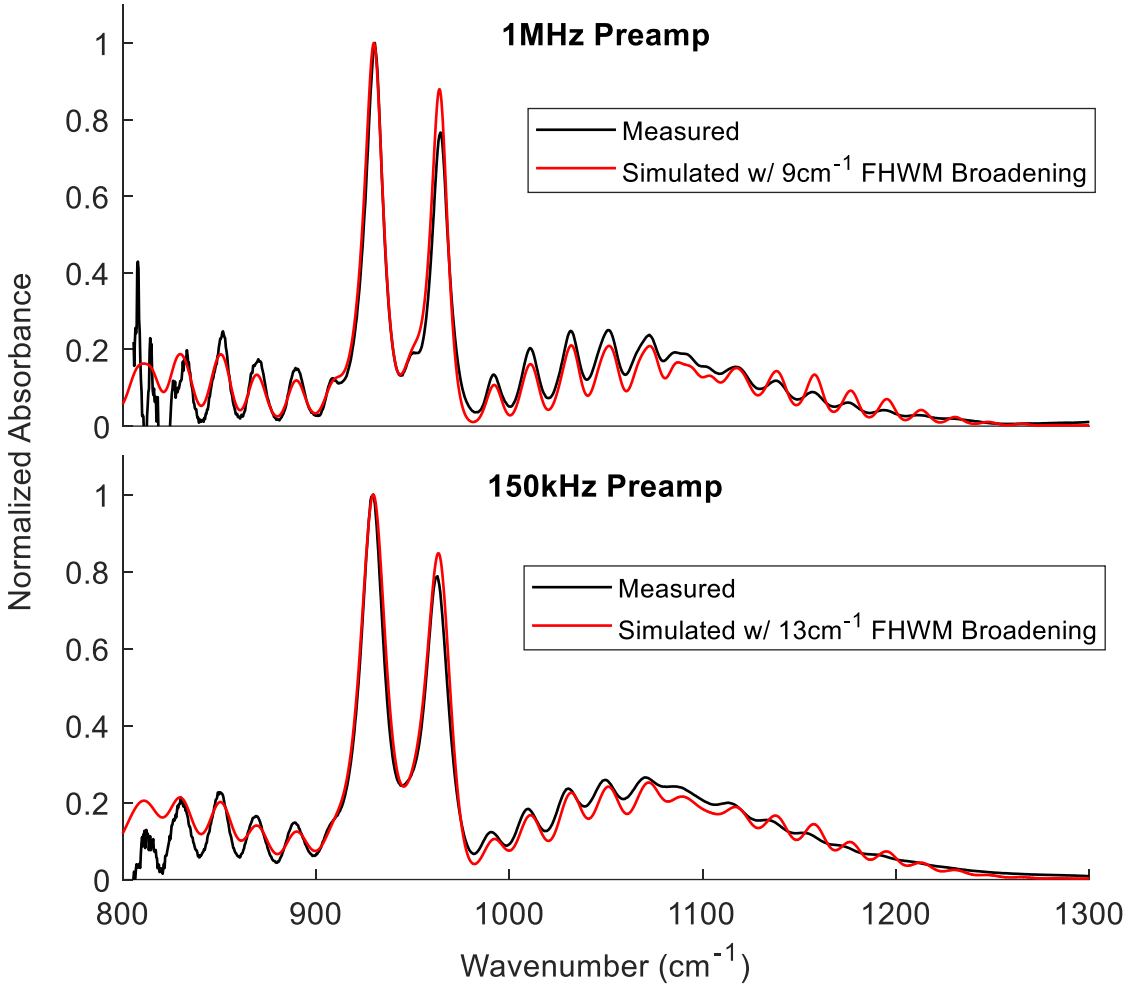

Figure 2.16 - Ammonia calibration and resolution determination for 1MHz Preamp and 150kHz Preamp

Polystyrene calibration films have five NIST traceable absorption features within the measurement range. While they do not have as many features to calibrate the spectrum as ammonia, the film can be implemented rapidly to collect calibrations before each trial. A reference spectrum of polystyrene absorption taken from NIST standard 1921b is provided in Figure 2.17 [58], and a measured spectrum obtained from the scanning spectrometer is given in Figure 2.18. A recommended algorithm for determining peak locations from measured absorption spectra is detailed in the NIST standard, and this algorithm was used whenever a calibration was determined. Unlike the ammonia calibration process, the calibration film was not iterative and easily automated. Given that these calibrations could be collected prior to each measurement and

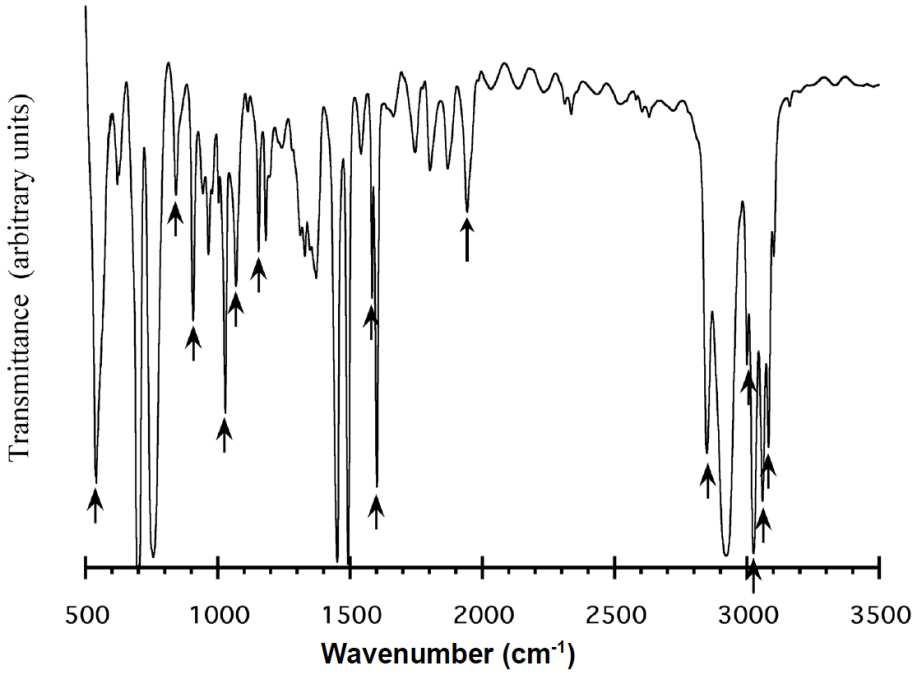

Figure 2.17 - Polystyrene transmittance spectrum, taken from NIST standard 1921b

ammonia calibrations could not, these calibration films were primarily used for wavelength calibration. Figure 2.19 shows the wavelength calibration sine function obtained using the polystyrene film. Here, both positive and negative first orders are fit simultaneously.

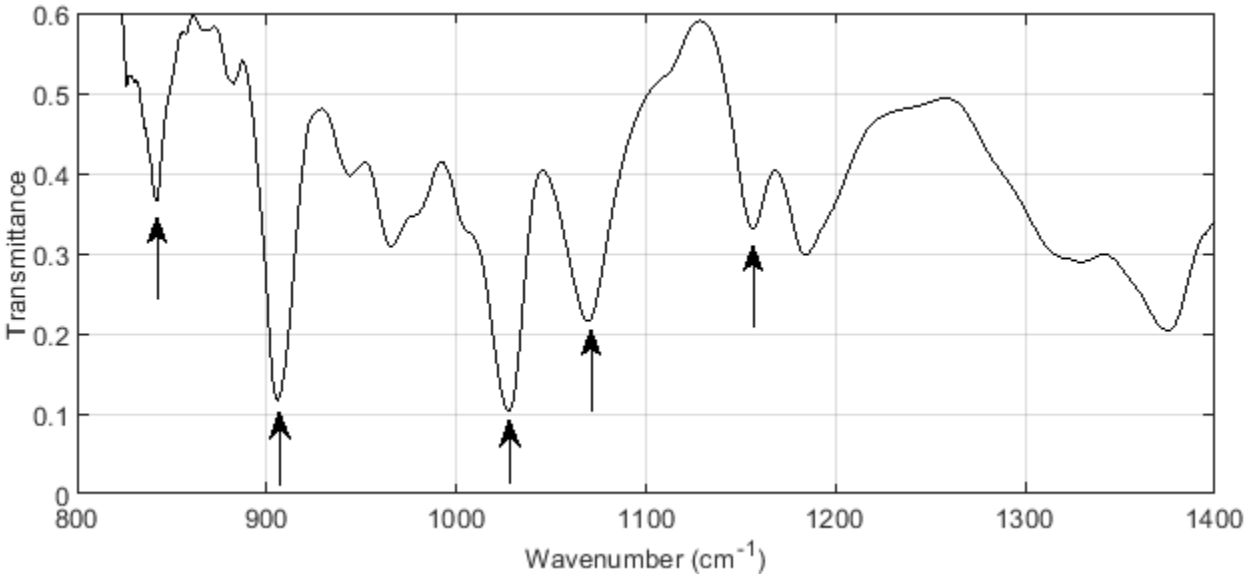

Figure 2.18 - Measured polystyrene transmittance spectrum with NIST traceable peaks indicated

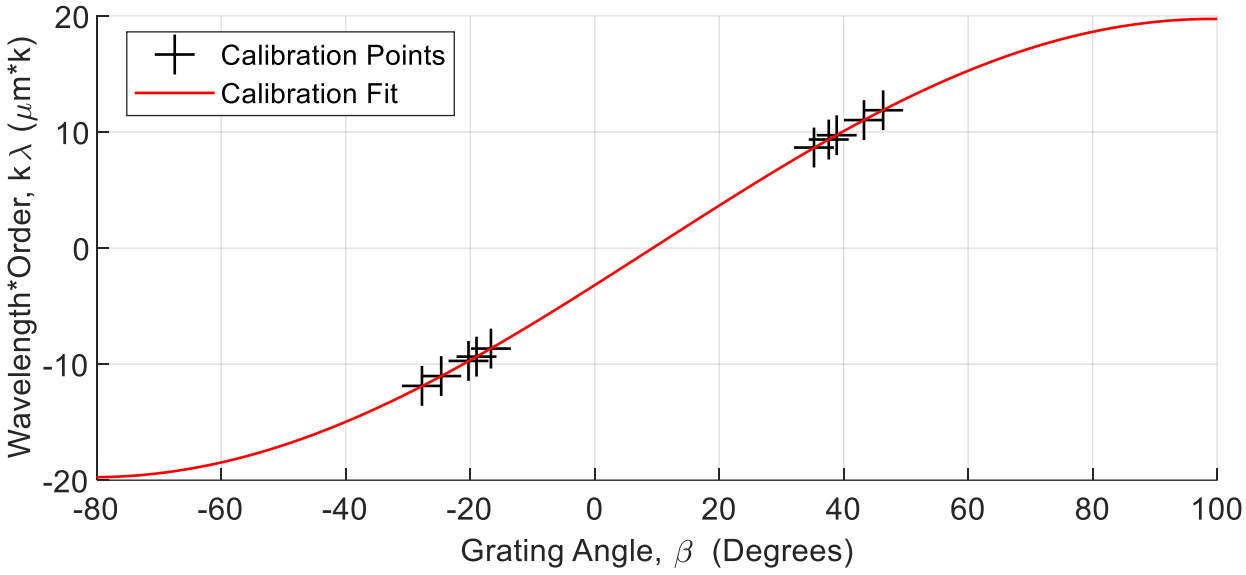

Figure 2.19 - Polystyrene calibration curve

2.4.2. *Dark Signal Correction*

A subtle issue relating to thermal background interference arises in the dark signal. On the back half of the grating's rotation, when the grating is faced away from the mirrors, the camera views the grating mount's aluminum body. Changes in the aluminum temperature are likely to be detectable on the detector, and the AC coupled nature of the detector causes those changes to affect the rest of the scan. Additionally, elements within the optical path prior to the grating would send some light along the optical path. This light would be dispersed when hitting the grating or be diffusely reflected off the aluminum mount when striking it. Considering both cases, changes in temperature of these elements have the potential to change the dark signal throughout the grating rotation.

What results from these effects is that the measured dark signal is complex and highly variable with time. An example of how variable these signals can be is given in Figure 2.20. Such changes in the dark can occur quickly to the extent that dark signals taken seconds to minutes before a light signal will not necessarily fit exactly. To account for this variation, a simple minimization routine was implemented to attempt to determine the dark signal at the time of data capture. In this routine, shown in Figure 2.21, an averaged dark signal taken just prior to the measurement was used as a starting point. Then, this dark was adjusted by scaling and then shifting the dark to best match

portions of the lamp signal outside of the diffracted intensity locations. This approach was found to be beneficial to perform the fit independently for the positive and negative first order scans.

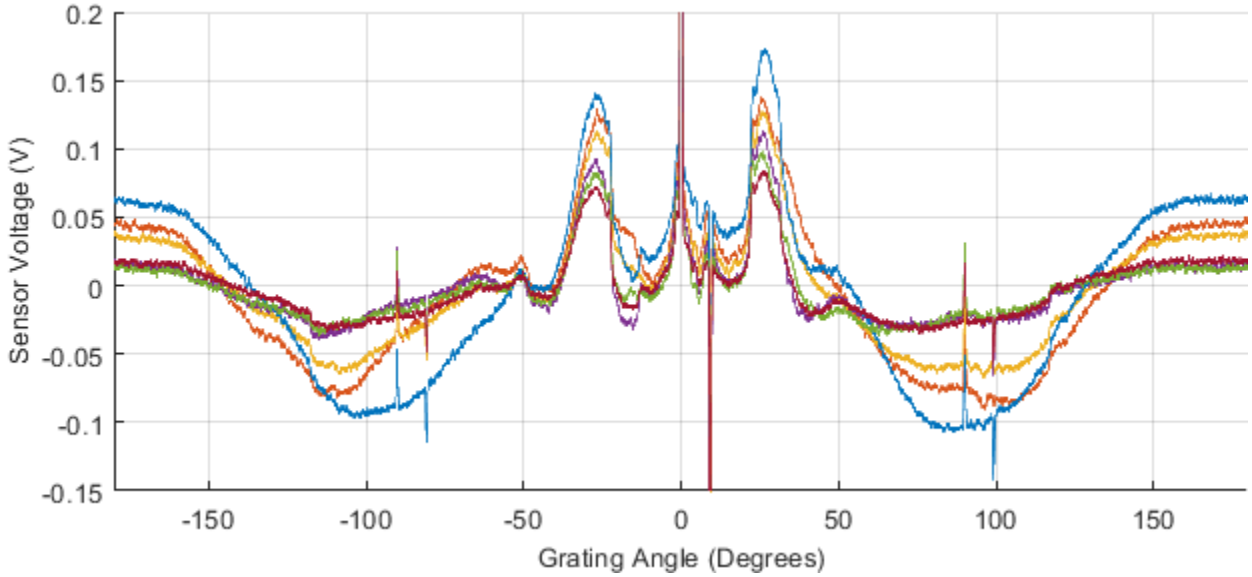

Figure 2.20 - Average dark signal for a full grating rotation measured from six different tests all at nominally the same condition

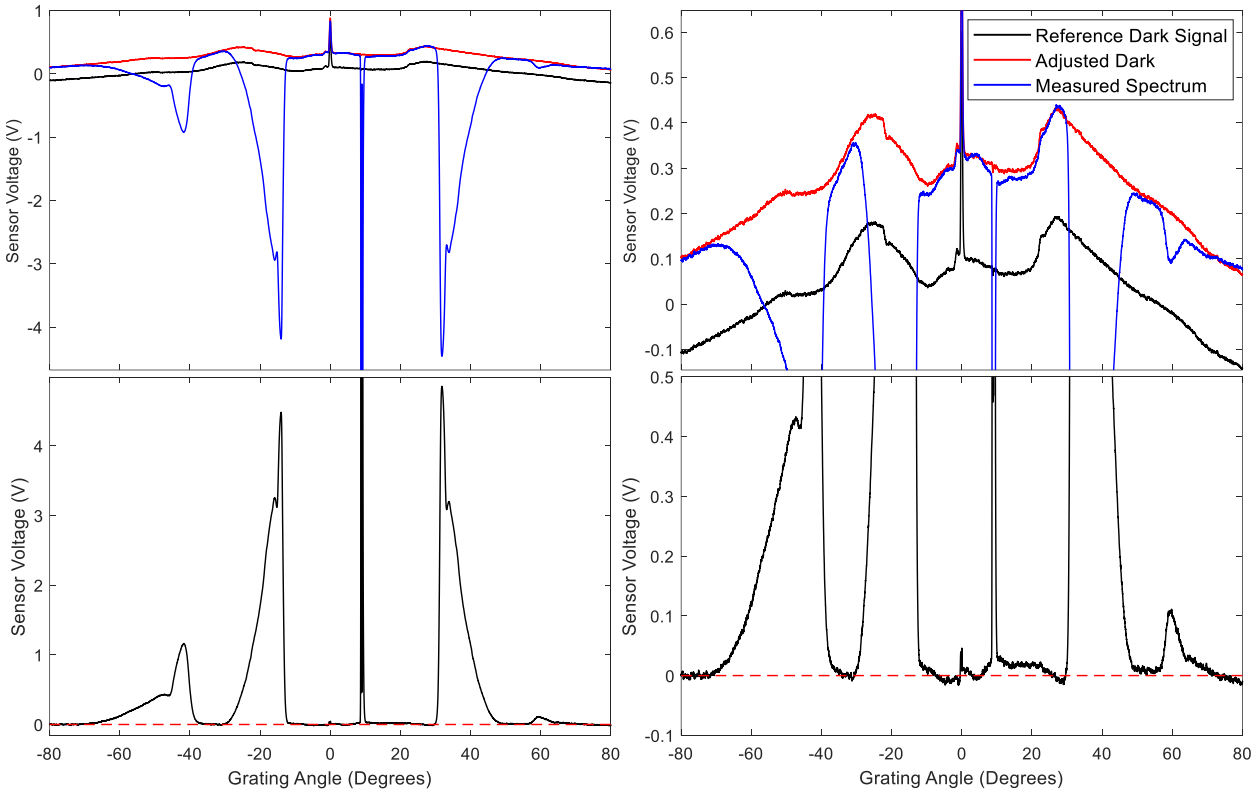

Figure 2.21 - Dark correction procedure (top) and dark corrected scan (bottom)

2.4.3. *Flash Signal Correction*

As discussed, thermal background radiation is a primary complication in infrared diagnostic measurements, especially in these experiments involving hot combustion gases. With burn temperatures in the range of 2000K to 3000K, the short-lived burns produce high intensity and rapidly varying flashes of infrared light. Such flashes interfere with absorption measurements and must be accounted for.

If no steps are taken to mitigate the flash signal interference, the light will be transmitted into the detector as depicted in Figure 2.22. The signal shown has two important characteristics: full detector saturation until 10ms and increased dispersed light intensity following recovery. Full saturation is important as it occurs throughout multiple grating rotations, implying that some light was entering the detector without passing through the spectrometer. This saturation occurred despite there being no direct line of sight between the detector and chamber window, meaning that light must have reflected around the instrument to make it into the detector. To prevent stray light from entering the detector, the spectrometer was enclosed inside a black shroud as shown in Figure

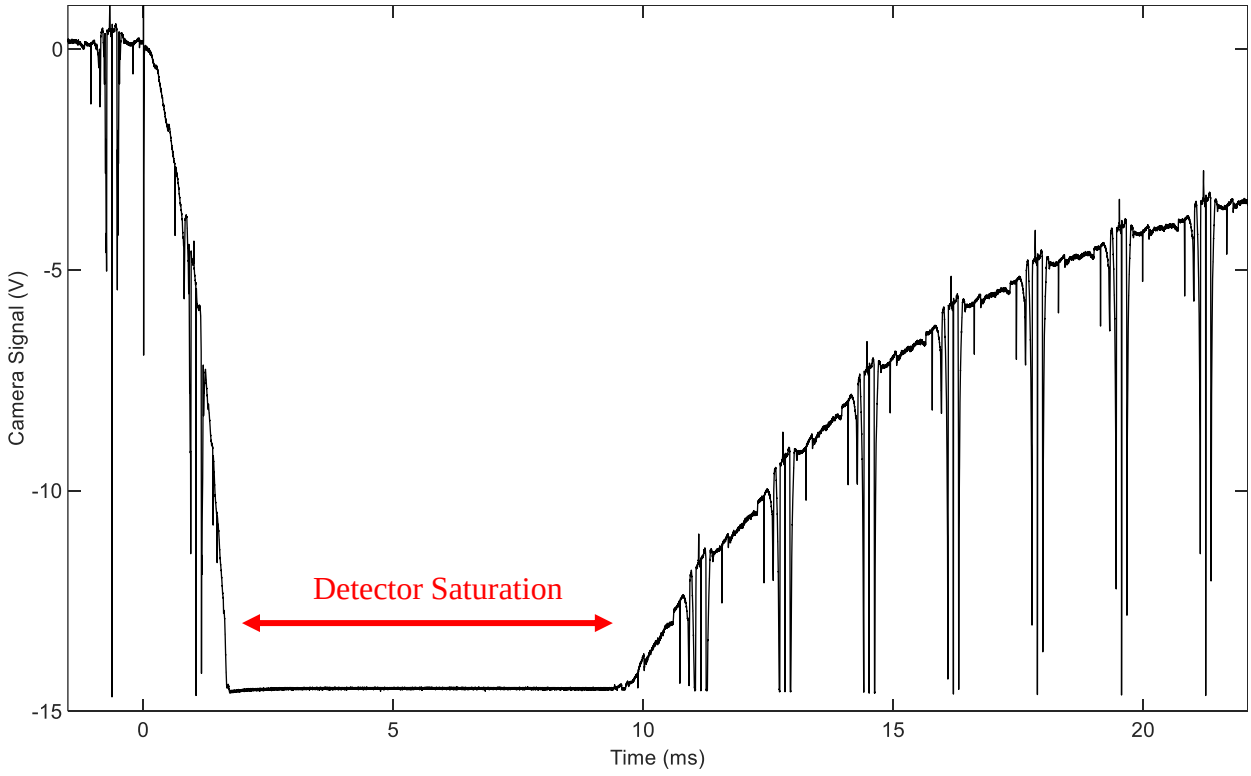

Figure 2.22 - Detector Saturation from Flash Signal

2.23. This method alone prevented full saturation but did not address the second issue of increased dispersed light intensity.

An increase in dispersed light intensity after ignition implies that some of the generated light is passed directly along the optical path through the spectrometer and into the detector. The presence of emitted light inside the dispersed spectra interferes with the equations described in Section 1.4.1 which assume no emission. For those equations to hold true, the emitted light measured during experiments would need to be accounted for. First, steps were taken to minimize the amount of emitted light entering the spectrometer. These included moving the combustion chamber as far from the spectrometer entrance as possible and adding a channeling tube with a pair of 1" diameter apertures between the chamber window and spectrometer entrance, also shown in Figure 2.23. Both of these measures were to prevent light that was not travelling parallel to the optical axis from entering the spectrometer. Implementing both did lower the intensity of dispersed emitted light, but they could not entirely remove the signal as some emission would be directly along the optical path. Any remaining emission signal would still need to be accounted for, and this was done by measuring the emission for a given test case and later subtracting it.

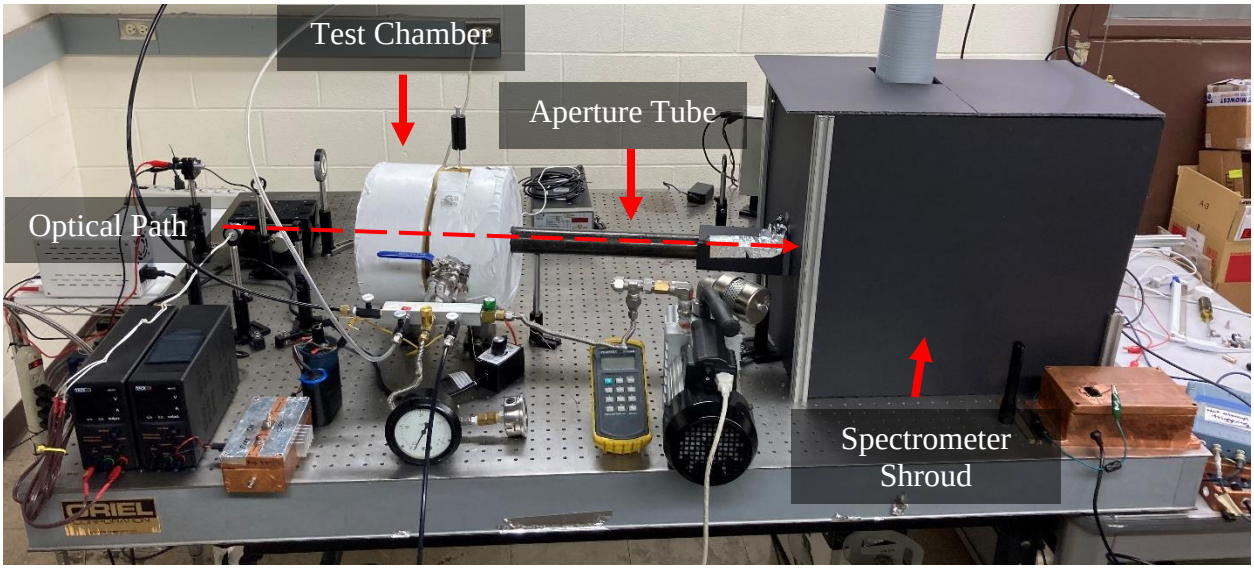

Figure 2.23 - Experimental setup with light blocking

CHAPTER 3: EXPERIMENTAL TECHNIQUE

Fulfillment of the purpose of this research required applying the diagnostic tool discussed in the previous chapter to a DIMP decomposition experiment. The primary decomposition environment of interest, for which a set of benchmark data was desired, was that of a constant volume fuel-oxidizer "closed bomb." A high level depiction of this experiment is in Figure 3.1. A closed cell chamber would be filled with a combustible mixture of gaseous fuel and oxidizer as well as a specific amount of vapor phase DIMP. This chamber would be outfitted with optical viewports and placed inside the measurement area of the scanning spectrometer. The spectrometer would be used to monitor the gases inside the chamber as the fuel and oxidizer were ignited and burned.

Design of this experiment consisted of three primary areas of focus. The first of these was the development of a method to introduce DIMP vapor into the chamber in a repeatable and reliable manner. Second was the design and construction of the closed chamber, with extreme emphasis placed on tailoring the design for maximal model validation utility. The final area was in the determination of reactants for specific and distinct combustion conditions, both in chemical species and concentrations, which would create fireballs that mimic explosive fireballs. Again, great emphasis was placed on maximizing model validation utility.

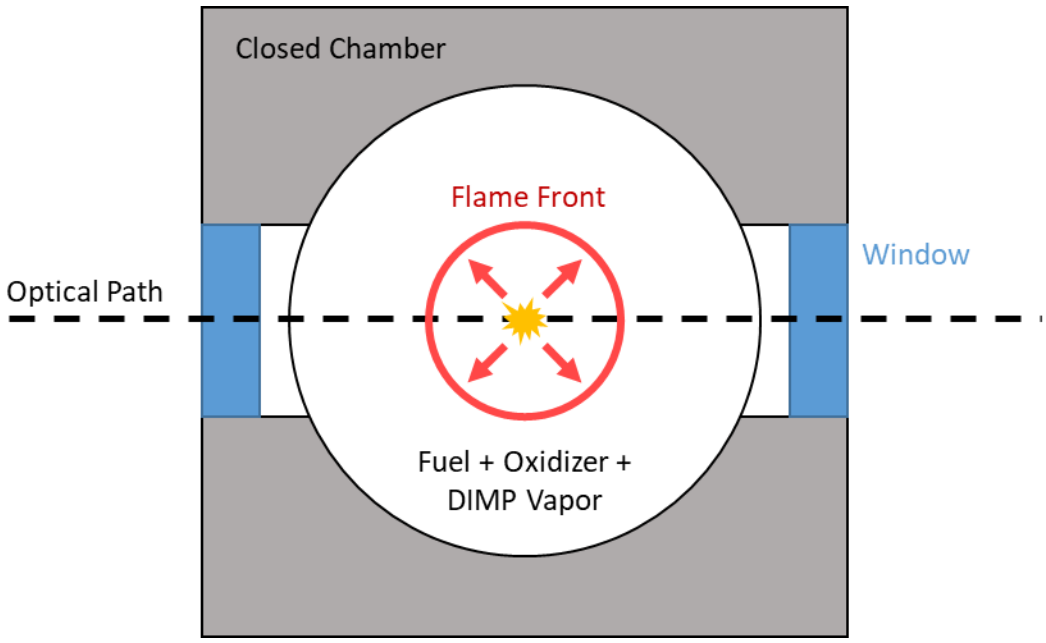

Figure 3.1 - High level experimental design of "closed bomb" DIMP decomposition experiments

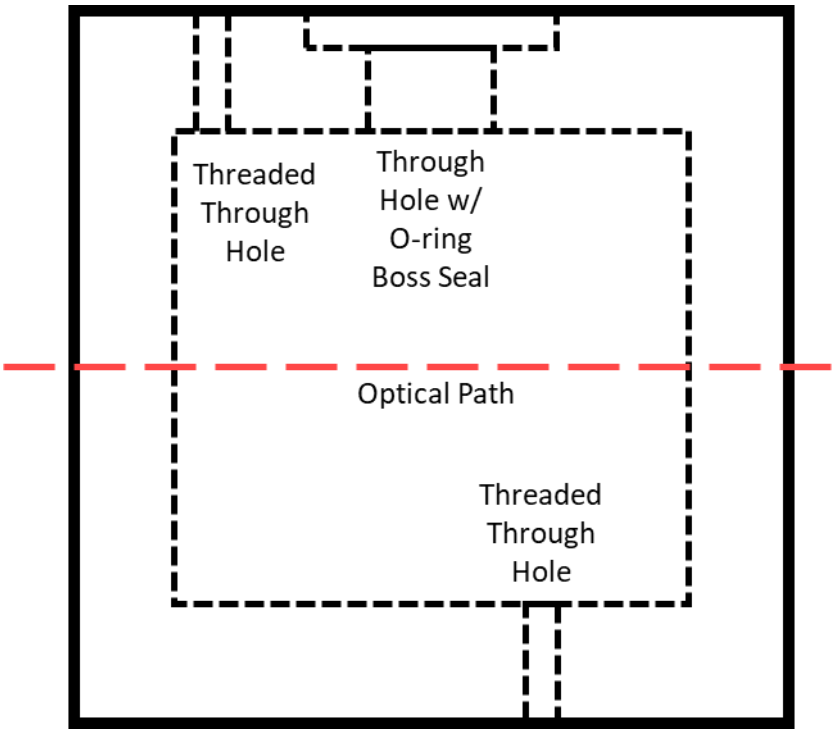

Figure 3.2 - Diagram of previous test chamber in which DIMP injection methods were tested

3.1. DIMP Vapor Introduction Strategies

Perhaps the single most persistent issue related to creating a repeatable DIMP decomposition experiment was the method of introducing the DIMP into the test chamber in a reliable and repeatable fashion. Like Sarin, DIMP is a liquid at room temperature, but measurements were to be taken on vapor phase DIMP. To create enough gaseous phase material, the chamber would need to be heated above the dew point temperature for the desired vapor pressure. Saturated vapor pressure of DIMP was recorded as a function of temperature in [59]. From this vapor pressure data it was determined that the test chamber needed to be heated to at least 70°C in order to ensure no condensation at one atmosphere of pressure.

The proposed DIMP introduction technique had to produce a known and repeatable amount of DIMP vapor in the test chamber. This requirement was made more challenging due to the need to completely vacuum the chamber in the process of setting the required gas fill concentrations. Vacuuming prevented the deposition of a fixed volume of DIMP liquid directly in the main chamber prior to sealing and vacuuming since the vacuum procedure would remove an unknown and variable amount of evaporated DIMP. As a result, any injection technique would need to introduce the DIMP after the vacuum procedure. Many different techniques were attempted, each

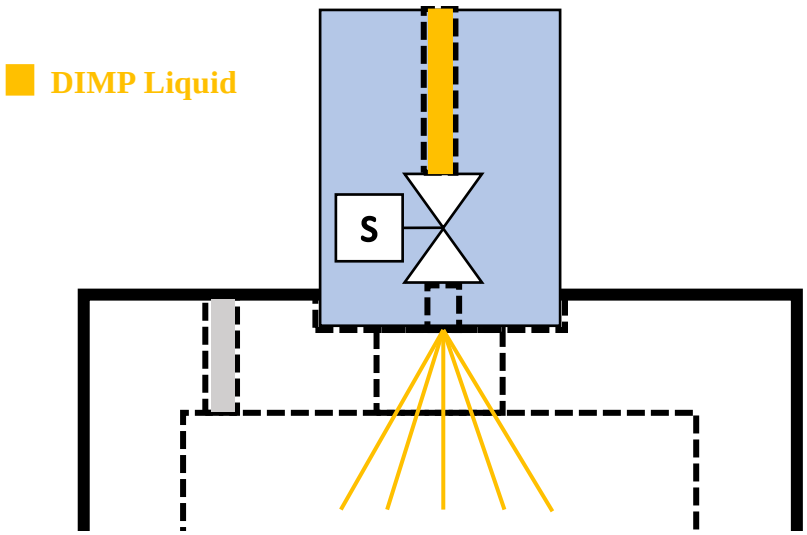

Figure 3.3 - Fuel Injector DIMP Injection diagram

with a significant issue that adversely affected performance. The failed techniques will be discussed here followed by a discussion of the successful technique.

In the following discussion diagrams of the techniques are provided to assist in the description. These diagrams depict the techniques as they were used in an early test chamber. That chamber, with a cross section depicted in Figure 3.2, was a cylindrical cavity with a base plate and lid plate. The lid had a threaded hole into the chamber, shown on the left, and a straight through hole with an O-ring boss seal, shown in the center. A threaded through hole was also made in the base plate, shown slightly to the right of center. Each of these access points was used at one time or another when attempting different injection strategies.

3.1.1. *Vehicle Fuel Injector*

The first failed technique used a vehicle fuel injector to spray liquid DIMP. In the operation of such a device, the injector could be fitted to the chamber with a vacuum seal allowing the liquid to spray into the evacuated chamber. Liquid DIMP could be fed into the exterior portion of the injector and would be isolated from the chamber volume through the injector's interior solenoid valve. To introduce the DIMP, the solenoid could be electronically triggered, temporarily allowing the liquid to be sprayed into the chamber.

This method had many attractive potential benefits, primarily that the spraying of DIMP would quickly aerosolize it to form a vapor. However, ultimately this technique failed due to

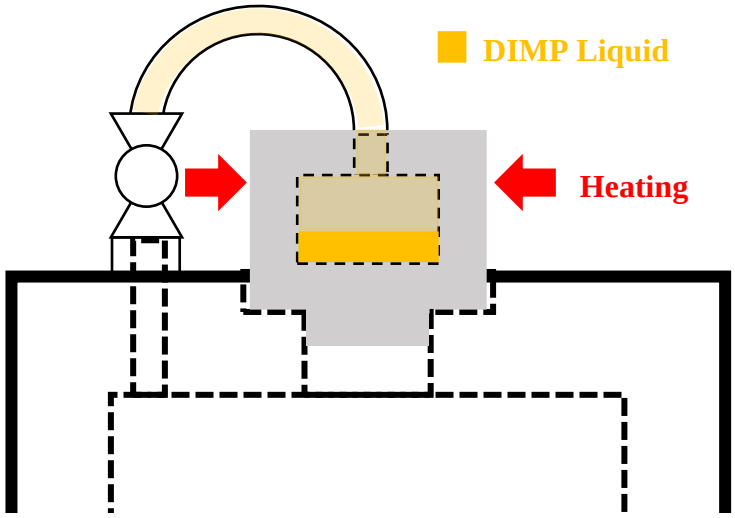

Figure 3.4 - Heated Side Arm DIMP injection diagram

incompatibilities of the DIMP liquid with the injectors. It was observed that injectors filled with DIMP would cease to function after only a short time of use. It is suspected that the cause of the malfunction is related to the reactive nature of DIMP. DIMP is known to react with many plastics and rubbers, making it highly likely that the DIMP was degrading components within the injectors.

3.1.2. *Heated Side Arms*

Next, several iterations of a heated side arm were attempted to inject DIMP in which some cavity filled with a reservoir of liquid DIMP was isolated from the main chamber volume via a ball valve. The operating principle was that these external cavities could be heated to temperatures higher than that of the chamber, creating high vapor pressure of DIMP gas which could then be introduced to the larger test cylinder by opening the valve.

These methods were subject to several difficulties that ultimately made them impractical. The pictured method, shown in Figure 3.4 with a large DIMP reservoir, was difficult to control the amount of DIMP vapor that was introduced. A long arm connecting the reservoir to the separating ball valve caused considerable condensation of DIMP vapor and DIMP's high molecular weight made it diffuse very slowly through the narrow arm. In addition, these iterations all eventually suffered from the fact that DIMP vapor would deteriorate the valve seal and cause chamber leaking.

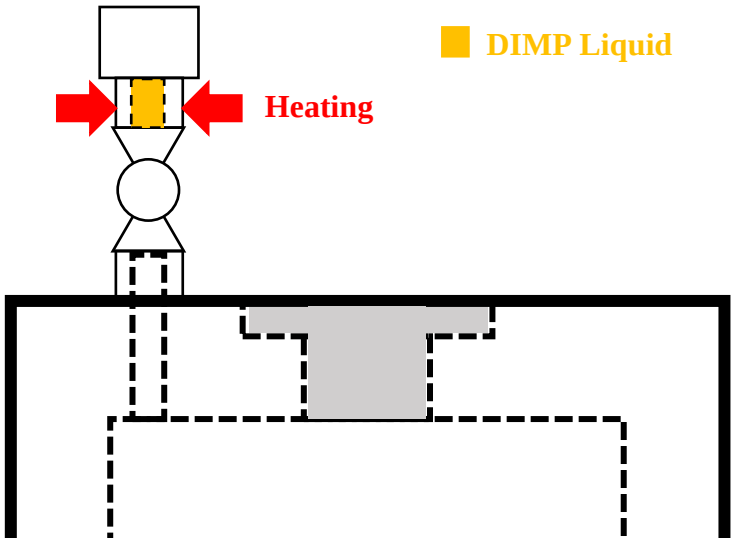

Figure 3.5 – Vertical Valve DIMP injection diagram

3.1.3. *Vertical Valve Loading*

The third attempt at DIMP injection amounts to a simplification on the previous heated sidearm, where the reservoir of liquid was replaced with a tightly controlled volume of liquid. Condensation issues were mitigated by removing the long section of pipe and instead loading the DIMP directly on top of the separating ball valve. Upon depositing the liquid, a cap was applied to the top of the valve, and then the valve was heated. Once the chamber had been filled with the test gas mixture, the valve would be opened to introduce DIMP into the main chamber.

This technique worked decently as an injection mechanism for a while. The primary benefit of this technique was tight control on the maximum amount of DIMP introduced into the system since the valve could be primed with a set volume of the substance. But two major issues with this technique compounded to degrade the quality of experimental results: long equilibrium times and leakage issues.

In this technique, upon opening the valve to a chamber primed with 0.2 bar of test gases, a slow rise in measured DIMP signal would be observed. Measured absorbance from DIMP signatures would take 10 minutes to equilibrate. Normally, this would not be an issue, but during this equilibration time, atmospheric gas would be leaking into the chamber at a variable, but always significant rate. This meant that the gas composition present in the chamber at the time of ignition was not known.

Many attempts were made to address the leak rate issue, but ultimately the cause was determined to be the valve which held the DIMP liquid. Inspection of the sealing O-rings within the valve revealed that the DIMP was degrading and compromising seal integrity.

3.1.4. *Vertical Cup*

Aside from the leaking issue, vertical valve loading showed great promise, and so the logical next step was to remove the need for a separating ball valve. The first attempt at doing this was to create a small vessel to hold the desired DIMP liquid volume and attach it upright to the chamber underside with a direct path to the chamber interior, as shown in Figure 3.6. To seal the cup inside the chamber, the cup was made to fit inside of a KF16 end cap that was attached to the chamber via small section of pipe. The cup would be distanced from the heated chamber, so it was thought that there would be minimal evaporation until the cup was independently heated. This assumption was supported by the fact that the chamber could be vacuumed with no measurable DIMP signal appearing. However, an absorption signal was absent even after independently heating the cup for many minutes. An attempt to measure an equilibration time saw no equilibrium obtained, even after 40 minutes of heating.

In a separate test trial, after 10 minutes of heating, the cup was removed, and it was observed that liquid remained in the cup. These findings suggested that heat transfer through the KF fitting, to the cup, and to the DIMP was poor and/or that the diffusion of DIMP was very slow, resulting in a saturated vapor at the bottom of the tube that prevented further evaporation of liquid. Removing

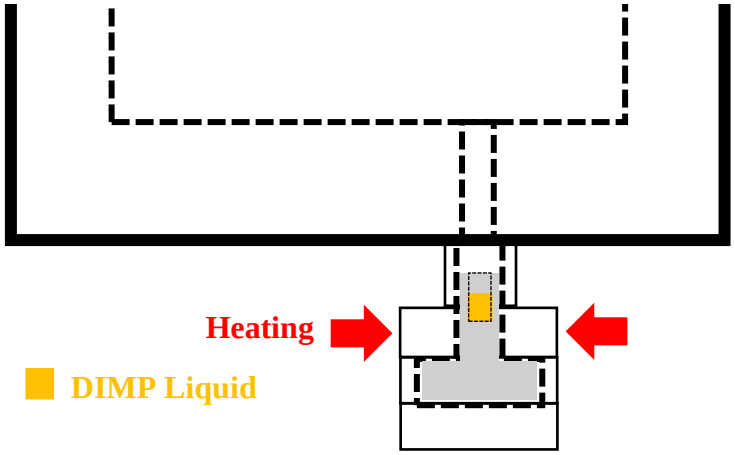

Figure 3.6 - Vertical Cup DIMP injection diagram

the ball valve alleviated the majority of the chamber leaking issues, although some leakage remained since the chamber was not designed to hold vacuum.

3.1.5. *Direct Heating Vertical Cup*

To address the potential issue of poor heat transfer to the liquid, a different cup was constructed with a hot wire running through the DIMP liquid as shown in Figure 3.7. The concept was that when DIMP vapor was desired, current could be applied through the wire, directly heating the DIMP liquid, and causing nearly instantaneous boiling. While the cup was tested and shown to successfully boil off the DIMP in an open environment, no rapid rise in DIMP signal was measured when it was installed in the chamber underside. This lack of signal suggested that the primary complication was the slow diffusion of DIMP vapor out of the deep hole in which it was being formed.

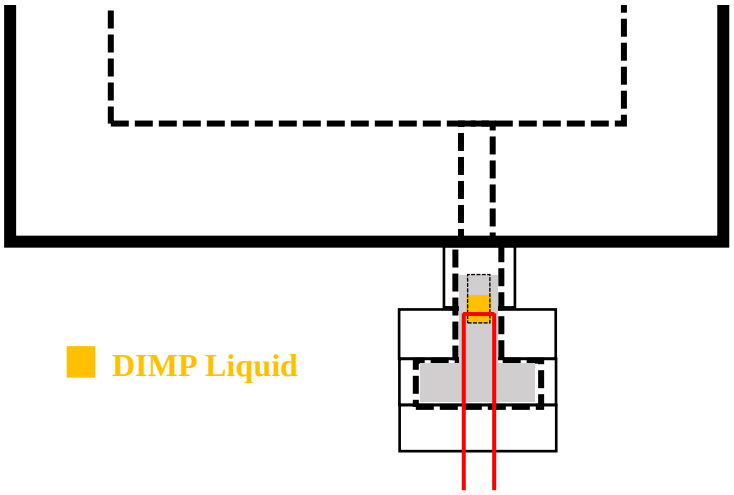

Figure 3.7 - Direct Heating DIMP injection diagram

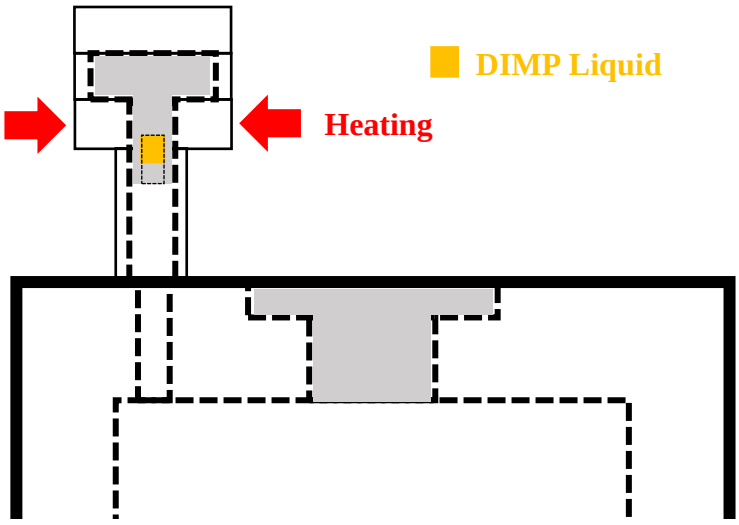

Figure 3.8 - Inverted cup DIMP injection diagram

3.1.6. *Inverted Vertical Cup*

With slow diffusion of DIMP assumed to be the primary factor in slow equilibration, the next injection technique leveraged gravity to assist in diffusion. To do this, the evaporation pipe and cup were inverted and relocated to the chamber lid, shown in Figure 3.8. Cup inversion was possible since the diameter of the hole containing liquid DIMP was small enough for the DIMP liquid to remain inside even with the cup inverted.

Initially, it was assumed that this pipe would need to be independently heated before any meaningful amount of DIMP would evaporate from the cavity, so vacuum could be pulled first, the chamber filled with test gases, and then heat applied to produce the DIMP vapor. Unfortunately, while inverting the cup did produce faster DIMP diffusion in the chamber, equilibration still took longer than 15 minutes to achieve. Thanks to collaborative work with Professor Mark Phillips, a fellow researcher working in the same area, an interesting phenomenon was discovered with this method. If the cup were loaded with liquid and the chamber held at total vacuum for a couple of minutes, a nearly instant jump in DIMP concentration would be measured. This jump would occur even absent of heating the DIMP pipe. It is hypothesized that the cause for the jump in concentration is a droplet of DIMP falling from the cup while under vacuum and rapidly evaporating during its fall. Upon back filling with the combustible gases, the DIMP concentration would rapidly rise and equilibrate as the rush of gas assisted mixing. No noticeable

decrease in DIMP vapor was observed upon opening the valve to fill with gas, implying that no vapor was lost in the process.

Thanks to the instant jump in concentration and the fast mixing, this technique required no additional wait time to fire after the gases were added. No wait time was highly desirable as it allowed for more frequent tests to be performed; however, there was considerable shot-to-shot variability in the concentration of DIMP that was evaporated. A potential cause for this is a variability was the size of droplet that fell from the cup, and a method with increased repeatability was necessary.

3.1.7. *Glass Syringe*

Findings from all previous DIMP injection strategies resulted in several important revelations about DIMP that informed the final injection strategy:

- DIMP reactivity with sealing materials prevents the use of certain valves
- DIMP evaporates within seconds when falling as droplets in vacuum
- DIMP diffusion is very slow, so opening the chamber to the gas manifold to fill with test gases results in little, if any, loss of DIMP

With these findings in mind, the goal for the next injection technique was to create known and repeatable droplets that could be introduced to the chamber on command, achieved through the use of a glass micro syringe. The syringe was adhered with silicone adhesive sealant to an aluminum insert which fit to a hole in the chamber lid. The syringe is delineated in 1μL increments, allowing for clear determination of injected DIMP volume. In operation, the syringe is loaded with the desired DIMP volume and the syringe plunger withdrawn partially to pull the liquid partially up the syringe. This ensures separation of the DIMP liquid from direct heat when the syringe is installed in the chamber, preventing premature evaporation. The syringe's clear glass body ensures that DIMP liquid can be confirmed visually to remain in the syringe without loss of volume during the vacuum process as well. After achieving adequate vacuum, the chamber would be sealed, the syringe plunger depressed, and the expected jump in DIMP concentration seen immediately upon depressing the plunger. Once DIMP vapor had partially equilibrated, as measured through the chamber's pressure gage, back fill would be started, assisting in the final mixing.

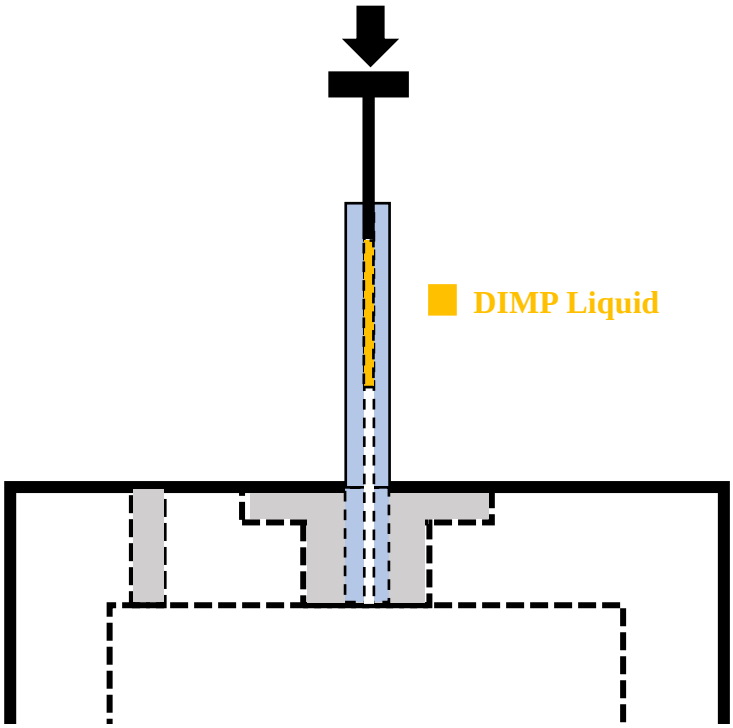

Figure 3.9 - Glass syringe DIMP injection diagram

This method is superior to all previous methods attempted for several reasons. First, the lack of any valves in contact with DIMP removes the potential for damaged valve seals that introduced leaks. Next, the introduction of DIMP as droplets into a totally evacuated chamber produces nearly instantaneous evaporation. Combined with the enhanced mixing associated with backfilling after DIMP introduction, this method requires no additional wait time for DIMP equilibration, speeding the measurement process. Finally, the rapidness of DIMP evaporation meant that the chamber need not be heated above 80°C. Reducing chamber temperature makes handling the chamber during operation easier and also reduces the amount of thermal background radiation captured by the scanning spectrometer during use.

3.2. Test Chamber Design

As mentioned, the goal of this work is to provide data with maximal utility toward modeling efforts. The first way in which utility is maximized is in the geometry in which these combustion events occur. Due to the high level of complexity surrounding combustion events, modeling efforts benefit greatly from exploiting symmetry. To achieve maximal symmetry utility, the test chamber

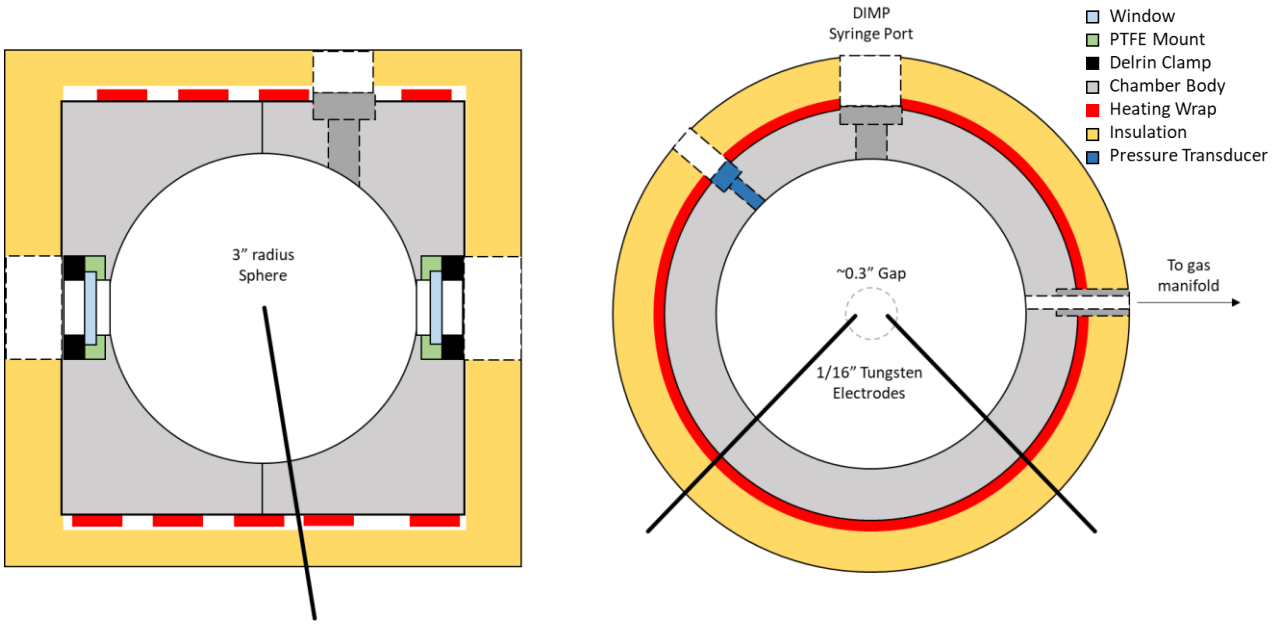

Figure 3.10 - Spherical test chamber diagram with side view (left) and front view (right)

in which these experiments were to be performed was designed with spherical symmetry, allowing for the use of one dimensional (1D) modeling techniques.

To achieve spherical symmetry the chamber was designed with a spherical cavity, made possible by machining a hemispherical cavity into the ends of two cylindrical rods. Bolting the two halves together results in a closed spherical volume. Machining drawings used in the construction of the test chamber are provided in Appendix B for a detailed description of the chamber. To assist in the discussion of the chamber design, a simplified schematic is given in Figure 3.10 and photographs in Figure 3.11. As shown, the chamber was made from two 8" diameter aluminum cylinders, both 3.8" in length.

Out of each aluminum cylinder were bored 6" diameter hemispheres, resulting in a 6" diameter spherical cavity when joined. A 1" diameter hole was drilled through the cylinder axis, serving as the viewing port, and window mounting holes were bored into the cylinder's outer face. Specific aspects of the chamber design will be discussed in the following subsections.

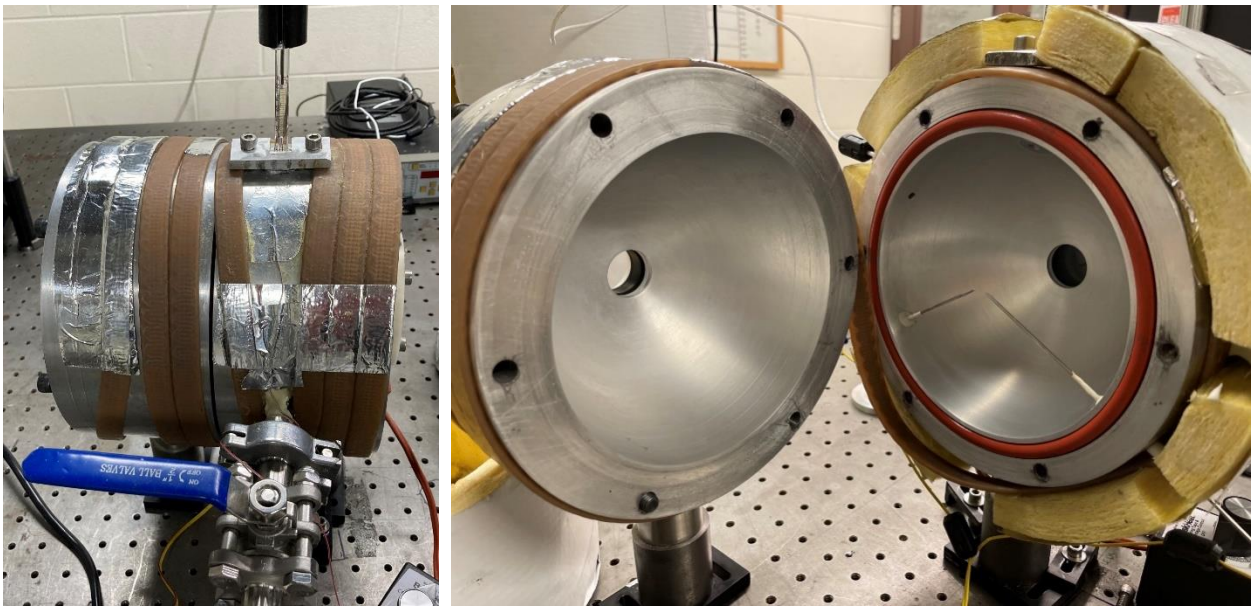

Figure 3.11 - Spherical chamber images closed with insulation removed (left) and opened (right)

3.2.1. *Vacuum Sealing*

Before addressing specific design aspects, a note on a prevalent underlying design criterion needs to be made. Previous iterations of test chamber designs suffered from leakage issues, and initial reactant pressure in these experiments is below atmospheric, meaning leakage of atmospheric gas into the chamber added uncertainty to the composition of reactant mixture at the time of ignition. To reduce this uncertainty, the spherical chamber was designed with maximal sealing capability in mind. All removable components of the chamber are sealed through O-ring seals and all permanent components are epoxied in place.

The effectiveness of an O-ring seal is affected primarily by the width of the O-ring cross section and the number of redundant O-rings. To maximize chamber sealing, all O-ring seals were designed with either the widest available O-ring or multiple O-rings. This consideration is perhaps best demonstrated by the seal between the two chamber halves. The O-ring used is a 400-dash number, or ¼" wide, the thickest readily available.

3.2.2. *Window Insert Design*

The design to install the optical windows into the test chamber was influenced by four main factors. First and foremost was the need to have the windows installed in a form of soft mounting that prevented direct contact of the window with the metal chamber body. Such soft mounting has been

shown to prevent window breakage in the presence of the rapid rises in temperature and pressure experienced during these constant volume combustion events. Secondly, the material used for these soft mounts would need to be chemically resistant to DIMP vapor wherever the mount was in contact with the chamber interior. A common choice of easy to machine plastics is Delrin acetal resin, but DIMP reacts with the material as shown from previous window mount iterations. A material which does not react with DIMP is PTFE and so was this material used to make the soft mount. Third, the presence of deep window wells has been declared a major area of uncertainty in modeling these environments. As such, the soft mounts were designed to minimize the depth of the window well. To do this, the PTFE insert which held the window was made as thin as possible, positioning the windows' inner faces as far inward as possible. Finally, the windows and their inserts needed to be removable and be well sealed when installed.

These requirements resulted in the window insert and window mount designs shown in Figure 3.12. Through careful consideration of the insert design, the mounting hole was made to be very simply a 1.868" diameter, 0.75" deep bore into the chamber's exterior face. The depth of the bore resulted in a seat at the bottom that was only 0.090" thick (2.3 mm) at its thinnest point. The precise diameter meant that inserts could seal against the circumference of the bore using a 223 O-ring piston seal. As shown, the inserts were designed in two parts, an inner PTFE part which held the window and outer Delrin part which backed against the window. Delrin could be used for the outer part as it would not contact DIMP vapor. The two-part design allowed for a double O-ring seal for

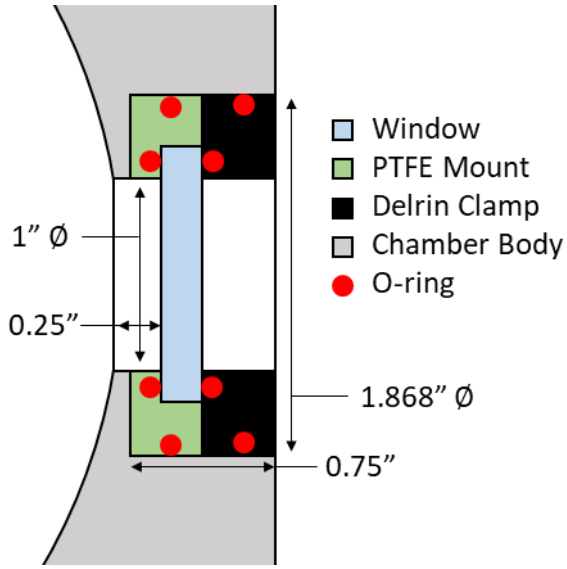

Figure 3.12 - Chamber window mount design

all potential leak paths. The windows themselves were sealed with O-Ring face seals on both sides, and both insert parts were sealed with piston seals on their perimeter. Having these piston seals allowed for the PTFE insert to be made thinner, requiring only enough thickness to construct the inner O-ring face gland, or only 0.16” (~6 mm) between the window’s inner face and the bottom of the insert. What resulted was a total window well depth of 0.25” (6.4 mm) per window.

Designing the window mounts in this way also allowed for flexibility in the size of window which could be used in the chamber. The 223 O-rings have an inner diameter of 1.609”, meaning that any window with a diameter less than 1.609” can be used in this chamber so long as an appropriately sized insert is made for it. Windows smaller than 1” diameter could potentially also be used with some changes to the insert design. Flexibility also extends to window thickness, as the insert thicknesses could be adjusted accordingly to keep the window well depth constant between multiple windows of varying thickness.

This flexibility is important as two different sized windows were eventually used in these experiments. For LWIR absorption measurements, 35mm diameter x 5mm thick BaF2 windows were used. For another set of measurements taken in the ultraviolet (UV) for burn temperature data, 1.5” diameter by 0.25” thick quartz windows were used. A set of inserts was made for both types of windows, keeping window well thickness at 0.25” throughout.

3.2.3. *Pressure Measurement*

Measuring chamber pressure during these constant volume combustions was another desirable parameter that was easily obtainable, and monitoring chamber pressure was necessary to ensure that the desired test gases were filled in desired amounts. As such, a piezoresistive pressure transducer, Kulite XTEL-190L, was installed into the chamber wall. These sensors are miniaturized and ruggedized to withstand harsh environments such as the fireballs being tested. As per the manufacturer [60] these gages work to measure pressure in “most conductive gases.” By virtue of being piezoresistive, these transducers are able to measure static pressure with linear output response. To minimize interference due to the presence of the sensor, the mounting hole was designed such that the sensing element would sit flush with the chamber’s interior wall. However, as manufactured, the sensing element sits slightly recessed into the chamber wall.

Installation of the Kulite sensor was achieved through a counter bored threaded hole in the chamber wall. The Kulite body is threaded for securing in place and had an O-ring boss seal; however, vacuum sealing was supplemented by also sealing the sensor with silicone adhesive.

3.2.4. *Chamber Heating*

As discussed, elevated chamber temperature was required to vaporize DIMP liquid, and uniform chamber heating was an important aspect of chamber design. Designing the spherical chamber with a cylindrical outer face allowed for the use of resistive heating wrap along the curved surface, leading to evenly dispersed heating around the entire outer surface. Additional temperature uniformity was obtained by covering the chamber with 1" thick fiberglass insulation. Finally, aluminum was used as the chamber material somewhat for ease of manufacturing but also because its high thermal conductivity promoted more temperature uniformity.

Chamber temperature was maintained at 80°C and controlled using the heating wrap's built in "percent on" controller. The combination of heater power and insulation resulted in the heater requiring only 5% on time to maintain 80°C. A thermocouple attached to the chamber exterior was used to monitor chamber temperature. Finally, elevated chamber temperature and the need to maintain chemical compatibility with DIMP lead to the use of high temperature silicon O-rings throughout the chamber design.

3.2.5. *DIMP Syringe Insert*

As with the previous chamber, the DIMP syringe needed to be removable, so it was necessary to fit the syringe into an aluminum insert. This insert is shown in Figure 3.13, where the glass syringe is again installed inside the insert using silicone adhesive. Excellent sealing of the insert against the chamber was achieved with three O-ring piston seals, similar to those used in the window inserts. The triple redundant seal ensured negligible leakage, and the use of male piston seals allowed for quick removal and installation as bolting the insert down was not necessary to achieve a good seal. Instead, a quickly installed retaining latch was all that was needed to keep the insert in place during the combustion pressure rise. The insert slides into a 0.605" (1.54cm) diameter hole in the chamber with a slight 1" diameter counter bore. For the interior portion of the insert, the shape is tailored to closely match the spherical curve.

Figure 3.13 - DIMP syringe insert

3.2.6. *Electrode Design*

Maintaining spherical symmetry of the combustion event requires that the combustion reaction be initiated from the center of the spherical volume. Reliable ignition of the test mixtures is achieved through an electrical spark gap discharge. However, producing a spark at sphere center requires bringing electrodes into the test volume, close enough to allow for spark formation. While introducing additional material into the chamber interferes with symmetry, it is necessary, so the footprint of the electrodes was minimized. Minimal interference was achieved by using 1/16" welding rods as the sparking electrodes made from tungsten, a material that would occupy minimal volume while remaining rigidly fixed in position.

3.2.7. *Spark Generation*

Another complication of the center ignition comes from the fact that the optical path for absorption measurements travels through the center of the sphere. Placing any material in the 1" diameter optical path would reduce signal level. To minimize the amount of occlusion, the spark gap between electrodes was made ~0.3" (~7.6 mm) wide. Creating an electrical arc across this distance requires a high voltage source. A typical high voltage source used is a RISI brand fireset, a device

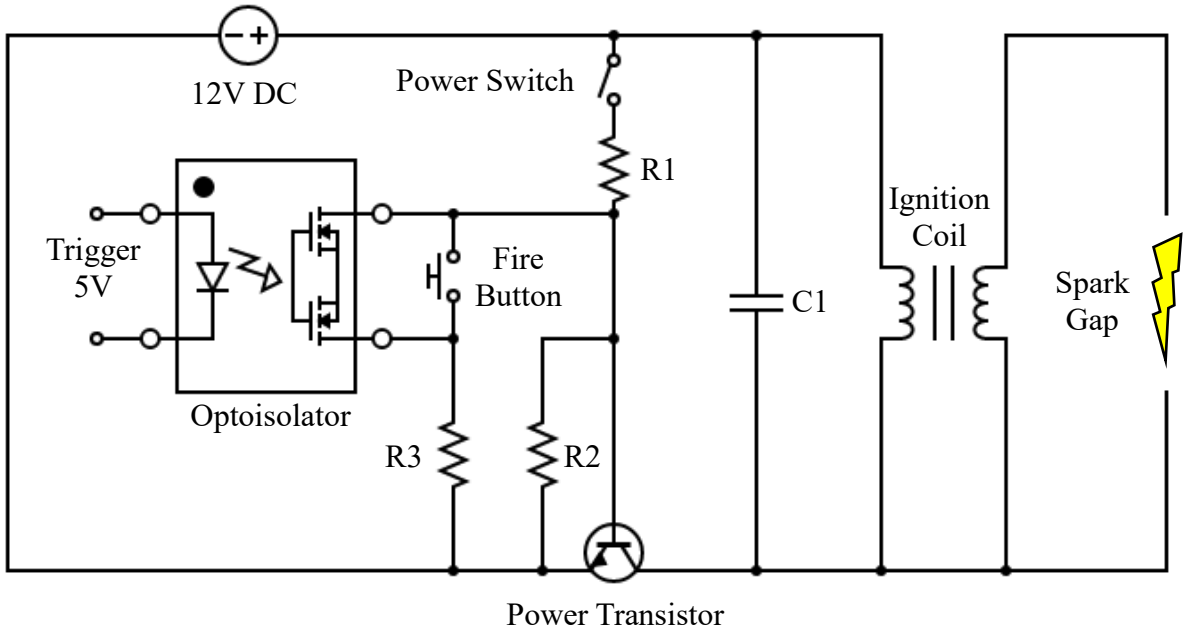

Figure 3.14 – Spark Generation Circuit

capable of charging a 4kV capacitor from 120VAC and discharging the capacitor for a short 4kV pulse. Such devices are commonly used for detonation of exploding bridgewire detonators and had been used for air gap sparks over shorter distances in previous chamber iterations, but the wider gap in the spherical chamber required a much higher voltage to spark across. Instead, the high voltage sparks were created using a car ignition coil circuit, the electrical system used in gasoline engines that powers the spark plugs.

The electrical circuit for spark generation is quite simple and amplifies a low voltage 12V supply to produce a temporary voltage spike on the order of 10kV. The circuit design is detailed in Figure 3.14. The primary voltage generation components of the circuit are the capacitor in parallel with an ignition coil, which is essentially a transformer. To operate the circuit, a 12V DC power supply is applied, charging the capacitor C1 $(20\mu F, 450V)$ while pushing current through the ignition coil's primary inductive winding. Upon disconnecting the 12V supply, the ignition coil primary attempts to continue driving the same level of current by spiking the voltage across the coil. The coupling of the primary and secondary windings of the ignition coil causes the secondary coil to experience an amplified voltage spike, creating the desired >10kV across the secondary.

A custom circuit was designed for driving the ignition coil in such a way that it could be electronically or manually triggered. Upon engaging the power switch, the 12V supply energizes

the power transistor through a simple voltage divider comprised of R1 (6.3kΩ) and R2 (6.3$k\Omega$), closing the transistor and allowing current to flow through the ignition coil primary. To interrupt the current flow and generate the spark, the transistor gate voltage is dropped below its trigger threshold through adding a parallel resistor, R3 (300Ω) whose resistance is much smaller than that of R2. Triggering was is done either manually by closing the R3 branch with a push button, or electronically by sending a 5V trigger signal to the optoisolator (NTE3047).

3.2.8. *Gas Fill Manifold*

The final component of chamber design was the gas manifold used to fill the chamber with test gases. A gas manifold such as the one pictured in Figure 3.15 reduces leakage by restricting the number of access points to the chamber. For this manifold, five gas lines are collected into a single space which is connected to the main chamber via a blue-handled KF-16 ball valve. This valve uses chemically resistant PTFE sealing surfaces and is therefore compatible for use with DIMP, and it is rated for high vacuum use. As such, this single valve can be used to quickly and effectively seal the chamber from the manifold. A single access point also reduces the number of features on the chamber interior by requiring only a single access hole for gases.

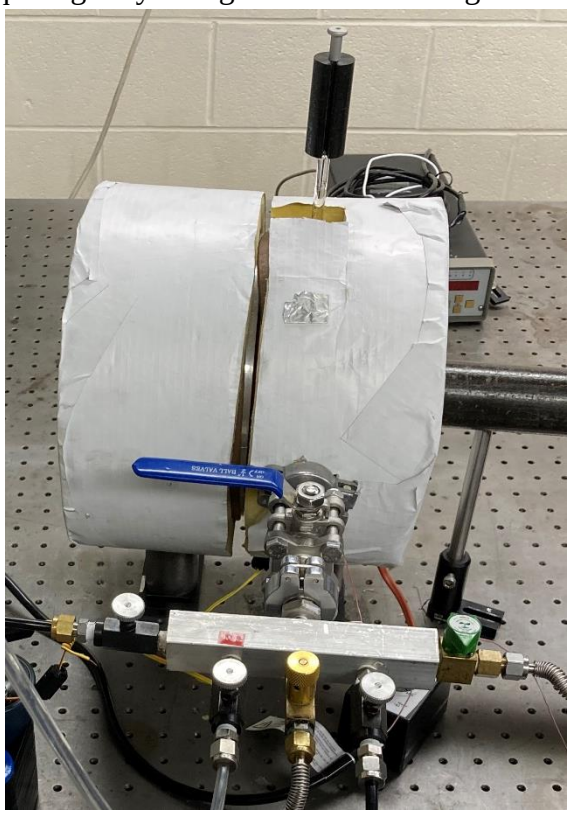

Figure 3.15 - Test chamber gas manifold

The five lines leading to the manifold are connected through standard ball or needle valves. A vacuum pump is connected through the ball valve through a short line, and reactant gases are connected to the needle valves, allowing for precise filling of each gas into the chamber.

3.3. Test Conditions

Highly complex chemical reactions make complete modeling of combustion environments almost impossible to do in practice. By necessity, computational models of combustion events require simplifying assumptions to bring computational cost to a practical level. Chemical kinetics mechanisms, the set of chemical reactions considered in a computational model, are the major area in which simplifications are made. In reality, there exist untenably many chemical reactions and chemical species that could possibly occur or exist in all but the simplest combustion reactions; however, most of these reactions are too infrequent and species too inconsequential to make a measurable impact on the bulk reaction. Reduced chemical kinetics mechanisms seek to consider only the assumed reactions and species deemed important. As one progresses to more complex combustion reactions with complex fuel and oxidizer molecules, even the reduced chemical kinetics mechanisms become computationally taxing, and uncertainties in the validity of those mechanisms increase.

In this study the choice of experimental combustion reactants was made to create the simplest possible combustion environment to model, keeping computation times minimal without adding undue uncertainty. For this simple environment, H_2 and O_2 were chosen as the fuel and oxidizer, respectively. The combustion of these two species has been widely studied and is well understood, allowing the combustion event to be modeled with high confidence. Reduced chemical kinetics mechanisms exist for this reaction as simple as the single step reaction: $H_2 + O_2 \rightarrow H_2O$, but higher fidelity mechanisms are also available. Additionally, 1-D transient computations with full chemistry and transport are relatively simple.

Fireball temperatures were desired in the range of 2000-2500K. However, depending on the stoichiometry, pure hydrogen and oxygen flames are too high temperature, approaching 3500K at stoichiometric conditions. An inert diluent species would need to be added to the reactant mixture to decrease to the desired temperatures. As collecting a benchmark data set requires a variety of distinct conditions, diluent species and concentration would need to be varied to tailor the combustion environment. For this work, primary interest was focused on adjusting temperature of

the burned mixture and adjusting the amount of available oxygen. Temperature variations would clearly lead to variation in decomposition rate, as has been demonstrated by other studies, and varying oxygen concentration was thought to change decomposition through altering the potential for oxidation reactions.

Determining a set of test conditions was largely an iterative process guided by a few criteria. The first of these was to ensure window integrity when exposed to the combusted conditions. As mentioned, the BaF_2 windows used were susceptible to thermal and mechanical shock, so relatively mild reacted conditions would be necessary. However, target temperatures were set at 2000-2500K, so window integrity could only be ensured through reducing burn pressure. In this regard, an upper limit of 2 bar was set on burn temperature. This pressure limit required that initial reactant mixtures be at sub-atmospheric pressure, and an initial pressure of 0.2 bar was chosen.

The second criterion was that the set of conditions test the two independent variables while keeping all other variables constant, including keeping the initial pressure constant at 0.2 bar throughout. Adjusting oxygen concentration while keeping all else constant was easily achieved through the use of N_2 as the diluent species by virtue of the fact that N_2 and O_2 have nearly identical specific heats. So long as sufficient oxygen remains to complete the reaction, the O_2 could be replaced with N_2 mole for mole while keeping temperature and pressure constant. Reducing temperature could be achieved through replacing N_2 mole for mole with a higher specific heat gas, such as CO_2.

Finally, all test conditions would need to ignite under spark ignition. Ignitability proved to be a challenging criterion to meet and was the source of the iterative nature of the search for test cases. Organophosphorus compounds such as DIMP are known to be flame suppressants [61], a property which caused the ignitability issues. In many cases, a reactant mixture that would ignite without

Table 3.1 - Combustion Chamber test conditions

Test Case	Partial Pressure N_2 (torr)	Partial Pressure CO_2 (torr)	Partial Pressure O_2 (torr)	Partial Pressure H_2 (torr)	Liquid DIMP Added (μL)
A	62	-	50	40	50
B	82	-	30	40	50
C	-	62	50	40	50
D	-	82	30	40	50

the presence of DIMP would then fail to ignite once DIMP was added. This effect was more prominent for lower oxygen concentrations and cases with CO_2 as the diluent species.

Following the outlined criteria, four distinct test cases were determined and summarized in Table 3.1. These test conditions are distinguished by the partial pressure of gases in the initial mixture in torr and the amount of DIMP in μL of liquid added to the chamber. Fully evaporated, the 50μL of DIMP liquid used in all tests is estimated to achieve a partial pressure of approximately 3.2 torr.

Explicitly stated, cases A and B test a variation in oxygen content while keeping flame temperature nominally constant. Cases A and C represent a change in temperature while keeping oxygen content the same, and the same is true for B and D only with less oxygen. However, due to the different specific heats of O_2 and CO_2, cases C and D do not represent the same temperature.

Previous experiments performed with a different chamber resulted in a group of three conditions closely resembling cases A, B, and C except with 10 torr less oxygen and 10 torr more diluent, equating to stoichiometric oxygen for the case B equivalent without DIMP. However, when attempted in the new chamber, the case resembling B consistently failed to ignite. As it had been well established that cases with more oxygen were more likely to burn, the decision was made to increase the oxygen content to the levels listed in the Table 1. A 10 torr increase was not chosen arbitrarily, however. Instead, an oxygen balance on the initial mixture including DIMP was performed.

$$X\ O_2 + 40\ H_2 + 3.2\ C_7H_{17}O_3P\ (DIMP) \rightarrow Y\ H_2O + Z\ CO_2 + 3.2\ CH_3O_2P\ (MOPO) \qquad (14)$$

Performing the balance as shown where it was assumed that the phosphorus in DIMP terminated at methyl(oxo)phosphoniumolate (MOPO) as suggested by Zegers and Fisher [62] resulted in a stoichiometric oxygen partial pressure of 47.3 torr. As an aside, this number was unchanged if phosphorus instead terminated at MPA. If it was instead assumed that phosphorus would terminate as PO or PO2 as suggested by Korobeinichev, the stoichiometric oxygen partial pressure would rise to 53 or 54.6 torr. To split the probability of either method dominating, the oxygen content was raised to 50 torr to achieve close to stoichiometric conditions in these tests. Increasing the low oxygen cases to 30 torr of oxygen successfully brought case B into the flammable regime as expected, but it allowed case D to burn as well.

3.4. Operating Procedure

The operating procedure for conducting combustion chamber measurements will be presented in this section. An overview of the procedure will be provided first, followed by more detailed descriptions of individual tasks in the following subsections.

Beginning from a cleaned and preheated chamber, the testing procedure is as follows: First, the chamber is pumped down with the attached vacuum pump while Dark, I_0, and Polystyrene calibration film measurements are taken. Next, the pump is shut off, and the DIMP syringe is removed and loaded according to the procedure outlined in the previous section. With the syringe insert reinstalled, the pump is turned back on and the chamber brought down to vacuum. During this time, the syringe body would be monitored to ensure that the liquid remained inside. On occasion, liquid would begin flowing into the chamber during the vacuum process, presumably due to a poor seal on the plunger head allowing some air to flow past and force the DIMP down. In the event this happened, the chamber would need to be cleaned again before the next test.

Should the DIMP liquid remain inside the syringe, chamber pressure was monitored until it reached the same level achieved during the cleaning vacuum stage within 0.2 torr. Upon reaching desired pressure, that pressure voltage was recorded, the chamber sealed, and the plunger depressed fully. As the DIMP vaporized, a measurable increase in pressure voltage would be observed which would be monitored until it reached a stable value. At this point, the chamber would be filled with the desired test gases. To prevent backflow of evaporated DIMP into the gas manifold, the manifold would be slightly pressurized with the diluent gas (N_2 or CO_2) and the chamber valve opened halfway. Diluent gas would be introduced into the chamber until the desired partial pressure of the gas was reached. Then the diluent supply valve would be shut, and the oxygen supply valve opened. Oxygen would flow in until its desired partial pressure was achieved, and then the same would be done for hydrogen. Upon reaching desired hydrogen partial pressure, the chamber would be sealed shut again.

At this point, the chamber was ready for ignition and the globar was turned on. The globar was given enough time for the current supplied to it to equilibrate and the light output to stabilize. Then the valve supplying air to the turbine motor was opened and the grating brought up to speed. The next step was dependent on whether an absorption measurement or a reference flash signal measurement was to be acquired.

In the event of an absorption measurement, data acquisition devices were armed and the chamber immediately fired. If a flash measurement was desired, a measurement of the initial absorption signal was made without firing the chamber. Then the globar was turned off, a light blocking barrier placed between the globar and chamber, the data acquisition devices armed, and the chamber fired. Regardless of the measurement type, immediately after firing, the chamber would be vacuumed down. Then the globar would be turned off, if it was on, and the air valve to the motor shut. Finally, both the pressure data and MCT data would be saved to the computer and the cleaning procedure started.

In performing flash measurements, the addition step of measuring a pre-fire absorption spectrum allowed for the determination of the initial DIMP concentration for that experiment. This information would be used later to determine the consistency of DIMP injection amount and allow any flash measurements taken with outlier DIMP concentrations to be identified and discarded.

3.4.1. *Data Acquisition*

MCT detector voltage and Kulite pressure gage voltages were recorded using a pair of 4424 PicoScope digital oscilloscopes. Each scope used one channel for triggering and another for measuring one of the desired quantities. In this way, the fastest sampling interval for these devices of 50ns could be maintained for up to 1 second of capture time. While an unnecessary time resolution for pressure measurement, these rapid sampling rates were important for MCT detector readings and resolving voltage spikes used for inductively triggering the scopes for those runs prior to the implementation of electronically triggering the spark circuit. Both scopes were set with a 5% pre-trigger capture time, allowing for determination of conditions within the chamber just prior to firing.

For cases in which the spark was manually triggered, PicoScopes were inductively triggered. A coil of wire was wrapped around one of the high voltage lines leading to the sparking electrodes inside the chamber. Upon the spark jumping, the rush of current would produce a voltage in the coil which was attached to the PicoScope trigger channel. For cases in which the spark was electronically triggered, the circuit trigger pulse was also sent to the PicoScopes. In either case, no attempt was made to trigger the spark at a specific time in the grating rotation, so timing of the first scan relative to ignition was not controlled.

3.4.2. *DIMP loading procedure*

Maintaining consistent DIMP volume injections was critical to obtaining repeatable measurements. Loading DIMP liquid into the syringe began by removing the syringe insert from the chamber. A small notch in the insert allowed it to be pried out of its slot. Then, the syringe plunger was withdrawn completely and set aside. DIMP liquid was then removed from a supply bottle using a separate microsyringe with a capacity slightly larger than 50µL. DIMP liquid was sourced from Alfa-Aesar in a 95% purity. The microsyringe was then used to deposit the liquid into the top of the glass syringe and the plunger inserted. Ensuring that the DIMP liquid was in direct contact with the plunger with no air gaps anywhere in the liquid was critical, as any air would expand upon the vacuuming process and prematurely inject DIMP liquid into the chamber. To ensure the absence of any bubbles, the plunger was worked in and out of the syringe body while holding the body upside down. With enough movement, any trapped bubbles would be removed from the liquid.

Next, a Kimwipe was wadded up and held against the exit hole of the syringe, and the plunger depressed to the 47µL mark. The Kimwipe was then discarded, and the plunger withdrawn back to the ~100µL mark. A spacer, the black rod shown in Figure 3.16, was then added to the

Figure 3.16 – DIMP injection loading. A – Plunger spacer, B – loading microsyringe, C – DIMP bottle, D – Syringe body/aluminum insert, E – Syringe plunger

withdrawn portion of the plunger, and the plunger depressed as much as the spacer would allow. The syringe insert would then be reinstalled into the chamber.

Top loading the syringe with a separate microsyringe was deemed necessary to prevent the incorporation of additional DIMP liquid. Withdrawing liquid from the DIMP vial using the glass syringe would require submerging a portion of the syringe into the liquid, resulting in an unwanted amount of liquid sticking to the syringe body. As an aside, needles were not used with the glass syringe for two reasons. First, other researchers working with DIMP have reported issues with having the DIMP liquid in contact with stainless steel, and the needles were made of stainless steel, so they were avoided to avoid potential complications. Second, the needle would hold some portion of liquid inside their volume that could not be physically removed through depression of the plunger. It was unclear whether this liquid would reliably remain within the needle or reliably evaporate out during tests.

Overfilling and then discarding the excess directly into a Kimwipe was also done to ensure repeatable injection volumes. DIMP liquid has high surface tension, which warrants special attention when attempting to draw repeatable volumes in the small quantities used. While microsyringes like the one used for filling are made to deposit precise volumes of liquid, the amount of DIMP which sticks to the exterior of the pipetting tip becomes a significant portion of the deposited amount. As such, it was found unreliable to use the microsyringe's designed value. Discarding the excess directly into a Kimwipe that was in direct contact with the syringe exit hole was also necessary to overcome the DIMP surface tension. If ejected into air, the DIMP would pool as a droplet that would either be withdrawn back into the syringe when the plunger was withdrawn or stick to the surfaces of the syringe. In either case, additional DIMP would be incorporated into the chamber. Depositing into the absorbing Kimwipe prevents the formation of a droplet. When discarding the excess, the plunger is depressed to 47μL because the plunger was found to have a small cavity ~3μL in volume between the zero delineation and the exit hole. In this way, 50μL of DIMP remained in the syringe.

3.4.3. *Chamber Cleaning*

Cleaning the test chamber between test runs was a critical step in maintaining tightly controlled test conditions. Improper chamber cleaning was found to have a significant impact on the amount

of DIMP that evaporated in the subsequent experiment, but the detailed cleaning procedure was found to result in good repeatability.

Chamber cleaning began immediately after the shot, and the first step was to allow the chamber to vacuum down. During this time, a couple hundred microliters of isopropyl was injected through the glass syringe to flush out any remaining DIMP. Then, while vacuuming continued, the bolts locking the two chamber halves together were removed. Afterward, the pump would be shut off and the chamber allowed back to atmospheric pressure by removing the syringe plunger. Once possible, the chamber halves were separated, exposing the inside. Isopropyl soaked Kimwipes were then scrubbed against the chamber's interior surface in an attempt to remove any combustion product that may have clung to the walls. Then, the windows were also cleaned by directly wiping their inner surface with an isopropyl dampened Kimwipe, again to remove any buildup that may interfere with light transmission. After completing wipe down, the chamber would be reassembled and vacuumed down. Critically, for reasons that will be discussed later in Chapter 4, the chamber would need to be continuously vacuumed for at least 10 minutes before the next test. Without proper vacuum time, it was found that the concentration of evaporated DIMP vapor would be highly variable.

3.4.4. *Window fouling and Polishing*

As mentioned, the BaF2 windows were subject to degradation upon being exposed to the high water vapor concentration post combustion environment. As such, these windows would need to be removed and polished periodically to retain high signal level. However, sensitivity to thermal shock prevented removing the windows directly from the chamber while it was at elevated temperature. Previous experience with NaCl windows had shown that doing so would crack the window. Therefore, prior to polishing the windows, the chamber heating was turned off and the chamber allowed to slowly cool to room temperature over the course of a couple hours.

After being sufficiently cooled, windows were removed from the window mounts and thoroughly cleaned with isopropyl alcohol to remove any vacuum grease or other contaminate from the surfaces. Then, using 6000 grit sandpaper, the windows were lightly dry sanded on their inward facing face until no visible traces of fouling remained. Only minimal sanding was necessary to polish these windows, requiring only 30-60 seconds. Figure 3.17 shows the before and after of this polishing process. Windows were then reinserted into chamber, and the chamber heating turned

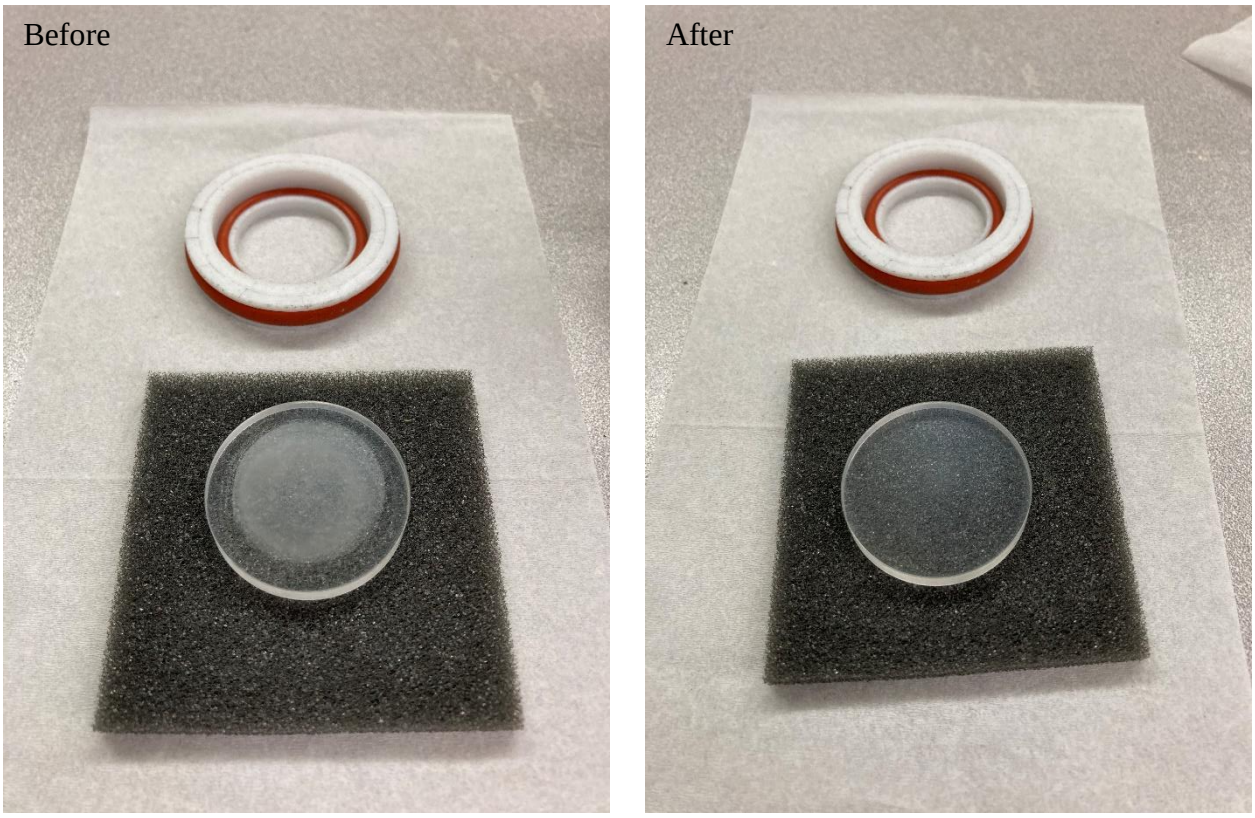

Figure 3.17 – BaF_2 window polishing before and after

back on to slowly raise the temperature back to 80ºC over about 2 hours. Polishing would be performed as needed, but typically occurred after completion of a given test case or at the end of the day where heating or cooling could happen later.

3.5. Temperature Sensitive Measurements

Temperature information is of great interest to the target modeling community as a way to validate models, and absorption spectroscopy is again a useful tool for collecting that information. As mentioned, determination of temperature information from absorption spectra requires that the features being measured are temperature sensitive. Unfortunately, spectra obtained from the scanning spectrometer were not useful in determining temperature information due to the lack of resolved temperature sensitive transitions. While temperature sensitive water vapor transitions occur in the measured region, the spectrometer's resolution is insufficient to distinguish individual transitions. Consequently, a separate experiment needed to be performed.

One common choice of temperature measurement, especially in combustion environments, is to probe water vapor transitions in the near infrared since water is abundant in combustion products.

Many water vapor line pairs exist that are very temperature sensitive and near enough to be scanned using tunable diode laser absorption spectroscopy (TDLAS). An attempt was made to use TDLAS in this work, but the results were found to be insufficient due to a lack of temperature sensitivity of the scanned water lines at the higher temperatures being studied and interference from atmospheric water vapor. Due to the path-averaged nature of absorption measurements, even a miniscule amount of room temperature water vapor in the optical path would have a significant effect on the measurement.

A second, more fruitful approach was to probe the hydroxyl molecule, OH. As a critical radical species involved in hydrocarbon combustion, OH is present during all combustion events tested. Furthermore, OH's A-X transition band, located in ultraviolet, is highly temperature sensitive and suitable for obtaining temperature measurements [63], [64]. As a radical species, OH does not exist outside of the combustion environment making interference from the path outside of the test chamber irrelevant. Operating in the ultraviolet additionally allows for the use of fast array detectors and conventional dispersive spectrometers while avoiding interference from thermal background.

As a result, compared to the collection of infrared absorption spectra, collection of UV OH spectra was a straightforward process. Absorption spectra were obtained using a Spex270 spectrometer outfitted with a 4320 gr/mm grating. Spectral images were collected on a Hamamatsu linear array detector, fit with a 2148 element array capable of collecting spectral images every 360μs with a maximum of 100 images. Incident light required for absorption was generated from a Xenon arc lamp source, which produced continuous light of sufficient intensity to halfway saturate the detector when operating at 358.5μs exposure. Spectral calibration was done using mercury and iron calibration lamps, and the spectrometer was calibrated to capture 300-320nm.

As H_2-O_2 flames are greatly complicated by the addition of DIMP vapor, these OH temperature measurements were also performed on the test cases without the addition of DIMP. These cases would serve as excellent validation that the models were behaving correctly without the added uncertainty associated with DIMP complexity. Three runs of each case were obtained without DIMP and another three runs each were obtained with DIMP.

The process for recording OH temperature measurements followed the same chamber preparation and DIMP loading steps as the scanning spectrometer measurements. Of notable difference was

the timing of dark and I_0 captures. There was an observed lack of absorbing features present in the reactant gas mixture, including DIMP. As such, dark and I_0 measurements were taken after filling the chamber with DIMP and test gases, just prior to igniting the mixture. The purpose of this was to collect all three measurements (dark, I_0, and shot) within as short a timeframe as possible since the camera used did not have an external cooler, meaning that the dark signal would increase in time as the camera warmed.

3.6. Experimental Test Matrix

The necessary measurements required to obtain the set of benchmark data were as follows:

(1) Absorbance data of LWIR DIMP decomposition (Decomposition),

(2) Emission data of LWIR DIMP decomposition (Flash)

(3) UV OH absorbance data without DIMP (OH w/o DIMP)

(4) UV OH absorbance data with DIMP (OH w/ DIMP)

Even having taken the detailed precautions to improve experimental repeatability, measurement variability was still a concern. The observed effect that small changes in amount of DIMP present could have on the burn conditions necessitated that many repeats of the experiments had to be performed. This applied to the measurement of emission signals most of all, as accurate accounting of the emission signal was critical to determining absorbance accurately. Further need for repeats arose from the possibility that some tests may need to be thrown out as outliers. With these considerations, the goal was established to collect the test matrix in Table 3.2, composed of five repeat runs of LWIR absorbance data and three repeats each of the remaining measurements.

Table 3.2 - Spherical combustion chamber test matrix

	Case A	Case B	Case C	Case D
Decomposition	5	5	5	5
Flash	3	3	3	3
OH w/o DIMP	3	3	3	3
OH w/ DIMP	3	3	3	3

In the process of collecting trustworthy data for the desired test matrix of 56 runs, the experiment was performed a total of 94 times. For the purposes of recording data, a numbered run was

designated any time a burn measurement was attempted, meaning that, except for OH w/o DIMP measurements, DIMP liquid was deposited into the chamber and spark ignition was attempted. The large disparity between test matrix totals and actual runs performed is a result of three main contributors: (1) A requirement to adjust experimental conditions, (2) the 1MHz preamplifier malfunctioning partway through testing, and (3) errors in conducting the experiment resulting in lost tests.

As discussed, oxygen content in these cases needed to be adjusted in order to get each case to reliably burn, but the first 15 tests were performed prior to this realization. During this period other kinks related to operating the new spherical chamber were ironed out as well, including DIMP volume injection amount and cleaning procedures, meaning that these initial shots do not constitute well controlled data.

The following runs, 16-29, were all performed on Case A and B and resulted in a full LWIR data set on Case B and a partial LWIR data set on Case A. However, following test 29, a discharge occurred between the preamp power supply and the preamp housing which resulted in the 1MHz preamp becoming inoperable. The decision was made to continue operation with the slower 150kHz amplifier while the faster amp was sent off for repair. However, this required collecting Case A and B measurements again to keep a consistent resolution throughout all four cases. Tests 30 through 69 were then performed as Decomposition and Flash measurements on all four cases. Of these, seven runs were lost due to either premature DIMP injection, in which DIMP liquid exited the syringe while the chamber was vacuuming, or incorrect partial pressures of fill gases. Finally, runs 70-94 were performed as OH absorption measurements with and without DIMP with

Table 3.3 - Spherical combustion chamber numbered tests

	Decomp 1MHz	**Flash 1MHz**	**Decomp 150 kHz**	**Flash 150 kHz**	**OH w/o DIMP**	**OH w/ DIMP**
Case A	25, 26, 28	27	52, 53, 55, 57, 58	51, 54, 56	70, 71, 72	83, 84, 85
Case B	16, 19, 21, 24	18, 20, 23	62, 63, 65, 67, 69	64, 66, 68	73, 74, 75	86, 87, 88
Case C	-	-	33, 35, 36, 37, 38	32, 34, 36	76, 77, 79	89, 90, 91
Case D	-	-	39, 40, 42, 44, 46	41, 43, 45	80, 81, 82	92, 93, 94

a single test lost due to the camera not being armed prior to firing. A summary of the numbered shots is provided in Table 3.3.

3.7. Supplemental Explosive Tests

While the primary focus of this research is aimed at constant volume "closed bombs," there is a wider interest in measuring DIMP decomposition inside explosively generated fireballs. To satisfy this interest, a set of supplemental experiments were performed in which DIMP vapor was exposed to small scale (<1g) high explosive charge detonations, and the reaction of DIMP vapor inside the resulting fireball was measured. These tests were all performed with the higher resolution 1MHz preamplifier.

3.7.1. *Explosive Blast Chamber*

Small scale explosive blasts in this study were contained within a benchtop blast chamber as pictured in Figure 3.18. Comprised of an aluminum tube (3/4" wall thickness, 6.5" inner diameter, and 12" height) with ¾" thick disks for a base and lid, this chamber has cylindrical symmetry. As with the combustion chamber, this chamber was also wrapped in resistive heating wrap and insulation, but while the combustion chamber was maintained at 80°C, this chamber was kept slightly cooler at 70°C to ensure the safety of using explosives at these elevated temperatures. According to the manufacturer, the exploding bridgewire detonators used to initiate the explosive charge can be safely maintained at 70°C for up to one hour, and PETN, the explosive compound used for the charges, has a similar rated temperature stability [65].

As visible in the picture, this chamber has eight 1" optical ports built into its walls, four ports at a height of 4" and another four at a height of 8". In this work, only the bottom ports were used for spectral measurements, but one of the top ports was used to house the same Kulite pressure transducer used in the spherical chamber. For the spectrometer viewing ports, sacrificial 1" diameter NaCl windows were used for their good transmittance and affordable price. These windows were placed as close to the chamber inner wall as possible to avoid any window well uncertainty. This placement was done using a pair of optical retaining rings sandwiching the window with the inner ring as far inward as possible. Windows used in such a manner were highly likely to shatter when exposed to the detonation blast, however breakage was seen only on the higher end of charge masses tested.

Figure 3.18 - Explosive blast chamber

3.7.2. *Charge Initiation*

Due to the small scale of these charges, the method of initiation would have a significant effect on the fireball shape. Spherically expanding fireballs would be ideal from a modeling perspective due to their relative simplicity, so design of charge initiation originally focused on creating a spherical detonation from a 1g charge. Charges pressed into hemispheres will detonate spherically provided that they are initiated at their radial center. However, since point initiations are not physically achievable, the spot size which is initiated must be significantly smaller than the charge diameter for this to remain the case.

To achieve a sufficiently small initiation spot size, the initiation strategy detailed in Figure 3.19 was devised. Here, a small steel anvil (1” diameter, 0.5” height) was machined as shown with a drilled-out portion sized to house an RP-2 detonator. A 1 mm diameter hole was drilled between the detonator housing cavity and the anvil surface on which the charge would be placed. Connecting the detonator and anvil surface was now a short cone section reducing in diameter from the detonator diameter to 1 mm diameter, and this portion would be filled with ~20mg of PETN. Upon ignition, the detonator would initiate this small PETN booster charge, and the

detonation front would be confined down to 1mm in diameter, where it would then initiate the charge sitting on top of the anvil. This steel anvil was inserted into a plastic Delrin holder before installing the whole assembly into the chamber base. The Delrin would act as a shock absorbing buffer, preventing damage to the chamber base.

While this method was successful in creating a spherical blast wave, the 1g charges were found to be too large for the desired measurements. Instead, less ideally shaped pucks were used to allow for easy tailoring of charge mass. Maintaining an approximation of point source ignition was still desirable for these cylindrical charges however, so the same initiation strategy was used. Additionally, reduced charge masses were of a comparable size compared to the masses of explosive inside the detonator, and this method was also assumed to block at least a portion of the detonator's output.

3.7.3. *Charge Preparation*

Explosive test charges were prepared from PETN powder that was pressed in dies to form solid pucks. Two sizes of die were used in this work, a #7 drill bit diameter (0.201") and a size N drill bit diameter (0.302"), and the process for each die was identical. First, the desired mass of PETN powder was weighed out using a high precision scale. Then, the die was brushed with calcium stearate, a releasing agent to assist in extraction of the pressed pellets. The pre-weighed powder was then poured into the die and the die inserted into a manual press. Pressure was exerted onto

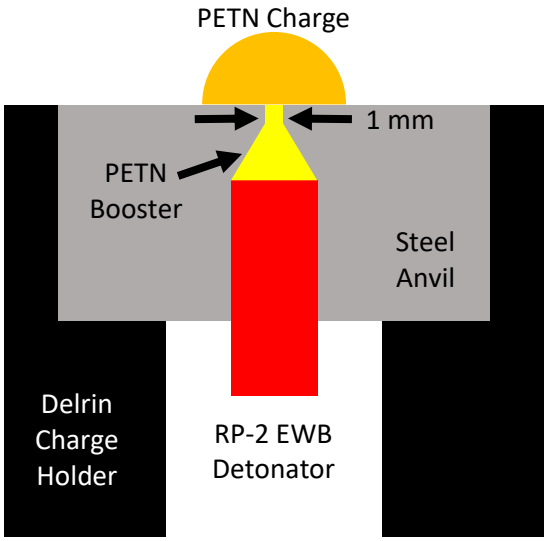

Figure 3.19 - High explosive charge design

the powder to compress the powder into a solid mass, but excess pressure was avoided as it was found to result in crumbled charges. After sufficient force was applied, the charge would be extracted from the die and reweighed to determine its final mass.

3.7.4. *Test Conditions*

Testing a range of distinctly different conditions with clearly differing results was the primary goal of this supplemental work. Previous work had shown that 1g charges would fully decompose DIMP in the chamber, but smaller mass charges could result in only partial decomposition. Therefore, this work sought to find the limit on charge mass which would result in total decomposition. As an additional parameter, the effect of chamber fill gas on the DIMP decomposition was investigated. While the chamber was not designed to hold vacuum, gas connection ports in the lid allowed the closed chamber to be purged with a flow of a desired gas. For this study, two chamber environments, air and N_2, were tested.

Finding charge mass limits for decomposition was a trial-and-error process. Tests would be performed with a largely arbitrary charge mass and the results processed to determine full or partial decomposition. Experiments in air started with a 250mg charge that was subsequently decreased to 191mg and 141mg. Nitrogen tests began at 250mg and increased to 450mg and 714mg. The resulting test matrix is provided in Table 3.4. Notably, these small-scale explosive tests did not exhibit the same severity of emitted light found in the combustion experiments, so reasonable absorbance calculations could be obtained without determining and subtracting a flash signal. While it is possible that emitted light is present, no dedicated measurements of it were made for this work. Finally, DIMP liquid was added in the amount of 200µL to keep the gas concentration comparable to that found in the combustion chamber tests.

Table 3.4 – Explosive Chamber Test Conditions

Test Number	Charge Mass (mg)	Gas Environment	DIMP Volume
1	267	Air	200µL
2	203	Air	200µL
3	141	Air	200µL
4	250	N2 Purge	200µL
5	442	N2 Purge	200µL
6	736	N2 Purge	200µL

3.7.5. *Procedure*

When compared to the combustion chamber procedure, the process for explosive chamber experiments was drastically simplified, due primarily to the fact that the explosive chamber was not vacuumed prior to the test. DIMP injection was as simple a matter as depositing the desired volume of liquid into the chamber through a valve in the lid. Diffusion of vapor did remain an issue, however, so a non-invasive mechanism for promoting stirring was necessary. The solution chosen was to incorporate a stir rod into the chamber made from a thin aluminum disk. A long handle attached to the disk allowed it to be moved up and down within the closed chamber to cycle the gases around until approximate equilibrium was obtained. To minimize the footprint of the stir rod so that it did not interfere with modeling of the chamber geometry, it would then be retracted to sit flush with the chamber lid.

To perform these experiments a charge assembly with a charge of desired mass would be assembled and inserted into the explosive chamber. If necessary, the charge assembly would be epoxied into the slot. A detonator gas expansion chamber would then be bolted underneath the chamber, the purpose of which was to contain the products of the RP-2 detonator while allowing them to expand and depressurize. At this point, dark and I_0 measurement were collected in the same way as in the combustion experiments. If tests were to be performed in a nitrogen purge, a compressed N_2 line would be attached to a valve on the chamber lid and allowed to flow into the chamber at a slow rate. After a few minutes of purge, or immediately if the test were in air, 200μL of DIMP liquid would be dropped through a valve in the lid. With the spectrometer grating rotating at a slow speed, the intensity signal was monitored while the DIMP vapor was mixed using the stir rod. Once an equilibrium had been achieved, the stir rod was retracted and the nitrogen purge valve shut if applicable. After performing a final check that the chamber was bolted shut, the detonator wires were attached to the initiating fireset, the spectrometer set to full speed, collecting PicoScopes primed, and the fireset armed. Following detonation, the spectrometer was immediately stopped, collected data saved, and globar turned off.

Cleaning the explosive chamber post-shot began by holding a special exhaust trunk over the chamber lid while unbolting it. The trunk would suction in any detonation product gases and unreacted or partially reacted DIMP. After all visible smoke had been removed, the interior walls

were cleaned using an isopropyl-soaked Kimwipe and any solid debris resulting from the detonation removed.

3.7.6. *Detonation Fireball Imaging*

Confirmation of the fireball shape was accomplished through high-speed imaging of the detonation event. To gain wide optical access to the chamber interior, an equivalent test chamber was constructed from an acrylic tube with the same inner geometry as the aluminum chamber. This tube is shown in Figure 3.20 and uses the same base and lid pieces as the actual chamber, so the same charge preparation and initiation procedure could be performed.

Images of the event were captured using a HSFC-PRO high-speed framing camera. This model captures four images with nanosecond timing precision. Images were captured across two tests, both with charge masses of 250mg in air and without the addition of DIMP vapor. Image timing was staggered across the two tests, resulting in images captured at six times during detonation. These images are shown in Figure 3.20. It is important to note that these images were taken with different camera apertures and exposure times, so relative intensity between images has no interpretable meaning. What these images show is a decidedly non-spherical fireball with preferential growth upward. Still, the fireball is at least cylindrically symmetric. At a later time, the outward expanding fireball can be seen impacting the chamber walls.

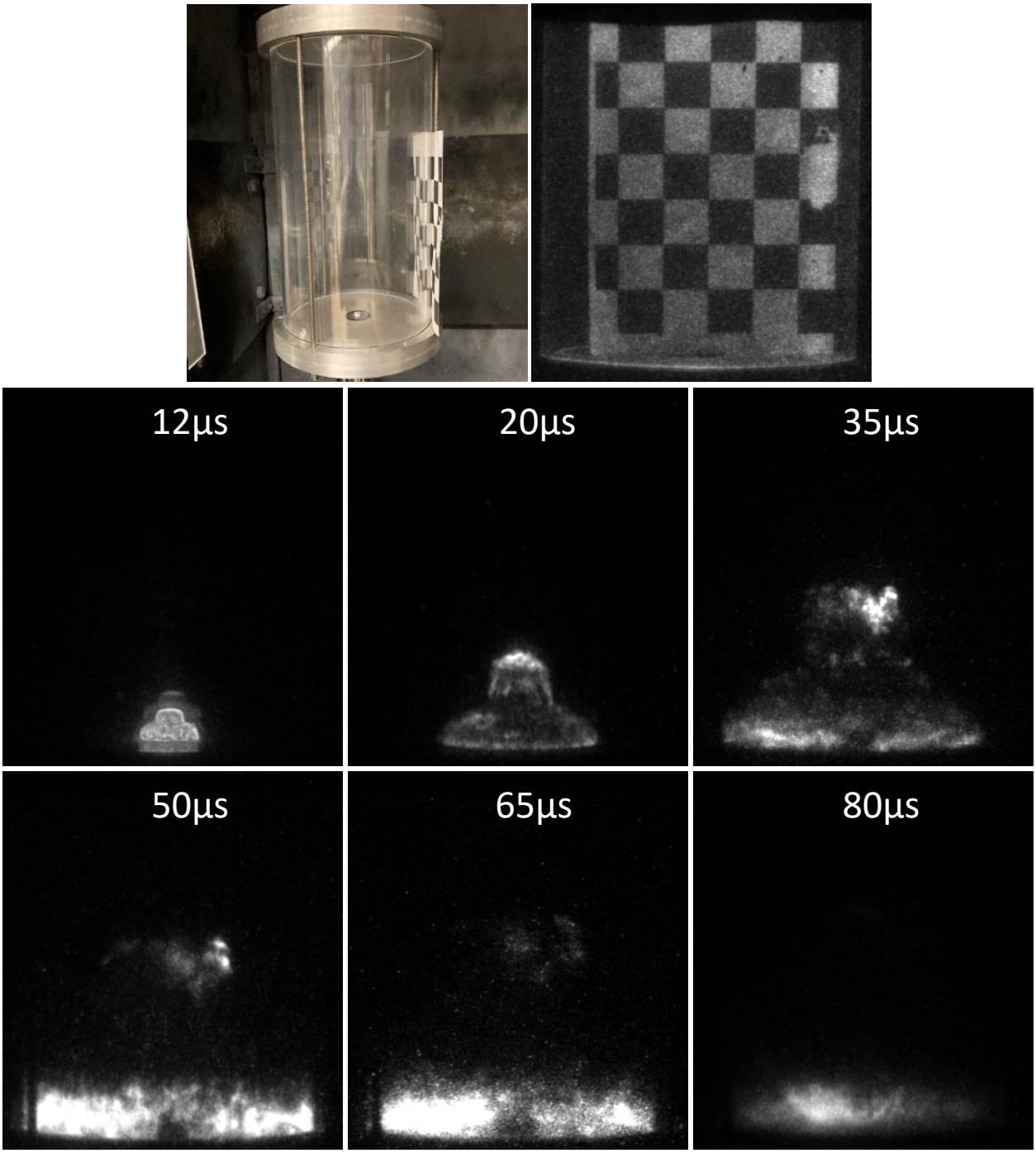

Figure 3.20 - Explosive charge detonation images

CHAPTER 4: RESULTS AND DISCUSSION

In this chapter, results obtained from the previously described experiments will be presented. First will be results pertaining to the repeatability of various experimental aspects. These include chamber leakage, fill gas concentration, and DIMP vapor concentration. Following these results will include discussion on the variability of DIMP decomposition experiments, observed through burn pressure profiles. Next, the results of emission flash measurements will be presented as well as the process for subtracting those signals from decomposition measurements. Finally, calculated absorbance data for closed bomb tests, both LWIR and UV OH, and LWIR absorbance from explosive experiments will be presented and discussed.

4.1. Chamber Leak Rate

As discussed previously, chamber leak rate was a major source of experimental variability in prior experiments performed on a previous chamber. While significant effort was taken in the design of the test chamber to minimize leakage, measurement of the leak rate was necessary to ensure that it was sufficiently low. To check leak rate, the chamber was fully vacuumed down while at temperature, then sealed, and left to sit for over two days while maintaining temperature. Over the course of 66.5 hours, the test chamber leaked 13.76 torr of air, averaging 0.207 torr/hour or 0.0035 torr/min. This represents a two order-of-magnitude improvement in leak rate as compared to the previous test chamber. Considering that the measured leak rate is worst case (beginning at full vacuum) and no more than 10 minutes elapse between sealing the chamber and firing, this leak rate is considered negligible.

4.2. H_2/O_2/Diluent Concentration Repeatability

Repeatability in the concentration of reactant species, both H2/O2/diluent concentrations and DIMP concentrations, was critical to producing repeatable fireball environments. Verification of H_2/O_2/diluent concentration is possible through analysis of the OH temperature measurements performed without the presence of DIMP. Pressure data and OH absorbance data are obtained from three experiments at each of the four conditions without the addition of DIMP. Pressure data, given in Figure 4.1, show extremely repeatable traces with the sole exception being the first test on Case A.

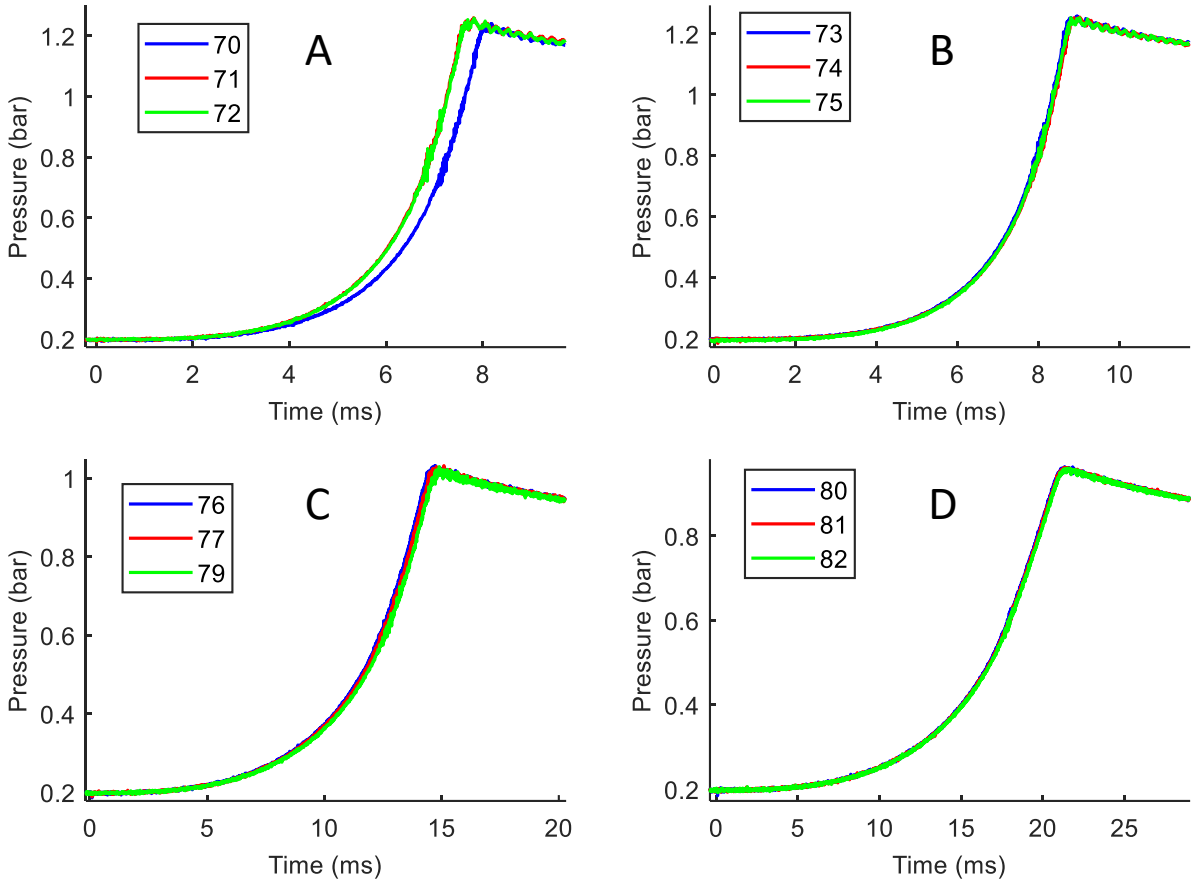

Figure 4.1 – Burn pressures without DIMP for cases A, B, C, and D

As a higher fidelity indicator of burn environment repeatability, integrated absorbance of the entire collected OH spectrum is given in Figure 4.2. More information on the OH absorbance measurements is provided in Section 4.8. Once again, repeatability between tests is very good among all cases. Interestingly, the Case A run 70 profile shows better agreement in OH signature than in pressure. Based on these two results, the H_2/O_2/Diluent concentration is concluded to be highly repeatable and not a significant source of variability.

4.3. DIMP Concentration Repeatability

The final primary source of experimental variability lies in the concentration of DIMP vapor present at the time of ignition, and due to the significant effect DIMP has on burn conditions, DIMP variability is potentially the largest source of experimental variation. Of the numbered tests performed, 42 were successful cases in which DIMP vapor was deposited and initial concentration

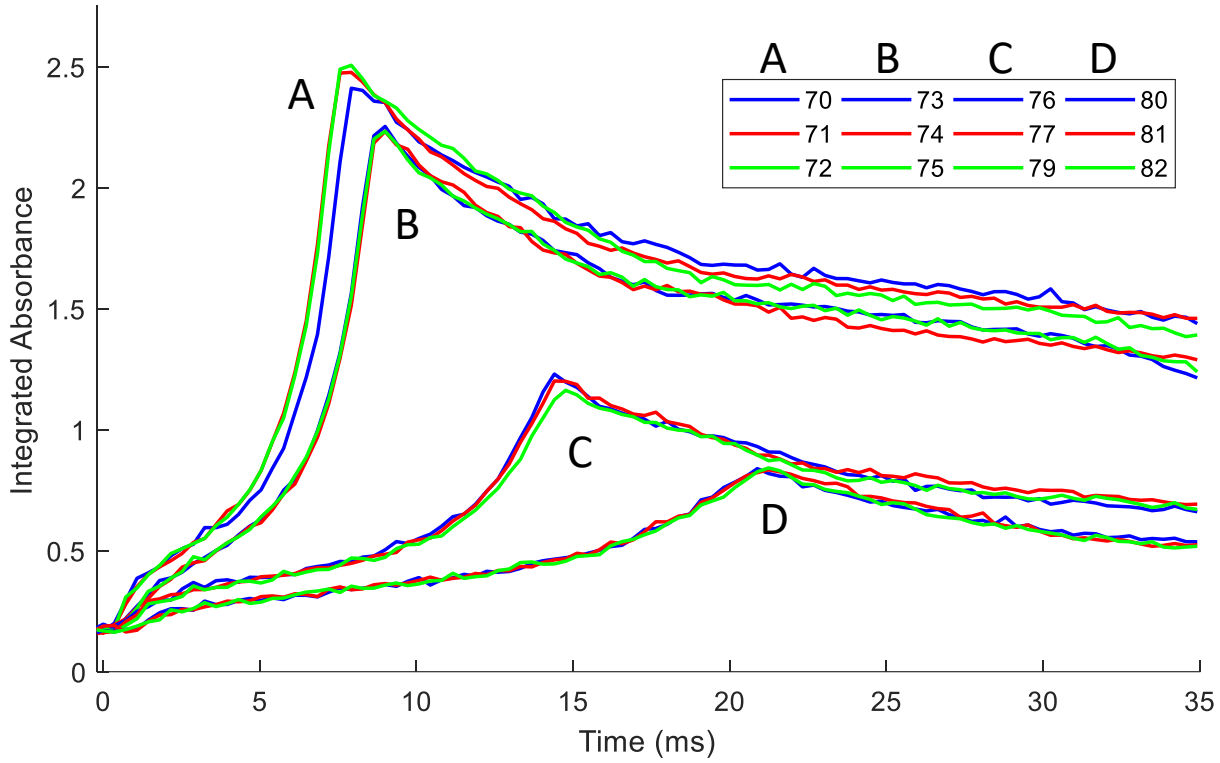

Figure 4.2 – Integrated absorbance of OH signals for case A, B, C, and D without DIMP

data of the vapor just prior to ignition was recorded. These recorded initial spectra are provided in Figure 4.3 with each individual figure corresponding to a single lettered case for clarity. In all figures, the y axis scale is chosen to cut off the primary DIMP feature at 1000 wavenumber because this feature exceeds an absorbance of 3 in all cases. Due to the way in which absorbance in calculated from measured transmittance data, small uncertainties in measured transmittance can lead to very large changes in absorbance, making such large absorbance values unreliable. Instead, better comparison of DIMP injection repeatability is made through the remaining lower absorbance features. In general, repeatability in DIMP signature is good within a given grouping of consecutive runs, with only a few cases, such as 31 and 16, exhibiting clear deviation. In fact, Case A – 1 MHz preamp, Case B – 150 kHz preamp, and Case B – 1MHz preamp (aside from run 16) show nearly identical absorbance profiles, indicating that the injection method can be highly repeatable. However, the remaining three groupings of test runs show a greater degree of variability, primarily in the region of 1150-1250 cm^{-1}. As is apparent, normal DIMP spectra exhibit a primarily featureless section near 1220 cm^{-1}, but cases in which variability is present show

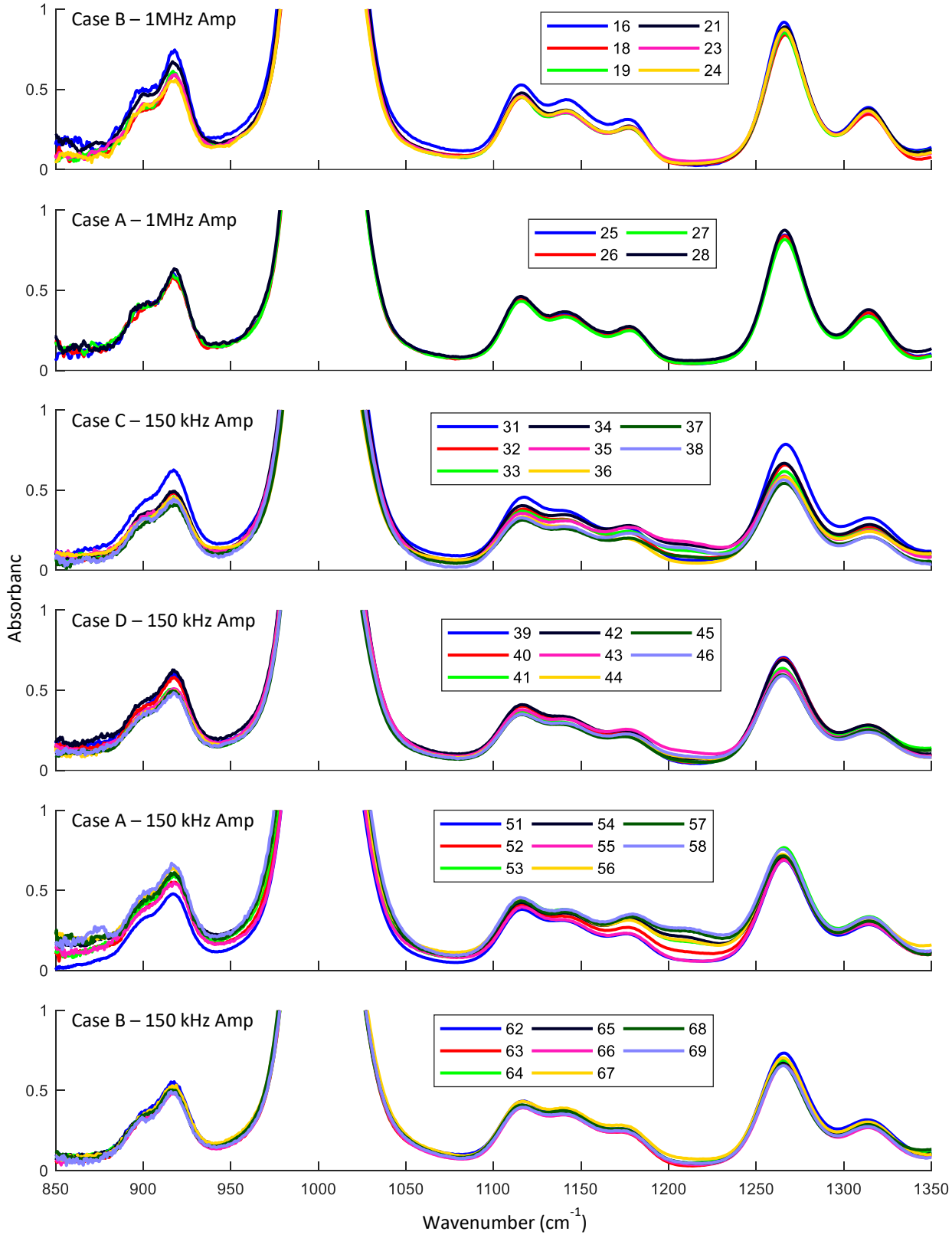

Figure 4.3 – Initial DIMP absorbance for all tests

markedly different behavior here. This is best seen in Case A – 150 kHz preamp cases where absorbance in the 1150-1250 cm^{-1} region rises higher than expected. In the worse cases a slight, but detectable, peak can be seen forming at ~1210 cm^{-1}. Some Case C – 150 kHz preamp runs show this peak formation as well, but Case D – 150 kHz cases are limited to a featureless rise in absorbance.

Overall, the intensity of DIMP absorption features, and therefore DIMP vapor concentration, demonstrates good repeatability, and the largest variability appears as result of these unexpected additional features. As such, high confidence is placed in the DIMP injection method for introducing a repeatable mass of DIMP during each trial. However, an alternate explanation for the observed variability is necessary.

In early testing an interesting phenomenon associated with DIMP evaporation was observed. Upon deposition of liquid, an immediate jump in chamber pressure would be observed as expected, but in almost all cases the pressure would begin to fall back down again. In most cases this drop would only be slight, but in some cases this pressure drop would be quite significant, dropping by approximately half the initial rise in the most extreme case. An initial thought was that DIMP vapor was potentially condensing after vaporizing. There was slight concern that after cleaning the chamber, the inside surfaces may have been cooled and not enough time was permitted to raise the temperature before injecting the DIMP. This theory was quickly dismissed as the aluminum body would quickly equilibrate, and the set temperature of 80°C was very conservative to prevent condensation.

Another theory arose from checking patterns in DIMP pressure behavior as they related to the chamber cleaning procedure. The first of these patterns was that no extreme drop in pressure was observed for the first DIMP inject of the day. This observation was significant because upon concluding testing for the day, the chamber was opened to atmosphere and maintained at ~80°C overnight. This chamber configuration would allow for material on the inner surface to be baked off and then escape. Next, it was observed that cleaning the chamber with isopropyl alcohol-soaked wipes would leave behind streaky white residue, a substance that was not present after leaving the chamber open overnight or after a successful shot. Finally, DIMP pressure drop was found to be most significant for cases prior to the implementation of a minimum 10-minute vacuum time during cleaning.

These patterns suggested that the cleaning process was leaving behind a substance that could have been reacting with DIMP vapor, although baking off the substance reduced its impact. The theory of a chemical reaction occurring is backed up by the presence a spectral feature not attributable to DIMP vapor. The identity or source of this species is not known and warrants further investigation; however, as discussed, aluminum oxides are known to act as a catalyst for DIMP destruction, and an oxide layer is certain to exist on the chamber's aluminum interior. It is possible that whatever substance left behind served to enhance the catalytic reaction. Either leaving the chamber open or holding it under vacuum could have removed the substance, reducing the catalytic reaction. The observed variability could then be explained by incomplete removal of the offending substance during those cases.

4.4. Experimental Variability in Burn Pressure

Figure 4.4 shows the pressure profiles for all experiments performed with the 150 kHz amplifier. It is immediately apparent that these signals do not contain the same level of repeatability as those without the presence of DIMP. Case A shows good repeatability, but the others do not. Case D in particular shows the most variation; however, this is to be expected given that this condition is near the limits of flammability. Most interestingly, Case C pressures contain two distinctive groupings, one with a more rapid pressure rise and another with a more gradual rise. From this observation, it was inferred that two different scenarios were taking place during the burn events in these cases. To further glean what this difference might be, an investigation into the generated flash signal was performed.

Figure 4.5 provides a metric of flash intensity vs. time for each test performed. For dedicated flash measurements, the plotted values are simply the integrated absorbance of the entire scan at a given time. For decomposition measurements, the plotted values are the integrated absorbance at a given time subtracted by the integrated absorbance pre-fire. These values give a qualitative proxy of the flash signal intensity vs. time.

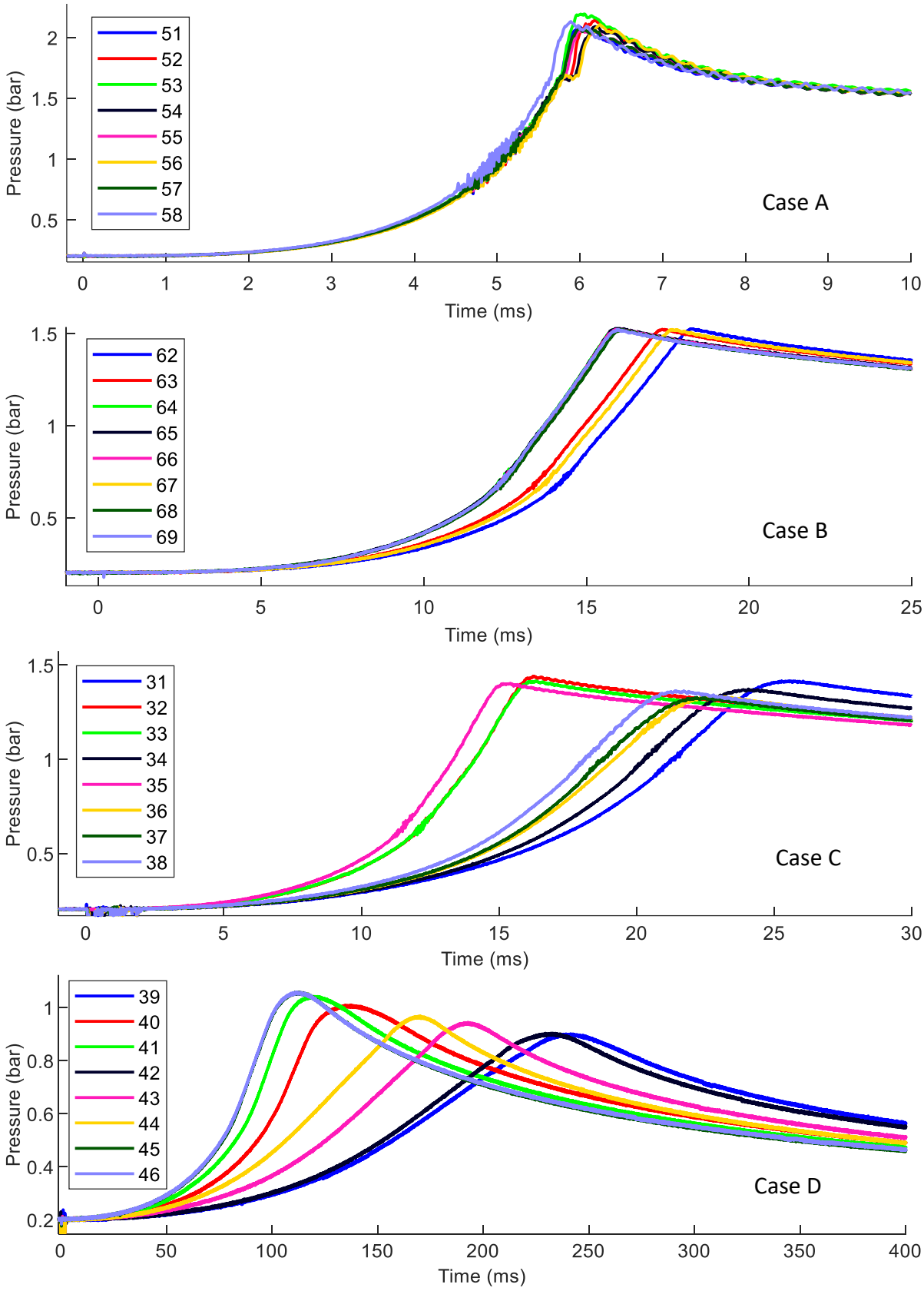

Figure 4.4 – Pressure Traces

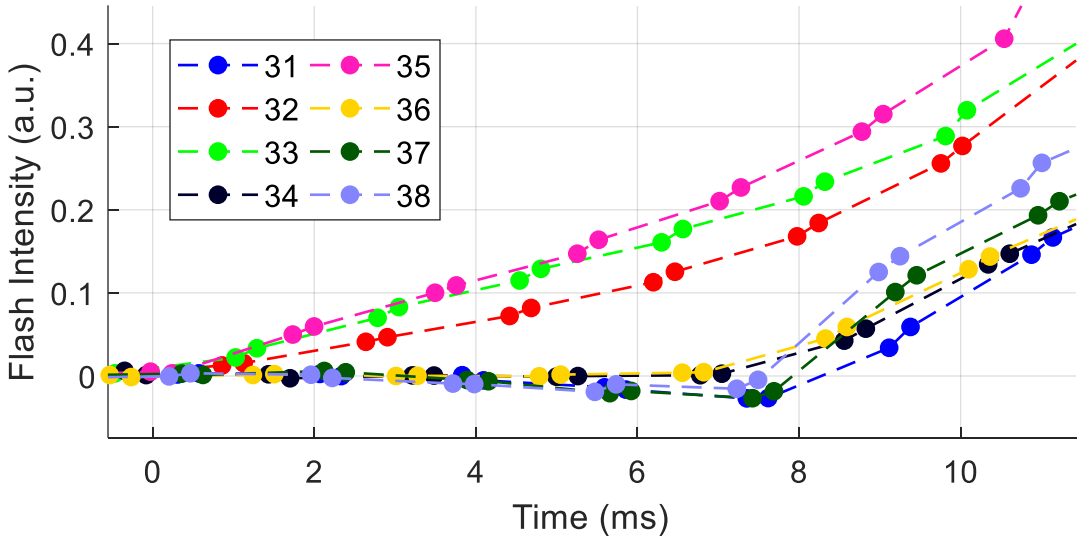

Figure 4.5 - Flash intensity - Case C

It is immediately apparent from the data that the cases with fast pressure rise (32, 33, & 35) all exhibit a flash signal which begins rising immediately upon sparking. This behavior is expected considering that ignition occurs within the optical path of the instrument, meaning that the created fireball emits into the spectrometer immediately. However, the remaining tests that showed slower pressure rise all have a significant delay before the flash signal begins to rise, suggesting that the fireball does not begin in the optical path at time zero. Furthermore, the observation that pressure is rising during this delay suggests that a fireball had formed. The conclusion was made that ignition did not occur between the sparking electrodes at chamber center, and instead, ignition likely occurred at the side wall. It was later found that, despite the sparking electrode being insulated from the chamber wall by approximately 1" of epoxy, a spark could run across the surface of the epoxy between the electrode and chamber wall should the spark gap's resistance be too high.

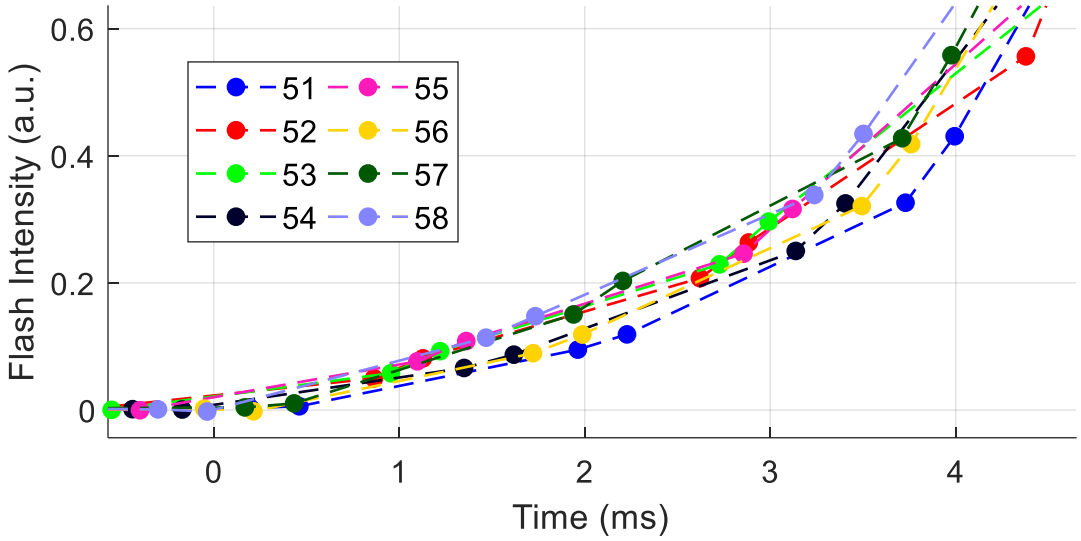

Figure 4.6 - Flash intensity - Case A

To determine the extent to which side ignition affected the measurements, the same proxy flash signal plots were made for the other groups of tests. Figure 4.6 and Figure 4.7 represent case A and B, respectively, and show no such delay in flash signal rise. In these plots, the three runs with lower values are all dedicated flash measurements, and they are separated from the other runs due only to the difference in how the proxy flash signal is calculated. Figure 4.8 corresponds to Case D runs. Here, the delay from side wall ignition is much greater and appears in four of the eight tests (39, 42, 43, 44).

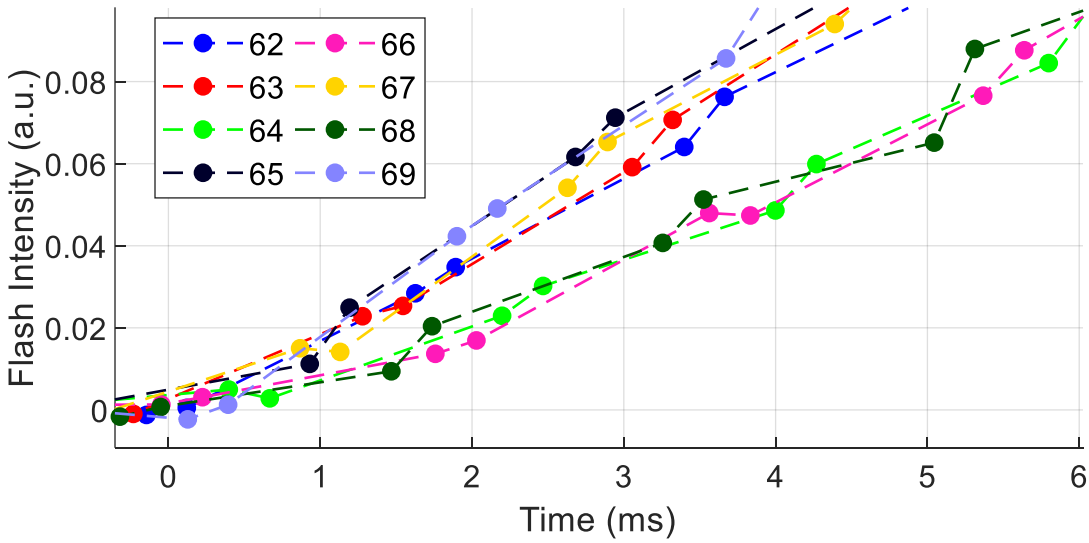

Figure 4.7 - Flash intensity - Case B

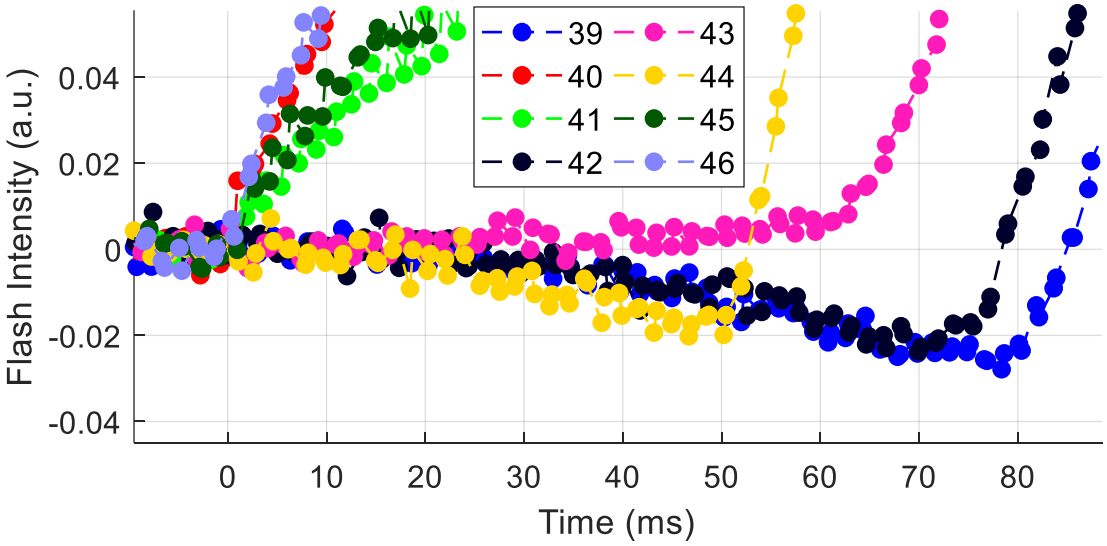

Figure 4.8 - Flash intensity - Case D

Side wall ignition only occurred in Case C and D measurements, the cases with CO_2 as the diluent species. This trend is in agreement with observed phenomena in a previous test chamber in which CO_2 fill cases would fail to generate a spark, whereas an N_2 fill counterpart would successfully spark.

In total, five runs from Case C (31, 34, 36, 37, 38) and four runs from Case D (39, 42, 43, 44) were all side wall ignited, making them unusable for 1D simulation. Beneficially, the large number of repeat measurements taken means that, despite the loss of these runs, the collected data set still contains repeat tests under each condition.

4.5. Flash Signals

Due to window fouling and experimental variability, the intensity and shape of flash measurements were not consistent between repeat experiments. This inconsistency was problematic as accurate determination of the flash signal interference was critical to obtaining accurate absorption information. As such, corrections needed to be applied to the flash data that would allow for determining the flash signal experienced on a given decomposition measurement from other experimentally measured values.

Additionally, as variability exists between the flash measurements themselves, corrections needed to be applied twice, once to individual flash signals to determine a characteristic average flash signal, and again to the average flash signal to apply it to each given decomposition measurement.

4.5.1. *Window Fouling Correction*

Window fouling between shots was an expected cause of variation between flash measurements. As window clarity deteriorated from shot to shot, the total amount of light that was passed by each window would decrease. This effect can be seen in Figure 4.9, which depicts the I_0 signal obtained from consecutive experiments performed on case B. Importantly, the effect of fouling does not show a flat decrease in signal across all wavelengths, but instead exhibits a slightly spectral response. Therefore, a wavelength dependent correction factor would need to be applied. Beneficially, these I_0 signals could provide this spectral response information and be used for the correction.

Critically, however, I_0 measurements record the light that has passed through both windows, while flash signal light passes only through one. As a result, a correction factor taken as the ratio between I_0 signals would over-predict the effect of fouling, and an assumption would need to be made regarding the relative effect of each window on the total drop in I_0. Ideally, the effect of each window would be equal given the symmetry of the chamber, and this was the assumption made.

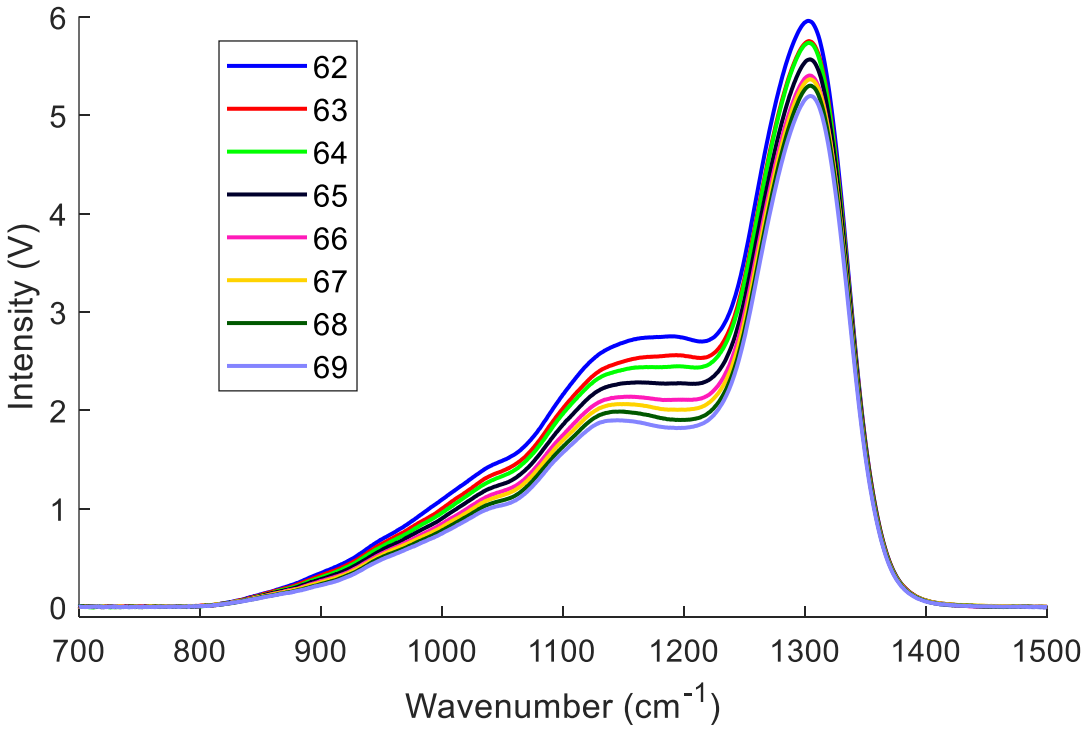

Figure 4.9 - Average I_0 signals for Case B runs showing window fouling effect on transmission

Calculation of the window fouling correction factor that would normalize measured flash signals was done using the equation:

$$C_F(\lambda) = 1 + \left[\frac{I_{0,REF}(\lambda)}{I_0(\lambda)} - 1\right]/2 \tag{14}$$

Here, $I_{0,REF}$ is a reference I_0 signal to which all flash signals would be normalized. Ultimately, the reference could be from any successful experiment of the given case but was taken as the test with the greatest I_0 intensity.

Applying this spectral correction factor to a group of flash signals has the effect demonstrated in Figure 4.10. Peak intensities of all runs become much closer, but some variation in the shape of the intensity profiles exist, with some peaks lagging in time. While not noticeable in wider views, these lags in intensity become significant on the short timescales over which the DIMP decomposition takes place. As correcting for emitted light is most critical during these early times, a second correction was necessary to account for the variation in shape. That correction came primarily from an empirical observation between the flash intensity time history and the chamber pressure time history. The two groups of signals were seen to share the same shape and relative behavior, with burn pressures lagging for the same tests in which flash signals lag. Based on this observation, a linear correlation between flash signal and pressure was assumed, resulting in a time correction factor given by:

$$C_F(t) = \frac{P_{REF}(t)}{P(t)} \tag{15}$$

Here, $P_{REF}(t)$ is the pressure profile from the same run used as reference for the spectral correction factor, and $P(t)$ is the pressure profile for the flash run being normalized. Applying this correction to the same flash spectrally corrected measurements in Figure 4.10 B produces the group of normalized flash signals given in Figure 4.10 C. Pressure correction has a lesser effect on the specific case shown, but for other cases the pressure correction is more crucial than the spectral correction. As such, both corrections are used for every case.

4.5.2. *Characteristic Flash Signal*

After applying these correction factors to each flash signal in a given case, the set of normalized flash signals needed to be condensed to a single reference signal. Given that the timing of scans

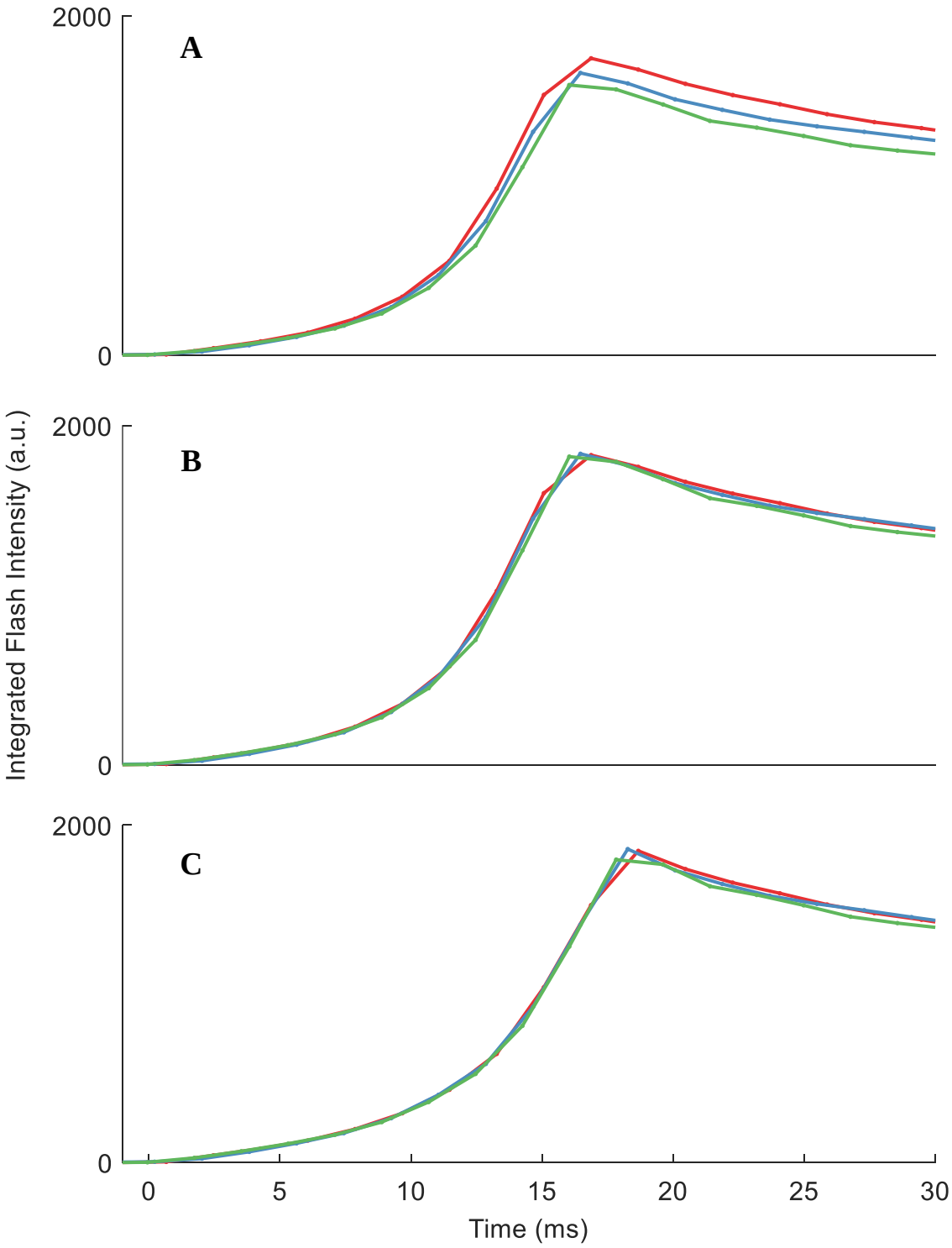

Figure 4.10 - Flash signal correction steps A.) Raw flash signal B.) With window fouling correction C.) With window fouling and pressure correction

relative to ignition was variable from shot to shot because of arbitrarily timed triggering and rotational speed variability, flash signals could not simply be averaged together. Instead, the intensity vs. time values from all flash signals were combined into a single signal. This signal provided flash intensities at each wavelength with greater time resolution than a single flash signal.

The process for determining the reference flash signal went as follows. First, the intensity vs. time values for a single wavelength were taken from the combined signal. These values were then fit with a series of spline functions with different smoothing parameters for different sections in time. Early time, comprising the initial intensity spike and rapid decay, was fit with a smoothing parameter extremely close to unity such that the fit essentially touched every provided data point. During this time, unlike for later times, points from the combined signal are primarily monotonically increasing or decreasing due to the rapid change overpowering any fluctuation between the different flash signals. Nearly exact fitting was also necessary during this time to capture the sharpness of the flash peak.

For mid time, during which intensity decay occurred at moderate pace and fluctuations between runs began to appear, the fit parameter was decreased to make the fit smoother. Finally, for late time, encompassing the very slowly decaying intensity tail where fluctuations were prominent, the fit was made even smoother.

All three splines were then combined to give a fit of the full-time capture window and the fit applied to the set of time 0-0.95s with 0.5ms step size. These calculated values were saved to a characteristic flash signal matrix for the corresponding wavelength, and the process repeated for all wavelengths in the first order scans. What resulted was a matrix of flash signals at every wavelength for the entire time window in even time increments. From this matrix, the normalized flash signal at any given time would be determined through linear interpolation between times in the matrix.

As mentioned, applying this characteristic flash signal to a given run required transforming the signal to the window fouling and burn profile conditions of the given run. This would be done by applying the inverse of the correction factors:

$$C_F'^{(\lambda)} = 1 + \left[\frac{I_0(\lambda)}{I_{0,REF}(\lambda)} - 1\right]/2 \qquad (16)$$

$$C_F^{\prime(t)} = \frac{P(t)}{P_{REF}(t)} \qquad (17)$$

Here, I_0 and $P(t)$ are conditions for the run being corrected and $I_{0,REF}$ and P_{REF} are the same reference conditions used to normalize the flash signals.

Flash corrections were applied to spectral scans from the run being corrected on an individual basis. In the process, the time at which the scan occurred was used to determine the characteristic flash signal and time dependent correction factor $C_F{}'(t)$. The spectral and time corrections were then applied to the characteristic flash, and the resulting intensity subtracted from the scan. This process was repeated for all scans throughout the capture window.

4.5.3. *Accuracy of Flash Correction*

To determine the accuracy of the described flash correction routine, the routine was applied to the flash signals themselves. Figure 4.11 shows the results of these corrections for case B measurements, where multiple lines are plotted representing scans at different times. Ideally, this would result in a flat zero signal at all times, however, there is some error in method made clear by the presence of a small amount of signal after subtraction. Notably, the error exists primarily at large wavenumber where signal is largest, and the sign of the error is different for the positive and negative orders. Most of the information to be gained from these spectra exists in the larger wavelength region, so this error is acceptable. However, this order-dependent difference does show up in the processed decomposition spectra, as will be discussed in the following section.

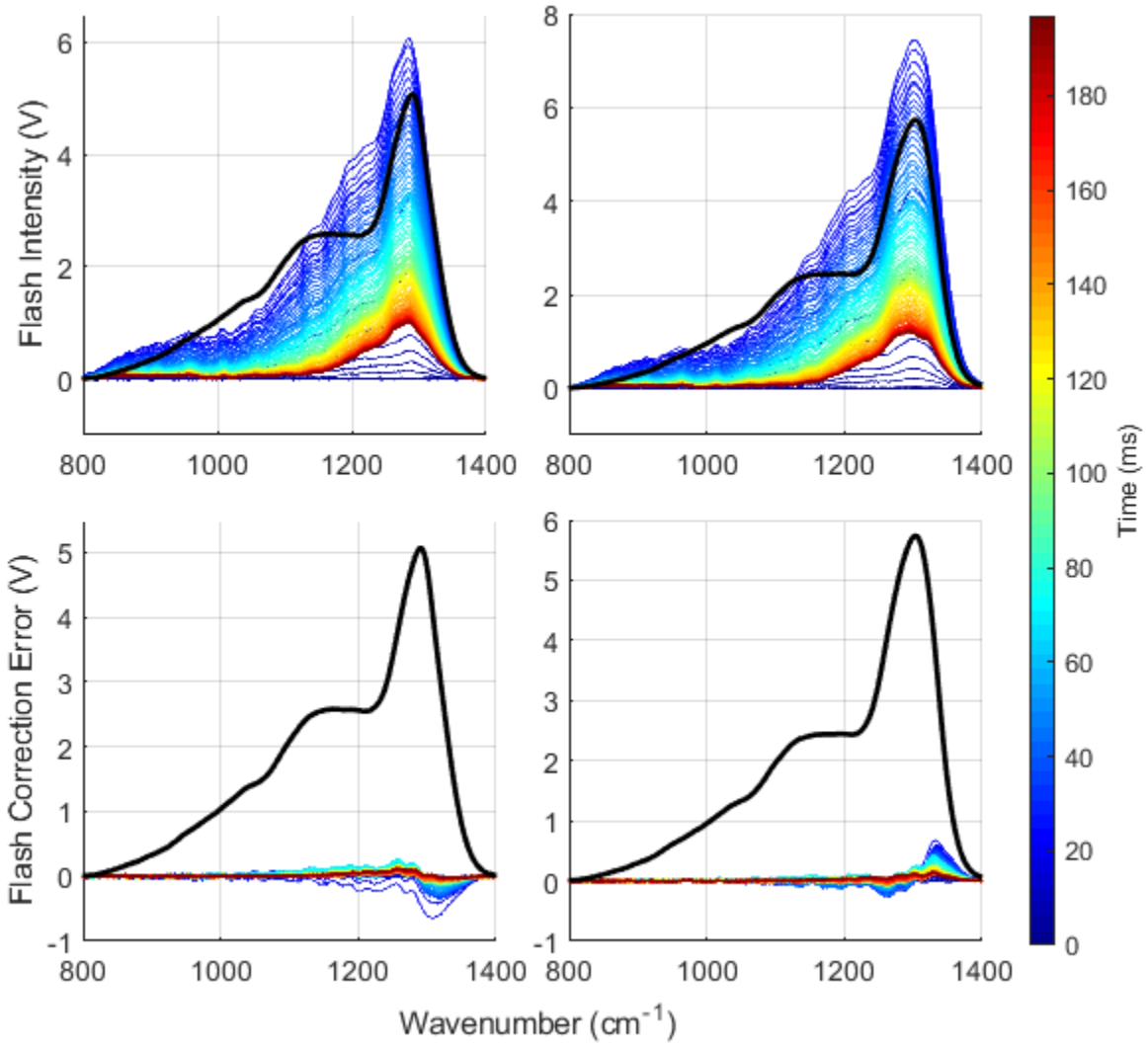

Figure 4.11 – Flash correction accuracy with -1st order flash signal (top left) +1st order flash signal (top right) -1st order flash correction error (bottom left) and +1st order flash correction error (bottom right)

4.6. DIMP Decomposition Results

This section will present the longwave infrared absorbance spectra obtained from successful tests performed. However, as discussed, the purpose of this work is to provide a set of benchmark data for model validation in the form of absorbance spectra that can be compared to a model predicted spectra. An in depth, quantitative analysis of DIMP behavior is beyond the scope of this work. Comments will largely be limited to qualitative remarks on absorbance data.

As displaying the over 1000 spectra per test is not feasible, a few different representations of the data will be made. Three representations are made for individual runs, and the first of these is a stacked absorbance plot. These plots provide individual absorbance scans as they were calculated, with no time averaging applied. For visual clarity, time resolved scans are offset with regular spacing, and dashed lines of corresponding color mark the zero of each scan. The purpose of these plots is to show the destruction of the DIMP signal, primarily at early time, as well as the rapidly changing spectra. To facilitate both goals, these spectra are provided with two different zooms. Wide zoom representations primarily show DIMP destruction through DIMP's primary features. Narrow zoom representations have a low wavenumber cutoff of 1050 cm^{-1} and focus on smaller absorbance features that develop at larger wavenumber.

Slower time evolution of features throughout the one second capture window are shown using the second representation, color mapped absorbance spectra. These plots overlap multiple spectra with line colors representing time as defined by the attached color map. Time averaging of 20 scans is applied to the plotted spectra, and every 40^{th} scan is plotted to keep the figure readable. Initial pre-fire DIMP absorbance is also provided as a solid black line. As these plots are focused on later time evolution, the y-axis scale is chosen to focus on the late time features.

Finally, Initial vs. Final absorbance plots are provided. These overlay the pre-spark absorbance with the average absorbance from the final 50 scans. To assist in viewing features in the final absorbance, initial absorbance is scaled down to ¼ of its true value. All spectra shown in this section were obtained from tests using the 150 kHz preamplifier. 1MHz amplifier spectra collected for Case A and Case B are provided in Appendix A.

4.6.1. *Case A 150 kHz*

Case A results are plotted from test 53 in Figure 4.12 - Figure 4.15. For this case, stacked absorbance plots are formed using consecutive scans, and no scans are skipped. As such, sequential scans alternate between +1 and -1 order, and the alternating sign error of the flash correction can be seen in the alternating upward and downward trend in absorbance at large wavenumber.

Although no Case A tests indicated side wall ignition, the final two runs (57 and 58) had anomalous absorbance calculations resembling an issue with an incorrect I_0 measurement. The first three cases all agreed well and showed no anomalies, so the last two are discarded in the set of benchmark data.

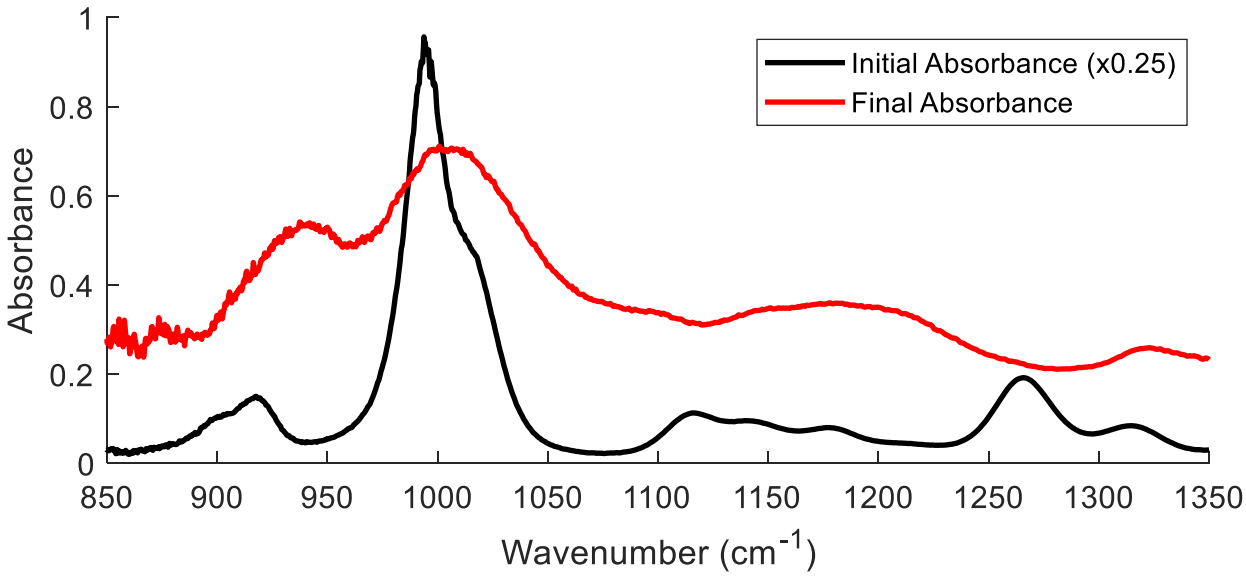

Figure 4.12 - Case A Initial vs. Final Absorbance

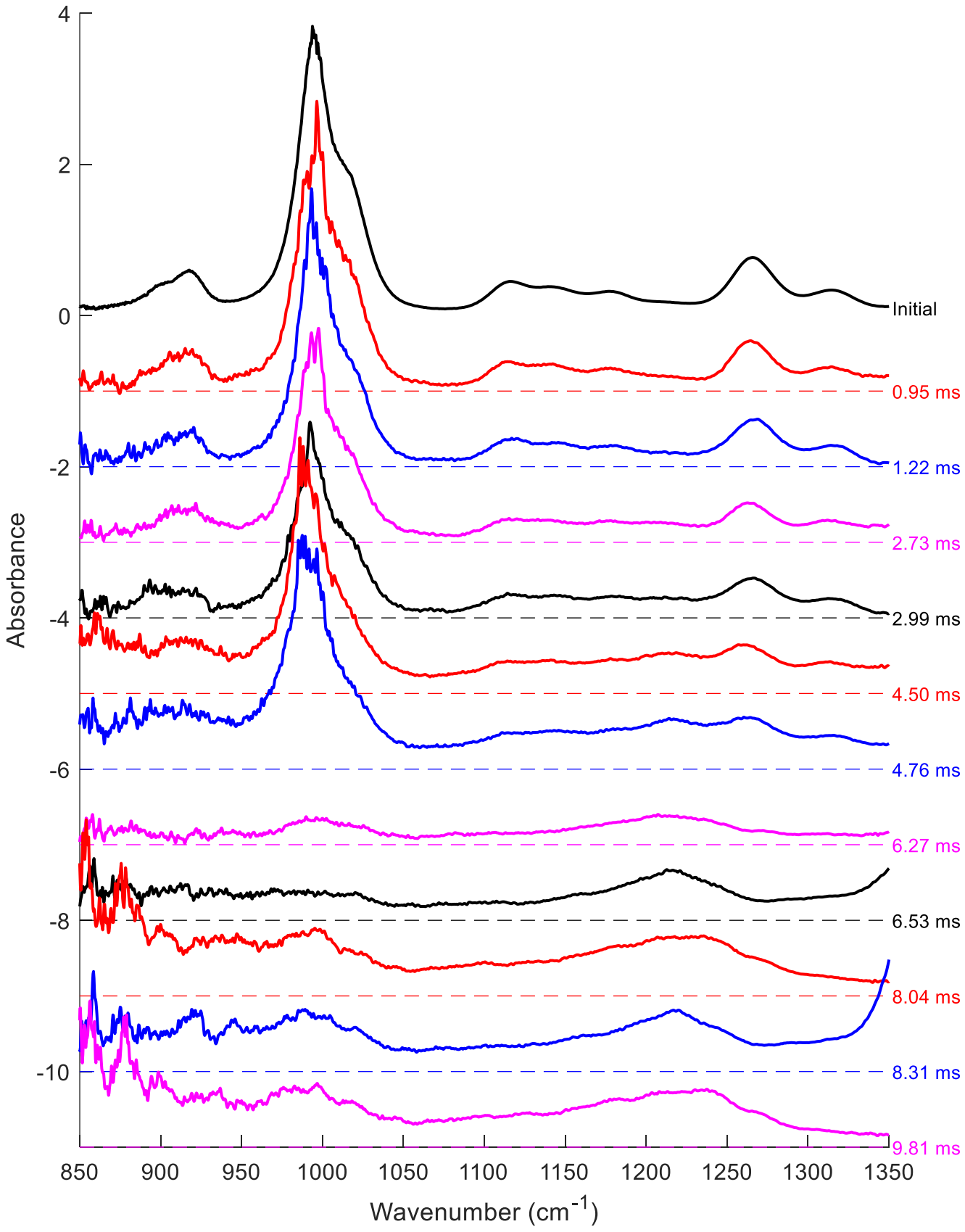

Figure 4.13 - Case A stacked absorbance plot – wide zoom

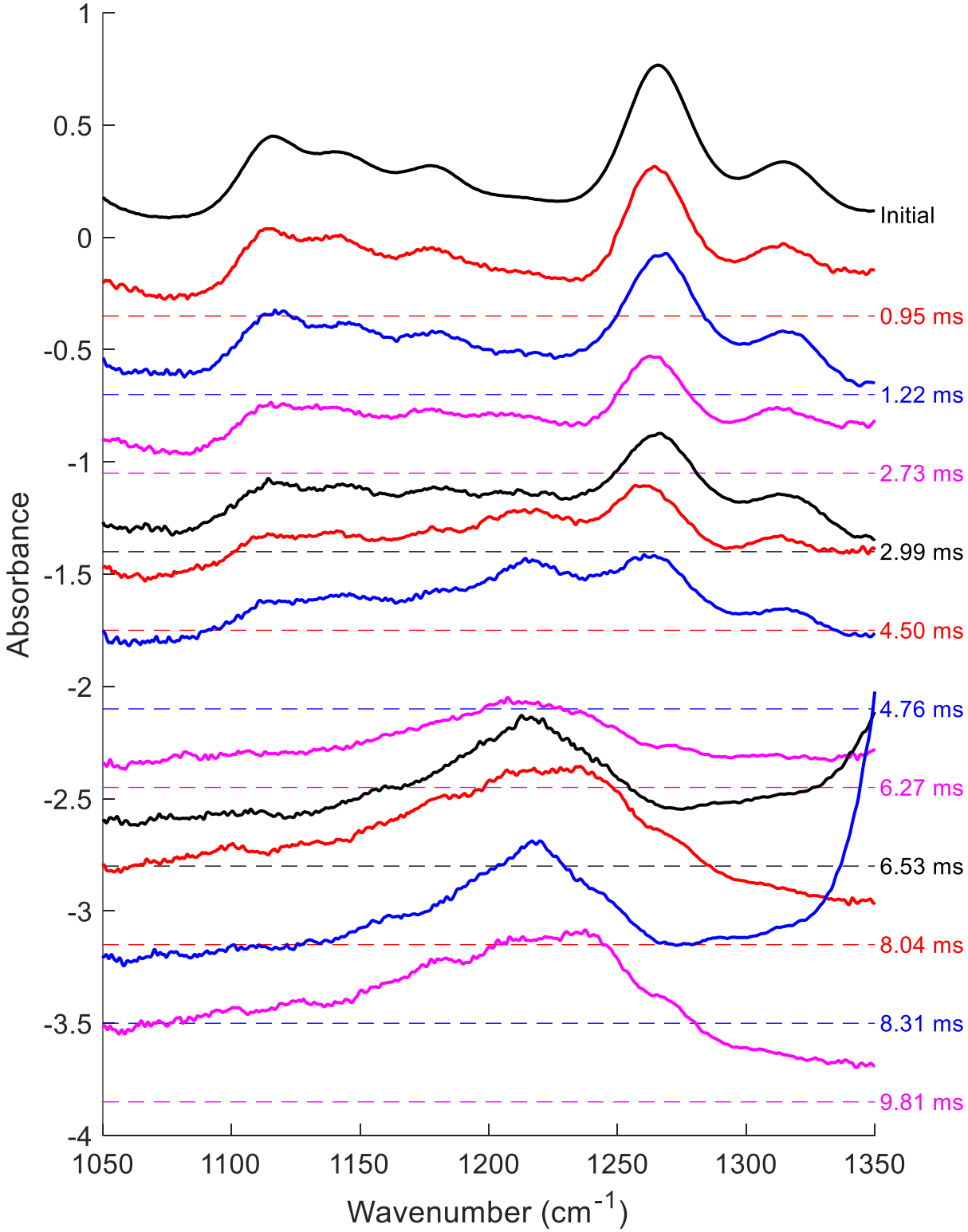

Figure 4.14 - Case A stacked absorbance plot – narrow zoom

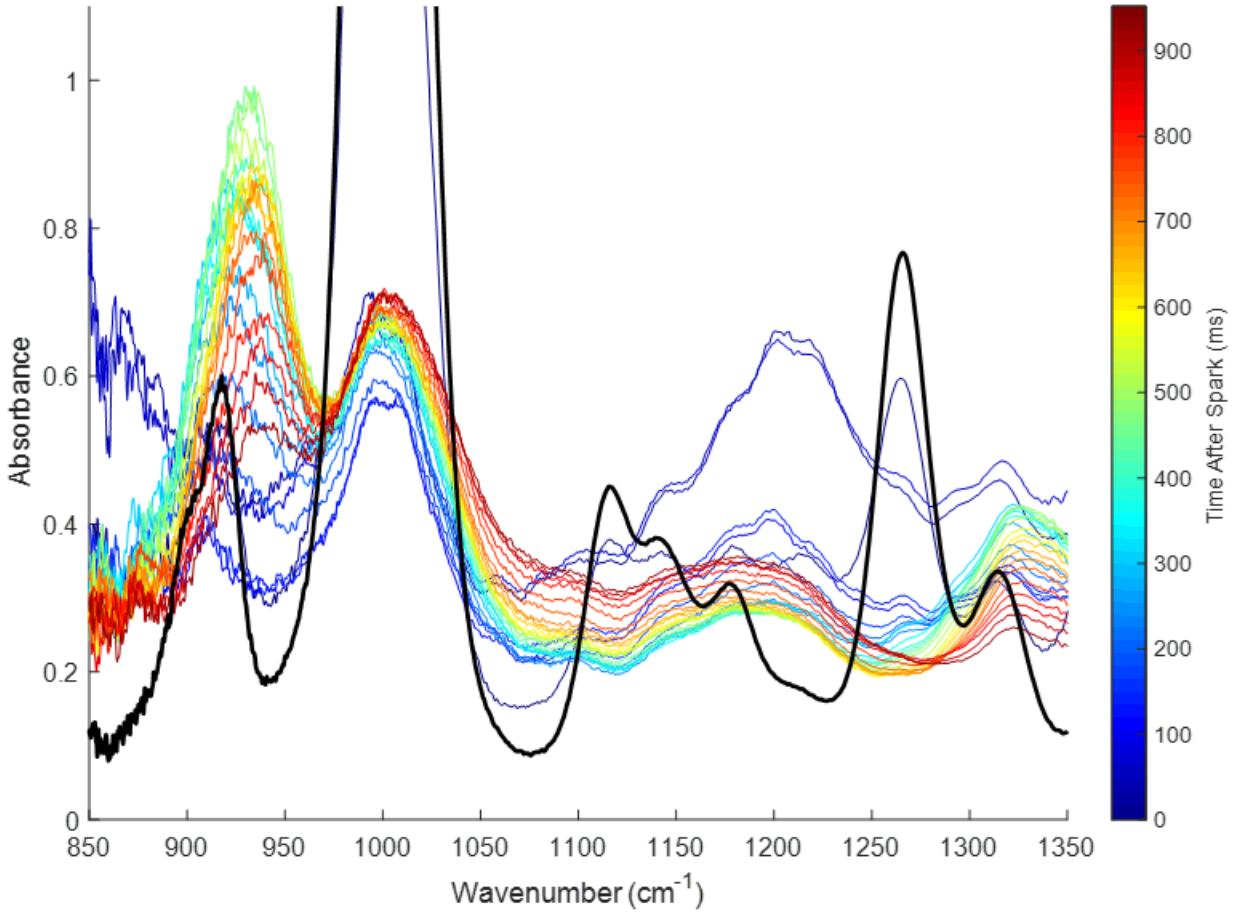

Figure 4.15 – Case A Color Mapped Absorbance

4.6.2. *Case B 150 kHz*

Case B results are plotted from test 69 in Figure 4.16 - Figure 4.19. Decomposition speed for this case was slower than for case A. As a result, stacked decomposition plots are provided with every third scan, still retaining the convention that shown scans alternate between +1 and -1 orders. Again, the alternating sign error from the flash correction can be seen with alternating upward and downward trends in absorbance at large wavenumber.

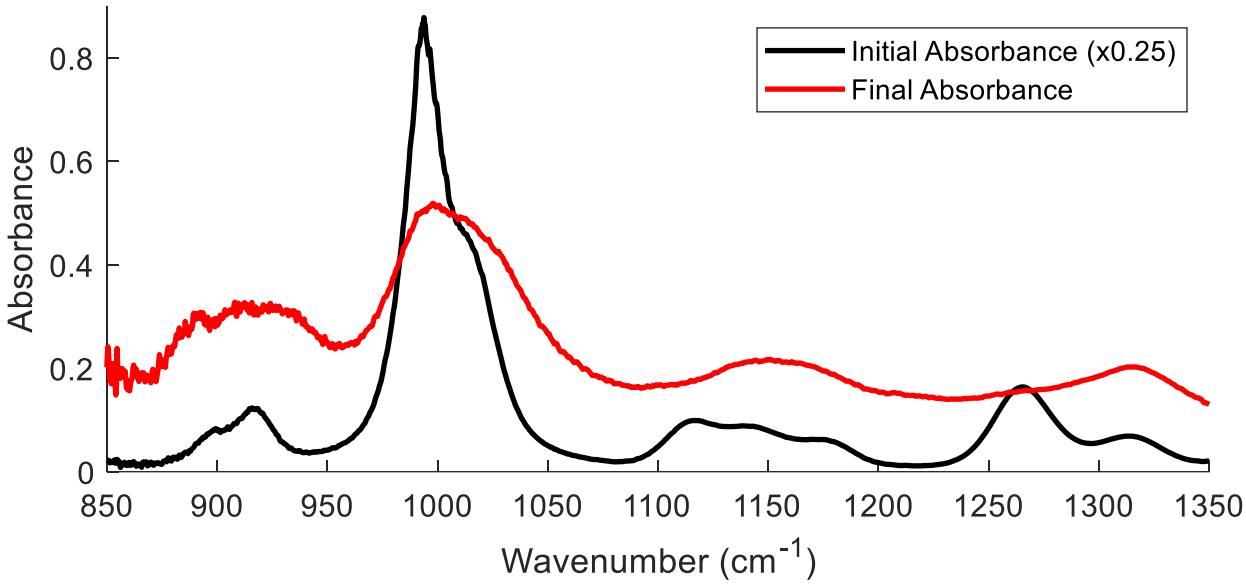

Figure 4.16 - Case B initial vs. final absorbance

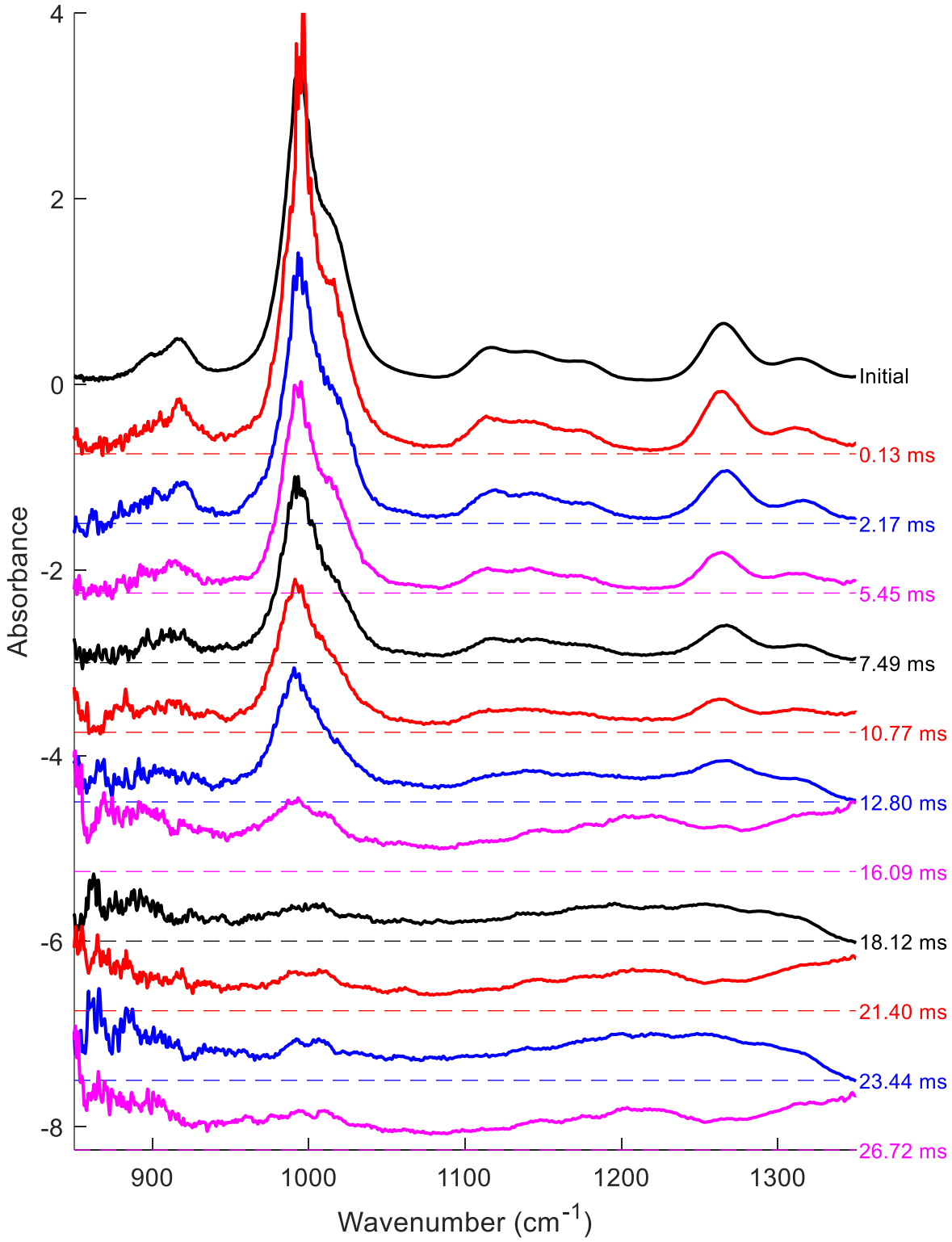

Figure 4.17 – Case B stacked absorbance – wide zoom

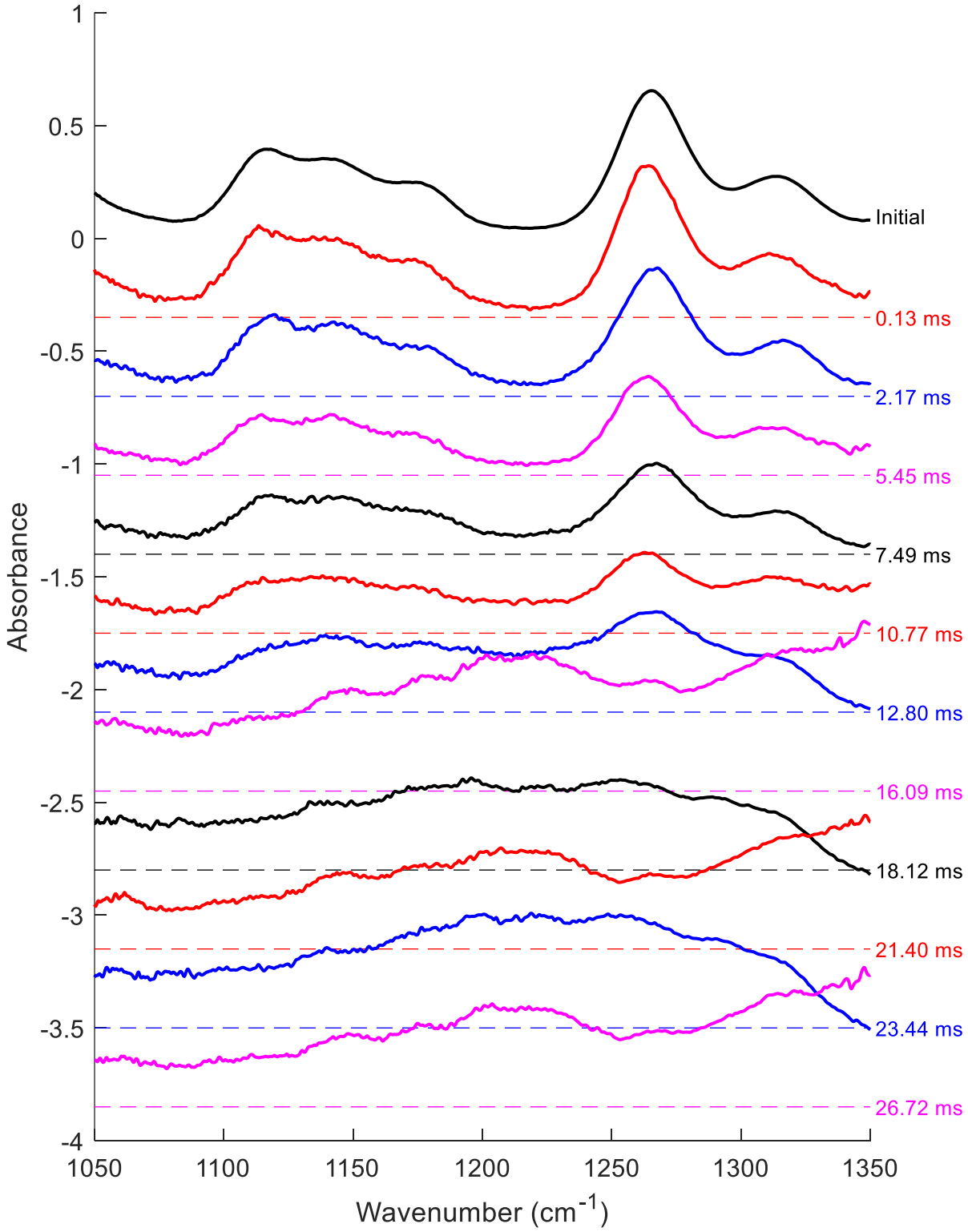

Figure 4.18 – Case B stacked absorbance – narrow zoom

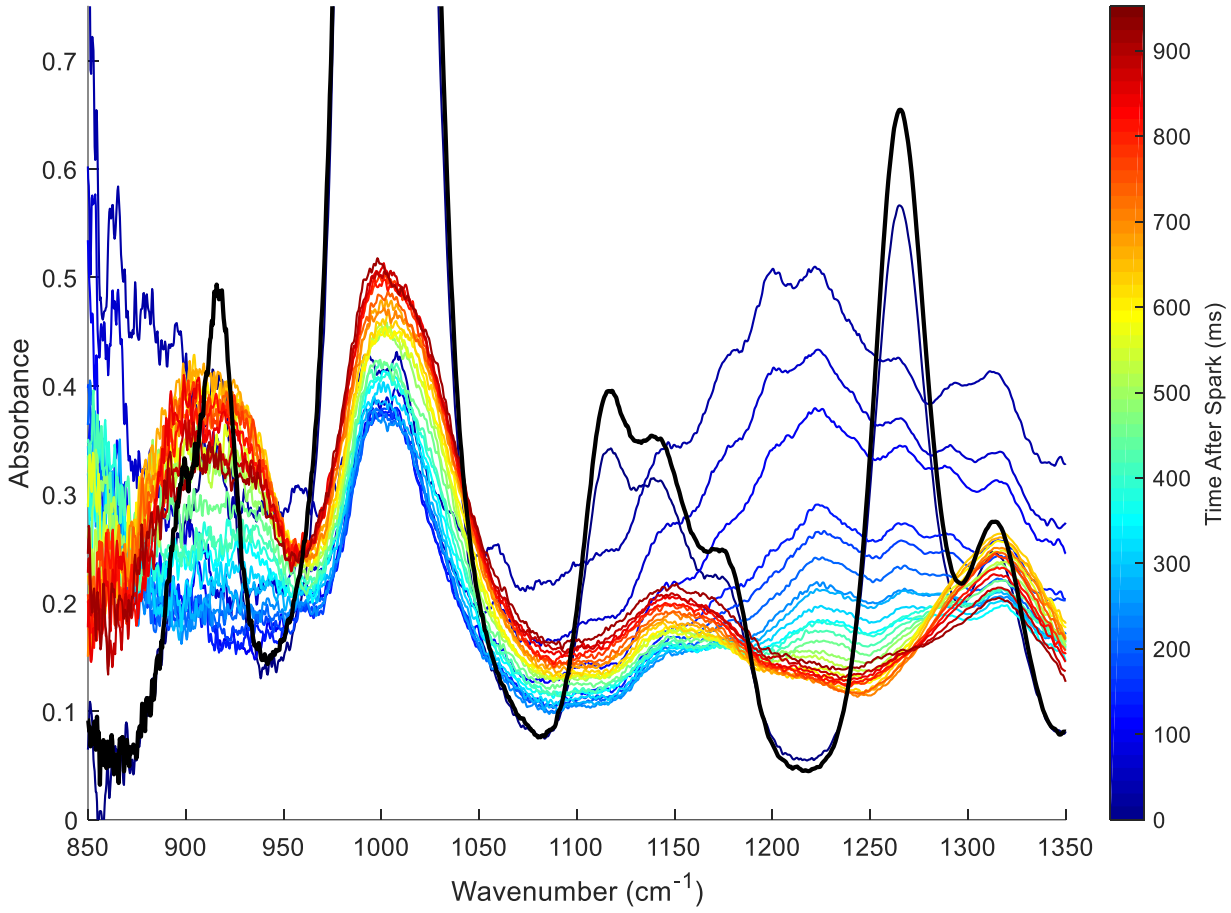

Figure 4.19 – Case B Color Mapped Absorbance

4.6.3. *Case C 150 kHz*

Case C results are plotted from test 35 in Figure 4.20 - Figure 4.23. Decomposition occurred at approximately the same speed as Case B, albeit slightly faster, so stacked absorbance plots are again provided with every third scan.

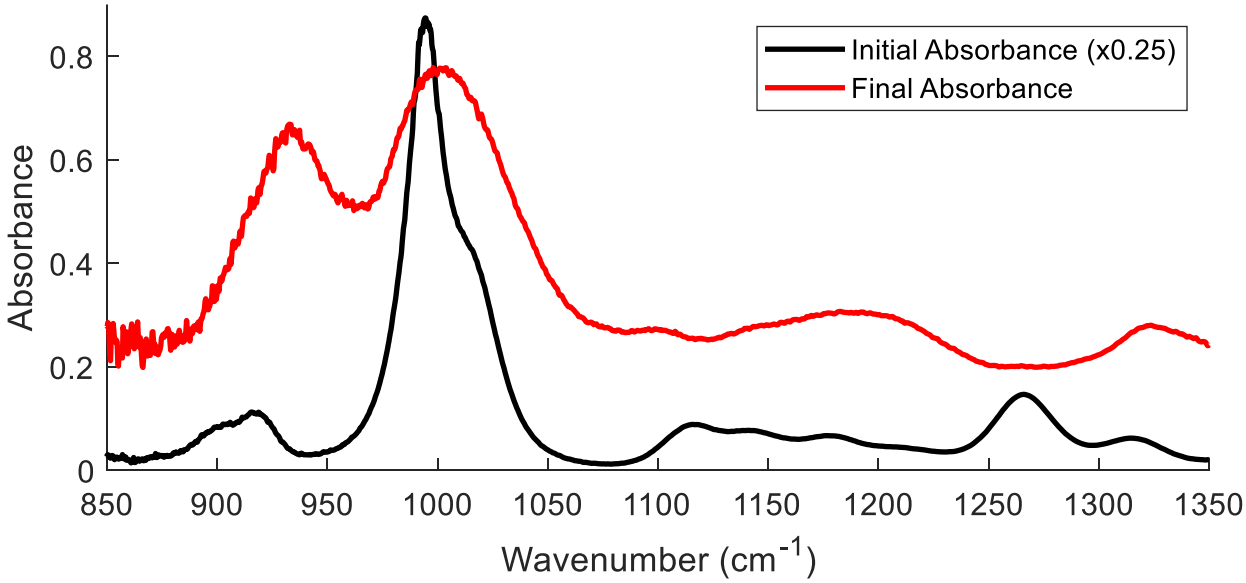

Figure 4.20 – Case C Initial vs. Final Absorbance

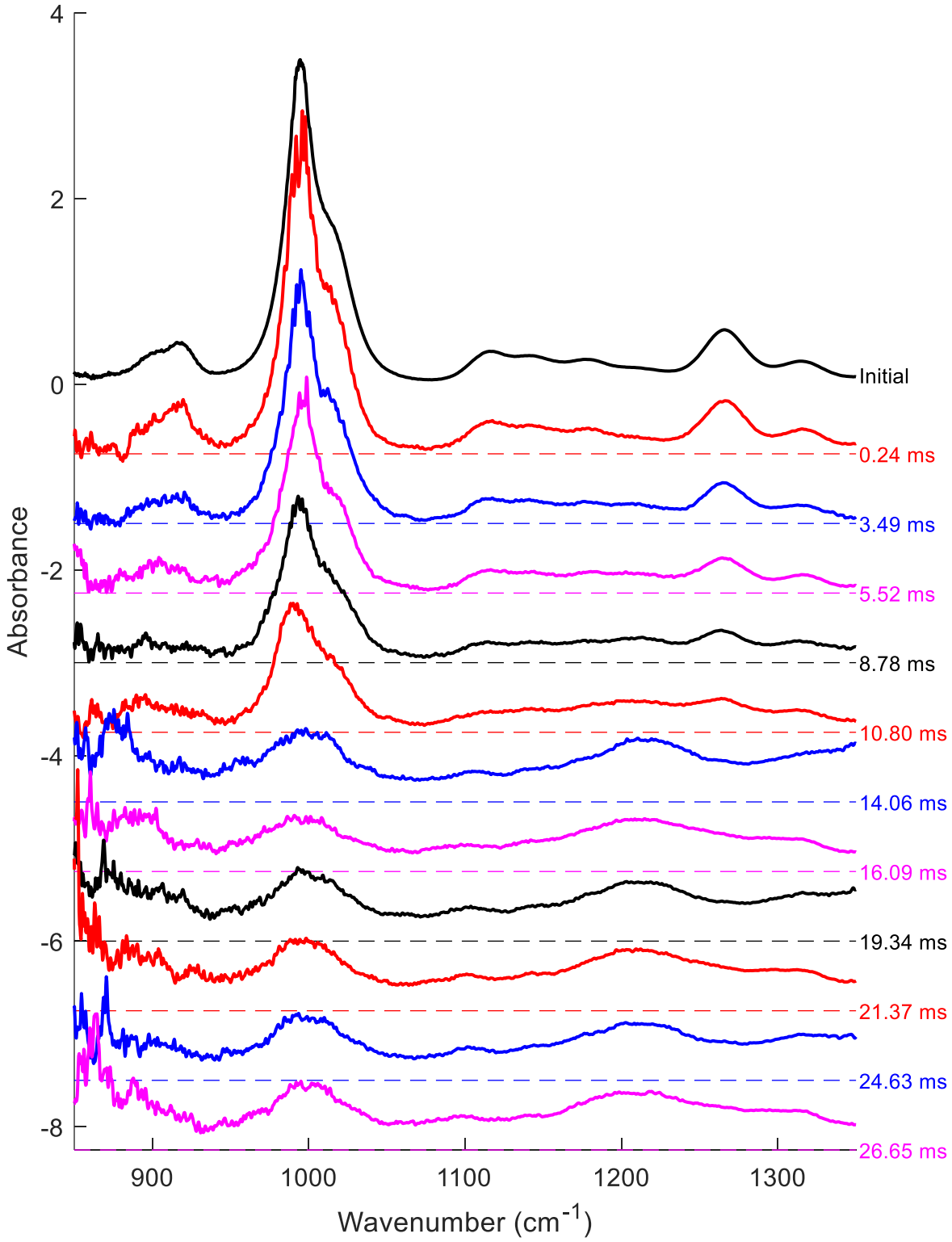

Figure 4.21 - Case C stacked absorbance - wide zoom

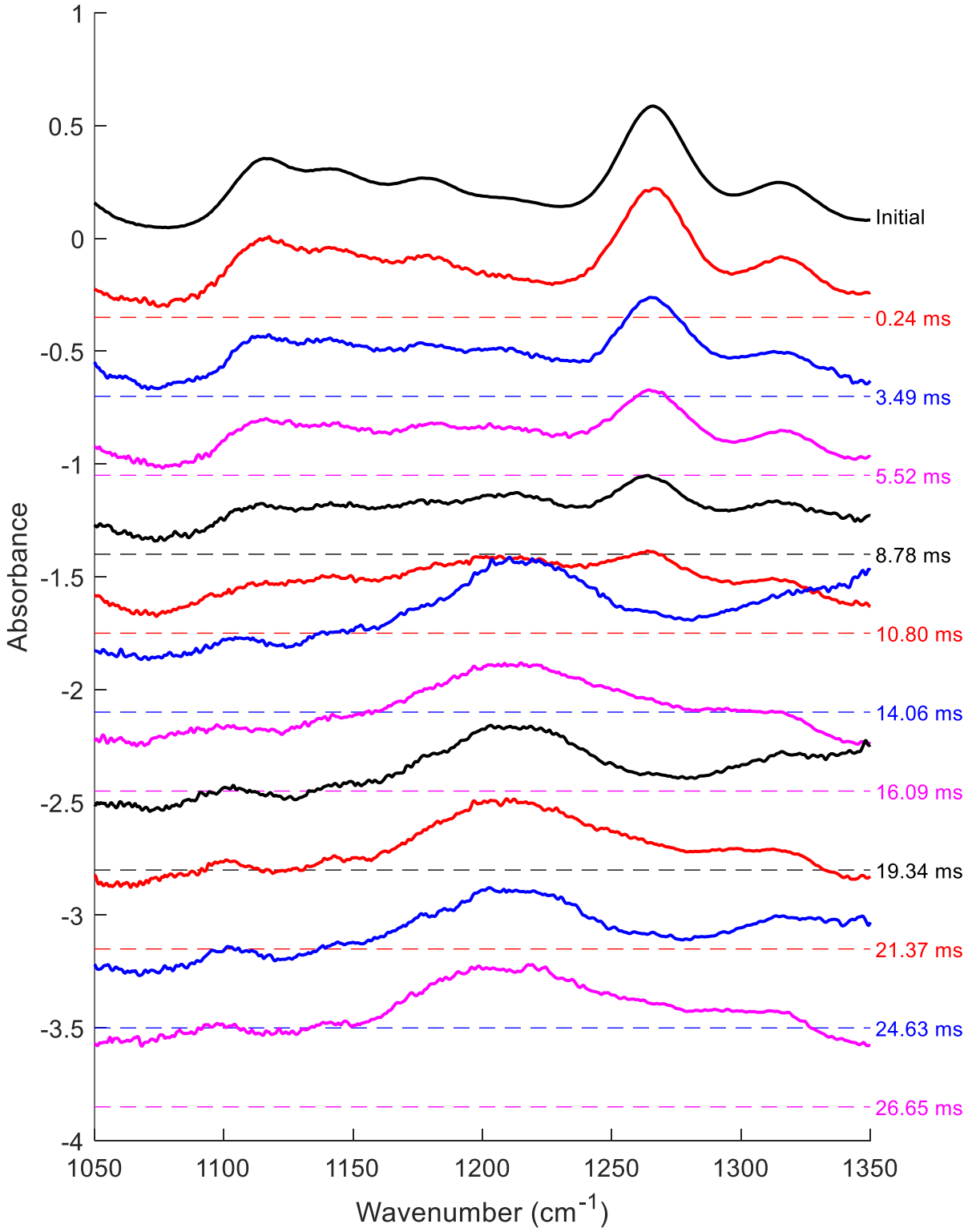

Figure 4.22 - Case C stacked absorbance - narrow zoom

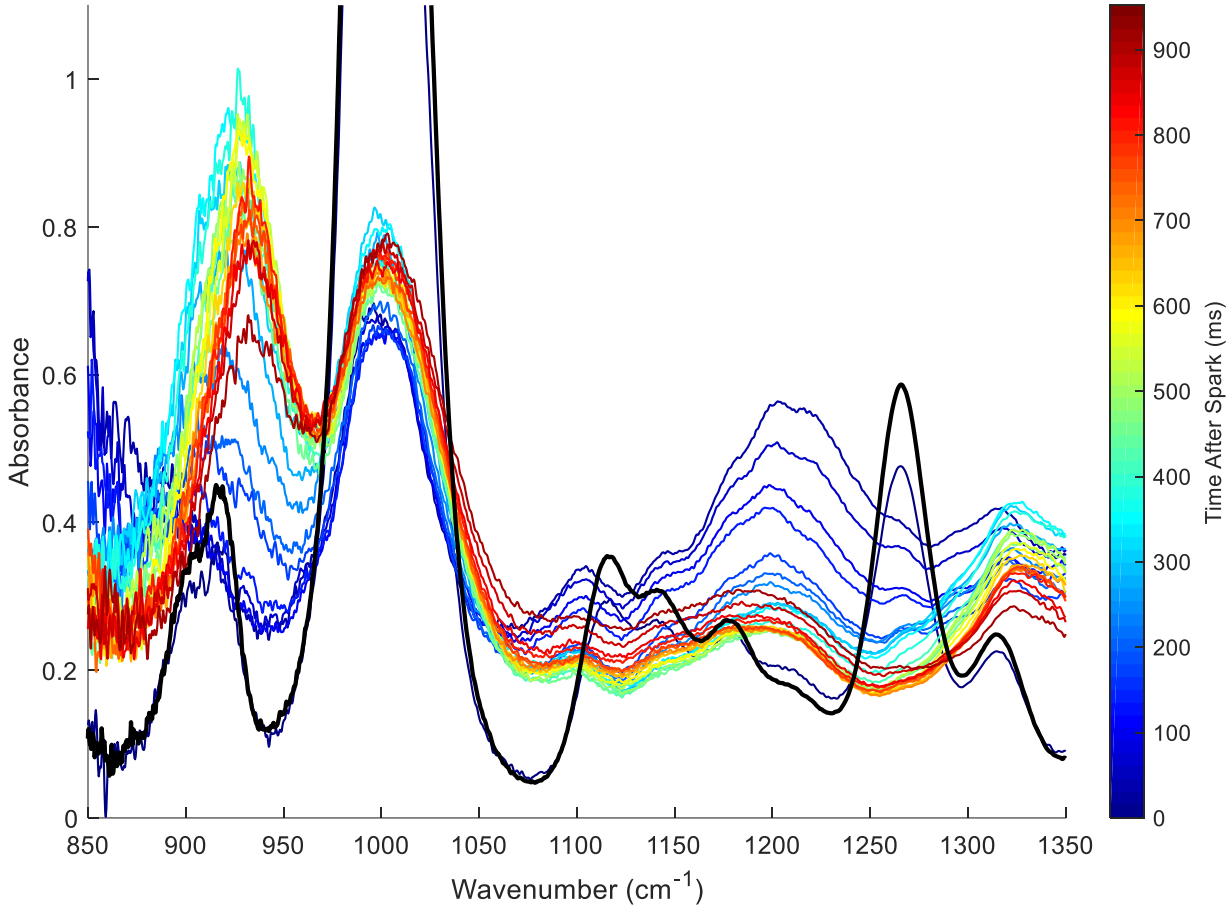

Figure 4.23 - Case C color mapped absorbance

4.6.4. *Case D 150 kHz*

Case D results are plotted from test 46 in Figure 4.24 - Figure 4.27. Decomposition occurred much slower in this case, orders of magnitude slower than for case A. To compensate, stacked absorbance plots are provided with every 17th scan.

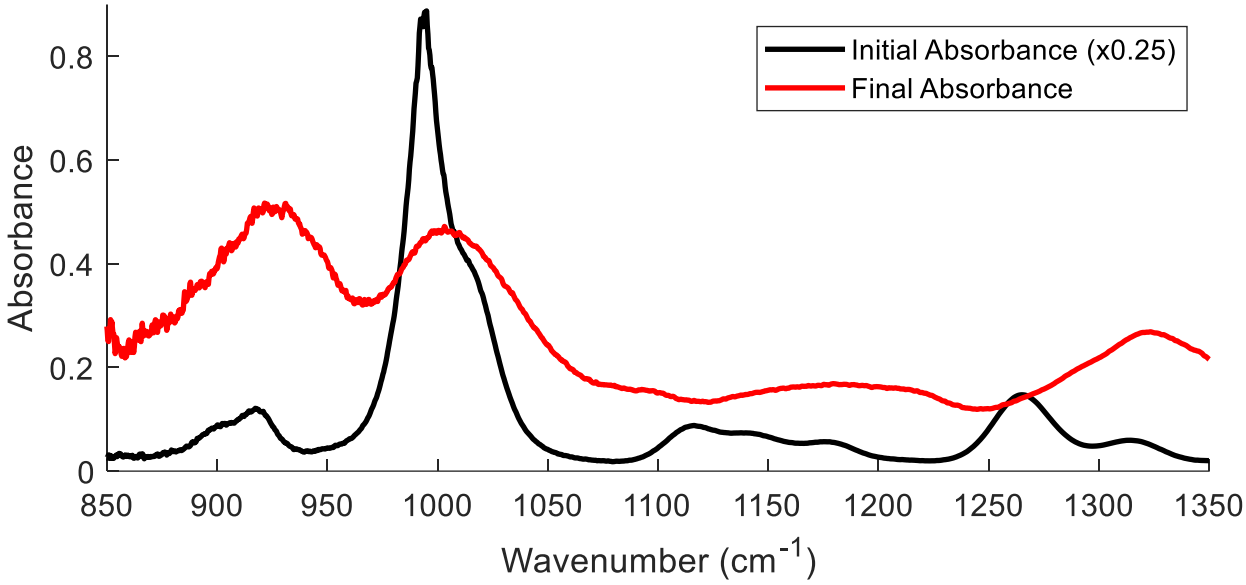

Figure 4.24 – Case D Initial vs. Final Absorbance

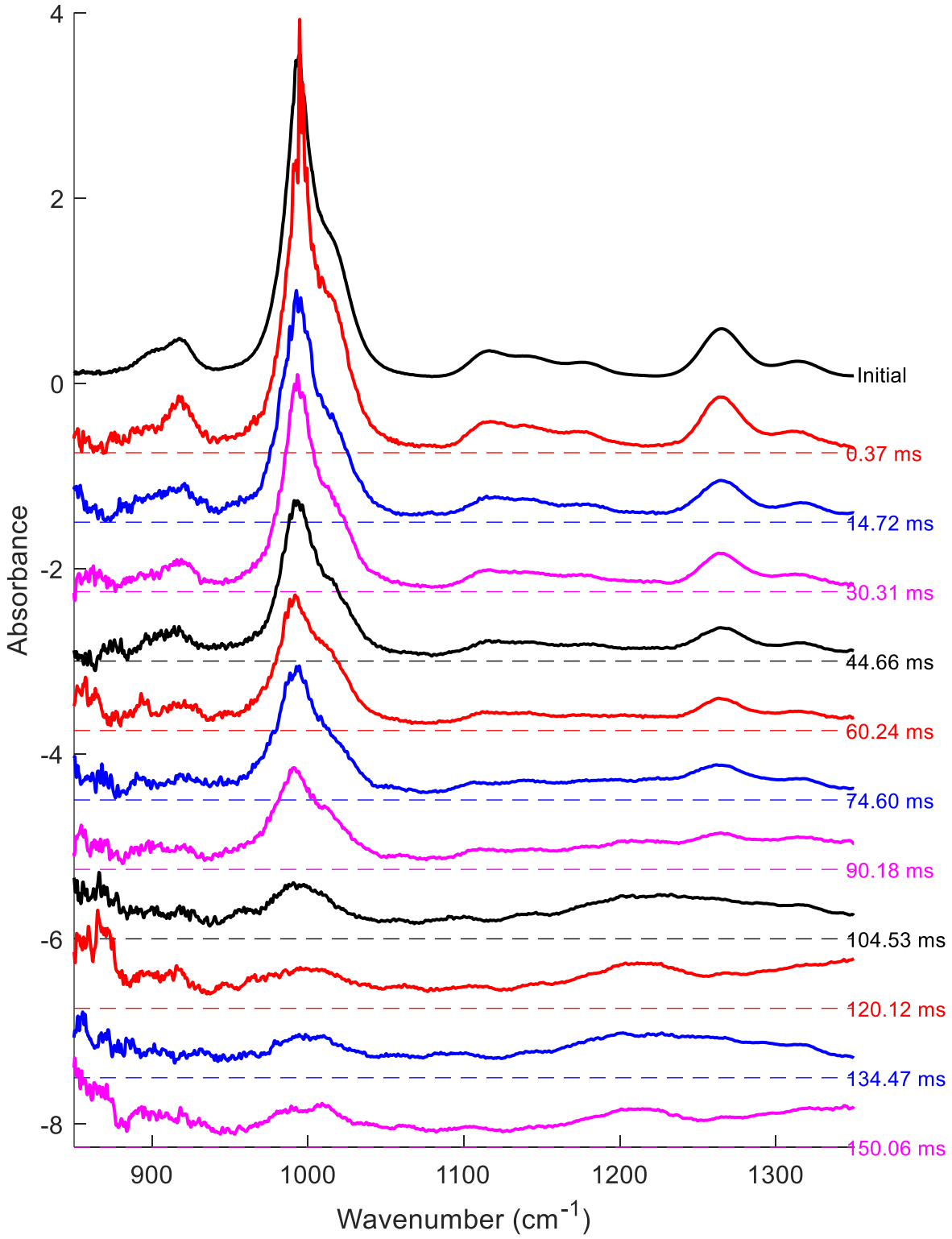

Figure 4.25 - Case D stacked absorbance - wide zoom

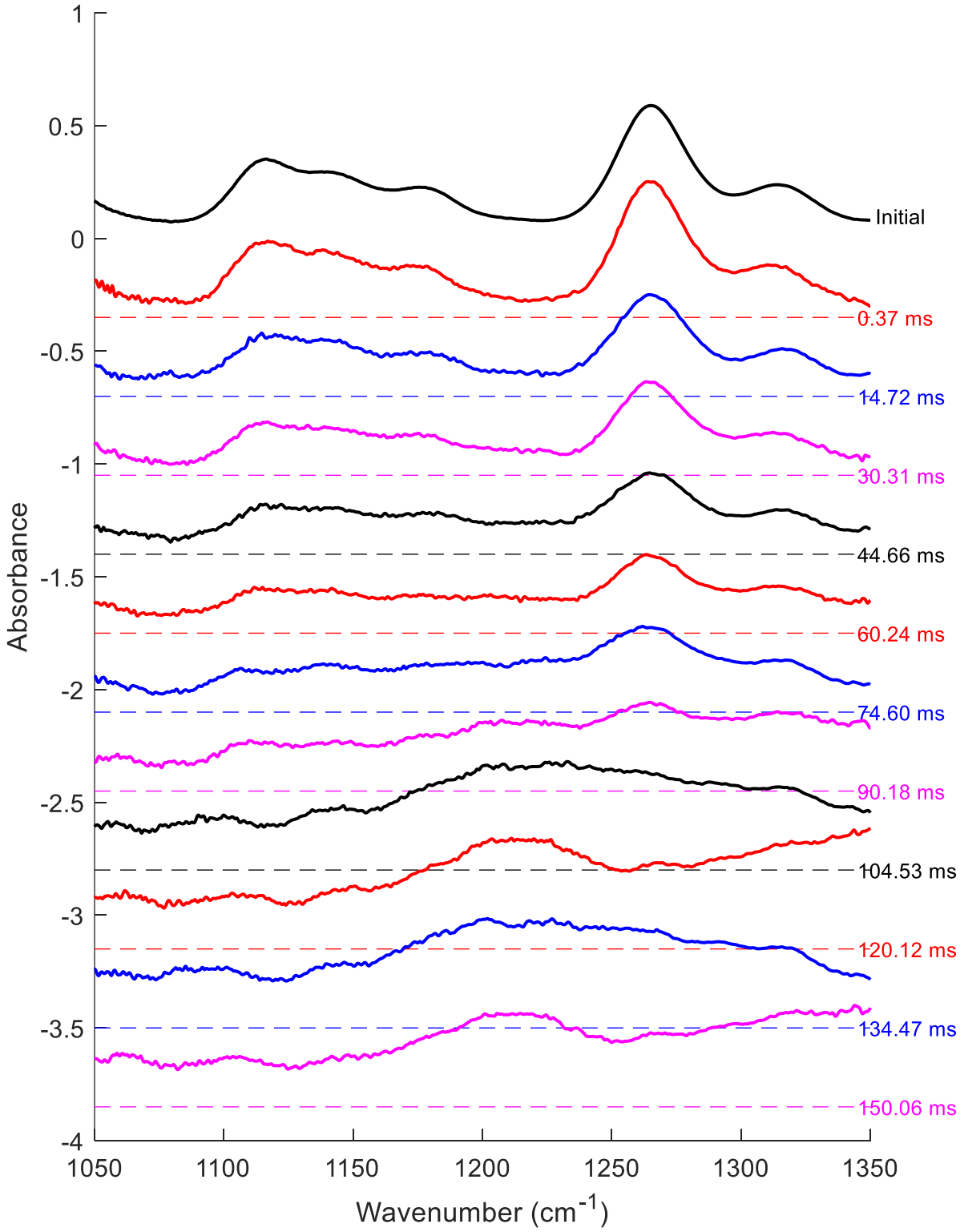

Figure 4.26 - Case D stacked absorbance - narrow zoom

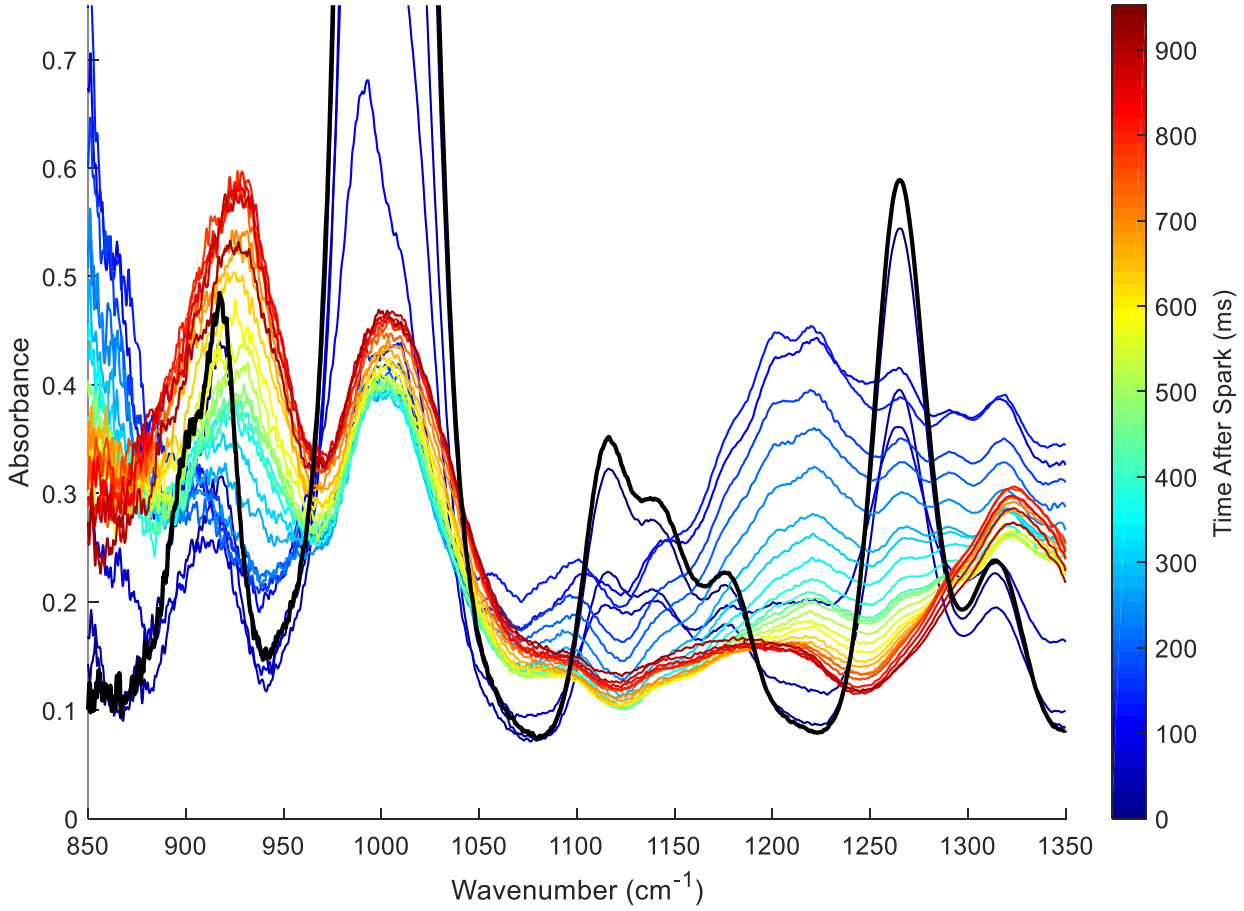

Figure 4.27 - Case D color mapped absorbance

4.6.5. *All Tests Summary*

Simultaneous comparison of multiple tests for experimental repeatability and the difference in conditions is best done through comparison of time histories of peak decay. The metric used for this visualization is the integrated absorbance of the collected spectra encompassing the primary DIMP spectral peak at 1000cm^{-1}. It is important to make clear that integrated absorbance collected in this manner is purely qualitative. Although integrated absorbance is related to species concentration, a myriad of factors including pressure variation, interfering product features, and temperature variation greatly complicate the conversion of integrated absorbance to species concentrations. As such, these plots should not be taken as measures of DIMP decay directly, except in the sense that the absence of integrated absorbance does indicate the absence of DIMP vapor. However, as product species could absorb within the integration zone, DIMP could be removed even if absorbance is present.

Figure 4.28 provides integrated absorbance for each case. In general, tests within each case all agree very well, both in decay speed and decay shape. Most cases show very good agreement in initial integrated absorbance, indicating once again the good repeatability in DIMP vapor concentration. Figure 4.29 plots two tests from each case, including cases done with the 1MHz amplifier.

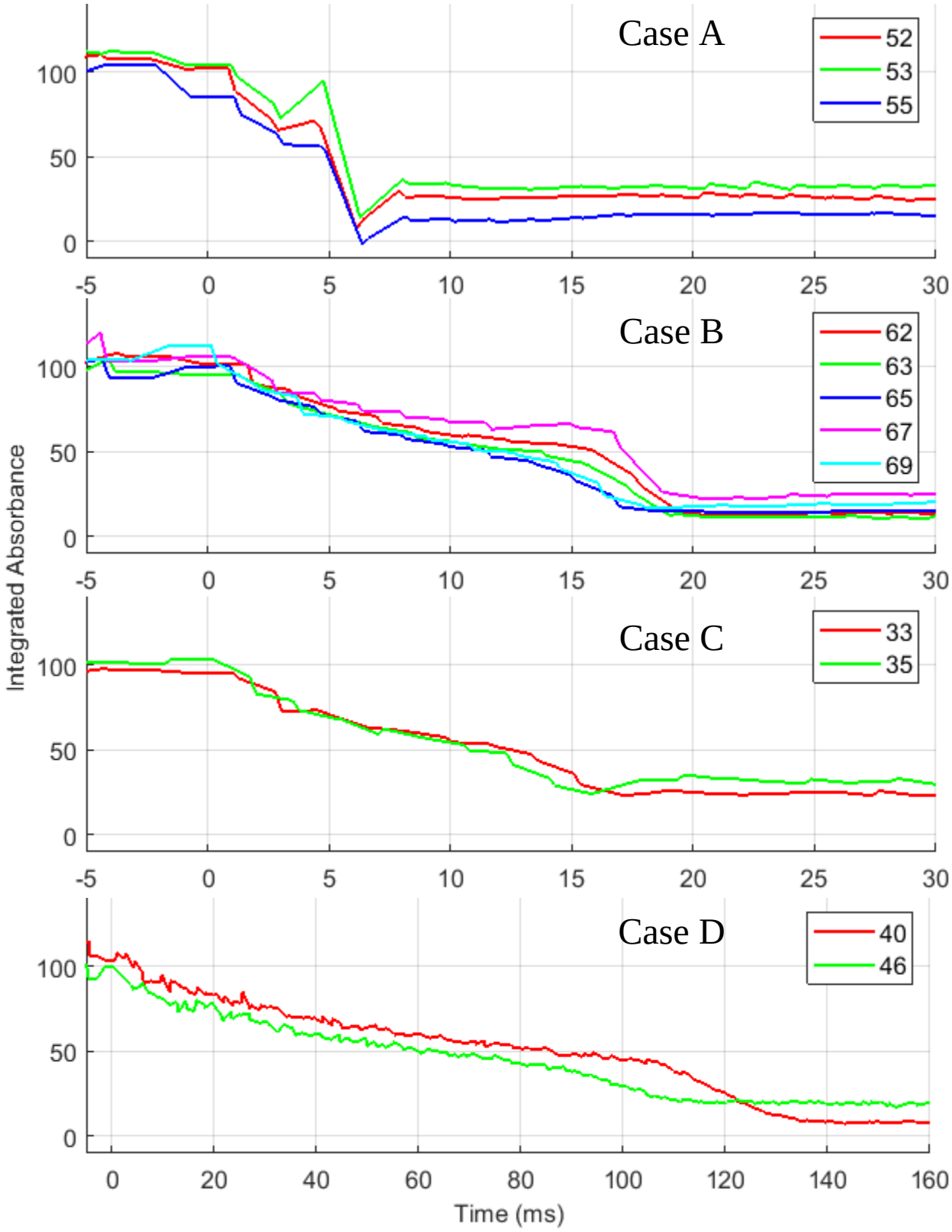

Figure 4.28 – Integrated absorbance of DIMP peak vs. time for all cases

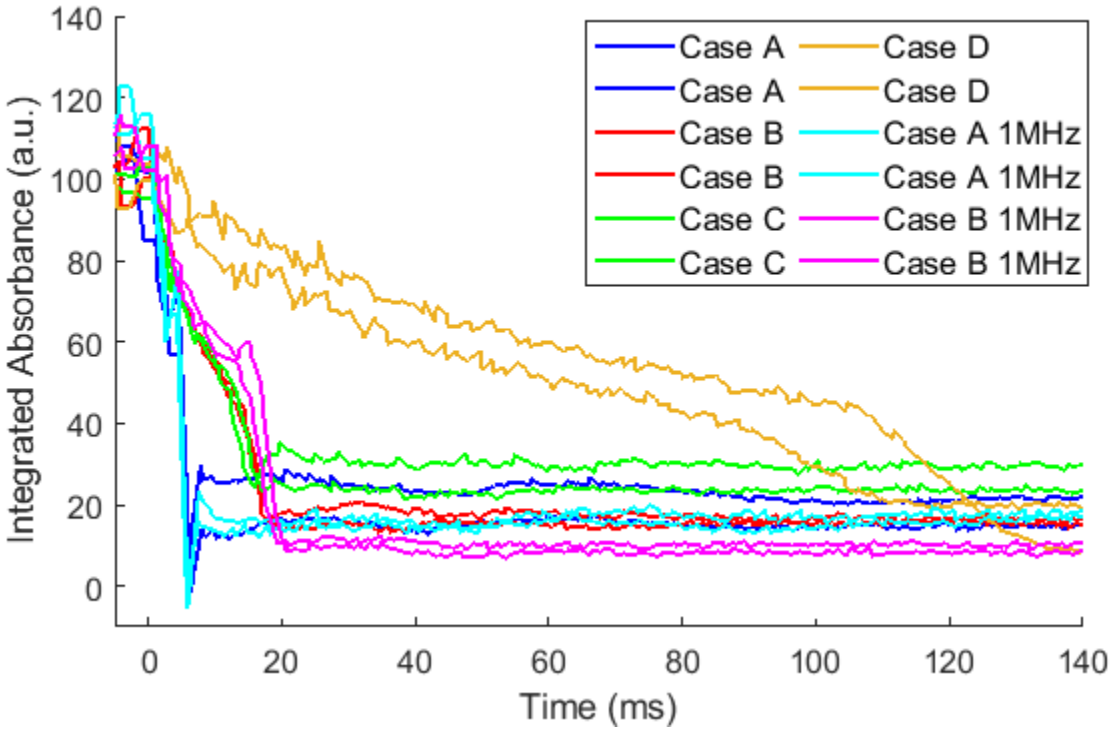

Figure 4.29 - Integrated absorbance of DIMP peak comparison

4.7. DIMP Decomposition Discussion

4.7.1. *DIMP Destruction Rate*

Each of the four cases tested produced a different decay rate in absorbance at the primary DIMP feature at 1000cm^{-1}. The trends generally follow expectations with the fastest decay coming from Case A, the hottest and most oxygen rich. Cases B and C demonstrated similar decay rates with Case C occurring slightly faster. This similarity was slightly unexpected, as Case B was hotter than Case C, suggesting that the additional oxygen in Case C was significant. Case D decayed over orders of magnitude greater time scales, likely a cause of slow flame speed resulting from proximity to flammability limit of the mixture.

Interestingly, all cases exhibited the same trend in absorbance decay: an initial slow decay followed by a sudden rapid decay. Such an identifiable and characteristic feature would be useful in simulation comparison.

4.7.2. *Product Features*

Beyond the destruction of DIMP signature, the collected spectra show complex features indicating the presence of product species. In this section, these features will be discussed qualitatively for a comparison of similarities and differences between different tests. This discussion is beneficial to determine how well the collected data constitutes a set of benchmark data by investigating whether different cases produced measurably different results.

850cm^{-1} – 1050cm^{-1} Region

All cases tested showed the formation of two features between 850cm^{-1} and 1050cm^{-1} occurring and changing on relatively slow timescales. These features are best observed in each case's Initial vs. Final absorbance plots (Figure 4.12, 4.16, 4.20, and 4.24) and color-mapped absorbance plots (Figure 4.15, 4.19, 4.23, and 4.27). Each case shows a different behavior in the long-term evolution of these features as well as their final shapes.

Always, the two features manifest as broad peaks, with the larger wavenumber feature location slightly shifted to higher wavenumber from the main DIMP feature. In general, this feature appears very soon after ignition and varies only slightly during the entire capture window, slowly growing in absorbance without changing shape.

The lower wavenumber feature shows much more variation from case to case. In Case A, this feature begins to appear later than the other. This feature grows in strength, reaching a maximum greater than the longer wavenumber peak around 500ms, before decaying through the end of the measurement time to a value lower than the other feature. Throughout, the peak location shifts from low wavenumber to high wavenumber.

In Case B, the lower wavenumber feature does not begin to appear until after 300ms. It grows in intensity, peaking around 700ms, before decaying as well, but it never becomes more intense than the higher wavenumber feature. Unlike for case A, the peak location does not shift, and remains closer to 900cm^{-1} throughout.

For Case C, this feature behaves very similarly as for Case A. It again rises and falls, peaking with greater intensity than the higher wavenumber feature, and it shifts toward higher wavenumber throughout. Case D is somewhat unique in that the feature increases in intensity until the very end

of the capture window, only appearing to decrease on the last plotted scan. As such, it is higher intensity than the higher wavenumber feature at the end of the measurement, and, like for Case B, the feature location does not shift.

Despite these features appearing and evolving over relatively long timescales, the case-to-case differences observed provide interesting variations that could prove useful in model validation. One interesting observation is that peak shifts occur only for Case A and C, the higher oxygen cases. This suggests an oxygen dependent reaction taking place.

1100cm^{-1} Region

Some cases produce a slight feature at 1100cm^{-1}. This can be seen in Case C and Case D final absorbance plots (Figure 4.20 and 4.24). The feature evolves during the measurement time visible in color mapped absorbance plots, typically becoming less prominent or even vanishing at late time.

1100cm^{-1} – 1250cm^{-1} Region

Most cases show a broad and short peak in the region between 1100 and 1250 wavenumber that occurs at late time, but the peak position and shape of this feature is variable.

1100cm^{-1} – 1350cm^{-1} Region

All cases have an early time feature that exists between 1100 and 1350 wavenumber. The formation of this feature can be seen in stacked absorption plots (Figure 4.14, 4.18, 4.22, and 4.26) beginning as a peak centered near 1220cm^{-1}. Through viewing time averaged version of this feature in the color mapped plots, the feature can be seen to have much finer structure than the other absorption features. Many peaks occur within the feature, but these all disappear by the end of the capture window.

Each case exhibits variation in the persistence of this feature. Case A, the most rapidly reacting case, has this feature exist for the shortest amount of time. Case C has it persist longer, followed by Case B, followed by Case D.

1325cm^{-1} Region

All cases have a peak feature that occurs at 1325 wavenumber. In most cases, intensity of this feature peaks midway through the capture window and has begun to decrease by the end. Despite this feature existing at the large wavenumber end of the range where flash signal correction error is greatest, flash error is not present at late time, so this late time measured feature can be trusted as real.

4.7.3. *Comparison to Known Products*

As discussed, there are a number of complicating factors that make quantitative determination of these products beyond the scope of this research. Furthermore, spectral overlap and the lack of high temperature reference spectra for many possible species makes the assignment of features to a chemical species difficult. As such, even definitive assignments of features to chemical species are not a goal of this research, but spectral features can be compared to available references to provide possible candidates. Reference absorption spectra for expected decomposition products were provided earlier in Figure 1.6. An important distinction to note is that these reference spectra are for species at room temperature and observed spectra are at much higher temperature. Temperature dependence of these spectra is certainly significant but has generally not been well characterized.

The primary absorption feature of DIMP is a result of the molecule's P-O-C bond stretching, and the persistence of an absorption in this region suggests the presence of a molecule with the same bond. Likely candidates are the phosphorus containing decomposition products of DIMP, IMP or MPA, or unreacted DIMP. These spectra lack the characteristic shoulder seen in DIMP, suggesting that the absorption near 1000cm^{-1} is caused by one of or possibly both of the other two, and based on NIST reference spectra, MPA would be expected to have another absorption feature of similar strength at 956cm^{-1}. At early time such a feature is not recognizable, suggesting IMP as the more likely candidate. IMP formation is further supported by the peak near 1220 cm^{-1} at early time. The growth of this feature along with the simultaneous presence of the triple peak feature between 1100cm^{-1} and 1200cm^{-1} shared by DIMP and IMP suggests the conversion of DIMP into IMP. Additionally, the observed feature near 1220 cm^{-1} that appeared in some initial DIMP spectra in Figure 4.3 could also be a result of IMP production.

Propene and ethylene are both hydrocarbon decomposition products theorized to be indicative of DIMP destruction through pyrolysis. Both of these species exhibit absorbance only on the lower wavenumber end of the measurement range, in the vicinity of the lowest wavenumber feature discussed. It is possible that this measured feature is due to these species. While propene has a sharp feature at 911cm^{-1} and ethylene has one at 948cm^{-1}, both features would be broadened considerably by the 10cm^{-1} resolution of the scanning spectrometer.

For Case B, the lowest wavenumber feature is centered around 910cm^{-1}, strongly suggesting that it is caused by propene as no other available reference spectra show considerable absorption at that location. In the other test cases the lowest wavenumber feature shifts position from lower wavenumber to higher wavenumber throughout the measurement window. This shift could be caused by the decomposition of propene into ethylene, gradually changing the relative contributions of both to the combined absorbance feature.

Acetone and isopropyl alcohol were two hydrocarbon species assumed to indicate radical destruction of DIMP. IPA reference spectra have four broad absorption peaks all with comparable strengths. This absorption pattern is not readily apparent in any recorded spectra, suggesting that IPA either does not form or does not accumulate in any significant amount. Acetone absorbance is expected to occur primarily at a broad feature centered at 1215cm^{-1} and from an equally strong feature that is cut off on the large wavenumber edge of the measurement window. Considering this signature, acetone is a potential contributor to the early time absorbance feature observed around 1220cm^{-1}. Here, the lack of a measured signal corresponding to the cut off acetone feature is likely caused by the error in flash signal correction which makes the large wavenumber measurements unreliable at early time.

Importantly, the product species listed here do not account for all the absorption features measured. These features, primarily the early time absorbance in the 1100cm^{-1} to 1350cm^{-1} region and the absorbance in the 1325cm^{-1} region remain from unidentified sources. Further investigation of these spectra will be necessary to determine the species responsible for these features.

4.8. Temperature Data

Each OH temperature test performed produced 99 time-resolved frames of data. Figure 4.30 shows what a single frame of this data would typically look like. As shown in the figure these spectra are highly resolved and have good signal to noise. To present the large quantity of data collected from the 24 temperature tests in a manner conducive to judging repeatability, the metric of integrated absorbance is again used. However, in this case, absorbance is integrated across the entire wavelength range from 304nm to 320nm.

Figure 4.2 presented earlier provided the integrated absorbance for all cases without the addition of DIMP vapor, and these showed exceptional repeatability. Figure 4.31 - Figure 4.33 provide the integrated absorbance for each case with the addition of DIMP, but these figures are also provided with the pressure measurement of each shot.

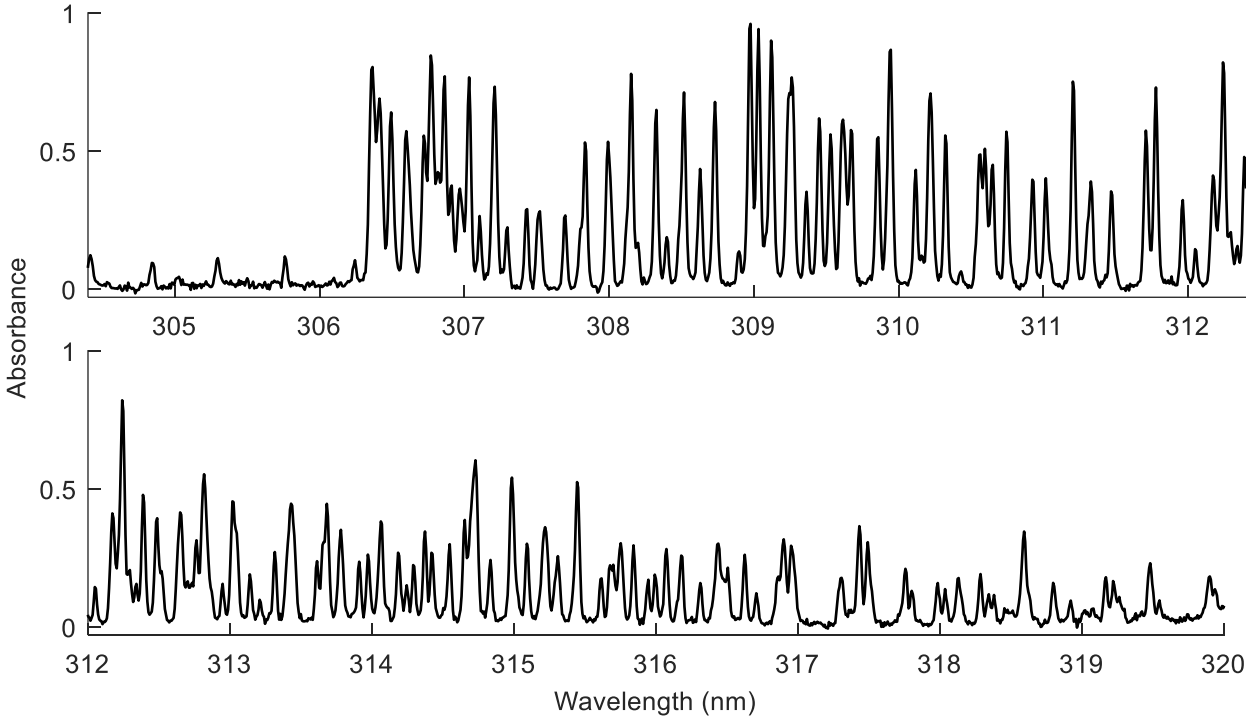

Figure 4.30 - Measured OH absorption spectrum, single frame

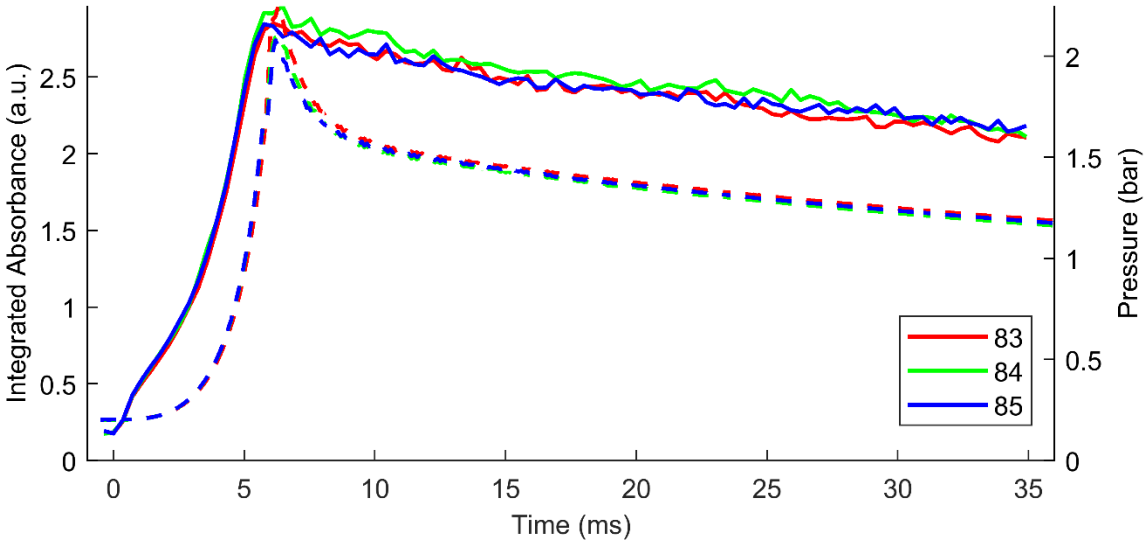

Figure 4.31 - Integrated OH absorbance (solid lines) and pressure (dashed) for Case A

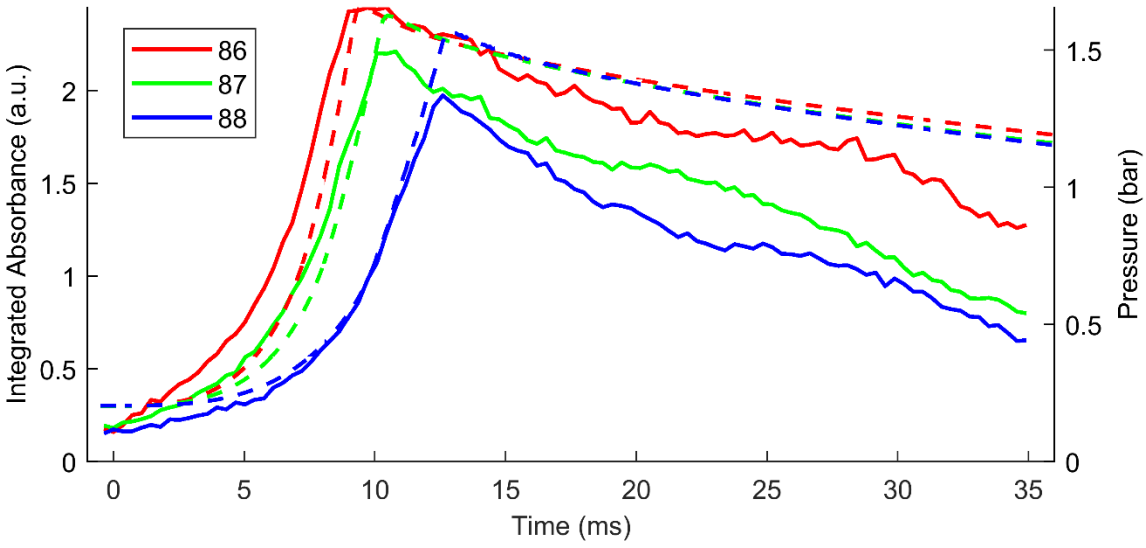

Figure 4.32 - Integrated OH absorbance (solid lines) and pressure (dashed) for Case B

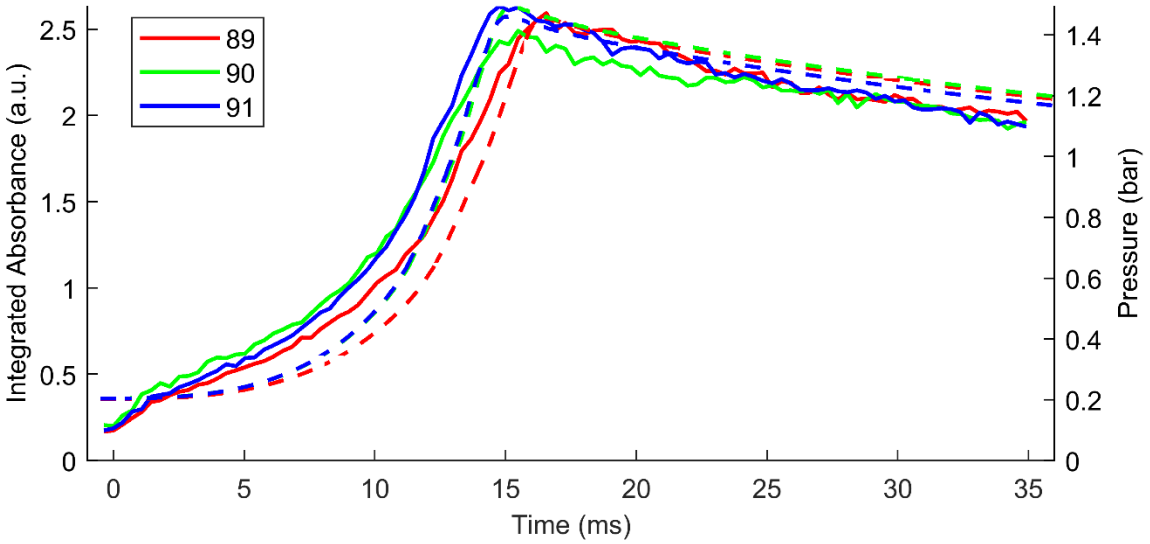

Figure 4.33 - Integrated OH absorbance (solid lines) and pressure (dashed) for Case C

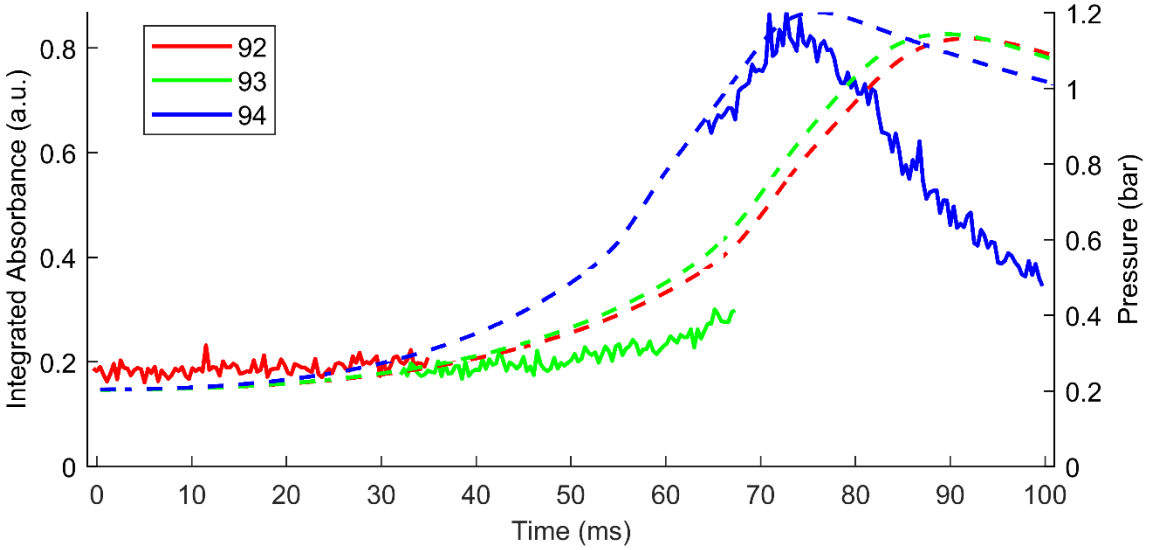

Figure 4.34 - Integrated OH absorbance (solid lines) and pressure (dashed) for Case D

Repeatability of the tests with DIMP was expectedly less than for the cases without. Much of this variability can be explained from the already established variability in DIMP concentration, but some contribution is likely from a small leak that formed in the gas manifold during these final shots. The leak would have added some uncertainty in the actual gas fill concentrations.

Both high oxygen content cases exhibited very good repeatability with Case A measurements overlapping almost perfectly. Additionally, none of the Case C measurements indicate side wall ignition. Case B measurements did not agree as well, however, both in terms of integrated absorbance and burn pressure. Finally, Case D measurements resulted in only one good test. The first run showed almost no OH signal until the final few frames. As it was understood that this Case reacted slower, the frame timing was delayed for the second shot. Again, very little signal was seen until the end, so timing was pushed back once again. The last shot captured an unexpectedly large amount of OH signal. Comparing the integrated absorbance and pressure traces indicates that the first two tests were likely side wall ignited, explaining the lack of OH signal immediately after ignition. Fortunately, the final shot does capture the peak in OH signal, which should be useful for determining temperature in this case.

As with the OH measurement without DIMP, each case produces a distinctively different OH integrated absorbance profile. While this is likely not a good metric for comparison to simulation, it does indicate that simulated OH spectra from each case should be distinguishable.

4.8.1. *Comparison to Simulation*

Computational models of the spherical combustion chamber have been completed for cases without the addition of DIMP. However, the model output for OH does not produce expected OH absorption spectra. Instead, it produces spatial and temporal data for OH concentration, local temperature, and chamber pressure. From this information, absorbance of the predicted OH profiles can be determined using the equations presented in Chapter 1.

As demonstrated in Figure 4.35, the localized spectral absorption coefficient k can be determined for each spatial cell of simulated data. The light transmitted from the first cell to the next will depend on the absorption coefficient and the length of the first cell. This transmitted light exiting the first cell then becomes the input light of the second cell, and so on. Using this reasoning, the final transmittance becomes the product of the exponential e^{kl} for all cells along the simulated

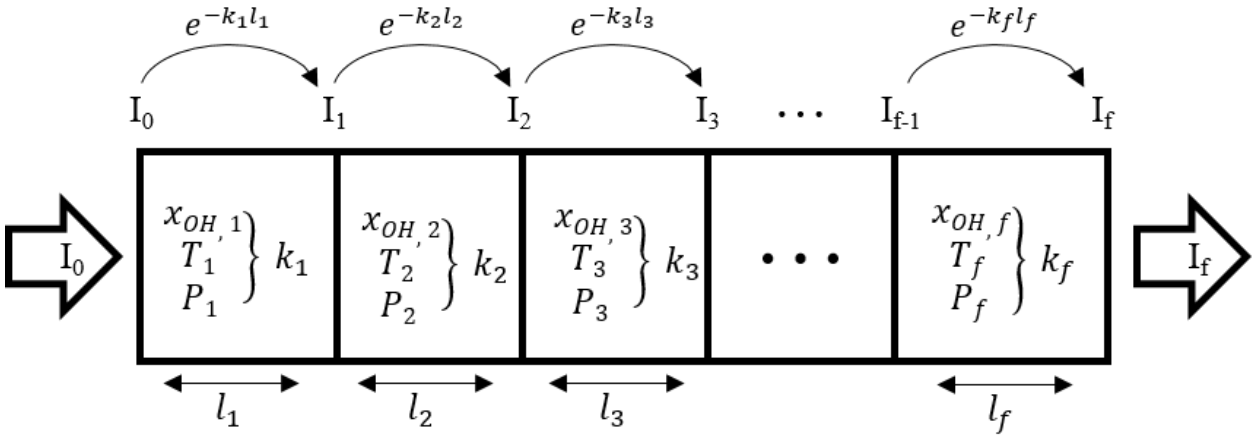

Figure 4.35 - Determining predicted absorbance from spatial concentration and temperature data

volume, and the final absorbance becomes the summation of all kl terms as shown in the equations. In the event of a highly non-uniform temperature distribution, simulating spectra in this way accurately captures temperature variations.

$$\frac{I_f}{I_0} = (e^{-k_1 l_1}) * (e^{-k_2 l_2}) * (e^{-k_3 l_3}) * \ldots * (e^{-k_f l_f}) \tag{18}$$

$$Absorbance = k_1 l_1 + k_2 l_2 + k_3 l_3 + \cdots + k_f l_f \tag{19}$$

Preliminary data comparison to simulated spectra obtained in the described manner is provided in Figure 4.36. The shown comparison used data obtained from Case D measurements without DIMP at 30ms after ignition. Three simulated spectra are provided. The first used the temperature, pressure, and concentration profiles as they were predicted from the model. The other two used the pressure and concentration profiles as they were predicted but with the temperature profiles either increased or decreased by a flat 200K.

In general, the magnitude of predicted absorbance features agrees well with the measured results, indicating that predicted OH concentrations are accurate. However, as visible in the figure, larger absorbing features are largely insensitive to the temperature changes imposed. Temperature sensitivity is instead found in some of the weaker absorbing features, requiring that temperature comparisons be made in narrower wavelength regions containing these temperature sensitive features. Figure 4.36 shows one of these temperature sensitive regions. In the region shown, simulation from the unchanged temperature profile does appear to match better than the

simulations from the altered temperature profiles. This agreement suggests that the simulated temperature profile is more accurate, at least in this specific region. However, additional investigation into which specific wavelength regions provide the best temperature comparison will be needed in the future.

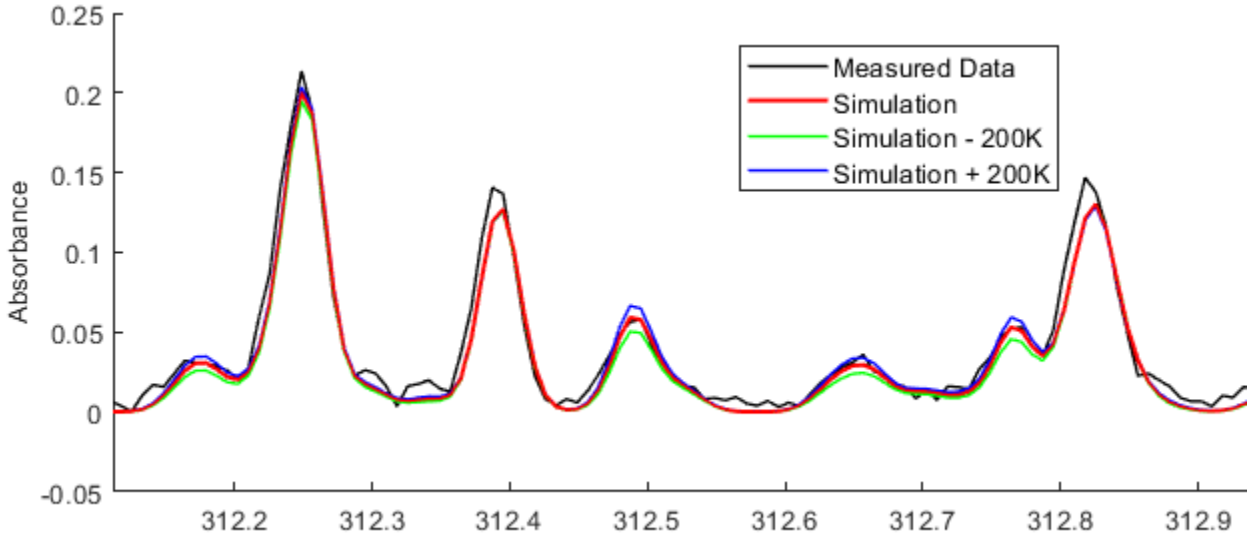

Figure 4.36 - Comparison of measured OH absorbance spectrum with simulated spectra obtained from model predicted profiles

4.9. Explosive Chamber Results

The final data set to review is from the explosive test chamber. These results are presented in the same manner as the combustion chamber LWIR absorbance data, except without zoomed-in views of the stacked absorbance plots. All stacked absorbance plots represent consecutive scans.

4.9.1. *Test 1 – 267mg PETN in Air*

Test 1 resulted in very fast, full decomposition of DIMP signal. After the initial decomposition from detonation, a structured product spectrum forms that appears to ride on an ever-increasing flat absorbance baseline, likely due to scattered light loss. The product spectrum shows clear features at 935cm^{-1} and 1100cm^{-1} and several features at higher wavenumber. Additionally, initial decomposition shows the primary DIMP feature shift slightly to lower wavenumber.

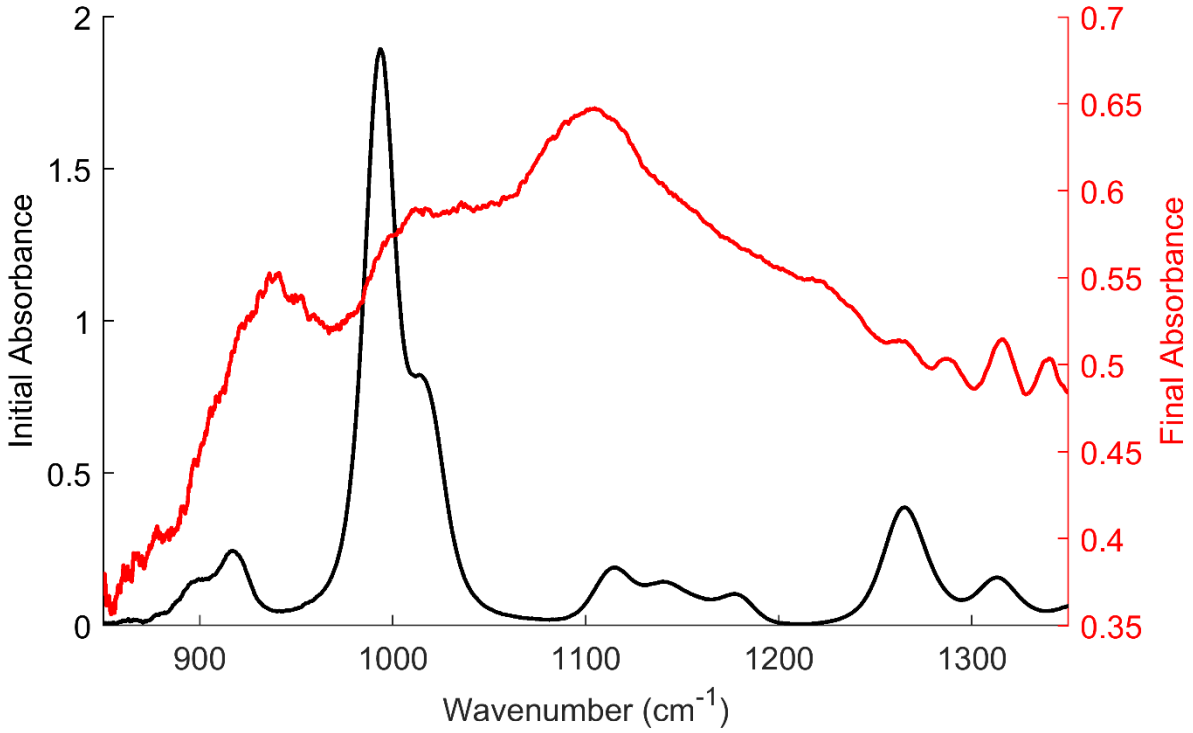

Figure 4.37 – Explosive Test 1 Initial vs. Final Absorbance

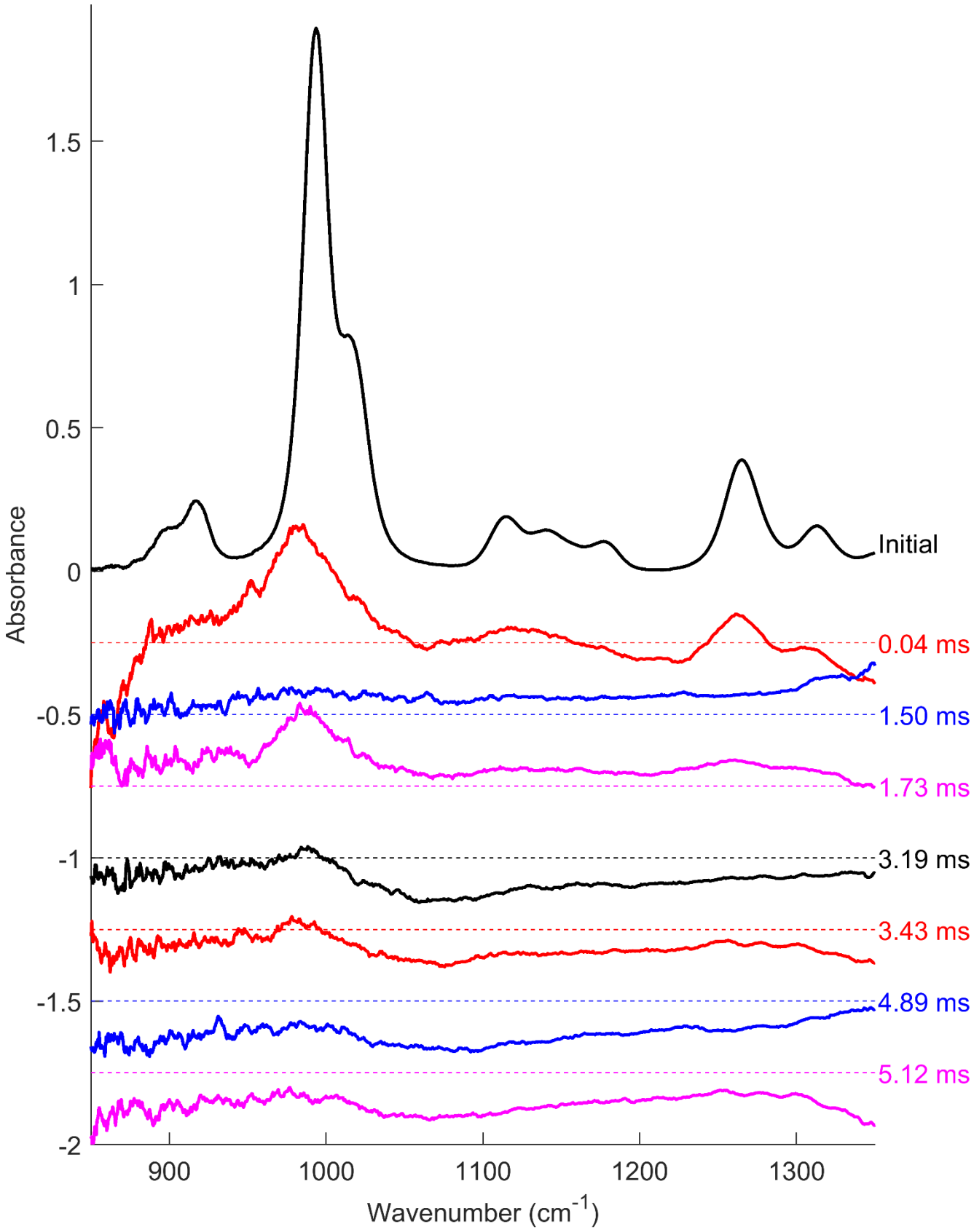

Figure 4.38 - Explosive Test 1 stacked absorbance plot

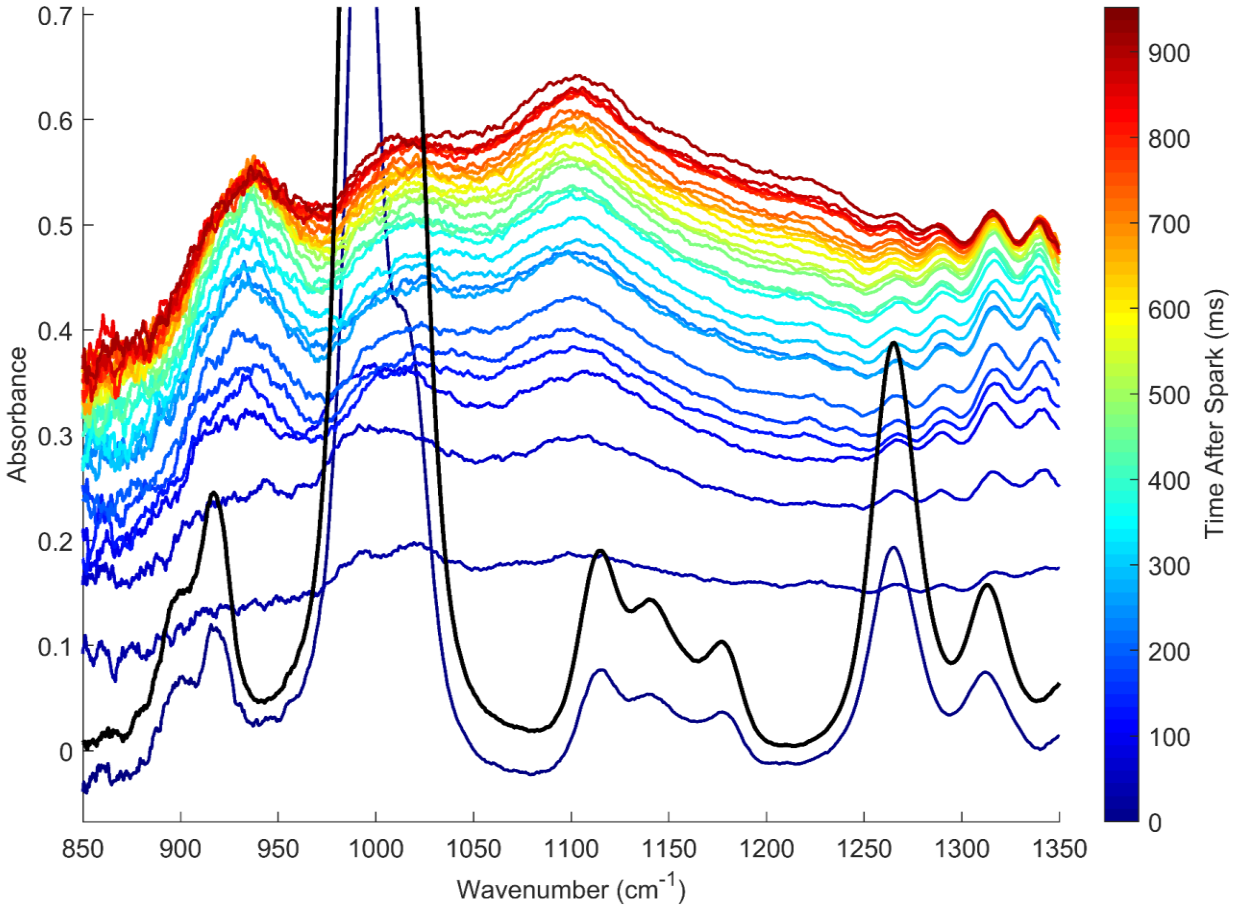

Figure 4.39 – Explosive Test 1 Color Mapped Absorbance

4.9.2. *Test 2 – 203mg PETN in Air*

Test 2 had an issue with the measured I_0 signal, resulting in a poor absorbance calculation especially at low wavenumber. Still, the absorbance spectra show the initial complete removal of DIMP signal within the first few milliseconds and the short-lived formation of a wide spectral feature around 1115cm^{-1}. However, as the chamber conditions settle, a clear DIMP signal returns with a few other absorption features. Additional features include the peak at 1100cm^{-1}, a bump around 1210cm^{-1}, and a peak at 1340cm^{-1}. Again, initial DIMP decomposition sees the main DIMP feature shift to low wavenumber.

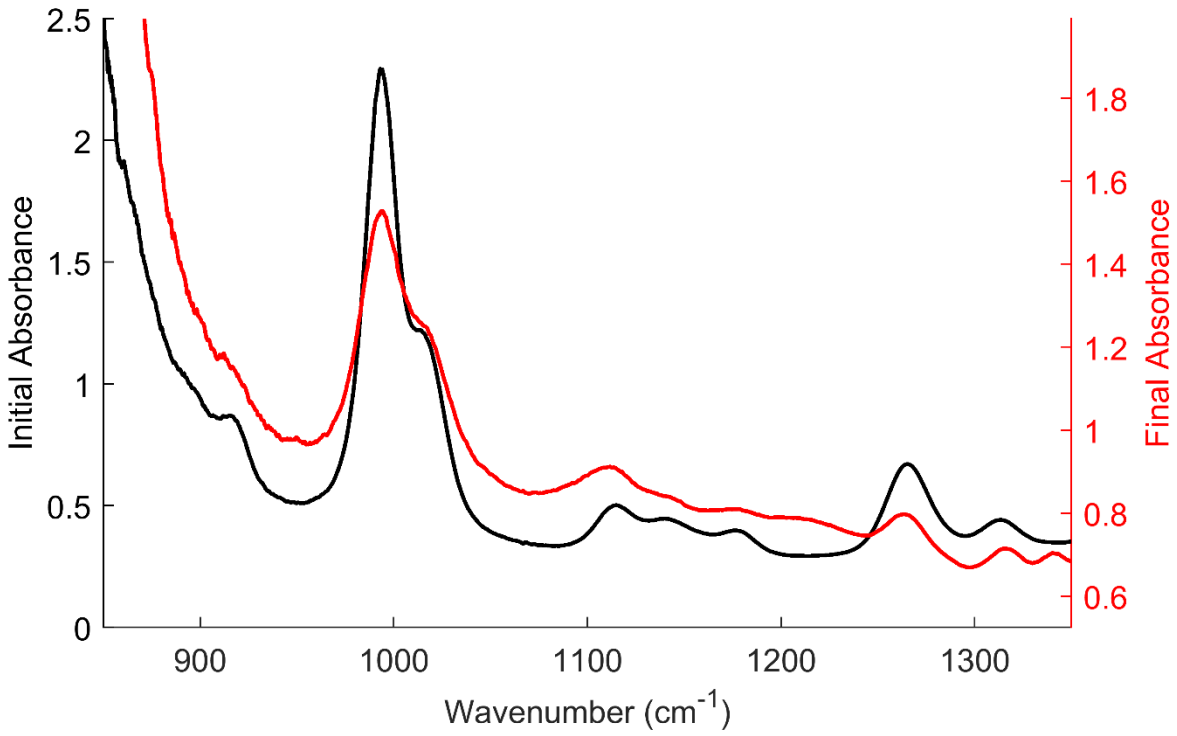

Figure 4.40 – Explosive Test 2 Initial vs. Final Absorbance

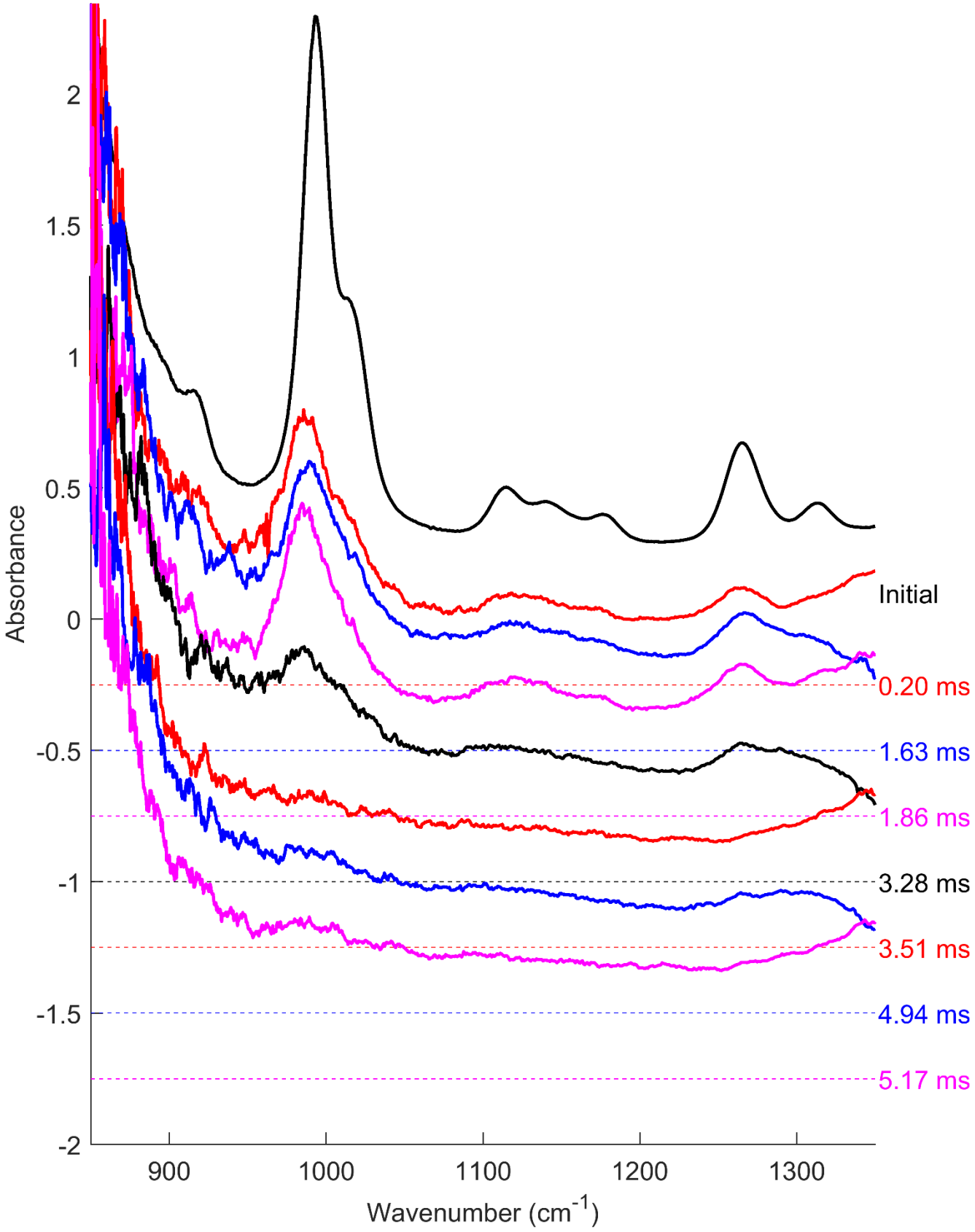

Figure 4.41 - Explosive Test 2 stacked absorbance plot

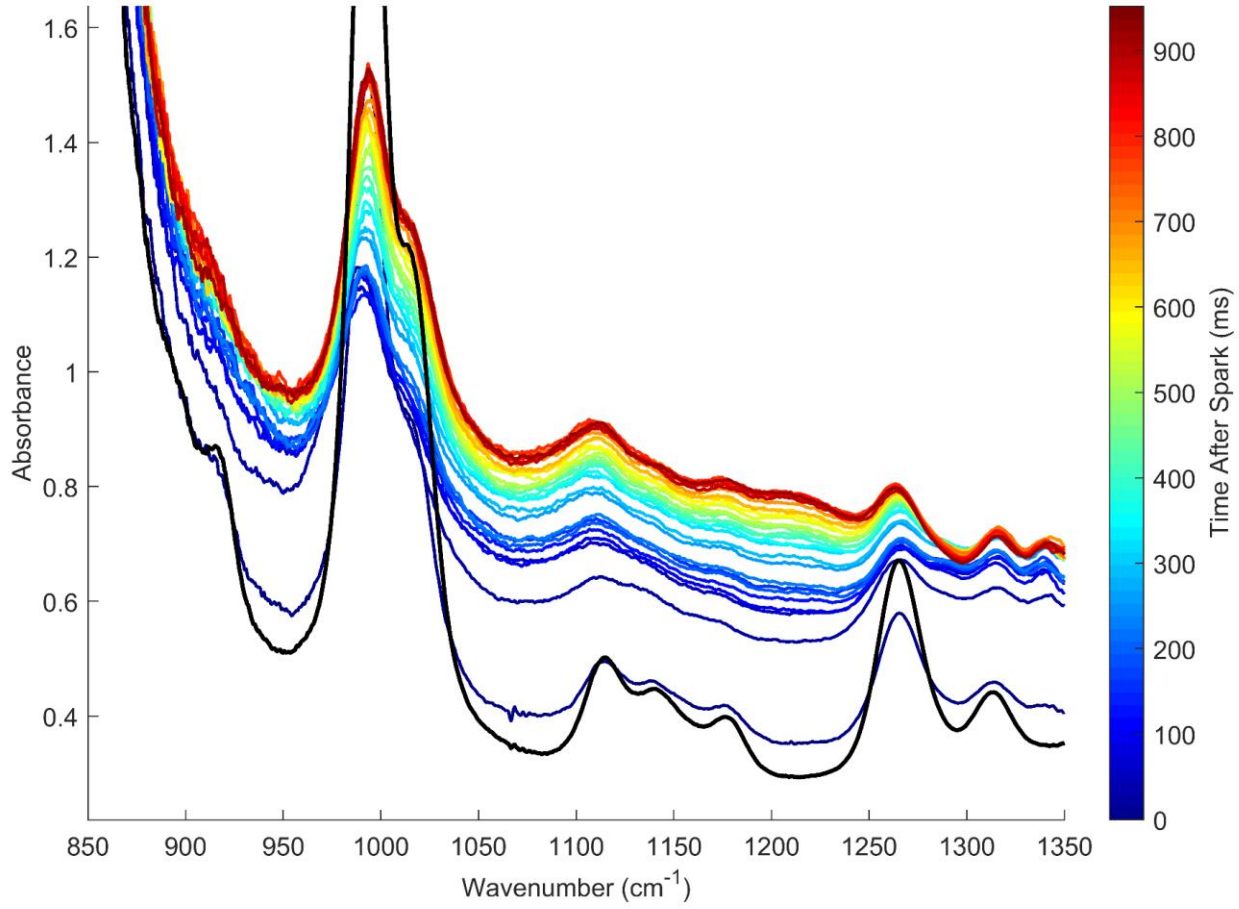

Figure 4.42 – Explosive Test 2 Color Mapped Absorbance

4.9.3. *Test 3 – 141mg PETN in Air*

Test 3 had a very low charge mass that saw incomplete DIMP decomposition. Unlike the previous tests, at no point did the DIMP signal entirely disappear. Final absorbance suggests that, after the chamber had settled, DIMP concentration had been reduced by half. The only clearly identifiable product feature that appears is the 1340cm^{-1} feature at late time and the wide absorbance feature around 1115cm^{-1}.

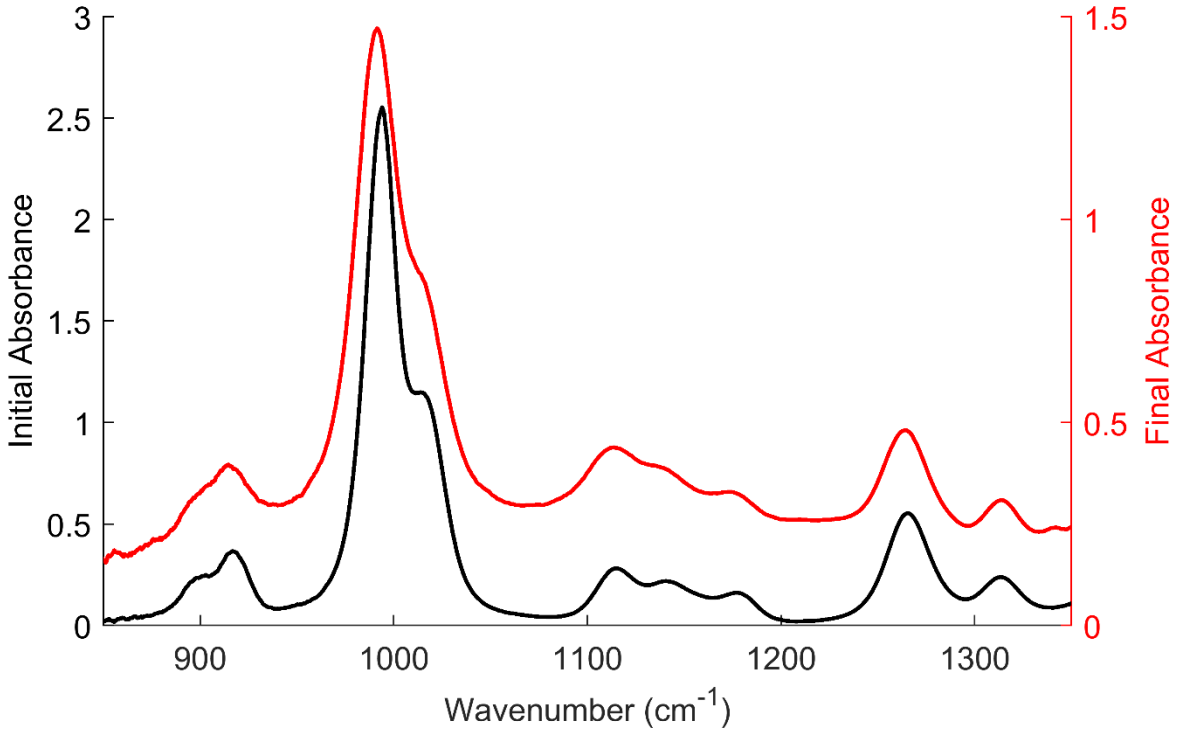

Figure 4.43 – Explosive Test 3 Initial vs. Final Absorbance

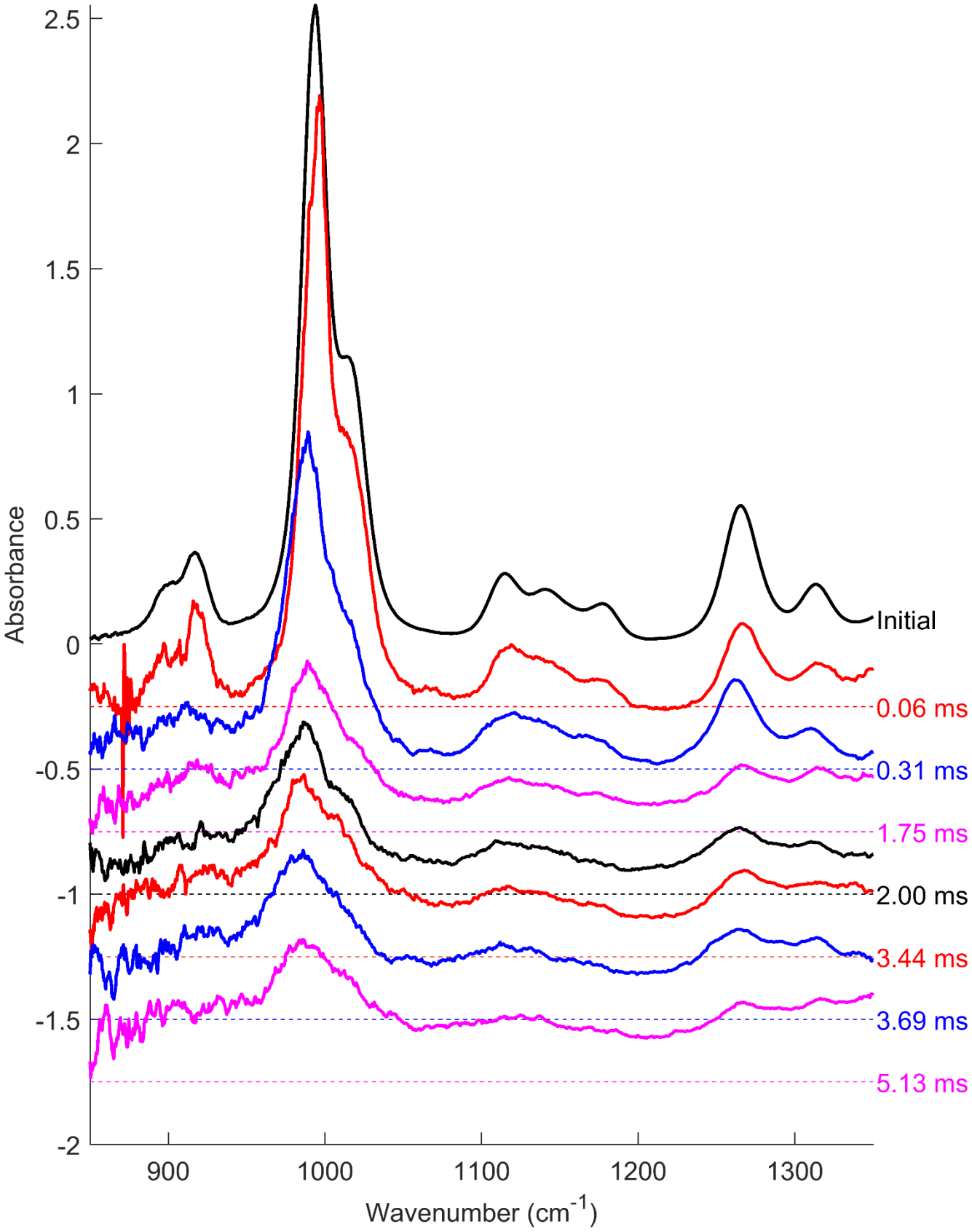

Figure 4.44 - Explosive Test 3 stacked absorbance plot

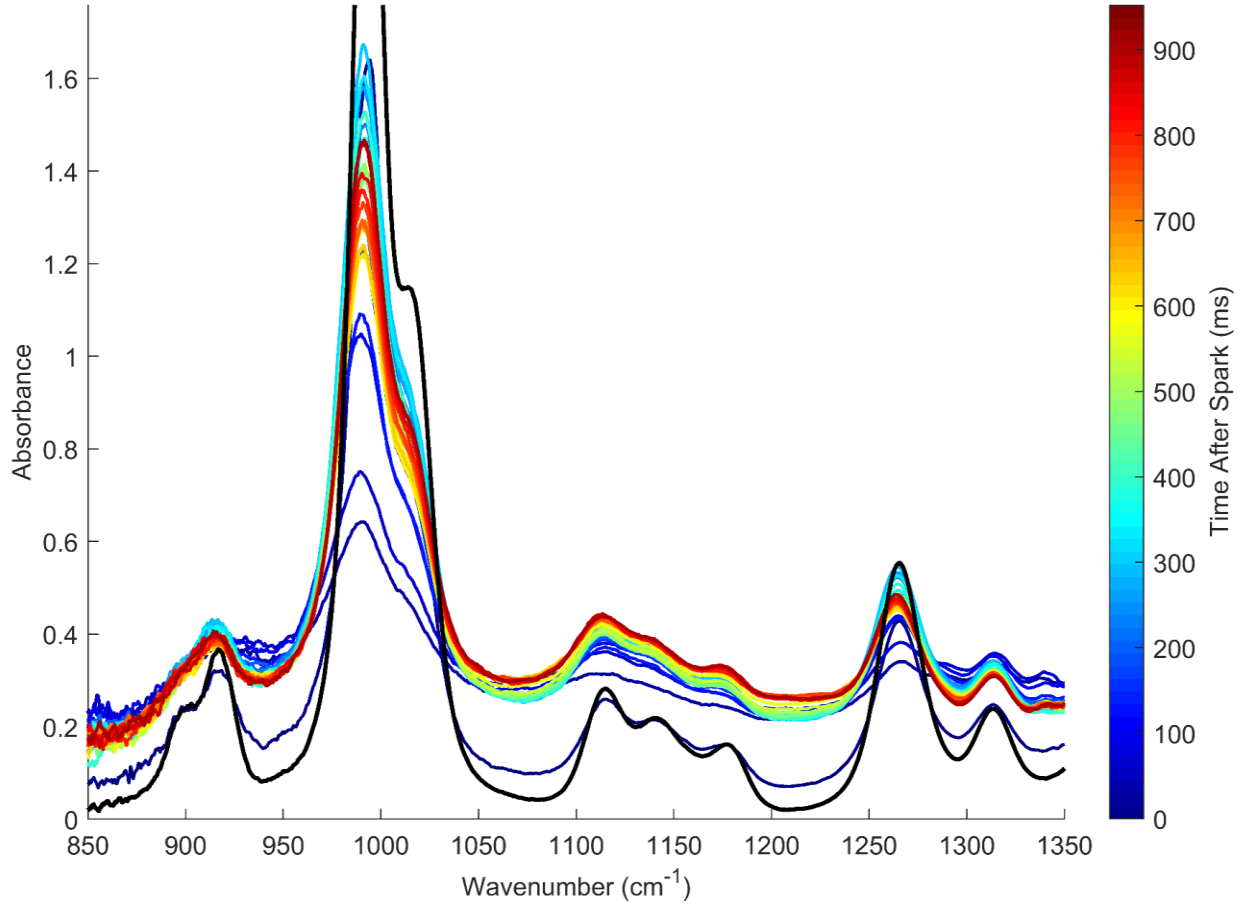

Figure 4.45 – Explosive Test 3 Color Mapped Absorbance

4.9.4. *Test 4 – 250mg PETN in N_2*

Test 4 resulted much the same as Test 3 despite the increase in charge mass, suggesting again the importance of oxygen to the decomposition reaction. Here, DIMP signal never fully disappears, and final absorbance suggests less than half of the DIMP had been destroyed. No clear product features are observed at late time, although the absorbance near 915cm^{-1} broadened. During initial decomposition, the wide absorbance feature can be observed slightly shifted to lower wavenumber around 1100cm^{-1}.

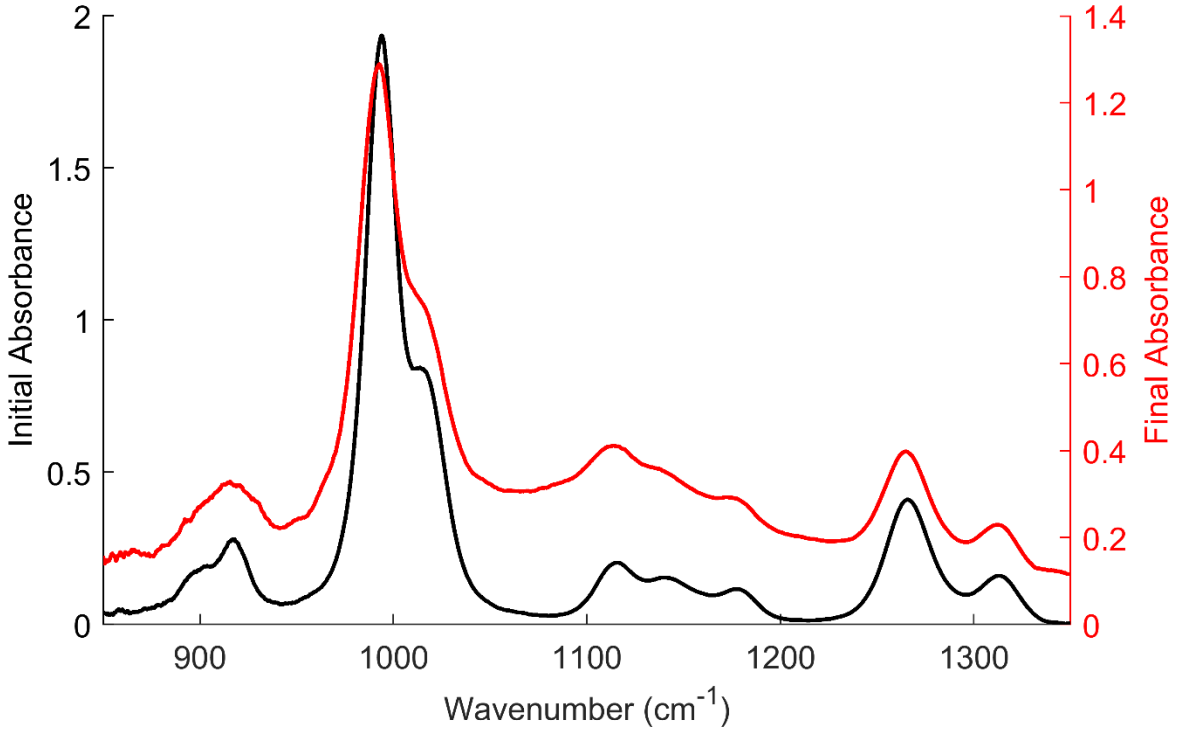

Figure 4.46 – Explosive Test 4 Initial vs. Final Absorbance

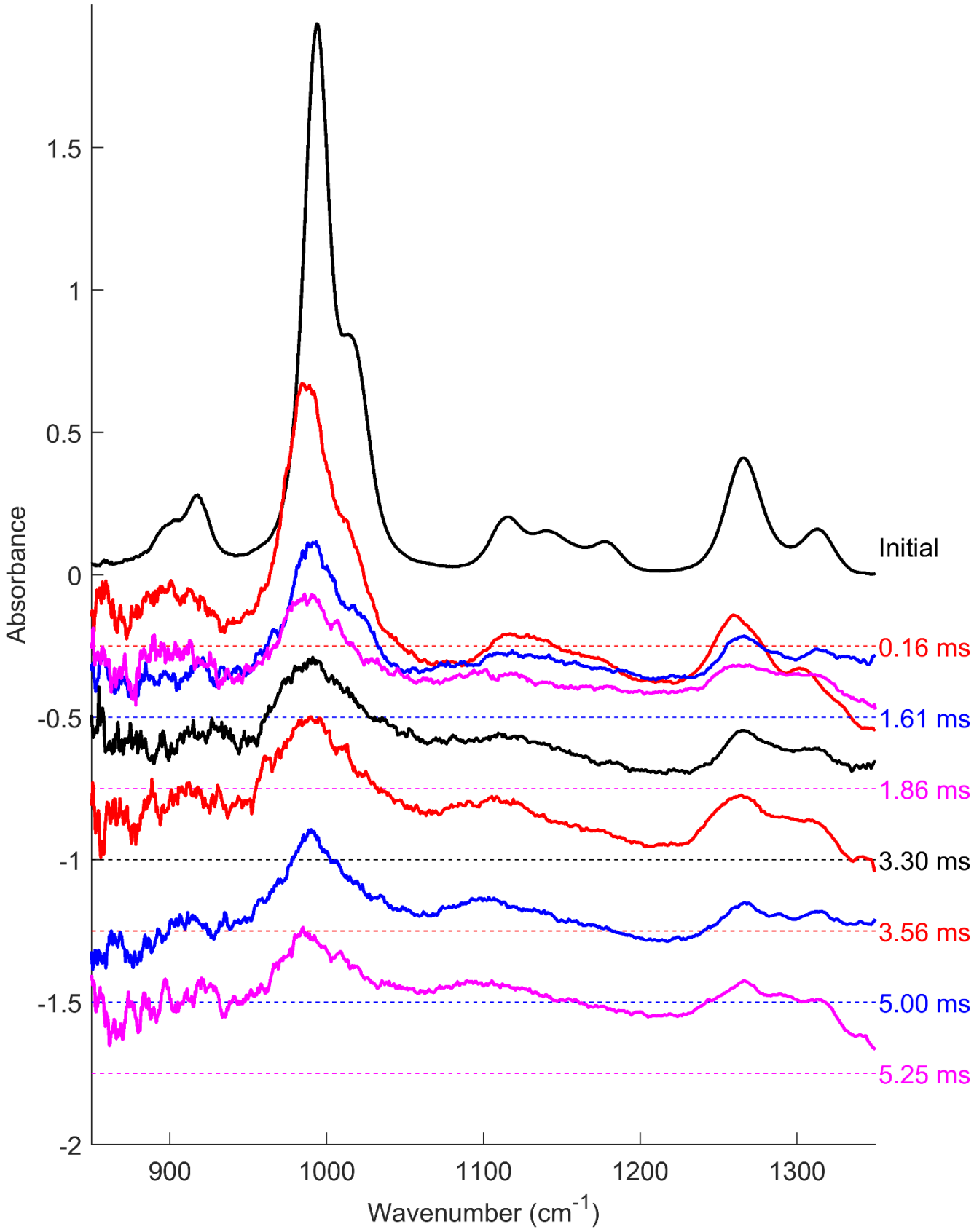

Figure 4.47 - Explosive Test 4 stacked absorbance plot

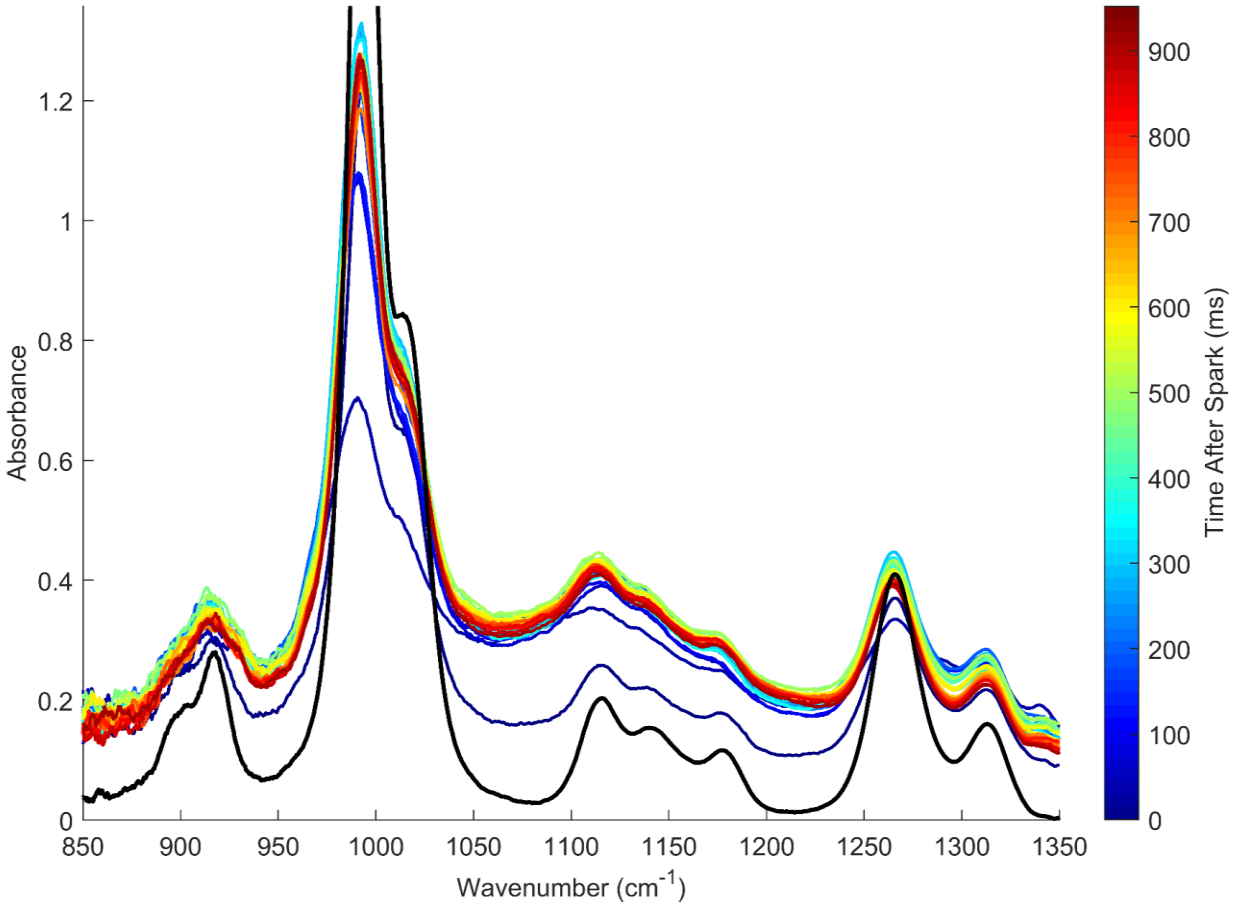

Figure 4.48 – Explosive Test 4 Color Mapped Absorbance

4.9.5. *Test 5 – 442mg PETN in N_2*

Despite the increased charge mass, Test 5 saw incomplete DIMP decomposition as well. However, this case does show the emergence of a potential product feature at 1115cm^{-1}, a slight bump at 1220cm^{-1}, and a sharpening of the peak at 915cm^{-1},

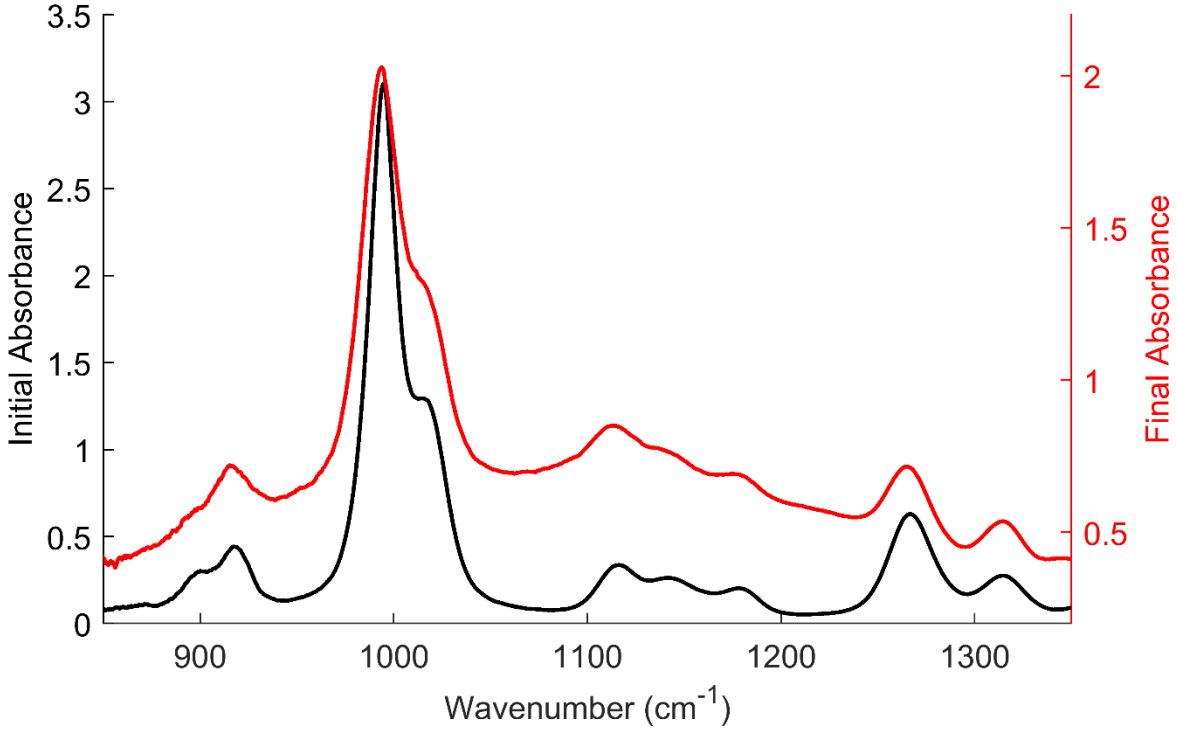

Figure 4.49 – Explosive Test 5 Initial vs. Final Absorbance

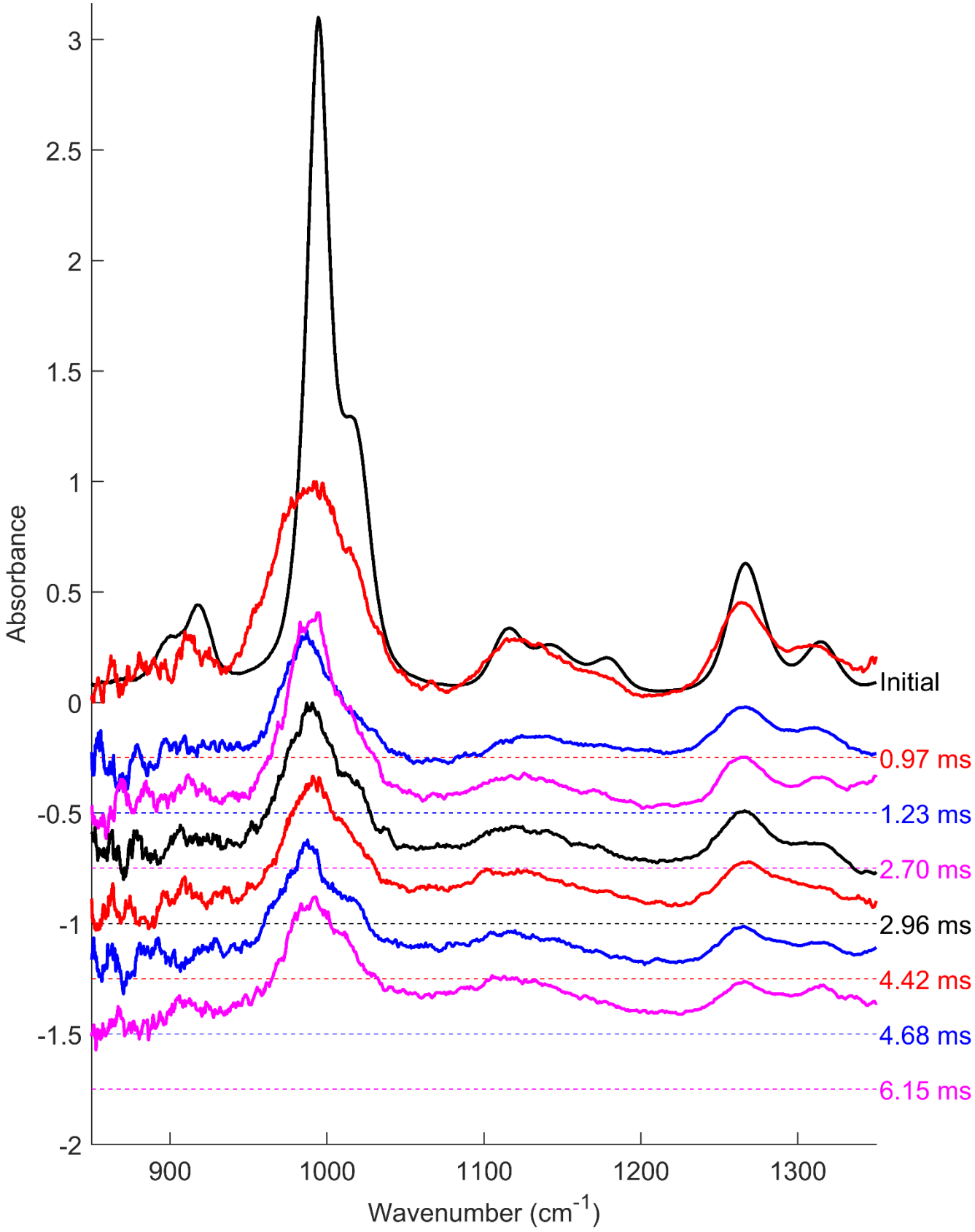

Figure 4.50 - Explosive Test 5 stacked absorbance plot

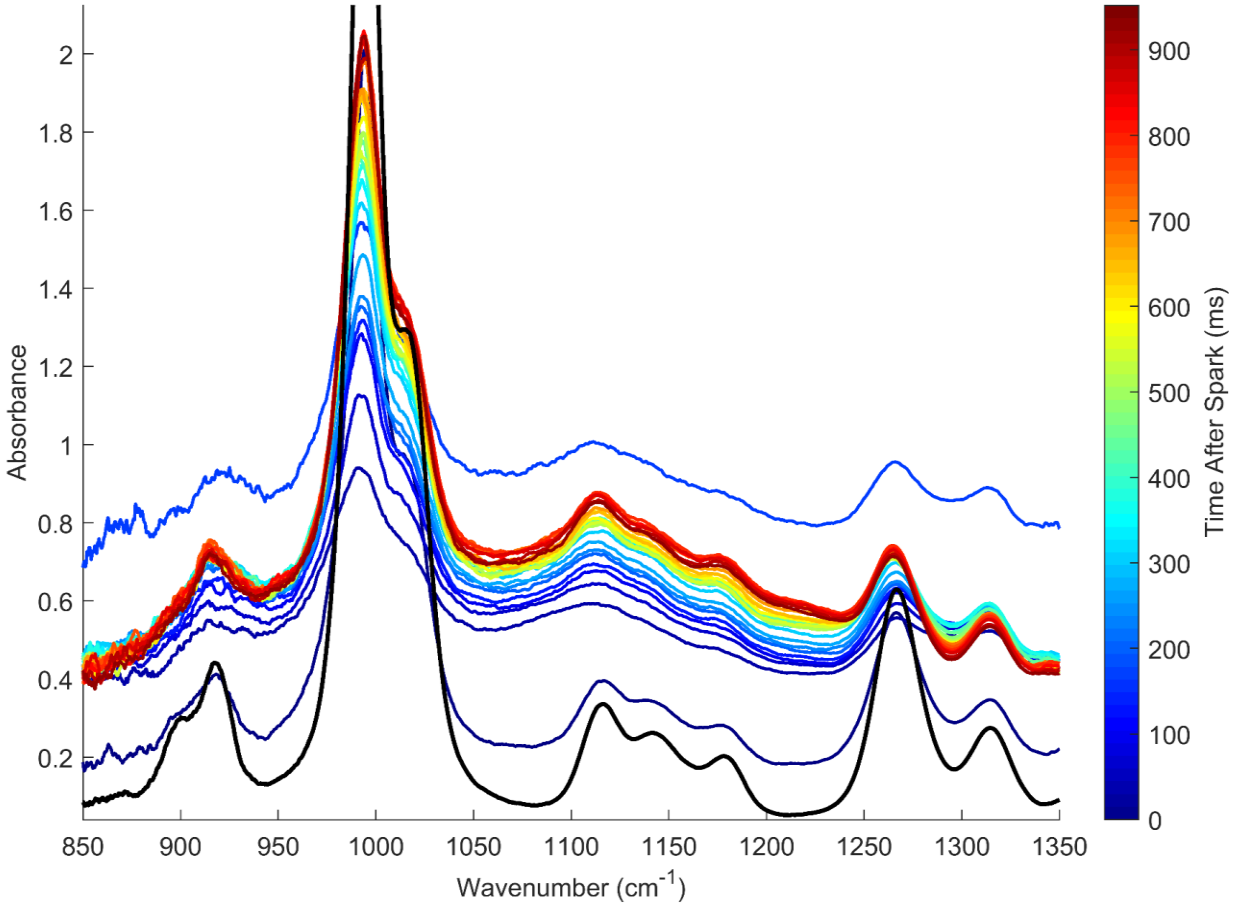

Figure 4.51 – Explosive Test 5 Color Mapped Absorbance

4.9.6. *Test 6 – 736mg PETN in N_2*

Test 6 did result in what appears to be initial complete DIMP destruction, although final absorbance suggests that a small amount remained after the chamber settled. This case showed very interesting product features including a sharp peak at 915cm^{-1}, some structured absorbance around 945cm^{-1}, broader and flatter absorbance between 1075cm^{-1} and 1250cm^{-1}, a peak at 1315cm^{-1} too large to be DIMP, and a peak at 1340cm^{-1}. Additionally, the feature around the primary DIMP feature flattened out greatly.

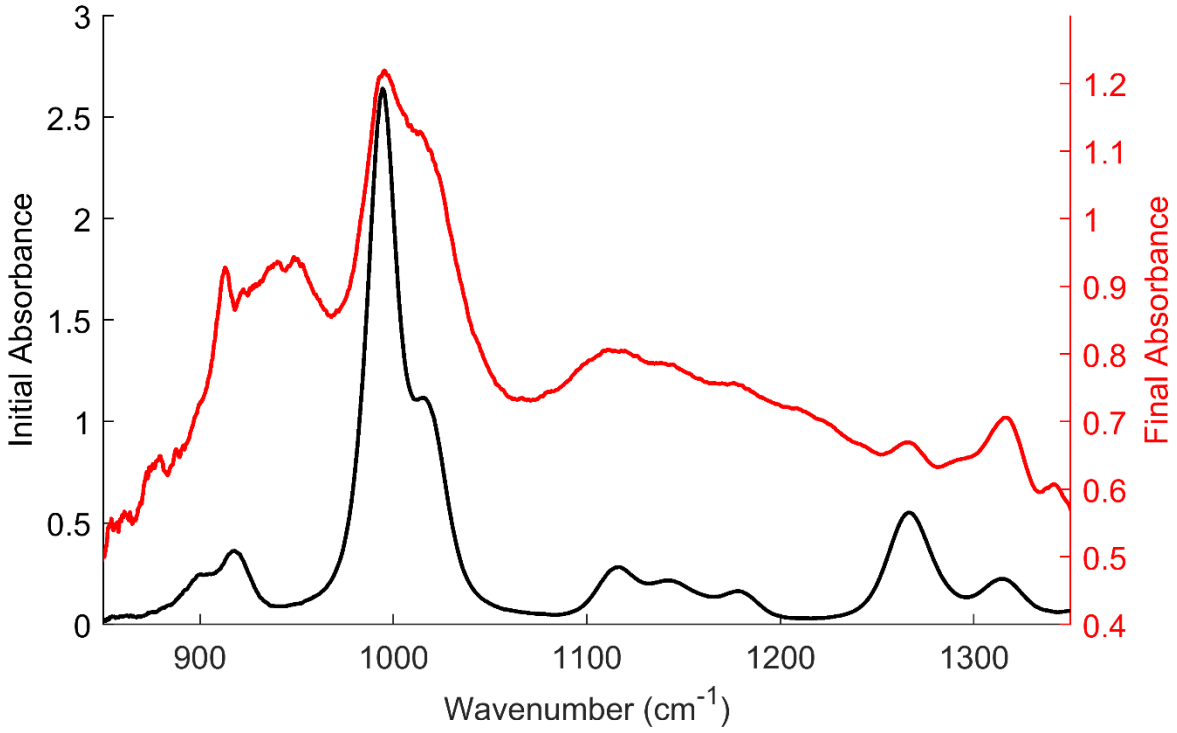

Figure 4.52 – Explosive Test 6 Initial vs. Final Absorbance

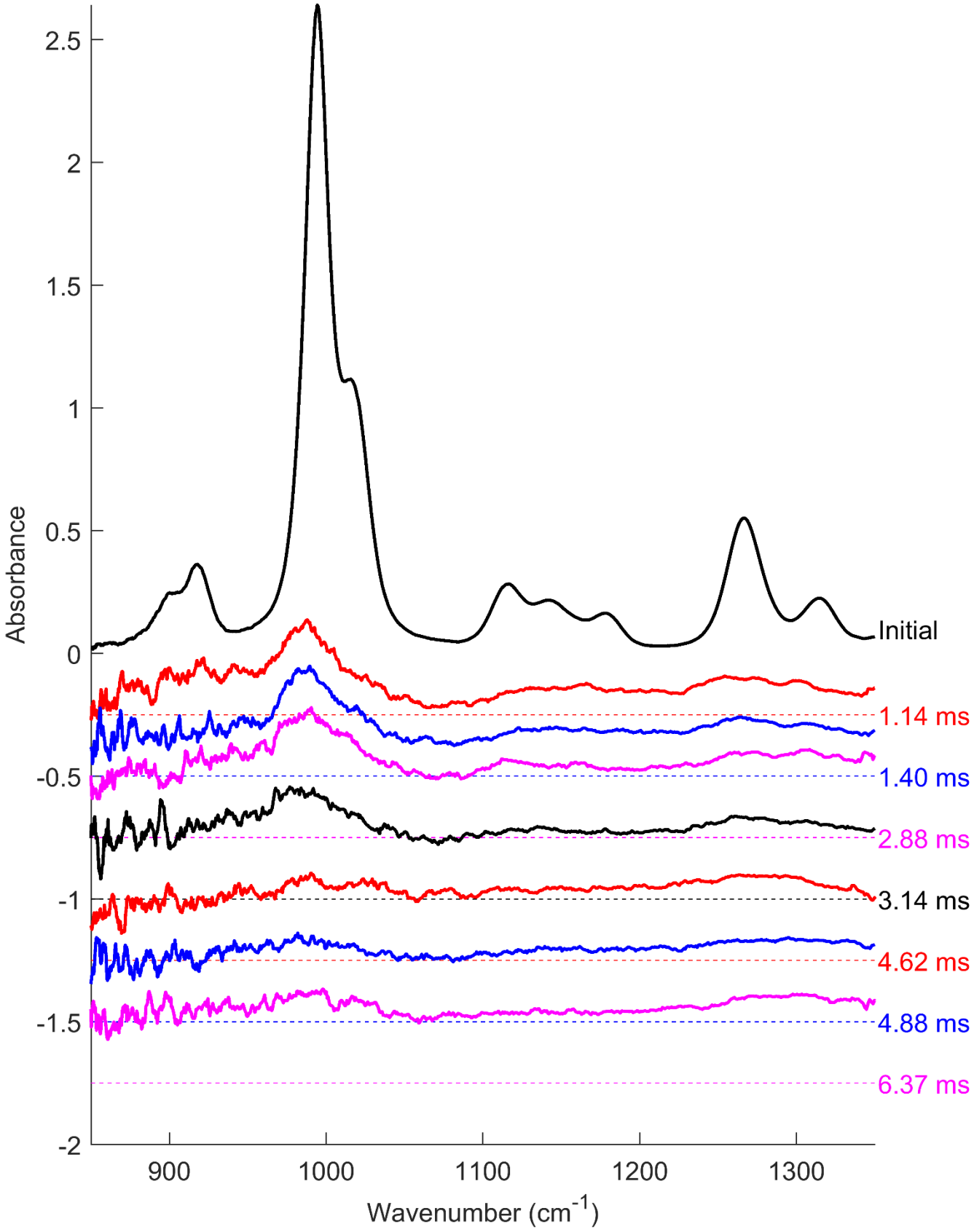

Figure 4.53 - Explosive Test 6 stacked absorbance plot

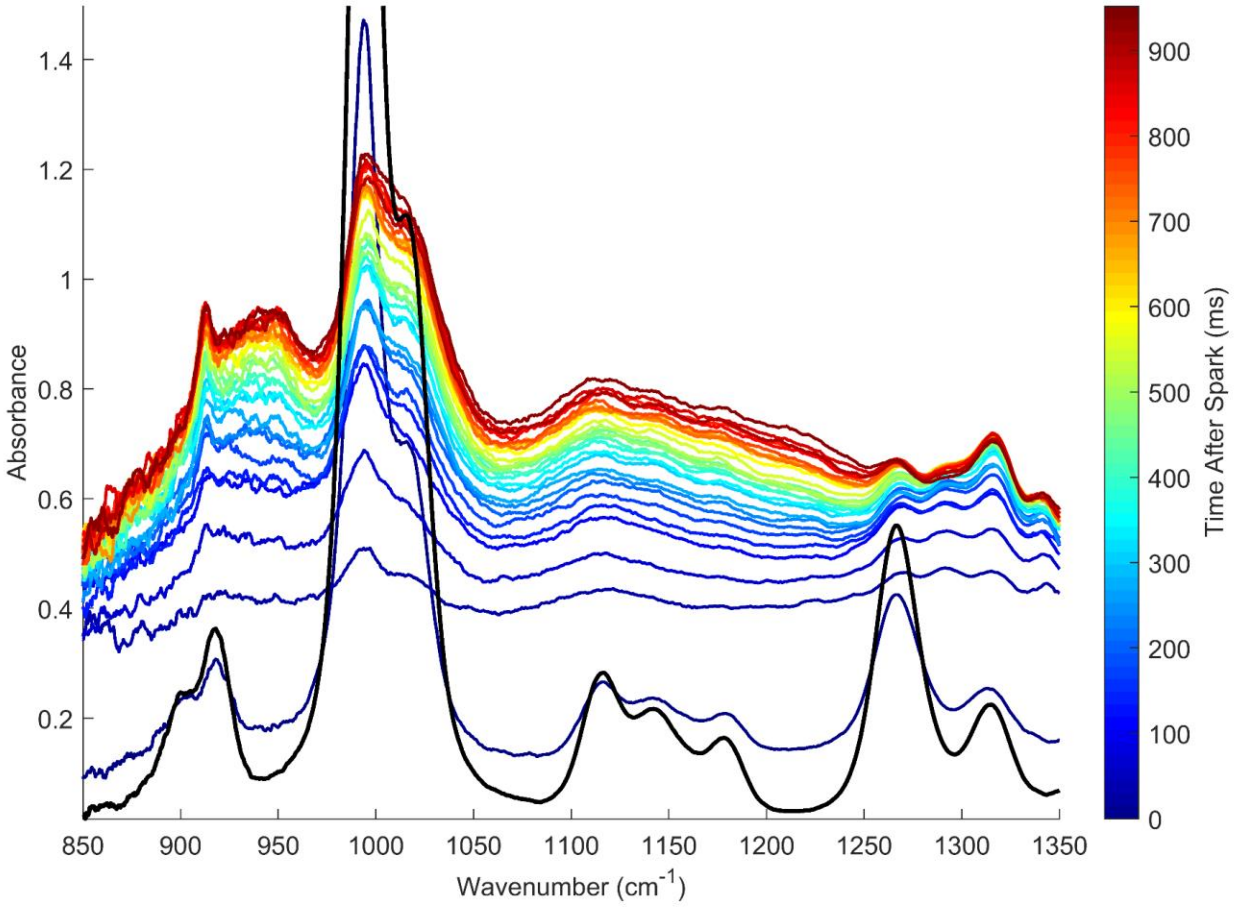

Figure 4.54 – Explosive Test 6 Color Mapped Absorbance

4.9.7. *Explosive Tests Discussion*

The six explosive decomposition experiments provide an interesting glimpse into the conditions one might expect to witness in future explosive fireball experiments. Even though the six experiments performed represent a small portion of the experimental parameter space, a great deal of variation in the product spectra was observed. One key observation is that, even in low charge mass cases, the bulk of early time decomposition occurs in less than 5ms. In larger charge mass cases, these interactions could essentially be complete after a single scan of the spectrometer. These tests demonstrate that the designed spectrometer can be used to measure explosive environments, although future explosive decomposition studies would benefit greatly from increased spectrometer speeds.

Another observation comes from the stacked absorption plots from Test 1. From the first to the second to the third scans, the DIMP signal vanishes then reappears. This behavior suggests that the blast wave physically pushes the DIMP vapor out of the measurement path in some cases. Later time reemergence of DIMP signal in cases without complete decomposition suggests that either displaced DIMP or DIMP originally far from the charge is not destroyed by the weakening blast, and this DIMP travels back into the path while the chamber settles. Unsurprisingly, this suggests significant spatial variation in the explosive chamber that would be worth studying, and this can be done with the two heights of optical path allowed by the current chamber.

Finally, DIMP decomposition has been shown to be highly dependent on the available oxygen in these tests. Despite comparable charge masses, Test 1 and Test 4 behaved very differently with the nitrogen-filled Test 4 showing much less decomposition. In fact, increasing charge mass by almost a factor of three in Test 6 with nitrogen fill still resulted in less DIMP destruction than Test 1. Further investigations would need to continue testing this oxygen dependence.

CHAPTER 5: CONCLUSIONS AND FUTURE WORK

5.1. Conclusions

This research has resulted in the construction and validation of a new infrared diagnostic instrument that outperforms all other instruments in the longwave infrared in terms of its combined scan width, scan speed, and spectral resolution. The instrument is a rotating grating dispersive scanning spectrometer which scans at an average repetition rate of 1.2 kHz through 37,000 rpm rotation of a single diffraction grating. Unlike other similar instruments, the designed spectrometer is high throughput at f/2, but it retains $10cm^{-1}$ spectral resolution through careful design to minimize optical aberrations. The existence of this new spectrometer is a significant achievement in that it allows for high value measurements not previously available.

Another significant outcome of this research has been the development of an experimental technique that allows for the measurement of chemical nerve agent simulants inside fireballs. A test chamber was built, and operating procedures have been developed specifically for these measurements to assist in the validation of computation models. The technique and instrument together allow for previously unobtainable measurements to be obtained on nerve agent destruction in previously unmeasured transient fireball environments. These measurements in turn provide highly valuable information for CWMD agent defeat in the form of validation data for computational models. Applicability of the instrument and technique extends far beyond the experiments discussed to a wide range of agent simulants and fireball types.

Finally, this research has resulted in the successful completion of the stated research goal: to collect a robust set of benchmark data on DIMP decomposition inside fireball environments. Four closed bomb environments with distinct reactant conditions and measurably distinct burn profiles have been extensively tested, and repeat time-resolved LWIR absorbance spectra have been obtained for each. Additionally, multiple repeat measurements of highly temperature sensitive UV OH absorbance spectra have been collected for each case. Together, these two data sets allow for validation of computational models both in terms of DIMP decomposition behavior and predicted temperature. These validations can be performed through comparison of collected spectra with model simulated spectra, a technique which circumvents the issue of path averaging present in

absorption measurements. If a model accurately predicts path averaged spectra, then relevant reaction rates and pathways can be determined from model predicted values.

In terms of the quality of data obtained from the devised experiment and spectrometer, the following conclusions can be made. Experimental test conditions aside from DIMP vapor present at time of ignition have been proven to be highly repeatable through comparison of burn pressure profiles and OH absorbance signatures across multiple repeats. The source of experimental variability in DIMP decomposition measurements is attributed primarily to the amount of DIMP vapor present. Measurement of DIMP absorbance pre-fire across many tests show very good repeatability in DIMP vapor, with some variability. While DIMP vapor variability is generally small, the effect of that variability on the mixture burn parameters can be significant depending on the case studied.

Validation of computational models in these measured transient fireball environments constitutes a significant step toward the ultimate goal of developing predictive models for nerve agent defeat in real-world applications. Such applications would likely involve explosive fireballs which are highly complex and difficult to simulate environments. It is necessary that such models be validated in incremental steps of increasing complexity. The closed bomb environments tested are a valuable step in complexity for which no explicit validation data had previously been obtained.

5.2. Future Work

Future work regarding this instrument and experiment can broadly be grouped into two categories: System Improvements and Future Experiments.

5.2.1. *System Improvements*

Increase Scan Frequency

Spectral collection frequency could be increased by a factor of two or three by increasing the number of gratings in the grating mount. Concepts for two grating and three grating systems are in the early stages of development. These designs would by necessity push the gratings' reflective surfaces off of the axis of rotation, causing complications. Primarily, the gratings' position will change along with their angles, moving the grating out of the path of the collimated beam. Strategies will need to be developed for maintaining that the

entire collimated beam impacts the diffraction grating throughout the full range of grating rotation required.

Implement Trigger Timing

A fairly simple improvement would be to trigger the spark timing based on the position of the rotating grating. Adding this feature would allow for the timing of the first scan after ignition to be controlled, either improving consistency of scan timing between tests or allowing tight control for capturing very early time features.

Window Polishing

As described, the infrared windows used required periodic polishing due to window fouling. In the process of polishing the windows, approximately two minutes are needed for the actual polishing process while about 4 hours are needed for cooling and reheating the chamber. These large swaths of down time could be mitigated by devising a way to polish the windows without removing them. An additional benefit of this would be that the windows could be polished between every test, reducing uncertainty associated with variable transmittance from test to test.

Independent Flash Intensity Measurement

Incorporating an independent measurement of flash signal intensity that would improve the accuracy of flash signal corrections would further improve measured results. A non-spectral measurement of LWIR light intensity, such as through a photodiode or other MCT detector with direct line of sight to the chamber interior, may provide such a measurement.

5.2.2. *Future Experiments*

Investigate DIMP evaporation phenomena

The observed variability in initial DIMP signature and the observed increase then decrease in pressure following DIMP injection warrant further study. This is an area in which collaboration with Dr. Mark Phillips could prove very beneficial, as his system is well suited to taking measurements on the multi-seconds to minutes long timescales over which pressure variations were observed. Alternatively, the existing spectrometer system could be modified with a slower regulated speed motor, allowing for measurements over longer

timescales. If further investigation supports the hypothesis that the aluminum oxide layer is the cause of evaporation variability, coating the chamber's interior surface with a non-reactive material may be beneficial.

Higher Pressure Cases

Experimental conditions in this work were chosen to keep burn pressures conservatively low so as to ensure the integrity of chamber windows. A future test of developed models would involve measurements at increased pressures, more akin to those found in explosive fireballs.

Lower DIMP Concentration Cases

These tests were all performed with DIMP vapor concentrations that resulted in initial DIMP absorbance close to 4, which a very high absorbance value. Therefore, these measurements could be performed with less DIMP vapor. This may have the added benefit of reducing burn variability due to variation in DIMP vapor.

Progress to increasingly complex hydrocarbon fuels

Hydrogen fuel was used in this study as it is the simplest fuel to model. More rigorous tests of developed models will be performed with more complex fuels which would greatly complicate chemical kinetics. Additional tests can be performed on progressively more complex hydrocarbon fuels, e.g. CH_4 or C_2H_6.

Explosive Fireball Experiments

Ultimate model validation requires measurements be made in the explosive fireball environment. Preliminary measurements of DIMP destruction in explosive fireballs have been made as part of this work. These results show that measurement speeds greater than 1.2 kHz are needed for the explosive fireball. Additional experiments can be made in a wider range of explosive fireballs once scan frequency improvements are made.

References

[1] Afshari Reza, “Use of Chemical Wafare Agents in Ancient History,” *Asia Pac J. Med Toxicol*, vol. 7, pp. 54–59, 2018.

[2] M. Hughes and W. J. Philpott, “THE PALGRAVE CONCISE HISTORICAL ATLAS OF THE FIRST WORLD WAR,” 2005.

[3] James Brown Scott, Ed., *The Hague Conventions and Declarations of 1889 and 1907 accompanied by Tables of Signatures, Ratifications and Adhesions of the Various Powers, and Texts of Reservations*. 1915.

[4] K. Coleman, *A History of Chemical Warfare*. 2005.

[5] “Protocol for the Prohibition of the Use in War of Asphyxiating, Poisonous or Other Gases, and of Bacteriological Methods of Warfare (Geneva Protocol).” https://2009-2017.state.gov/t/isn/4784.htm (accessed Sep. 12, 2022).

[6] UN. General Assembly (32nd sess. : 1977), “32/84. Prohibition of the development and manufacture of new types of weapons of mass destruction and new systems of such weapons.”

[7] S. OZDEMİR, “Iran-Iraq War: The Employment of Chemical Weapons,” *The Journal of Iranian Studies*, vol. 6, no. 1, pp. 105–133, 2022, doi: 10.33201/iranian.1084350.

[8] S. Rose and A. Baravi, “The meaning of Halabja: chemical warfare in Kurdistan,” *Race Cl*, vol. 30, no. 1, pp. 74–77, 1988.

[9] A. T. Tu, “Aum Shinrikyo’s Chemical and Biological Weapons: More Than Sarin,” *Forensic Sci Rev*, vol. 26, no. 2, 2014, [Online]. Available: www.forensicsciencereview.com

[10] M. M. Blum and R. V. S. M. Mamidanna, “Analytical chemistry and the Chemical Weapons Convention,” *Anal Bioanal Chem*, vol. 406, no. 21, pp. 5067–5069, 2014, doi: 10.1007/s00216-014-7931-4.

[11] J. Zarocostas, “Syria chemical attacks: preparing for the unconscionable,” *Lancet*, vol. 389, no. 10078, p. 1501, Apr. 2017, doi: 10.1016/S0140-6736(17)30997-2.

[12] N. B. Munro *et al.*, “RESEA The Sources, Fate, and Toxicity of Chemical Warfare Agent Degradation Products,” 1999. [Online]. Available: http://ehpnetl.niehs.nihgov/docs/l999/107p933-974munro/abstract.html

[13] Y.-C. Yang, J. A. Baker, and J. R. Ward, “Decontamination of Chemical Warfare Agents,” 1992. [Online]. Available: https://pubs.acs.org/sharingguidelines

[14] L. Bromberg and T. A. Hatton, “Nerve agent destruction by recyclable catalytic magnetic nanoparticles,” *Ind Eng Chem Res*, vol. 44, no. 21, pp. 7991–7998, Oct. 2005, doi: 10.1021/ie0506926.

[15] D. A. Trubitsyn and A. v. Vorontsov, “Experimental study of dimethyl methylphosphonate decomposition over anatase TiO2,” *Journal of Physical Chemistry B*, vol. 109, no. 46, pp. 21884–21892, Nov. 2005, doi: 10.1021/jp053793q.

[16] S.-T. Lin and K. J. Klabunde, “Thermally Activated Magnesium Oxide Surface Chemistry. Adsorption and Decomposition of Phosphorus Compounds,” 1985. [Online]. Available: https://pubs.acs.org/sharingguidelines

[17] M. B. Mitchell, V. N. Sheinker, and E. A. Mintz, “Adsorption and Decomposition of Dimethyl Methylphosphonate on Metal Oxides,” *Journal of Physical Chemistry*, vol. 101, pp. 11192–11203, 1997, [Online]. Available: https://pubs.acs.org/sharingguidelines

[18] A. Knott *et al.*, “Subscale testing of prompt agent defeat formulations,” in *AIP Conference Proceedings*, Jan. 2017, vol. 1793. doi: 10.1063/1.4971529.
[19] R. M. Mohamed, “UV-assisted photocatalytic synthesis of TiO2-reduced graphene oxide with enhanced photocatalytic activity in decomposition of sarin in gas phase,” *Desalination Water Treat*, vol. 50, no. 1–3, pp. 147–156, Dec. 2012, doi: 10.1080/19443994.2012.708560.
[20] J. Epstein *et al.*, “The Chlorine-catalyzed Hydrolysis of Isopropyl Methylphosphonofluoridate (Sarin) in Aqueous Solution,” 1956. [Online]. Available: https://pubs.acs.org/sharingguidelines
[21] X. Shan, J. C. Vincent, S. Kirkpatrick, M. D. Walker, M. R. Sambrook, and D. C. Clary, “A Combined Theoretical and Experimental Study of Sarin (GB) Decomposition at High Temperatures,” *Journal of Physical Chemistry A*, vol. 121, no. 33, pp. 6200–6210, Aug. 2017, doi: 10.1021/acs.jpca.7b04282.
[22] R. S. Thompson, M. R. Brann, E. H. Purdy, J. D. Graham, A. A. McMillan, and S. J. Sibener, “Rapid Laser-Induced Temperature Jump Decomposition of the Nerve Agent Simulant Diisopropyl Methylphosphonate under Atmospheric Conditions,” *Journal of Physical Chemistry C*, vol. 123, no. 35, pp. 21564–21570, Jun. 2019, doi: 10.1021/acs.jpcc.9b05381.
[23] E. J. P. Zegers and E. M. Fisher, “Gas-phase pyrolysis of diethyl methylphosphonate,” *Combustion Science and Technology*, vol. 116–117, no. 1–6, pp. 69–89, 1996, doi: 10.1080/00102209608935544.
[24] B. Yuan and H. Eilers, “T-jump pyrolysis and combustion of diisopropyl methylphosphonate,” *Combust Flame*, vol. 199, pp. 69–84, Jan. 2019, doi: 10.1016/j.combustflame.2018.10.013.
[25] O. P. Korobeinichev, A. A. Chernov, and T. A. Bolshova, “The Chemistry of the Destruction of Organophosphorus Compounds in Flames-IV: Destruction of DIMP in a Flame of H 2 O 2 Ar,” *Combust Flame*, vol. 123, pp. 412–420, 2000.
[26] S. Neupane *et al.*, “Shock Tube/Laser Absorption and Kinetic Modeling Study of Triethyl Phosphate Combustion,” *Journal of Physical Chemistry A*, vol. 122, no. 15, pp. 3829–3836, Apr. 2018, doi: 10.1021/acs.jpca.8b00800.
[27] E. I. Senyurt, M. Schoenitz, and E. L. Dreizin, “Rapid destruction of sarin surrogates by gas phase reactions with focus on diisopropyl methylphosphonate (DIMP),” *Defence Technology*, vol. 17, no. 3. China Ordnance Industry Corporation, pp. 703–714, Jun. 01, 2021. doi: 10.1016/j.dt.2020.06.008.
[28] R. K. Hanson, R. M. Spearrin, and C. S. Goldenstein, “Quantitative Emission and Absorption,” in *Spectroscopy and Optical Diagnostics for Gases*, Springer, 2016, pp. 107–130.
[29] A. J. Mott and P. Rez, “Calculated infrared spectra of nerve agents and simulants,” *Spectrochim Acta A Mol Biomol Spectrosc*, vol. 91, pp. 256–260, Jun. 2012, doi: 10.1016/j.saa.2012.02.010.
[30] P. J. Linstrom and W. G. Mallard, Eds., *NIST Chemistry WebBook, NIST Standard Reference Database Number 69*.
[31] Boston Electronics, “IR-Si207 Emitter Datasheet.” [Online]. Available: www.boselec.com
[32] C. A. Mitchell, “Emissivity of Globar,” 1962.
[33] C. S. Rupert and J. Strong, “The Carbon Arc as an Infra-Red Source,” *J Opt Soc Am*, vol. 40, no. 7, pp. 455–459, 1950.

[34] C. S. Rupert, “Letters to the Editor A Water-Cooled Carbon Arc Source for Infrared Spectroscopy.”
[35] Z. Men, W. P. Bassett, K. S. Suslick, and D. D. Dlott, “Drop hammer with high-speed thermal imaging,” *Review of Scientific Instruments*, vol. 89, no. 11, Nov. 2018, doi: 10.1063/1.5051357.
[36] Z. Men, K. S. Suslick, and D. D. Dlott, “Thermal Explosions of Polymer-Bonded Explosives with High Time and Space Resolution,” *Journal of Physical Chemistry C*, vol. 122, no. 26, pp. 14289–14295, Jul. 2018, doi: 10.1021/acs.jpcc.8b02422.
[37] B. C. Smith, “How an FTIR Works,” in *Fundamentals of Fourier transform infrared spectroscopy*, CRC Press, 2011, pp. 19–54.
[38] A. Dutta, “Fourier Transform Infrared Spectroscopy,” in *Spectroscopic Methods for Nanomaterials Characterization*, vol. 2, Elsevier, 2017, pp. 73–93. doi: 10.1016/B978-0-323-46140-5.00004-2.
[39] “FT-IR Spectrometers.” https://www.thermofisher.com/search/browse/category/us/en/90207117/ft-ir+spectrometers (accessed Sep. 22, 2022).
[40] N. Pelin Ayerden *et al.*, “High-speed broadband FTIR system using MEMS,” *Appl Opt*, vol. 53, no. 31, p. 7267, Nov. 2014, doi: 10.1364/ao.53.007267.
[41] S. P. Heussler *et al.*, “Pulsed and high-speed FTIR spectroscopy,” in *Next-Generation Spectroscopic Technologies V*, May 2012, vol. 8374, p. 83740T. doi: 10.1117/12.919533.
[42] R. K. Rahman, J. Higgs, E. Ninnemann, J. Baker, A. E. Masunov, and S. S. Vasu, “Direct measurement of reaction rate for decomposition of diisopropyl methylphosphonate at high temperature using shock tube and laser absorption,” *Int J Chem Kinet*, vol. 54, no. 6, pp. 371–380, Jun. 2022, doi: 10.1002/kin.21566.
[43] M. C. Phillips and B. E. Brumfield, “ECQCL developments for rapid standoff chemical sensing,” in *Micro- and Nanotechnology Sensors, Systems, and Applications IX*, May 2017, vol. 10194, p. 101942T. doi: 10.1117/12.2263701.
[44] M. C. Phillips and B. E. Brumfield, “Standoff detection of turbulent chemical mixture plumes using a swept external cavity quantum cascade laser,” *Optical Engineering*, vol. 57, no. 01, p. 1, Aug. 2017, doi: 10.1117/1.oe.57.1.011003.
[45] M. C. Phillips, B. E. Bernacki, S. S. Harilal, J. Yeak, and R. J. Jones, “Standoff chemical plume detection in turbulent atmospheric conditions with a swept-wavelength external cavity quantum cascade laser,” *Opt Express*, vol. 28, no. 5, p. 7408, Mar. 2020, doi: 10.1364/oe.385850.
[46] G. C. Pimentel, “Rapid Advances in Rapid Scan Spectroscopy,” *Appl Opt*, vol. 7, no. 11, pp. 2155–2160, 1968.
[47] M. Kozuka and T. Isobe, “Infrared Absorption Spectrum of Gaseous CF3CO Radical; Recording on a Rapid-Scan Infrared Spectrometer,” *Bull Chem Soc Jpn*, vol. 49, no. 7, pp. 1766–1771, 1976.
[48] K. C. Herr and G. C. Pimentel, “A Rapid-Scan Infrared Spectrometer; Flash Photolytic Detection of Chloroformic Acid and of CF,” *Appl Opt*, vol. 4, no. 1, pp. 25–30, 1965.
[49] R. J. Jensen and G. C. Pimentel, “Kinetics of Decomposition of Chloroformic Acid Kinetics of Decomposition of Chloroformic Acid by Rapid-Scan Infrared Spectroscopy,” 1963. [Online]. Available: https://pubs.acs.org/sharingguidelines

[50] L. Y. Tan, A. M. Winer, and G. C. Pimentel, “Infrared spectrum of gaseous methyl radical by rapid scan spectroscopy,” *J Chem Phys*, vol. 57, no. 9, pp. 4028–4037, 1972, doi: 10.1063/1.1678876.
[51] T. Ogawa, G. A. Carlson, and G. C. Pimentel, “Reaction Rate of Trifluoromethyl Radicals Experimental Section,” *J Phys Chem*, vol. 74, no. 10, pp. 2090–2095, 1970.
[52] R. M. Hexter and C. W. Hand, “Infrared Spectroscopy at 20,000 Scans per Second,” *Appl Opt*, vol. 7, no. 11, pp. 2161–2165, 1968.
[53] C. W. Hand, P. Z. Kaufmann, and R. M. Hexter, “Kinetic Spectroscopy in the Infrared: a Rapid-Scan Infrared Spectrometer,” *Appl Opt*, vol. 5, no. 7, pp. 1097–1104, 1966.
[54] J. M. Lerner and A. Thevenon, “THE OPTICS OF SPECTROSCOPY A TUTORIAL.”
[55] Shelley Wright, “Crash course in intro to optics,” 2017.
[56] “LN2 Cooled HgCdTe Detectors.” http://irassociates.com/index.php?page=ln2-cooled (accessed Sep. 22, 2022).
[57] A. Kramida, Y. Ralchenko, and NIST ASD Team, “NIST Atomic Spectra Database,” *National Institute of Standards and Technology, Gaithersburg, MD.*, 2021. https://physics.nist.gov/asd (accessed Sep. 26, 2022).
[58] G. T. Fraser and S. J. Choquette, “Nation Institute of Standards and Technology Certificate - Standard Reference Material 1921b,” 2021.
[59] A. B. Butrow, J. H. Buchanan, and D. E. Tevault, “Vapor pressure of organophosphorus nerve agent simulant compounds,” *J Chem Eng Data*, vol. 54, no. 6, pp. 1876–1883, Jun. 2009, doi: 10.1021/je8010024.
[60] “XTEL-190 Miniature Ruggedized High Temperature Pressure Transducer.” https://kulite.com/products/product-advisor/product-catalog/miniature-ruggedized-high-temperature-pressure-transducer-xtel-190m/ (accessed Aug. 10, 2022).
[61] O. P. Korobeinichev, V. M. Shvartsberg, and A. G. Shmakov, “The chemistry of combustion of organophosphorus compounds,” *Russian Chemical Reviews*, vol. 76, no. 11, pp. 1094–1121, Nov. 2007, doi: 10.1070/rc2007v076n11abeh003713.
[62] E. J. P. Zegers and E. M. Fisher, “Gas-Phase Pyrolysis of Diisopropyl Methylphosphonate,” *Combust Flame*, vol. 115, pp. 230–240, 1998.
[63] A. T. Hartlieb, B. Atakan, and K. Kohse-Höinghaus, “Applied Physics B Lasers and Optics Temperature measurement in fuel-rich non-sooting low-pressure hydrocarbon flames,” *Appl. Phys. B*, vol. 70, pp. 435–445, 2000, doi: 10.1007/s003409900144.
[64] S. M. Jo, H. Shim, G. Park, O. J. Kwon, and J. G. Kim, “Temperature determination in a shock tube using hydroxyl radical A-X band emission,” *Physics of Fluids*, vol. 31, no. 2, Feb. 2019, doi: 10.1063/1.5082240.
[65] M. F. Foltz, “Aging of Pentaerythritol Tetranitrate (PETN),” 2009.

APPENDIX A: 1MHz COMBUSTION CHAMBER DATA

Case A

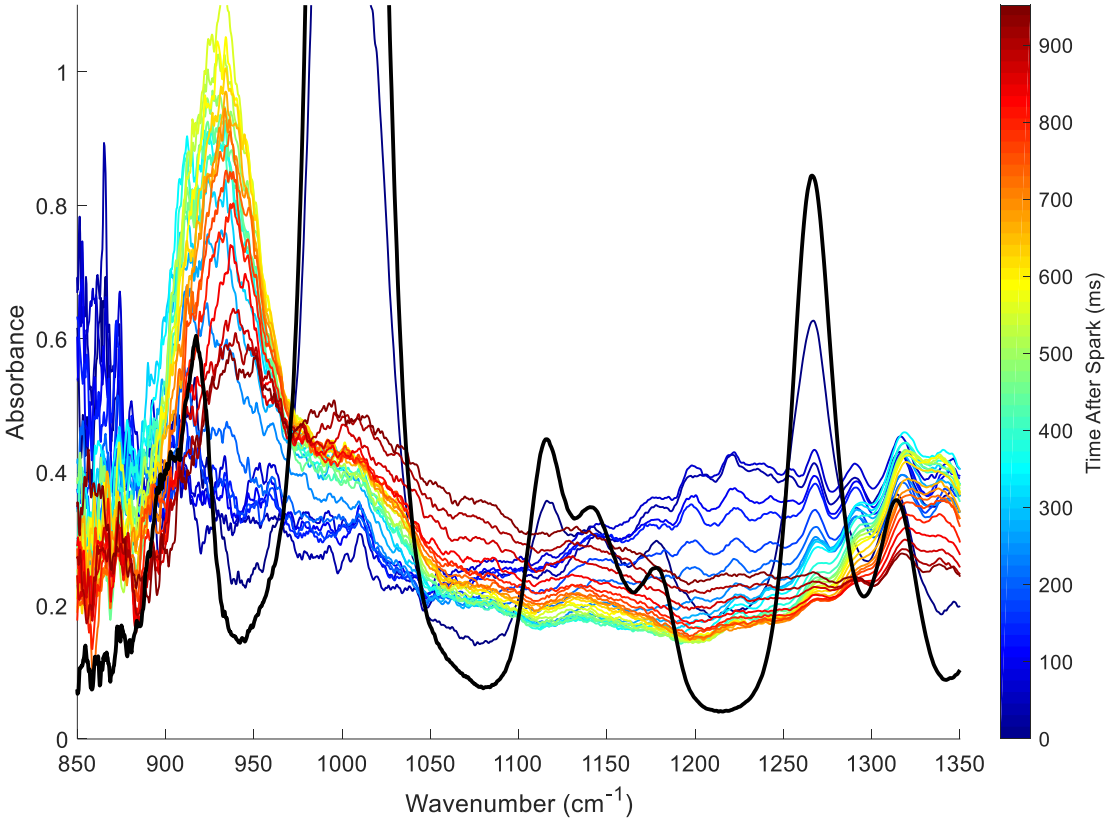

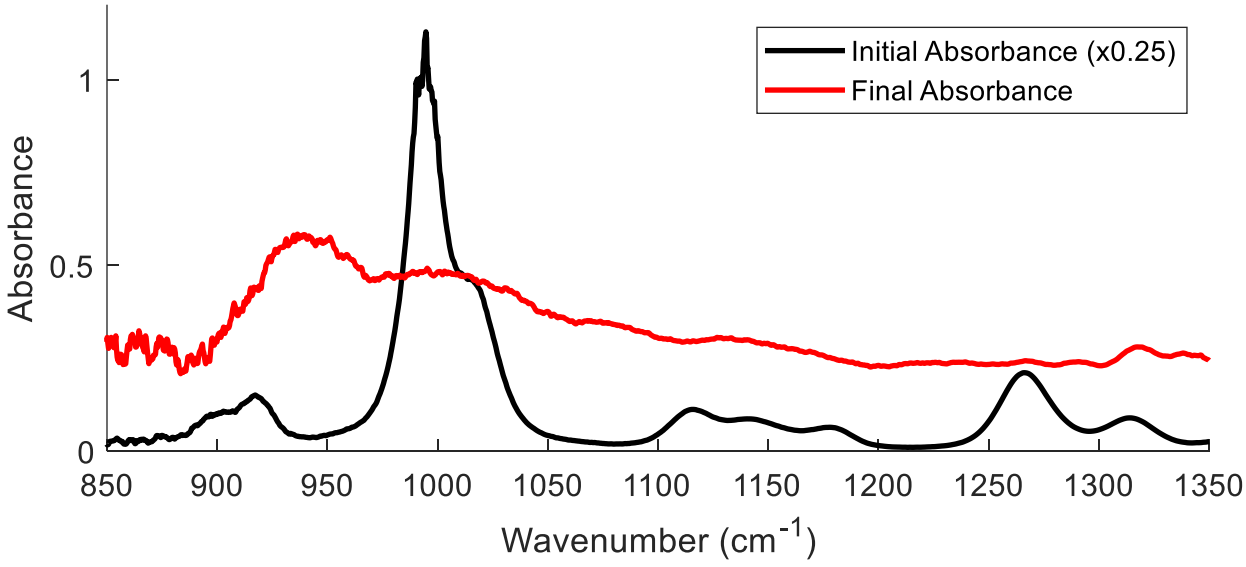

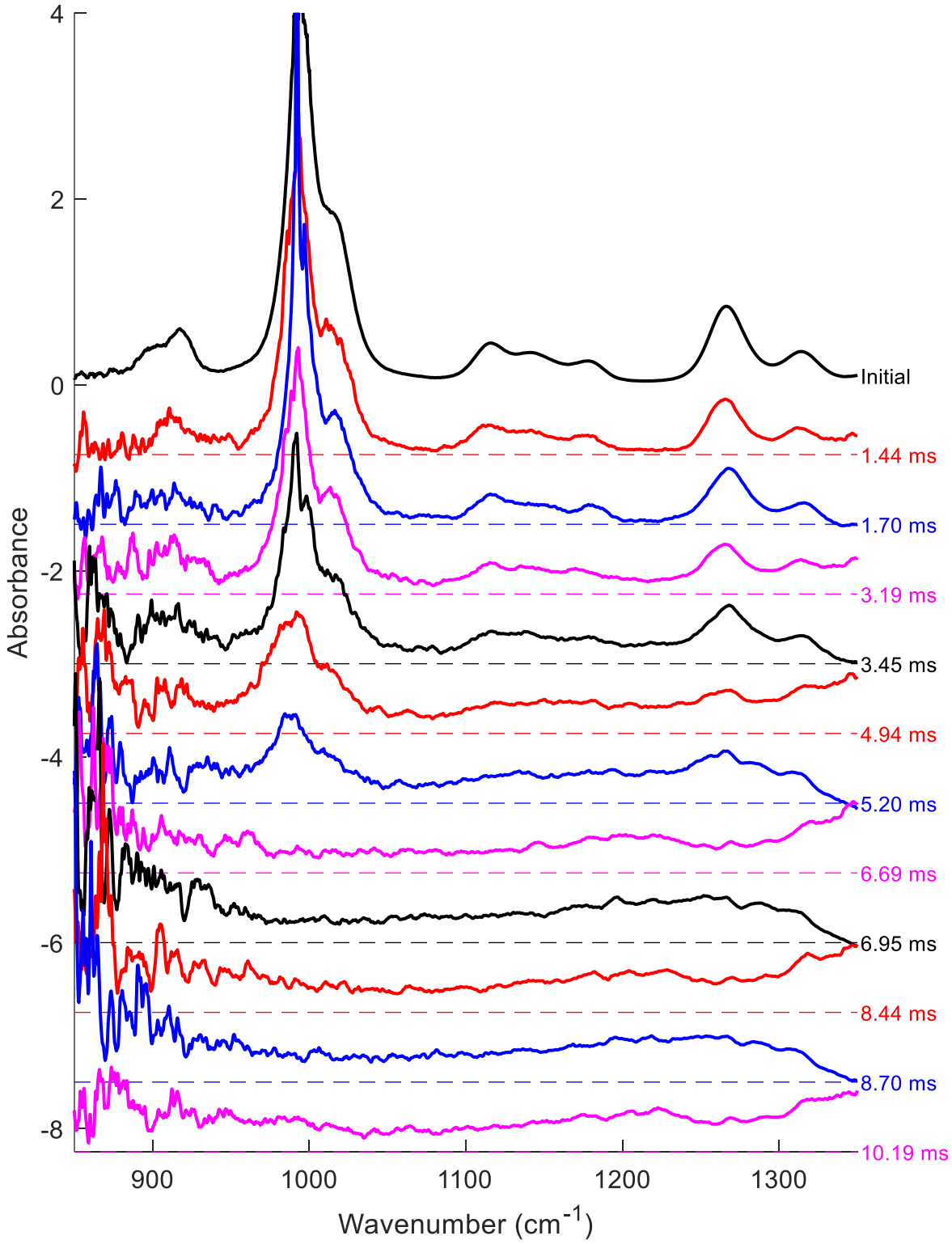
4
2
0
-2
-4
-6
-8
Absorbance
900
1000
1100
1200
1300
Wavenumber (cm-1)
Initial
1.44 ms
1.70 ms
3.19 ms
3.45 ms
4.94 ms
5.20 ms
6.69 ms
6.95 ms
8.44 ms
8.70 ms
10.19 ms

Case B

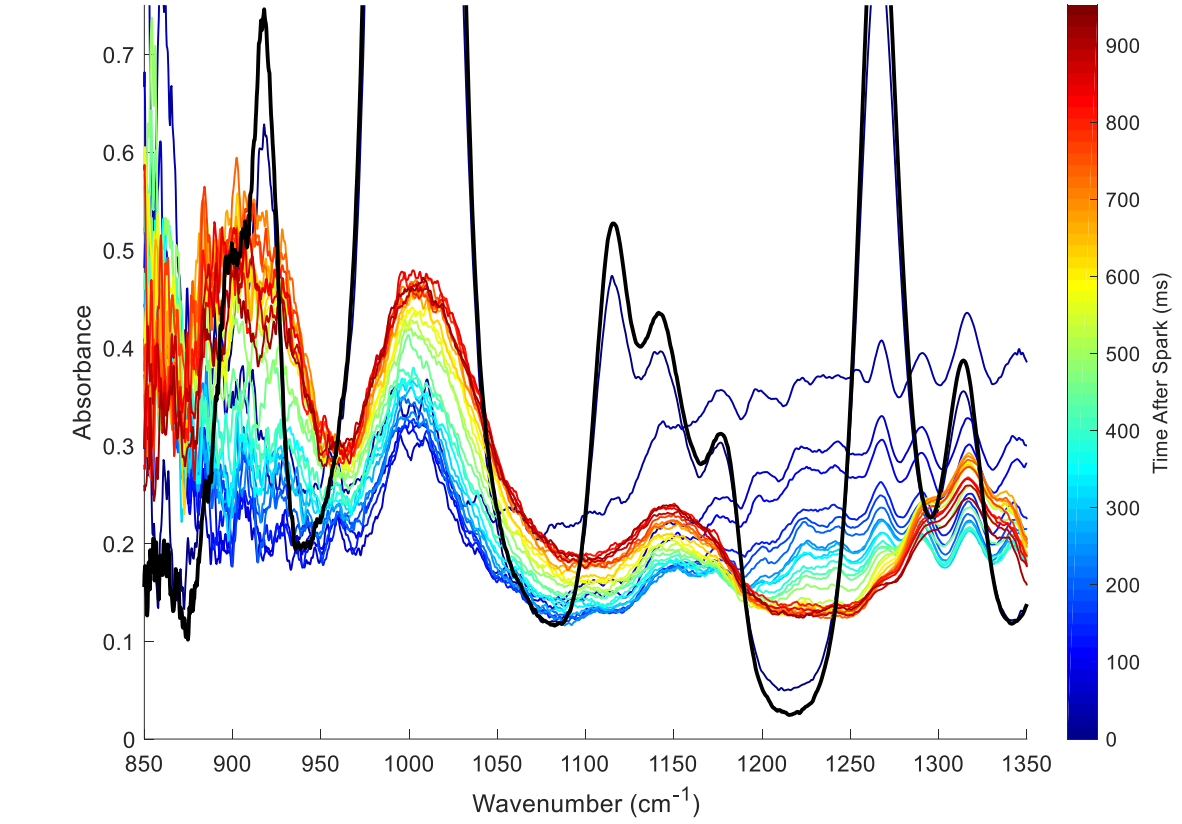
Absorbance
Wavenumber (cm-1)
Time After Spark (ms)
0
0.1
0.2
0.3
0.4
0.5
0.6
0.7
850
900
950
1000
1050
1100
1150
1200
1250
1300
1350
0
100
200
300
400
500
600
700
800
900

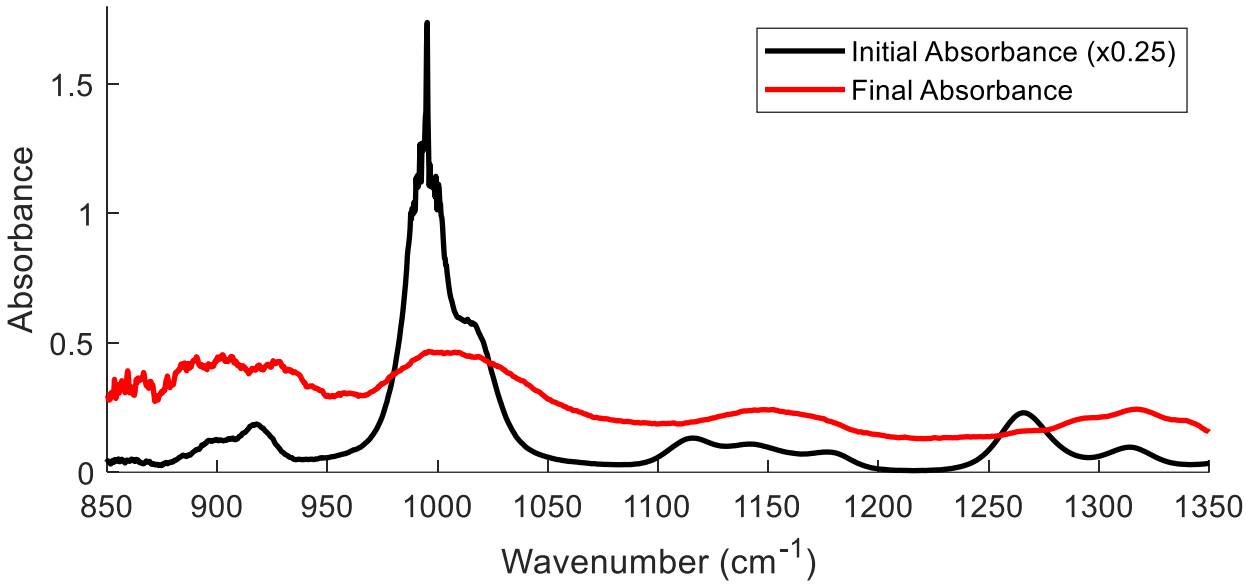
Initial Absorbance (x0.25)
Final Absorbance
Absorbance
Wavenumber (cm-1)
0
0.5
1
1.5
850
900
950
1000
1050
1100
1150
1200
1250
1300
1350

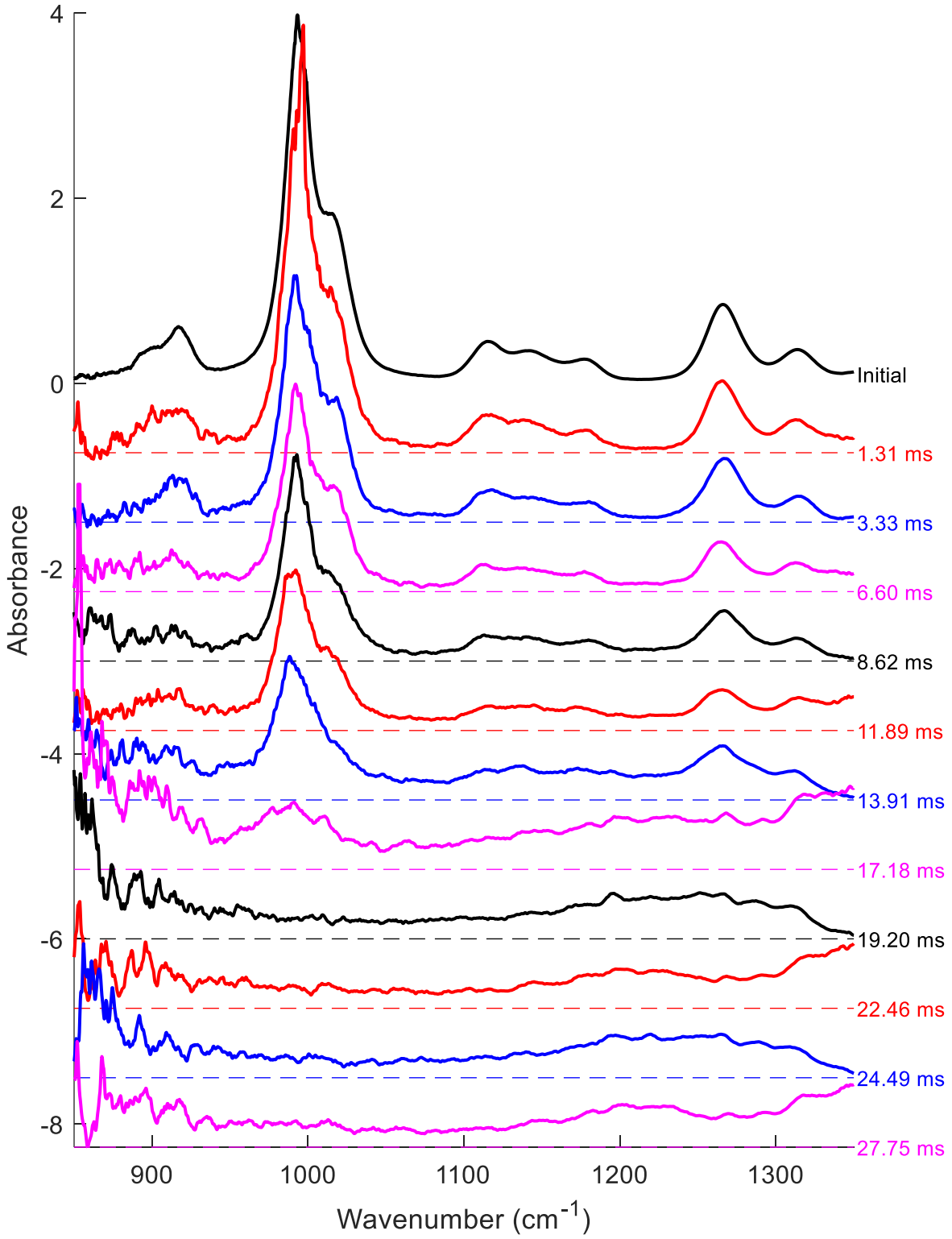
4
2
0
-2
-4
-6
-8
Absorbance
900
1000
1100
1200
1300
Wavenumber (cm-1)
Initial
1.31 ms
3.33 ms
6.60 ms
8.62 ms
11.89 ms
13.91 ms
17.18 ms
19.20 ms
22.46 ms
24.49 ms
27.75 ms

APPENDIX B: SPHERICAL CHAMBER DRAWINGS

Half 1

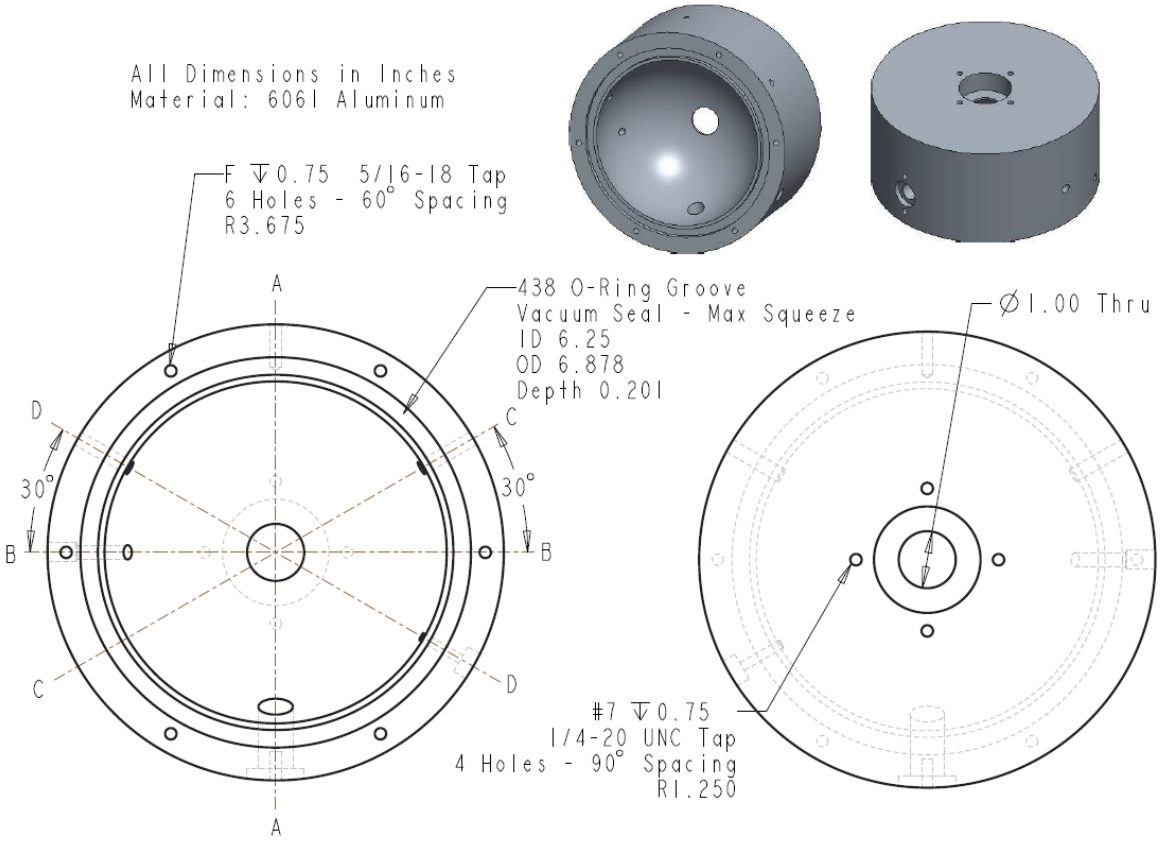

SECTION A-A

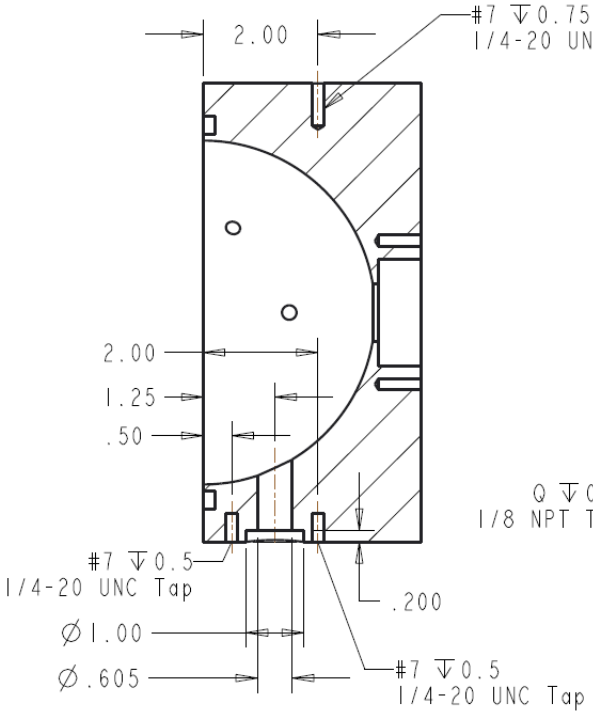

SECTION B-B

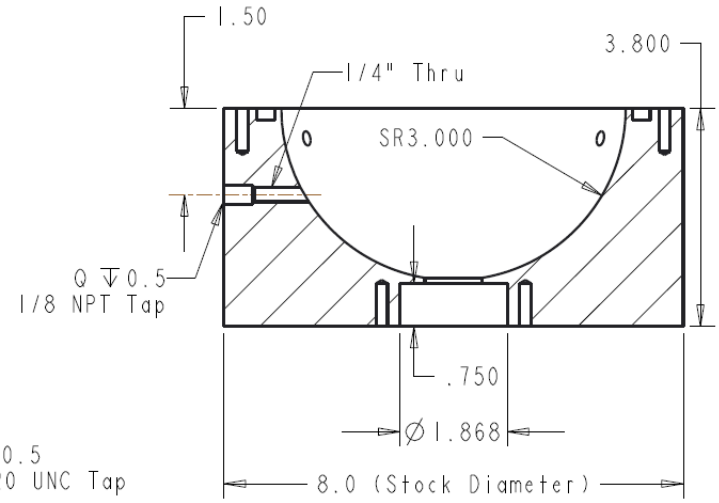

SECTION C-C

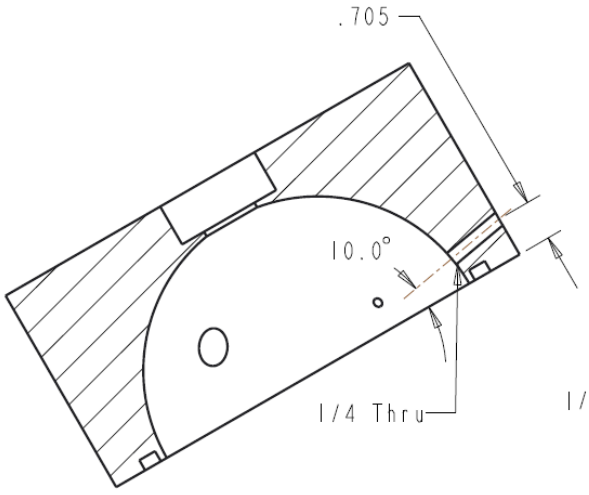

SECTION D-D

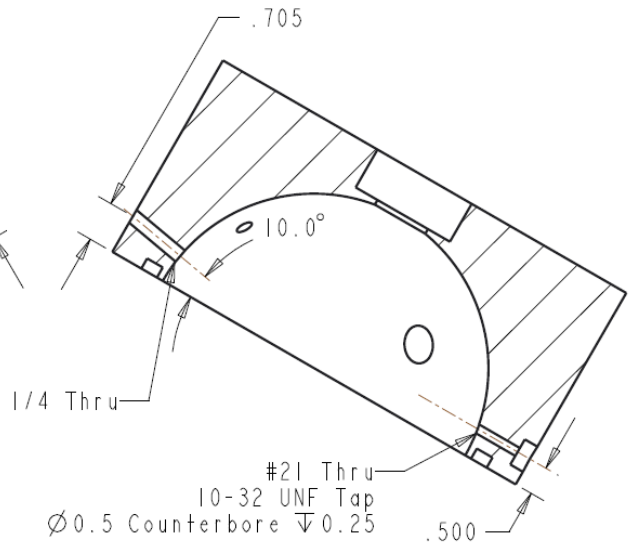

Half 2

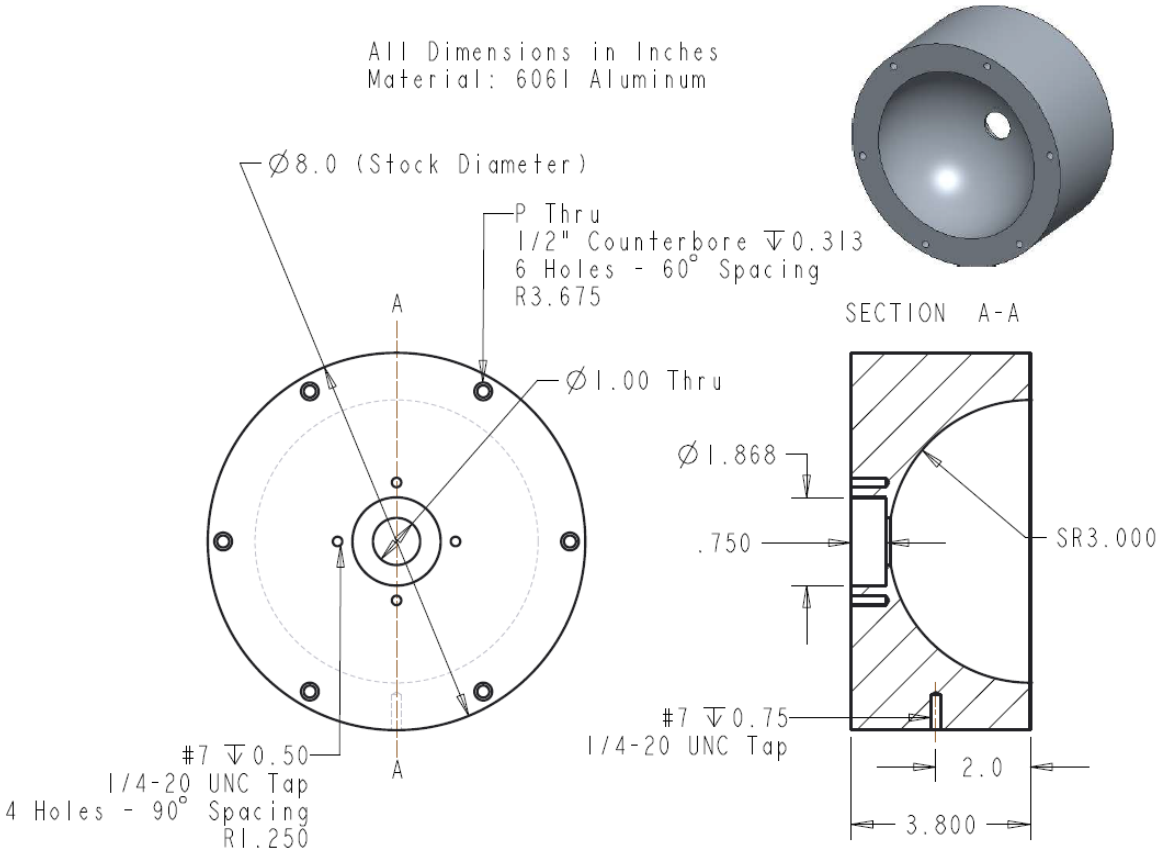
All Dimensions in Inches
Material: 6061 Aluminum
Ø8.0 (Stock Diameter)
P Thru
1/2" Counterbore ↧0.313
6 Holes - 60° Spacing
R3.675
Ø1.00 Thru
A
A
#7 ↧0.50
1/4-20 UNC Tap
4 Holes - 90° Spacing
R1.250
SECTION A-A
Ø1.868
.750
SR3.000
#7 ↧0.75
1/4-20 UNC Tap
2.0
3.800